Corrosion of Aluminium Alloys used in Automotive Radiators

by

Barbara Mariëlle de Leeuw, BSc. (Hons).

Submitted in partial fulfilment of the academic requirements for the degree of Master of Science in the School of Chemical and Physical Sciences,
University of Natal, Pietermaritzburg, June 1999.

THIS THESIS IS DEDICATED TO THE LOVING MEMORY OF MY BROTHER, RENÉ

(29/8/74 – 15/1/97)

ABSTRACT

The replacement of copper/brass radiators in the automotive industry with radiators made from aluminium components provided the basis of this research. Since aluminium is more susceptible to corrosion than either copper or brass, factors that contribute to its corrosion are of major interest and importance, and have been investigated. Three different aluminium alloys were selected for study because of a special interest in their corrosive behaviour by the automotive industry. These are the aluminium alloy AA 3003 (samples A and B) and two supplier specific alloys (sample D containing Zn and sample E containing Cu and Mg).

The various joining operations used in the automotive manufacturing process dictated the preparation of the aluminium alloys used for corrosion studies. Mechanically Assembled (MA) aluminium radiators use alloy samples as supplied by the aluminium industry and hence suitable experiments were carried out on the 'as-supplied' (AS) samples used for both finstock and tubestock material. The development of Composite Deposition (CD) Technology to braze together finstock and tubestock material introduced new challenges to corrosion research. To gain an insight into the corrosion of a Brazed aluminium radiator, all samples were subjected to a thermal profile identical to that experienced industrially under a Controlled Atmosphere Brazing (CAB) furnace. Two cases of interest emerged. Firstly the 'heat-treated' (HT) samples were used to evaluate the effect of heat treatment on the alloy's resistance to corrosion. Secondly, alloy samples treated with a Composite Powder Coating (CPC) and then subjected to the thermal profile provided a surface of an Al-Si melt which represented the brazed joint. Experiments on these samples yielded information on the Al-Si melt and the likely corrosion in a brazed joint.

The resulting corrosion of the AS, HT and CPC samples immersed in various corrosive electrolyte solutions for 60 minutes was examined using two microscopic techniques. Firstly, the actual surface pitting was examined using a Scanning Electron Microscope (SEM), and secondly, cross-sections of the samples mounted in a resin, then suitably polished and etched were examined using an optical microscope to further reveal the nature of corrosion of the samples. The nature of corrosion was best revealed in an acidified chloride solution. The AS samples showed delocalised crystallographic pitting consisting of coalesced pits at localised regions of the surface. The HT samples showed

localised crystallographic pitting consisting of many individual pits and intergranular corrosion both at and below the surface. Intergranular corrosion was most severe for HT sample E containing Cu and Mg. The CPC samples showed total corrosion of the surface layer and eutectic Al-Si melt, some crystallographic pitting of the α-Al filler metal, and crystallographic pitting including intergranular corrosion of the base alloy. The extent of corrosion was found to depend on the chemical composition of the aluminium alloys, the presence of Zn, Cu and Mg causing more severe corrosion of the aluminium alloys, with the effect of Zn being most severe.

The electrochemical investigation involved the measurement of two fundamentally important parameters. Firstly, the open circuit potentials (OCP) of the alloy samples immersed in the various corrosive electrolyte solutions were measured as a function of time. Secondly, the pitting potentials (E_p) of the alloy samples were measured using anodic polarisation techniques by extrapolation of the resulting log i vs E plots. The OCP and E_p of the AS samples were found to be influenced by the chemical composition of the aluminium alloys. Heat treatment of the AS samples was found to change their microstructure and solid solution composition which in turn affected the electrochemical results. The effect of the Composite melt layer on the electrochemistry of the CPC samples is discussed.

Micrographic and electrochemical results were used to assess the best combination of finstock and tubestock material that would yield an aluminium radiator most resistant to corrosion. The likely corrosion of the components in these combinations was assessed and these results were compared with the actual results obtained industrially using the SWAAT exposure test.

DECLARATION

The experimental work described in this thesis was carried out in the Department of Chemistry at the University of Natal, Pietermaritzburg, under the supervision of Doctor D. Jaganyi and the co-supervision of Honorary Associate Professor W.A. Hawksworth.

I hereby certify that this research is the result of my own investigation, which has not already been accepted in any substance for any degree, and is not concurrently submitted in candidature for any other degree.

Signed: 

B.M. de Leeuw, BSc. (Hons).

I hereby certify that the above statement is correct.

Signed: 

Supervisor: Dr. D. Jaganyi, MSc, PhD.

Signed: 

Co-supervisor: Honorary Associate Professor
W.A. Hawksworth, MSc, PhD.

School of Chemical and Physical Sciences
The University of Natal
Pietermaritzburg

ACKNOWLEDGEMENTS

To Mum and Dad, thank you for all the love and support you have given me, for always being there for me, for believing in me, and for being just the way you are. I love you both very much.

I am indebted to many people and organisations for their assistance during the course of this work. Firstly, I would like to mention that the Honorary Associate Professor W.A. Hawksworth was the supervisor of this research project until his retirement and became my co-supervisor until its completion. I would like to thank him for his guidance, encouragement, criticism, invaluable discussions and advice, both his confidence and his extreme patience in me, and for keeping my spirits high during times of doubt. Thanks also for the interesting and entertaining stories as only he can tell, and for all the advice on life itself. I also thank Dr. D. Jaganyi, who became the supervisor of this project after Prof. Hawksworth's retirement, for his help and advice.

Next my sincere thanks go to Turner and Newell (T&N) Holdings and their subsidiary Ferodo Heat Exchangers (FHE), for providing the opportunity for undertaking this work and for the financial support they have given me over the years*. Special thanks go to Dr. D.K. Hawksworth and Neill Cameron for all their help and assistance and for entertaining me during the many hours spent grinding, polishing and photographing my samples. I would also like to thank Prof. J.V. Wood, Prof. S. Harris, Sunil Khosla and the Material Science and Engineering department at Nottingham University for the initial help they provided me on the SEM and optical microscope, as well as for the invaluable advice on electrochemical measurements of aluminium.

My sincere gratitude also goes to Janet Poulter at Pietermaritzburg University for all her help and to Fiona Graham at the SEM unit at Durban University. To the guys at the Mechanical Instrument workshop, Paul the Glassblower and the Electronics workshop, thank you for all the help building (and fixing) my equipment, and for making tea breaks what they are. Last but not least, I would like to thank Joanne Smith for her friendship, for always being there for me in times of need, and for all the great times we have had and no doubt will continue to have.

---

* At the conclusion of this research project the US company Federal Mogul bought out T&N Holdings and have subsequently sold FHE to Behr South Africa.

LIST OF CONTENTS

1 INTRODUCTION

A radiator is a heat exchanger and is a very important component of any automotive engine system. Its primary function is to dissipate the energy generated in the combustion chamber and allow the internal combustion engine to operate within a specified temperature range. All radiators comprise three essential components as shown in Figure 1.1. The radiator core consists of aluminium side casings, with the tubestock and finstock running horizontally between the heat resistant plastic header and footer tanks.

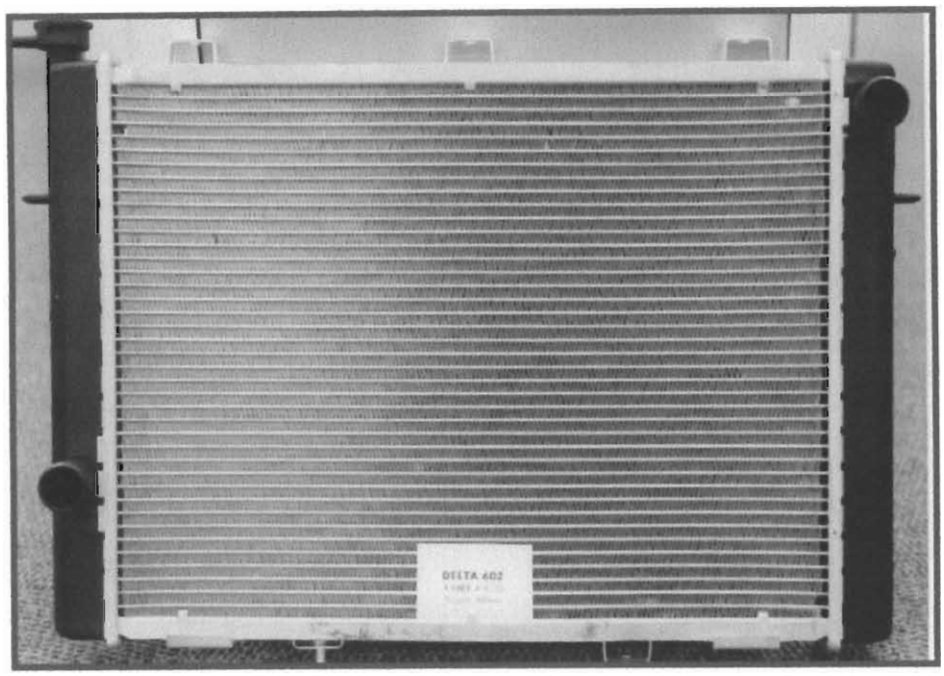

Figure 1.1 A typical radiator core.

Originally, all automotive radiators were made of a copper/brass combination that was chosen for its excellent thermal conductivity and resistance to corrosion. The rapid rise in world copper prices forced the automotive industries to source cheaper materials for radiator construction and this lead to the introduction of aluminium radiators. Besides the cost saving, a weight saving of 37% was also achieved [1]. Two major problems emerged as a result of the use of aluminium as a radiator material. Firstly the joining of the aluminium components was a major challenge, and secondly aluminium was more susceptible to corrosion than either copper or brass. These factors contribute to the

problem of designing heat exchangers that have higher levels of corrosion resistance and hence longer life expectancies.

Various component joining operations have been used in the manufacture of automotive aluminium radiators, among these are mechanical assembly, adhesive bonding and brazing. Nowadays brazing operations using a non-corrosive flux and clad-aluminium components are carried out predominantly under an inert nitrogen atmosphere in a funnel furnace. Brazing has also been carried out under vacuum. Alclad or clad-aluminium products are primarily used for sheet and tubestock material, and consist of a core clad to one or both surfaces with a metallurgically bonded layer of an alloy that is anodic to the core alloy, thus providing sacrificial protection.

The development of Composite Deposition (CD) Technology [2, 3] has allowed the brazing together of unclad aluminium components. The CD brazing process involves selective deposition and adherence of Composite Powder [4], an Aluminium-Silicon eutectic alloy filler metal coated with Nocolok^{TM} flux [5] (40% to 50% KF and 50% to 60% AlF_3), to the surface of the tubestock material which has been pre-coated with an organic adhesive. The different radiator components are then assembled together into a matrix or core assembly. The pre-brazed core assembly is subjected to a thermal profile under inert conditions (N_2) in a Controlled Atmosphere Brazing (CAB) furnace. Upon brazing and at its melting point the Composite Powder reacts with the component surface and forms a thin layer of eutectic Al-Si melt which flows into the areas of point contact and forms fillets between the finstock and tubestock. Duration in the furnace is dependent on the thermal mass of the product but is generally standardised to give a maximum temperature of 605°C within controlled bounds of heating and cooling rates. The heating profile could be deemed unique to the CD brazing process. Figure 1.2 shows a Brazed aluminium radiator as part of the internal combustion engine of a Mercedes Benz.

Figure 1.2 Brazed aluminium radiator of a Mercedes Benz.

The selection of aluminium alloys for use as finstock and tubestock is of utmost importance in the designing of radiator systems as this greatly influences their resistance to corrosion and hence life expectancy. Figure 1.3 shows an etched cross-section of finstock that is brazed via a layer of eutectic Al-Si filler alloy to the tubestock. For the radiator to achieve maximum durability the finstock should be slightly anodic, and the tubestock slightly cathodic, to the fillet join. In other words, the finstock should sacrificially protect the radiator by corroding preferentially to the fillet join and tubestock material. This will prevent perforation of the tubestock leading to leakage and hence premature failure, as well as delamination of the finstock from the tubestock resulting in loss of thermal and mechanical performance. The difference in potential between the finstock and tubestock in assembled form should not be too large as this will cause severe corrosion of the finstock and thus a decrease in thermal and mechanical performance. On the other hand, if the potential difference is too low the effect of sacrificial protection is lost.

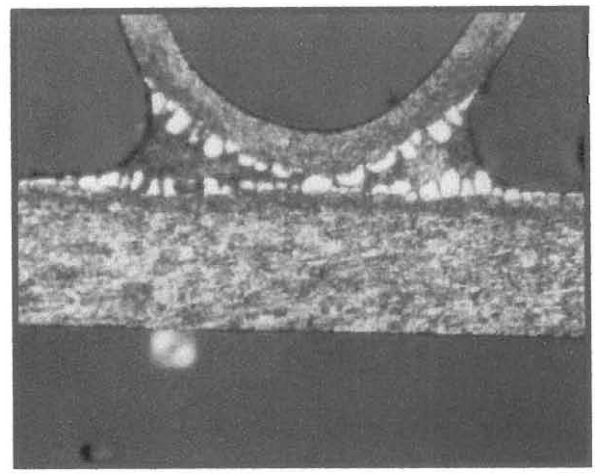

Figure 1.3 An etched cross-section of finstock brazed to tubestock via a layer of eutectic Al-Si filler alloy.

A variety of electrochemical parameters have been used in the determination of the corrosion behaviour of aluminium alloys in corrosive environments. Open circuit potentials (OCPs), also referred to as solution, corrosion, or rest potentials, are often used as a first diagnostic criterion to indicate which alloy or metal is the most anodic (or cathodic) in a couple [6-9], and have also been used in determining an alloy's resistance to corrosion [10, 11]. OCP measurements are also useful for investigating heat-treating, quenching and ageing practices [8, 9, 12-16]. The pitting potential, E_p, in a particular corrosive environment is that potential above which pits will initiate and below which they will not [8, 17-21], has been the subject of considerable study. These two parameters are quick and easy to determine, and when coupled with experiments to determine the extent and nature of corrosion, they can be useful in giving a simple but adequate interpretation of the corrosion behaviour of the aluminium alloy under study. For a more complete picture the protection potential and corrosion current (hence rate of corrosion) can be measured as well.

The metallurgical properties and chemical composition of an aluminium alloy ultimately determines its electrochemical behaviour and nature of corrosion in a particular corrosive environment. The OCP and E_p of an aluminium alloy are primarily determined by the composition of the aluminium rich solid solution and to a much lesser extent by microstructural intermetallic phases present in the matrix [8, 9, 22-24]. Microstructural intermetallic phases however, often have OCPs different from the solid solution matrix,

resulting in the formation of localised galvanic cells between the microstructural intermetallic phases and the matrix, which in turn will affect the nature of corrosion of the aluminium alloy [25-29]. The effect of alloying elements such as Zn, Cu, Fe, Mn, Si and Mg on the corrosion behaviour of aluminium and its alloys in various corrosive environments has been reviewed [6-10, 12, 13, 15, 17, 21-24, 27, 29, 30-53].

When an aluminium alloy is subjected to any form of thermal treatment its metallurgical properties are expected to change. The metallurgical changes expected would be those of crystal structure rearrangement and chemical compositional changes such as solid solution and microstructural phase distributions. The distributions of various solid solution and microstructural intermetallic phases are caused by the dissolution of elements into solid solution during heating, followed by the precipitation of solute from solid solution during cooling. These changes in turn influence the corrosion behaviour of aluminium alloys in different corrosive environments. Thermal treatment can also remove residual localised stress [54] resulting from the cold-rolling working process. The type and extent of microstructural changes that aluminium alloys undergo during thermal treatment depend on the alloy's complete thermal history and the amount of mechanical work and hence mechanical deformation the sample has been exposed to. Several publications deal with the effect of thermal treatment on the metallurgical and electrochemical properties of aluminium alloys [9, 12-15, 22, 30, 31, 34, 40, 43, 46, 50, 53-55], and are specific to the aluminium alloy and thermal profile used. Because of the uniqueness of the CD brazing thermal profile, no information can be found about its influence on the metallurgical and electrochemical properties of the aluminium alloys studied.

The corrosion of aluminium alloys in aqueous solutions is uniquely dependent upon the concentration and type of anion present. Pitting corrosion of aluminium alloys is most commonly produced by halide ions, of which chloride ions are the most frequently encountered in service. The effect of chloride ions on the corrosion behaviour of aluminium alloys has been extensively researched in acid, neutral, and basic media [7, 10, 13, 15, 16, 18, 22, 27, 32, 33, 37, 40, 42, 52, 53, 56-76]. Acid and basic media are said to promote oxide dissolution and therefore assist the pitting corrosion, whilst neutral media aid the oxide film growth thereby enhancing the alloy's natural resistance to corrosion process [42, 49, 56, 59, 73, 77-81]. It is a well known fact that the presence of nitrate ions

[1, 24, 50, 52, 72, 82-87] or sulfate ions [13, 24, 35, 37, 48, 72, 79, 85, 88] alter the corrosion behaviour of the aluminium alloy.

The automotive industry uses salt spray corrosion tests to determine an assembled radiator's resistance to corrosion. This very practical test involves no physical measurements and merely records the time taken for components of the radiator to disintegrate in the corrosive environment at an elevated temperature. A particular adaptation of the salt spray testing procedure used by T&N Holdings, known as the SWAAT (Salt Water Acetic Acid Test) exposure, uses a spray of 4.2% (m/v) NaCl acidified with acetic acid to a pH of 2.85. The test cycle consists of a 30 minute spray at 50°C, followed by a 90 minute dewing period, and leak tests are carried out at 150 kPa after 10 days of exposure and every 5 days thereafter.

The objective of this research was to investigate the effect of thermal profile and Composite Powder coating on the electrochemical properties and nature of corrosion of three aluminium alloys (AA 3003 and two supplier specific alloys) at 25°C in a 1M NaCl solution, with and without the addition of 0.5M H_2SO_4 and/or 0.5M $NaNO_3$. Sulfuric acid instead of acetic acid has been used to acidify the chloride solution to ensure accelerated corrosion of the alloy samples to give meaningful results over a shorter time period. The electrochemical properties of the aluminium alloys can be determined using two different techniques. The first technique involves immersion of the aluminium alloy in various corrosive electrolyte solutions under open circuit conditions and to record the variation of OCP (vs SCE) with time. Initial and final OCPs can be determined from this data. The second technique is derived from classical electrochemical methods [89-93] and makes use of successive multiple anodic polarisations to determine the pitting potential, E_p. The nature and extent of corrosion the aluminium alloys undergo after 60 minutes of immersion under open circuit conditions in the various corrosive electrolyte solutions is then examined using Scanning Electron Microscopy (SEM) and Optical Microscopy techniques. The data obtained from laboratory experiments can then be compared with SWAAT exposure results.

Most researchers employ various sample preparation techniques prior to electrochemical testing in order to ensure that the most reproducible surface will be exposed. These techniques can vary from grinding and polishing to chemical etching or pickling,

anodising, electropolishing, or any combination of the above. The only form of surface preparation that the components were exposed to during the manufacturing of aluminium radiators was a three-stage vapour degreasing process. To ensure that the electrochemical data obtained would not vary significantly from the real industrial situation, the samples used in this research have been exposed to the exact same surface treatment that the aluminium radiator components have been exposed to in the manufacturing process.

2 THEORY

2.1 CHEMICAL BACKGROUND

2.1.1 THE NATURE AND PROPERTIES OF ALUMINIUM OXIDES [94-98]

The oxide film that forms on aluminium, whether the metal is exposed to air or aqueous electrolyte, is of great interest since it is the product of aluminium corrosion and has the ability to suppress any further attack on the metal. This oxide film is also responsible for the electrochemistry and corrosion behaviour of aluminium. The nature of the oxide film formed on aluminium is dependent on the thermal and environmental conditions to which the metal has been exposed. Its composition in air or neutral water can range from an anhydrous oxide phase to a trihydroxide phase and more than one form can be present on the surface of aluminium at the same time.

Aluminium has only one oxide, alumina Al_2O_3, which exists as various polymorphs and hydrated species. Two anhydrous crystalline forms of alumina exist, namely α-Al_2O_3 or corundum, and γ-Al_2O_3. Corundum is a white crystalline solid that is the only thermally stable oxide of aluminium and can be prepared by heating γ-Al_2O_3 or any of the hydrous oxides above 1000°C. It is a common mineral in igneous and metamorphic rocks and is most commonly found in bauxite, the ore from which aluminium is produced. Corundum crystallises in a hexagonal rhombohedral system, is extremely hard and dense, and is resistant to hydration and attack by acids. Its applications include its use in ceramics, abrasives, chromatography, and as conductors for use in the electronics industry. γ-Al_2O_3 in contrast to α-Al_2O_3 is soft, less dense, readily takes up water and is relatively soluble in aqueous alkalis and acids. It is an excellent and selective absorbent and is used in dehydration, decolourisation and chromatography. γ-Al_2O_3 can be prepared by dehydrating any of the hydrous oxides below 450°C, and contains a distorted, badly organised microcrystalline structure of the spinel type.

There are four well-defined forms of hydrated aluminas: (1) the monohydrate $Al_2O_3.H_2O$ or AlOOH, as boehmite (γ-AlOOH) and diaspore (α-AlOOH), and (2) the trihydrate $Al_2O_3.3H_2O$ or $Al(OH)_3$, as gibbsite (γ-$Al_2O_3.3H_2O$) and bayerite (α-$Al_2O_3.3H_2O$). Of these, all but bayerite occur naturally in bauxite. The monohydrated aluminas or

oxyhydroxides of aluminium both exhibit orthorhombic crystal symmetry. Boehmite can easily be differentiated from diaspore due to structural differences in their respective crystal lattices. Boehmite is white in colour and can be prepared by hydrothermal decomposition of gibbsite. Diaspore is a relatively rare aluminium oxide that upon dehydration passes directly to corundum. The trihydrated aluminas or trihydroxides of aluminium all have hydroxyl structures that are approximately hexagonally close packed. Gibbsite, also known as hydrargillite, is the primary constituent of bauxite that, like bayerite, is white in appearance and crystallises with a monoclinic symmetry. Gibbsite is the most thermodynamically stable of the trihydroxides with bayerite tending to form as the initial crystalline phase, which then transforms to gibbsite.

2.1.2 OXIDE FORMATION IN AIR AND NEUTRAL WATER

Aluminium owes its excellent resistance to corrosion to the presence of a thin, compact, adherent and protective surface oxide film that, if damaged, reforms immediately in most environments. The nature and thickness of the oxide film formed differs when aluminium is exposed to air or neutral water.

The thickness of an air formed aluminium oxide film is determined solely by the temperature of the environment and is the same in oxygen, dry air, or moist air [8]. When exposed to air at temperatures of up to 400°C, aluminium rapidly becomes covered with a layer of amorphous aluminium oxide, also referred to as a barrier oxide film, which is between 20 Å and 100 Å thick [74, 99]. At temperatures greater than 500°C this oxide film can reach a thickness of about 200 Å [99]. In both cases the growth of the oxide layer increases rapidly at first but soon slows down to follow a logarithmic time growth law [100].

The oxide film that grows when aluminium is exposed to neutral water is remarkably different from the oxide film formed in air. This is because in neutral water the oxide growth continues to form a layer of hydrated porous aluminium oxide on top of the barrier oxide layer, thus resulting in an overall layer that is either duplex [8, 33, 47, 83, 100, 101] or triplex [78, 102] in nature, depending on temperature. The rate of growth of the porous layer decreases much less rapidly than the barrier layer and its thickness might reach several microns [8, 83, 100], depending on temperature. In general, the higher the

temperature, the thicker the layer becomes. The outer porous oxide layer is more susceptible to corrosion than the barrier oxide layer and according to Hunter and Fowle [103], the composition of this outer layer is dependent on the nature of the corroding medium.

The barrier oxide or gel layer is the so called amorphous aluminium hydroxide film. It is termed amorphous because it is without definite form or structure and does not reveal a distinct x-ray or electron diffraction pattern. This amorphous layer is not stable and ages or crystallises with time according to the following reactions [80, 104]:

(1) $Al + 3H_2O \rightleftharpoons Al(OH)_3$ (amorphous) $+ 3H^+$ (2.1)

(2) $2Al(OH)_3 \rightleftharpoons \gamma\text{-}Al_2O_3.H_2O$ (boehmite) $+ 2H_2O$ (2.2)

(3) $\gamma\text{-}Al_2O_3.H_2O + 2H_2O \rightleftharpoons \alpha\text{-}Al_2O_3.3H_2O$ (bayerite) (2.3)

(4) $\alpha\text{-}Al_2O_3.3H_2O \rightleftharpoons \gamma\text{-}Al_2O_3.3H_2O$ (gibbsite) (2.4)

Reactions (2.3) and (2.4) take place very slowly and exact temperature ranges have not been defined for the different transformations. However, the temperatures at which boehmite, gibbsite, bayerite and corundum become stable phases have been researched extensively.

According to Hart [102], below a critical temperature (60° to 70°C), film growth proceeds in three stages: (1) 'amorphous', (2) boehmite γ-AlOOH, (3) bayerite $\alpha\text{-}Al_2O_3.3H_2O$, the final oxide layer thus consisting of three layers. He found that above the critical temperature only boehmite forms on top of the amorphous oxide film, resulting in a film of duplex nature. Moshier *et al.* [78] are in agreement with Hart. Other work [100, 105] has shown that pseudoboehmite, a poorly crystalline form of boehmite, with a chemical formula $Al_2O_3.xH_2O$ (x = 1.8 to 2.5), forms first as a precursor in the formation of the trihydroxide phase and may be maintained on the surface for extended periods. Other workers [106] have considered that the duplex film developed at temperatures below 90°C consists of a pseudoboehmite and a bayerite layer. As the temperature is increased to 100°C, the bayerite layer is lost and the pseudoboehmite film becomes well crystallised. In the temperature range 100° to 374°C boehmite predominates and above 374°C the film becomes $\alpha\text{-}Al_2O_3$ or corundum. MacDonald and Butler [104] found gibbsite to be the

stable oxide form at room temperature that dehydrated on heating to boehmite and finally corundum.

2.1.3 POURBAIX DIAGRAMS

The protection of aluminium against corrosion in aqueous environments is dependent upon the stability of the various passivating oxide films formed, and is determined by their solubility in that environment. In the pH range 4 to 8, aluminium is said to be passive and its oxide film is slightly soluble under these conditions. Above and below this pH range the solubility of the oxide film increases, leading to the formation of the soluble reaction products $Al(OH)_4^-$ or AlO_2^- and Al^{3+}, and hence uniform dissolution of the aluminium, which is said to be in a state of corrosion. These states of solubility are expressed in Pourbaix (potential versus pH) diagrams, which use theoretical calculations of the thermodynamic stability of the aluminium oxide film exposed to water as a function of pH.

Deltombe, Vanleugenhaghe and Pourbaix [80, 107] have constructed a potential-pH diagram for the aluminium-water system at 25°C that is based on gibbsite being the most stable oxide of aluminium. This diagram is shown in Figure 2.1 and is valid only in the absence of substances with which aluminium can form soluble complexes or insoluble salts. The data used in constructing the potential-pH diagram represent equilibrium conditions, and many of the calculations have been based on the Nernst equation (2.5) given below.

$$E_{eq} = E^\circ - (RT/nF) \ln (a_R/a_O) \qquad (2.5)$$

Where E_{eq} = Half cell potential

E° = Standard half cell potential

R = Gas constant

T = Absolute temperature

n = Number of electrons transferred

F = Faraday constant

a = Activity of the oxidised (O) and reduced (R) species

The equations used in constructing Figure 2.1 are:

(a) $2H^+ + 2e^- \rightleftharpoons H_2$ (2.6)

(b) $O_2 + 4H^+ + 4e^- \rightleftharpoons H_2O$ (2.7)

(1) $Al^{3+} + 2H_2O \rightleftharpoons AlO_2^- + 4H^+$ (2.8)

(2) $Al + 3H_2O \rightleftharpoons Al_2O_3 + 6H^+ + 6e^-$ (2.9)

(3) $2Al^{3+} + 3H_2O \rightleftharpoons Al_2O_3 + 6H^+$ (2.10)

(4) $Al_2O_3 + H_2O \rightleftharpoons 2AlO_2^- + 2H^+$ (2.11)

(5) $Al^{3+} + 3e^- \rightleftharpoons Al$ (2.12)

(6) $AlO_2^- + 4H^+ + 3e^- \rightleftharpoons Al + 2H_2O$ (2.13)

Figure 2.1 illustrates the predicted regions of corrosion (Al^{3+} and AlO_2^-), passivity ($Al_2O_3.3H_2O$) and immunity (Al) of aluminium exposed to water at 25°C. However, the limits of the passive range of aluminium vary somewhat with temperature and with the nature of the oxide film present.

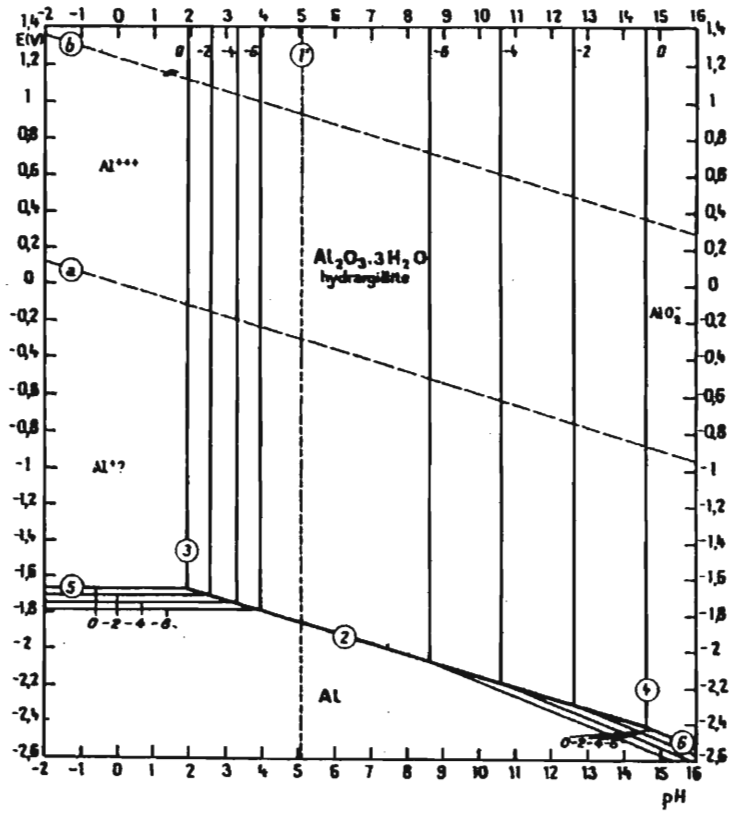

Figure 2.1 Potential-pH diagram for the aluminium-water system at 25°C. (Taken from reference [80])

MacDonald and Butler [104] have updated the data of Pourbaix *et al.* by extending the calculations used to elevated temperatures. They also considered three ionic aluminium species: Al^{3+}, $Al(OH)^{2+}$, and AlO_2^- in contrast to only Al^{3+} and AlO_2^- used by Pourbaix *et al.* $Al(OH)^{2+}$ represents the first hydrolysis product of Al^{3+} that predominates in very dilute solutions (< 10^{-3}M). In the range of 25°C to 150°C gibbsite was considered by MacDonald and Butler to represent the stable oxide of aluminium, while at temperatures above 150°C boehmite was considered thermodynamically stable and therefore used in constructing the diagrams. Figure 2.2 represents potential-pH diagrams for the aluminium-water system at 25°C, 100°C and 300°C respectively, which have been constructed by MacDonald and Butler based on the following reactions:

(1) $2H^+ + 2e^- \rightleftharpoons H_2$ (2.6)

(2) $O_2 + 4H^+ + 4e^- \rightleftharpoons H_2O$ (2.7)

(3) $Al(OH)^{2+} + H^+ \rightleftharpoons Al^{3+} + H_2O$ (2.14)

(4) $AlO_2^- + 3H^+ \rightleftharpoons Al(OH)^{2+} + H_2O$ (2.15)

(5) $Al_2O_3.H_2O + 6H^+ + 6e^- \rightleftharpoons 2Al + 4H_2O$ (2.16)

(6) $Al_2O_3.3H_2O + 6H^+ + 6e^- \rightleftharpoons 2Al + 6H_2O$ (2.17)

(7) $Al_2O_3.H_2O + 6H^+ \rightleftharpoons 2Al^{3+} + 4H_2O$ (2.18)

(8) $Al_2O_3.3H_2O + 6H^+ \rightleftharpoons 2Al^{3+} + 6H_2O$ (2.19)

(9) $2AlO_2^- + 2H^+ \rightleftharpoons Al_2O_3.H_2O$ (2.20)

(10) $2AlO_2^- + 2H^+ + 2H_2O \rightleftharpoons Al_2O_3.3H_2O$ (2.21)

(11) $Al^{3+} + 3e^- \rightleftharpoons Al$ (2.12)

(12) $Al(OH)^{2+} + H^+ + 3e^- \rightleftharpoons Al + H_2O$ (2.22)

(13) $Al_2O_3.H_2O + 4H^+ \rightleftharpoons 2Al(OH)^{2+} + 2H_2O$ (2.23)

(14) $Al_2O_3.3H_2O + 4H^+ \rightleftharpoons 2Al(OH)^{2+} + 4H_2O$ (2.24)

(15) $AlO_2^- + 4H^+ + 3e^- \rightleftharpoons Al + 2H_2O$ (2.25)

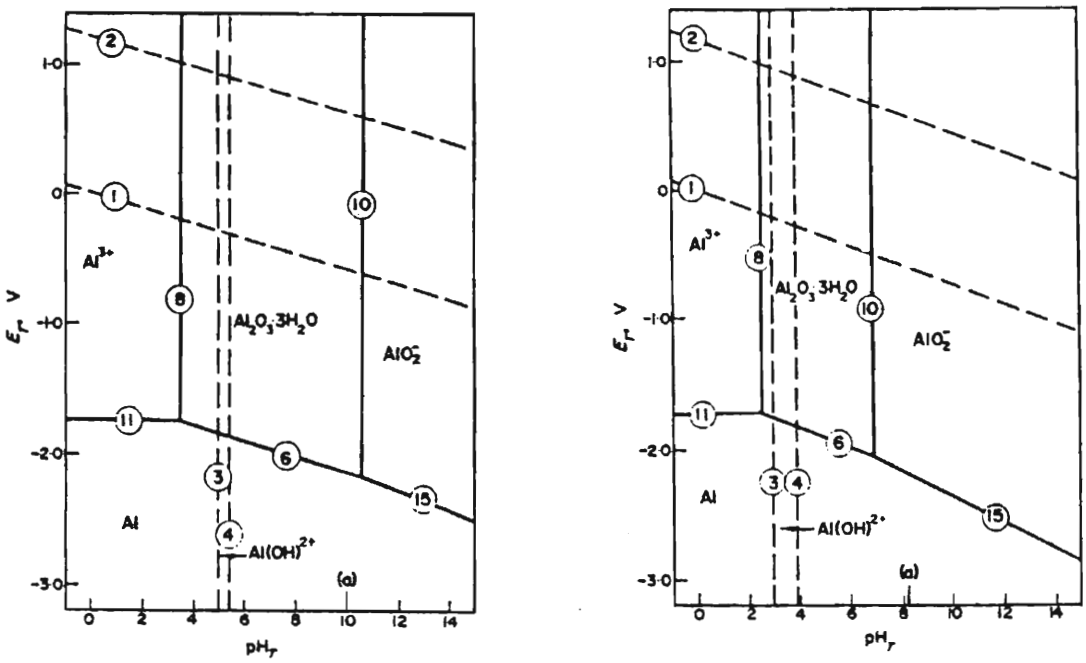

Figure 2.2 Potential-pH diagrams for the aluminium-water system at (a) 25°C, (b) 100°C and (c) 300°C.

Figure 2.3 shows the influence of pH on the solubility of five forms of hydrated alumina [77, 80]. The orders of increasing solubility of the various forms of alumina are gibbsite (hydrargillite), bayerite, boehmite, and amorphous aluminium hydroxide [56, 108].

TABLE I. Solubility of aluminium oxide and its hydrates

	Formula	log [Al^{+++}][OH$^-$]^3	log [AlO$_2^-$][H$^+$]	log (minimum solubility) (g-at Al/l)	log (solubility in pure water) (g-at Al/l)	pH on dissolution in water	Crystallographic system
Hydrargillite	$Al_2O_3 . 3H_2O$	−36·30	−14·60	−9·2	−7·8	6·8	Monocl.
Bayerite	$Al_2O_3 . 3H_2O$	−35·52	−13·82	−8·5	−7·2	6·7	Monocl.
Böhmite	γ-$Al_2O_3 . H_2O$	−34·02	−12·32	−7·0	−6·2	6·1	Tetr.
Corundum	α-Al_2O_3	−33·45	−11·76	−6·4	−5·9	5·9	Tetr.
Amorphous hydroxide	$Al(OH)_3$	−32·34	−10·64	−5·3	−5·3	5·3	Amorphous

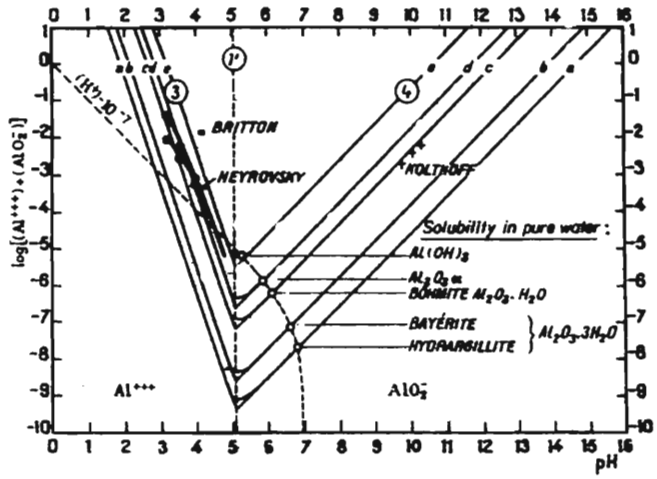

Figure 2.3 Influence of pH on the solubility of alumina and its hydrates at 25°C.

Although Pourbaix diagrams illustrate the corrosion behaviour of aluminium, they do not give a true kinetic representation since only thermodynamic data have been used in their construction. Pourbaix diagrams describe the equilibrium species present under a particular set of conditions and as such they do not take into account the kinetics of the reactions that might lead to metastable species or phases on the surface, the effect of alloying elements, and the effect of ionic species present in solution (e.g. aggressive chloride ions, passivating nitrates and sulfates). These effects can be significant and will change the areas of passivity and corrosion of aluminium. Pourbaix diagrams can therefore only be used as a guide to the corrosion behaviour of aluminium.

2.1.4 HYDROLYSIS OF THE ALUMINIUM ION

The primary process in the electrochemical corrosion of aluminium is the formation of the hexahydrated aluminium ion, $[Al(H_2O)_6]^{3+}$, referred to as Al^{3+} for simplicity. In neutral solutions, Al^{3+} undergoes hydrolysis according to the following set of reactions [40, 74, 81, 97, 109]:

(1) $Al^{3+} + H_2O \rightleftharpoons Al(OH)^{2+} + H^+$ (2.26)

(2) $Al^{3+} + 2H_2O \rightleftharpoons Al(OH)_2^+ + 2H^+$ (2.27)

(3) $Al^{3+} + 3H_2O \rightleftharpoons Al(OH)_3 + 3H^+$ (2.28)

(4) $Al^{3+} + 4H_2O \rightleftharpoons Al(OH)_4^- + 4H^+$ (2.29)

Strictly speaking, this hydrolysis takes place in successive stages [97], as indicated below:

(1) $Al^{3+} + H_2O \rightleftharpoons Al(OH)^{2+} + H^+$ (2.26)

(2) $Al(OH)^{2+} + H_2O \rightleftharpoons Al(OH)_2^+ + H^+$ (2.30)

(3) $Al(OH)_2^+ + H_2O \rightleftharpoons Al(OH)_3 + H^+$ (2.31)

(4) $Al(OH)_3 + H_2O \rightleftharpoons Al(OH)_4^- + H^+$ (2.32)

The dissolution of $Al(OH)_3$ in acids is merely a reversal of the hydrolysis. Baes and Mesmer [109] have reviewed the hydrolysis of Al^{3+} from studies of the hydrolysis of $AlCl_3$ solutions, and found that in very dilute solutions (< 10^{-3}M) the monomer $Al(OH)^{2+}$ appears to predominate, whilst in more concentrated solutions the polynuclear products $Al_2(OH)_2^{4+}$, $Al_3(OH)_4^{5+}$, and $Al_{13}O_4(OH)_{32}^{7+}$ have been proposed. Table 2.1 gives a summary of the hydrolysis products of Al^{3+} at 25°C.

Table 2.1 Summary of Al^{3+} hydrolysis at 25°C as taken from Baes and Mesmer [109].

$$\text{Log } Q_{xy} = \log K_{xy} + aI^{1/2}/(1 + I^{1/2}) + bm_X$$

Species or phase	Log K_{xy}	a	b	$\sigma(\log Q_{xy})$
$AlOH^{2+}$	−4.97	−2.044	0.52	±0.02
$Al(OH)_2^+$	−9.3	−3.066	0.55	?
$Al(OH)_3$	−15.0	−3.066	0.45	?
$Al(OH)_4^-$	−23.0	−2.044	0.36	±0.3
$Al_2(OH)_2^{4+}$	−7.7	0	(0)	±0.3
$Al_3(OH)_4^{5+}$	−13.94	1.022	(0)	±0.1
$Al_{13}O_4(OH)_{24}^{7+}$	−98.73	−18.40	3.55	±0.05
α-$Al(OH)_3$ (gibbsite) (log Q_{s10})	8.5	3.066	−0.45	±0.1

2.1.5 LOCALISED PITTING CORROSION OF ALUMINIUM AND ITS ALLOYS IN SOLUTIONS CONTAINING CHLORIDE IONS

The resistance of aluminium and its alloys to corrosion depends on the stability of the protective oxide film at the surface. The presence of aggressive ions in solution, in particular chloride ions, can cause extensive localised attack in the form of pitting corrosion.

Foley [61] has outlined a four-step process for the localised corrosion of aluminium and its alloys. This model has been generally accepted and comprises both the pit initiation (steps 1 to 3) and pit propagation (step 4) events. The steps in the model are listed below.

1. The adsorption of the reactive anion on the aluminium surface oxide film.
2. The chemical reaction of the adsorbed anion with the aluminium ion in the oxide or precipitated hydroxide film.
3. Thinning of the oxide film by dissolution and 'penetration' of the oxide film by the aggressive anion. (By penetration Foley means the formation of soluble compounds or transitory species at critical sites.)
4. Direct attack of the exposed metal by the anion (i.e. pit propagation). This can be assisted by an anodic potential and can occur simultaneously with step 3.

The adsorption of anions on aluminium oxide surfaces has been the subject of many studies. Richardson and Wood [110] found that the flaws in an oxide film took on the role of active centres which were preferential sites for the adsorption of chloride ions. These flaws may be 'residual' or 'mechanical' in origin. 'Residual' flaws are produced during film growth at impurity-rich regions and microstructural intermetallic phases in the metal and may be anodic or cathodic to the aluminium matrix, but since these are commonly associated with iron-rich constituents, they tend to be cathodic. 'Mechanical' flaws are associated with the relief of stress in the oxide film formed over mechanical surface defects such as scratch lines and are generally anodic as they effectively expose bare aluminium metal.

The adsorption of anions on the aluminium oxide surface leading to pitting is a competitive process and was found to depend on the potential. Augustynski [111] noted that the relative concentration of chloride ions in the oxide film increased from 3 to 12 atomic per

cent when the potential moved from the open circuit potential (OCP) to the pitting potential (E_p). He also found that adequate adsorption of anions does occur at the OCP in both acidic and neutral solutions since the aluminium oxide will be positively charged and therefore attract negative anions (i.e. an applied potential is not required for extensive adsorption).

Augustynski [111] observed from studies of nitrate-chloride solutions that nitrate ions retard the adsorption of chloride ions, and are therefore part of a competitive adsorption process with the chloride ions. Stirrup *et al.* [72] found that by considering the relative adsorbability of sulfate and nitrate ions, competitive adsorption is not the mode of inhibition by nitrate ions, and suggested instead that inhibition is caused by the formation of a more perfect oxide layer promoted by the oxidising anion. They also reported that sulfate ions have a greater tendency for adsorption than nitrate ions. Tomscányi *et al.* [68] found that competitive adsorption between sulfate and chloride ions does not take place. However, other workers disagree with this [35, 72, 85].

The chemical reaction step determines the type of species formed by the adsorbed anions with the aluminium oxide surface. A number of investigators have concluded from work on pitting of aluminium in chloride solutions that intermediate soluble complexes are formed. Several workers have also reported the observation that salt films are present during the dissolution of aluminium in chloride solutions [17, 64, 69, 112]. Foley and Nguyen [71, 113] established the reactions involved in the dissolution of aluminium in chloride solutions as:

(1) $Al \rightleftharpoons Al^{3+} + 3e^-$ (2.33)

(2) $Al^{3+} + H_2O \rightleftharpoons Al(OH)^{2+} + H^+$ (2.26)

(3) $Al^{3+} + Cl^- \rightleftharpoons AlCl^{2+}$ (2.34)

(4) $Al(OH)^{2+} + Cl^- \rightleftharpoons Al(OH)Cl^+$ (2.35)

(5) $AlCl^{2+} + 2H_2O \rightleftharpoons Al(OH)_2Cl + 2H^+$ (2.36)

(6) $Al(OH)Cl^+ + H_2O \rightleftharpoons Al(OH)_2Cl + H^+$ (2.37)

(7) $Al(OH)_2Cl + H_2O \rightleftharpoons Al(OH)_3 + H^+ + Cl^-$ (2.38)

(8) $2Al(OH)_3$ (amorphous) $\rightleftharpoons \gamma$-$Al_2O_3.H_2O$ (boehmite) $+ 2H_2O$ (2.2)

In the presence of sulfate ions, the following reactions, which are in agreement with Beccaria and Poggi [114], were also found to occur:

(9) $Al^{3+} + SO_4^{2-} \rightleftharpoons AlSO_4^{+}$ (2.39)

(10) $Al(OH)^{2+} + SO_4^{2-} \rightleftharpoons Al(OH)SO_4$ (2.40)

Foley and Nguyen [71] have also developed free potential energy surface diagrams, which are shown in Figure 2.4, for the dissolution of aluminium in solutions containing chloride ions and sulfate ions respectively. In Figure 2.4(a), the low energy compounds Al_2O_3 and $Al(OH)_3$ react with the chloride ion to pass through stages represented by the compounds $Al(OH)_2Cl$ and $Al(OH)Cl_2$, and finally through transitory complexes such as $AlCl^{2+}$ and $Al(OH)^{2+}$. A similar explanation follows for the energy surface diagram 2.4(b) involving the sulfate ion.

Foroulis and Thubrikar [70] suggested that the following reactions were involved in the dissolution of aluminium by chloride ions:

(1) $2Al(OH)_3 \rightleftharpoons Al(OH)_2^{+} + OH^{-}$ (2.41)

(2) $Al(OH)_2^{+} + Cl^{-} \rightleftharpoons Al(OH)_2Cl$ (2.42)

Ambat and Dwarakadasa [40, 42] proposed that the adsorption of chloride ions to susceptible parts of the oxide film lead to the formation at the film/solution interface of transitional chloride containing complexes by the reaction:

(1) $Al + nCl^{-} \rightleftharpoons AlCl_n^{(n-3)-} + 3e^{-}$ (2.43)

According to Foley [61] and others [53, 56], compounds such as $Al(OH)_2Cl$ and $Al(OH)Cl_2$ are present during aluminium dissolution in aqueous chloride solutions. Wong and Alkire [69] are in agreement with this and suggested that the compound $Al_2(OH)_5Cl$ also formed. Diggle *et al.* [66] suggested that the dissolution of porous oxide films on aluminium in chloride solutions appears to be chemical rather than electrochemical in nature, and proposed $AlOCl.H_2O$ (i.e. $Al(OH)_2Cl$) to be the soluble chloride complex formed in chloride solutions, and $[Al(OH)_2]_2SO_4$ to be formed in sulfate solutions. Tomcsányi *et al.* [68] dissagree with this and proposed that the pitting corrosion mechanism is an electrochemical process, followed by two heterogeneous chemical processes with the chloride ion as a chemical reaction partner, resulting in chloride containing complexes such as $(AlOOH)_3.AlOCl.H_2O$, $AlOCl$, $Al(OH)_2Cl$ and finally $AlCl_6^{3-}$.

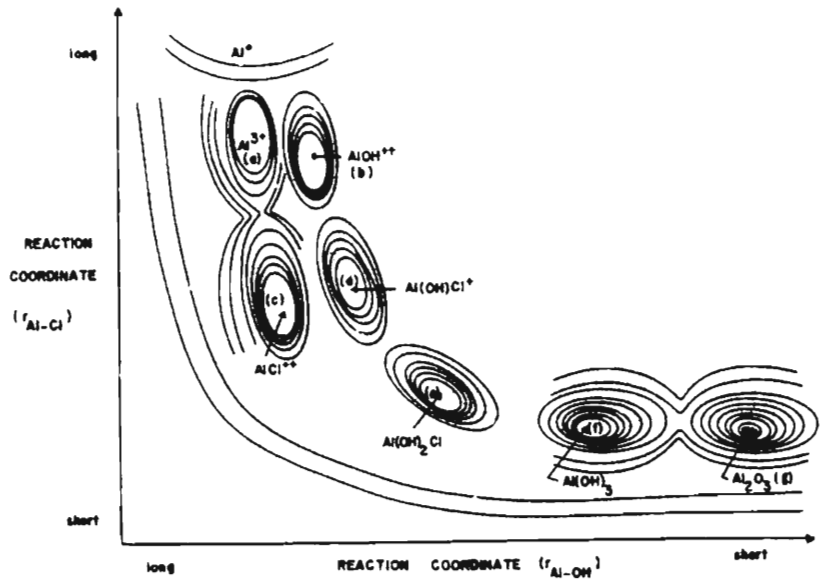

(a)

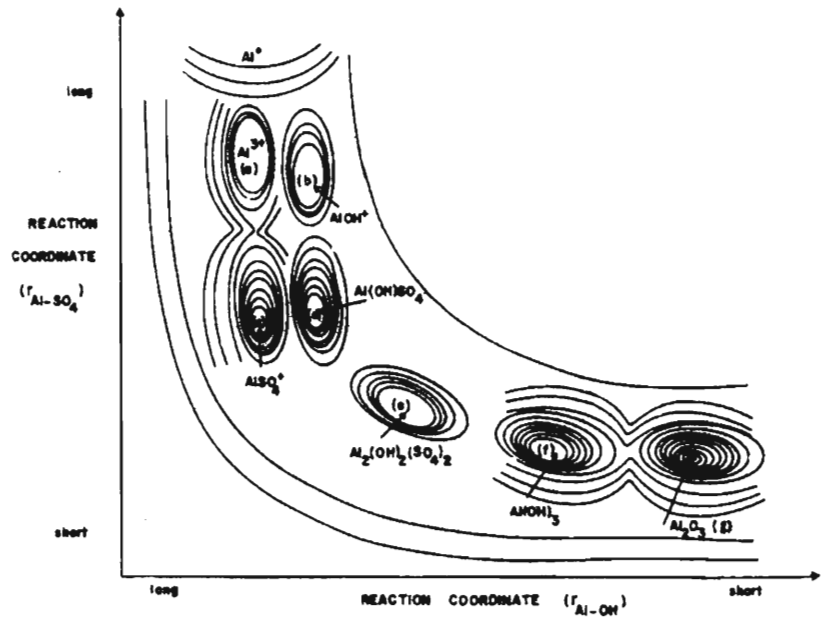

(b)

Figure 2.4 Potential energy surface diagrams for (a) Al-Cl and (b) Al-SO_4.

In summary, there appear to be many well-characterised aluminium-anion reaction products formed during the dissolution of aluminium and its alloys in both chloride and sulfate containing environments.

The thinning or dissolution of the aluminium oxide film, as described in Section 2.1.4, is expected to be a flaw assisted process and is not likely to occur uniformly over the whole surface. Once the aluminium oxide film is sufficiently thinned, rapid attack and pit

propagation is expected to occur as a result of the high degree of reactivity of metallic aluminium. This attack will be concentrated locally since the thinning of the aluminium oxide film is localised at flaws. The direct attack of the aluminium metal by pit propagation involves an environment that is constantly changing as the reaction proceeds. During pit initiation, the oxide film interacts with the solution it is in contact with [61].

A schematic representation of a pit cavity, as drawn up by Hübner and Wranglén [61, 85], is shown in Figure 2.5. This diagram shows a proposed mechanism of pit growth, as well as the changing environment in and around the pit cavity involving a number of reactions at any given time. The pH inside the naturally occurring pit has been found to differ substantially from that in the bulk solution, and lies between pH 3 to 4 [61, 69, 115, 116]. This can be explained in terms of the hydrolysis of the aluminium ion.

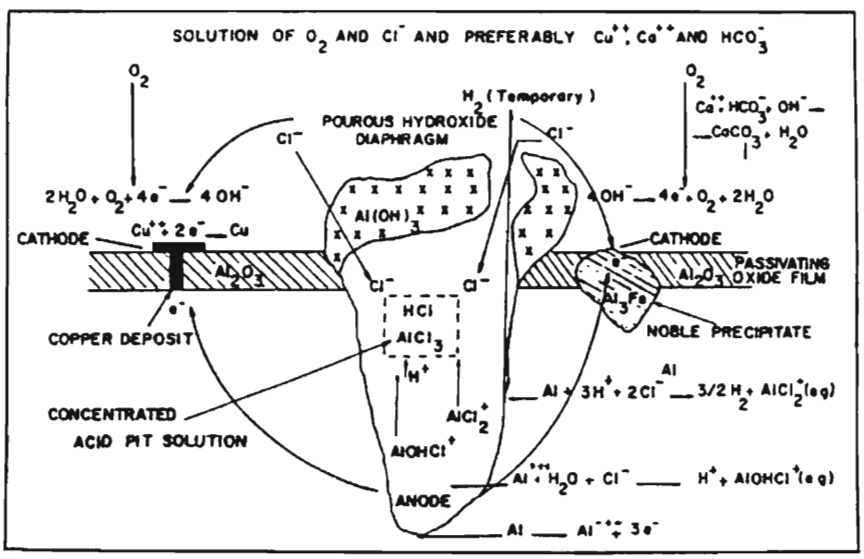

Figure 2.5 Mechanism of pit growth on aluminium.

For a naturally occurring pit in an electrolyte containing oxygen and aggressive anions such as chloride ions, it appears that a pit starts because of the electrochemical action produced by the presence of intermetallic particles and natural defects in the aluminium surface. Once initiated, the pit grows because dissolution of the aluminium produces a pit cavity, within which conditions favourable to further pitting are maintained. Pits cease to propagate if the corrosion product around the mouth stifles the action, or outward diffusion of pit electrolyte occurs [85].

2.2 ELECTROCHEMICAL BACKGROUND

2.2.1 CLASSICAL ELECTROCHEMICAL THEORY [89-93]

Electrode processes are heterogeneous reactions occurring at the solid-electrolyte interface and are characterised by the transfer of an electric charge across that interface. In general, an electrode process is a redox reaction, $O + ne^- \rightleftharpoons R$, where n = the number of electrons required to oxidise the reduced form R to the oxidised form O.

2.2.1(a) The single-step, single-electron transfer reaction

When a metal electrode M (i.e. R) is placed in a solution containing M^{n+} ions (i.e. O) the potential difference between the solid and solution will eventually reach an equilibrium potential, E_{eq}, when the rate of oxidation equals the rate of reduction.

The equilibrium potential may be expressed by the Nernst equation (2.5), described in Section 2.1.3. Deviation from E_{eq} causes a current to flow, either anodically to accelerate the oxidation reaction, or cathodically to favour the reduction reaction. The rate of charge transfer is dependent on the electrical potential difference between the solid and the electrolyte, so by controlling the potential at the surface of the electrode, one may control the rate and direction of the electrode reaction. (The apparatus used is discussed in Section 3.3.)

If this current is plotted as a function of the potential at the electrode's surface, a current-potential (i vs E) plot as shown in Figure 2.6 will be obtained. By convention, currents resulting from oxidation reactions are positive and called anodic (i_a), whilst currents due to reduction reactions are negative and called cathodic (i_c). The overall current (i) is the sum of the anodic and cathodic currents obtained. The exchange current density, i_0, is a measure of the rate of electron transfer between the reduced and oxidised species at E_{eq}, and is a function of temperature, electrolyte composition and concentration. Current is usually expressed as the current density, defined as current per unit surface area, which is a quantitative measure of the rate of the electron transfer process and hence the rate of corrosion.

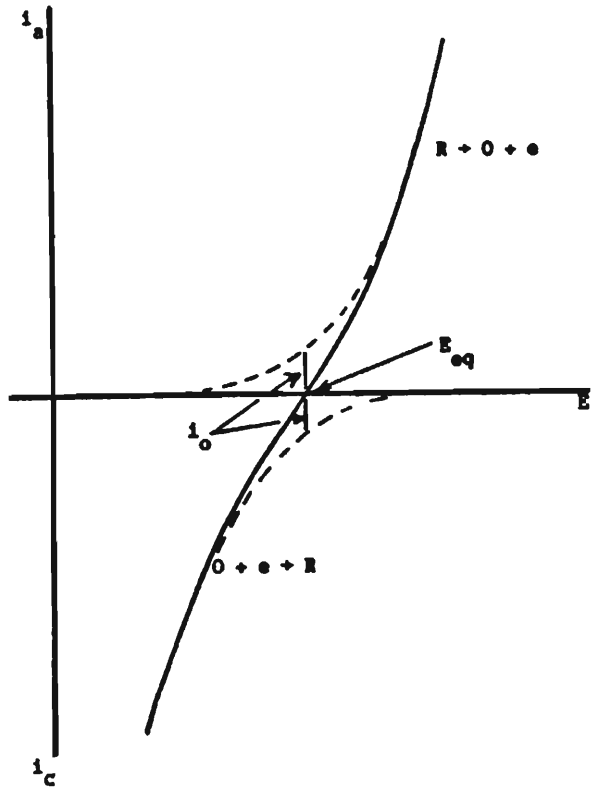

Figure 2.6 Current-potential plot for the system R/O.

The absolute potential difference across the electrified interface (ϕ), as described by Bockris and Reddy [92], is not measurable as a single quantity. For it to gain significance it has to be measured relative to another potential. Therefore the potential applied to the electrode surface may be expressed as either:

(1) E, the potential measured with respect to a reference electrode, or

(2) The overpotential, which is defined as $\eta = E - E_{eq}$ or $\phi - \phi_{eq}$, which is the driving force of the electron transfer reaction.

Anodic polarisation of the electrode occurs if the potential applied to the electrode is shifted from its equilibrium value in the positive direction, and one of the current-potential plots as shown in Figure 2.7 is often obtained.

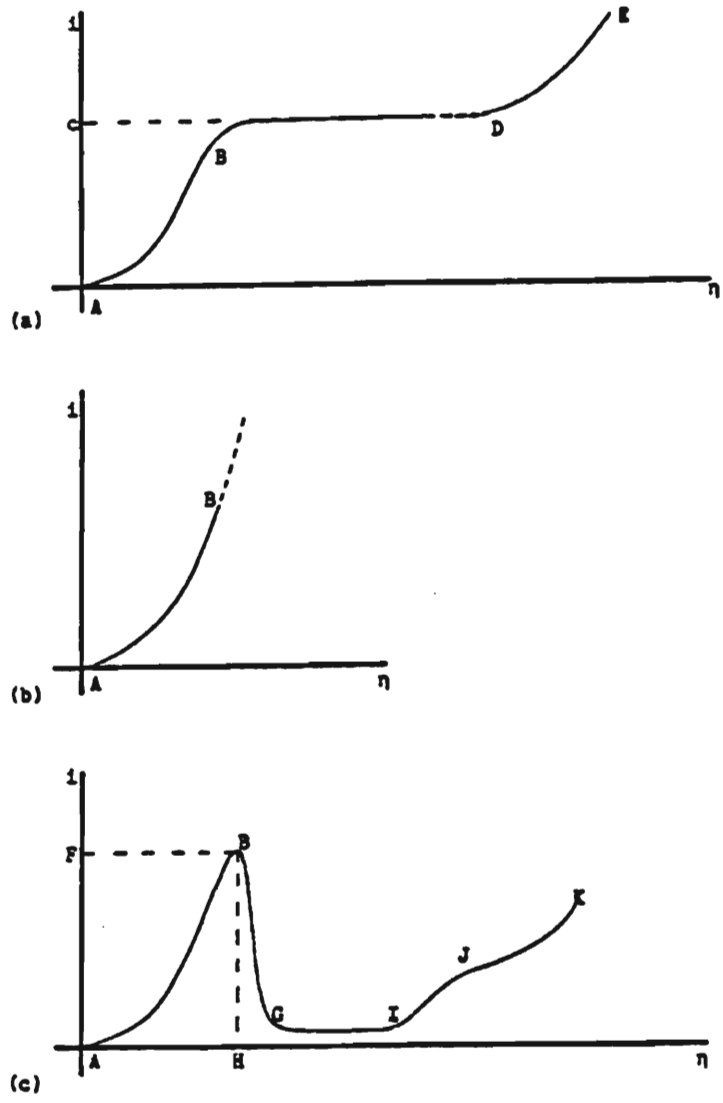

Figure 2.7 Current-potential curves showing three types of anodic behaviour.

The various points or regions in these graphs are described as follows:

The potential at point A is the equilibrium potential, E_{eq}. Region AB is the region of anodic metal dissolution, which is under activation control; i.e. the rate of reaction is dependent on the rate of the electron transfer reaction from the solution species to the metal electrode. The relationship between the current density and the overpotential in region AB is described by the Butler-Volmer equation:

$$i = i_0 [\exp \{(1-\beta)F\eta/RT\} - \exp \{-\beta F\eta/RT\}] \qquad (2.44)$$

where i is the net current density of the reaction and i_0 is the exchange current density. β is called the symmetry factor and is related to the potential difference across the double layer. It usually has a value of 0.5 [92].

Two limiting cases of the Butler-Volmer equation are important:

(1) Fast reversible systems with a low overpotential (< 20 mV). In this case the exponential terms in the Butler-Volmer equation can be expanded by using the approximation $e^x = 1 + x$ ($x << 1$), resulting in the reduced equation:

$$i = i_0 (F\eta/RT) \tag{2.45}$$

(2) Irreversible systems with a high overpotential (> 100 mV). Because $e^x >> e^{-x}$, the Butler-Volmer equation may be reduced to:

$$i = i_0 \exp \{(1-\beta)F\eta/RT\} \tag{2.46}$$

for $\eta > 100$ mV anodically, or

$$i = -i_0 \exp \{-\beta F\eta/RT\} \tag{2.47}$$

for $-\eta > 100$ mV cathodically.

These equations, which may be rewritten as:

$$\ln |i| = \ln i_0 + \{(1-\beta)F\eta/RT\} \tag{2.48}$$

and

$$\ln |i| = \ln i_0 \{-\beta F\eta/RT\} \tag{2.49}$$

respectively, are forms of the Tafel equation,

$$\eta = a + b \log i \tag{2.50}$$

and are widely used in electrochemistry.

If both R and O represent species in solution then a current-potential curve as shown in Figure 2.7(a) may be obtained. Region BD is the region of diffusion control, i.e. the rate of reaction depends on the rate at which reactant species are transported to the surface of the electrode. The Butler-Volmer equation breaks down in this region and the current density (point C), known as the limiting current density i_l, is independent of the potential. At sufficiently high potentials (~ 1.5V), oxygen evolution occurs at the surface of the electrode formed by decomposition of water, which causes the current to rise (region DE).

If R and O represent a metal in a solution of its ions, one would expect the current-potential behaviour to be as shown in Figure 2.7(b). The solution species M^{n+} does not participate in the dissolution reaction and hence the reaction remains under activation control.

Passivation of the electrode arises when the surface of the electrode becomes covered with a corrosion resistant film, usually an oxide, a hydroxide or a salt, and this causes the current to suddenly drop, as shown by region BG in Figure 2.7(c). The current density at which passivation sets in is known as the critical current density (F) and the corresponding potential is the Flade potential (H). In the region GI, the electrode is in a passive state and will not corrode. However, transpassive or secondary dissolution may occur at potentials that are more anodic (IJ), usually because of oxidation of the passive film. Oxygen evolution (JK) may or may not occur concurrently with secondary dissolution.

2.2.1(b) The multi-step, multi-electron transfer reaction

In the case of a multi-electron transfer reaction, $R \rightleftharpoons O + ne$, a number of steps are generally involved. Although the current-potential curves obtained for these reactions are similar to those shown in Figure 2.7, the rate of the reaction is defined by the rate of the slowest step known as the rate determining step (RDS). Provided all other steps in the reaction are at equilibrium, a generalised form of the Butler-Volmer equation can be derived to describe the current-potential relationship in the region AB:

$$i = i_0 [\exp \{\alpha_a F\eta/RT\} - \exp \{-\alpha_c F\eta/RT\}] \quad (2.51)$$

In this equation α_a and α_c are the transfer coefficients for the de-electronation and electronation reactions respectively, and bear the following relationships to the symmetry factor.

$$\alpha_a = (n - \gamma_b)/\nu - r\beta \quad (2.52)$$

$$\alpha_c = \gamma_b/\nu + r\beta \quad (2.53)$$

where n is the number of electrons transferred in the reaction,

γ_b is the number of one-electron transfers preceding the RDS,

r is the number of electrons transferred in the RDS,

ν is the number of times the RDS occurs to produce the overall reaction, and

β is the symmetry factor for the RDS.

The value of α_a and α_c define the Tafel slope and can be used as a guide in determining the mechanism of a reaction.

2.2.2 OPEN CIRCUIT POTENTIAL (OCP)

In a simple case involving the redox couple R/O, and another reducible species, O′, in solution, and in the absence of an applied potential (i.e. under open circuit conditions) the electrode placed in this solution will assume a potential, known as the mixed potential (E_m) or open circuit potential (OCP). At this value, the anodic current equals the sum of the currents due to the two cathodic reactions. In other words, the OCP is the compromise value lying between the equilibrium single potentials of the mutual R/O species present in the redox couple, as shown in Figure 2.8.

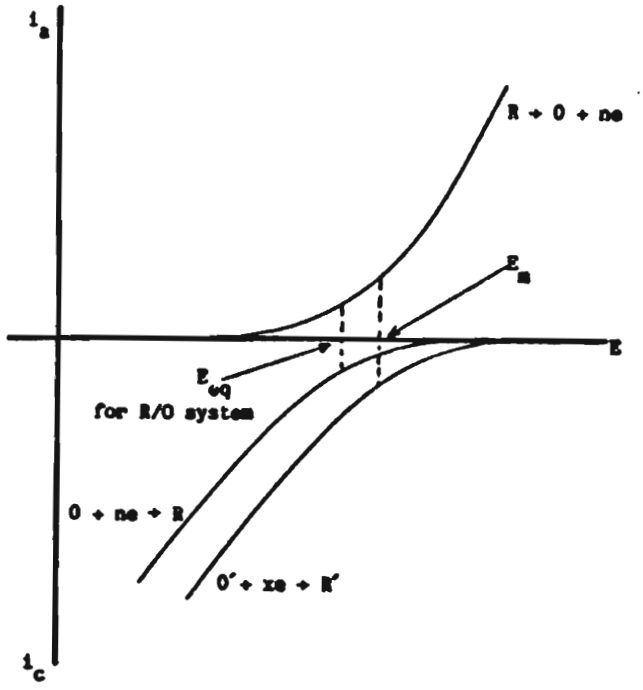

Figure 2.8 Diagram to illustrate a mixed or open circuit potential.

The accepted method for measuring the OCP of aluminium and its alloys is to record the variation of potential with time from the moment the aluminium sample is immersed in the electrolyte solution. With the passage of time, the chemical composition of the exposed aluminium surface changes due to corrosion taking place, and this is reflected by the changing OCP. This is why some authors also refer to the OCP as the corrosion potential [8, 9, 29].

The OCP of an aluminium alloy is primarily dependent on its chemical composition and metallurgical properties, the most influential being the composition of the aluminium rich solid solution, and to a much lesser degree the microstructural intermetallic phases present [8, 9, 22-24, 29]. Figure 2.9(a) shows the effect of certain alloying element additions on the OCP of aluminium. Other factors influencing the OCP include the type and concentration of ions present in solution, the pH and temperature, the total time of immersion, the thickness of the oxide film initially present, the presence of dissolved oxygen, the surface treatment used, and convection [6, 7, 10, 13, 16, 40, 42, 46, 50, 57-60, 67, 76, 81-84, 87, 117-119].

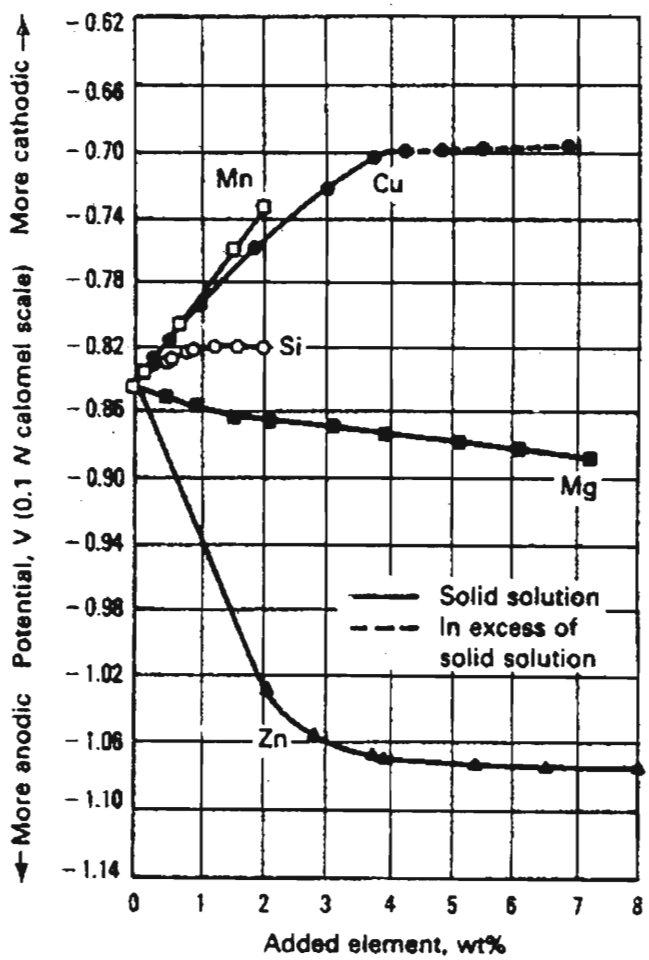

Figure 2.9(a) The effect of alloying elements on the OCP of aluminium [8].

2.2.2(a) Open circuit potentials of different metals and sacrificial anodes

The current-voltage (i-E) curves for some selected metals in acidic solution are shown in Figure 2.9(b).

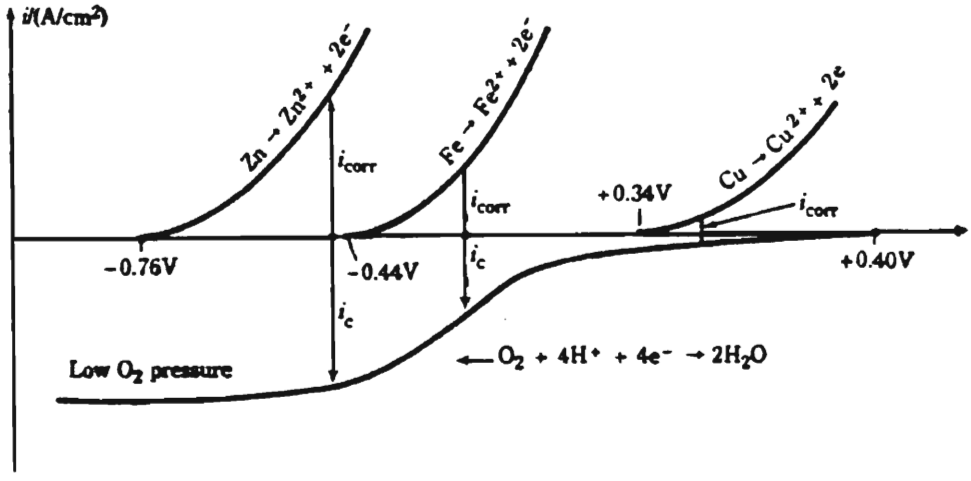

Figure 2.9(b) Oxygen corrosion in acid solution [92(b)].

Figure 2.9(b) shows that the corrosion current of Zn, which has a more negative potential than Fe, i.e. is more cathodic than Fe, is larger than the corrosion current for Fe. On the other hand, the corrosion current for Fe, which has a more negative potential than Cu, is larger than the corrosion current for Cu. If Zn and Fe are in electronic contact and are placed in an acid solution, Zn would corrode preferentially; i.e. it becomes sacrificial to Fe. This is the underlying principle of sacrificial anodes. In terms of OCPs, the metal with the more negative and hence cathodic OCP will corrode preferentially and therefore becomes the anodic area in the corrosion cell.

It is worth commenting on the contradiction apparent in Figure 2.9(a). The effect of alloying Zn with aluminium is to decrease its OCP, i.e. make it more negative and more cathodic in terms of accepted electrochemical convention. Metallurgists and automotive engineers describe the addition of Zn to aluminium as making the alloy more anodic, as can be seen in Figure 2.9(a). This description is based on the notion that the addition of Zn to aluminium decreases the OCP of the alloy and therefore makes it sacrificial, i.e. anodic, to the original aluminium reference material.

2.2.3 PITTING POTENTIAL (E_p)

The pitting potential, E_p, also referred to as the critical pitting potential, breakdown potential, or activation potential, is that electrochemical potential above which pits will initiate and below which they will not [19, 20, 23]. E_p reflects the ease by which aggressive ions such as chloride ions can 'penetrate' the exposed surface [61] and cause a sufficient amount of pit initiation to cause a sudden large increase in current. Pit initiation is an electrochemical process that involves electron transfer reactions.

Many different laboratory procedures have been developed for the measurement of E_p [19, 20, 23, 120]. These can be classified into two groups, namely current and potential controlled methods. Current controlled (galvanokinetic and galvanostatic) methods yield values of E_p that are usually larger than the corresponding results obtained by the more reliable potential controlled methods. Potential controlled methods are normally classified into potentiokinetic and potentiostatic methods, where the latter method involves observation of current with respect to time after a fresh specimen is subjected to a predetermined potential followed by inspection of the surface for pits. Three potentiokinetic methods can be described as follows: (1) Potentiodynamic method – a continuous change of potential at a constant rate; (2) Quasi-stationary method – a stepwise change of potential at a certain rate; (3) Stationary method – a stepwise change of potential where a constant current is allowed to reach a steady state at each step.

The potentiodynamic method measures E_p using anodic polarisation curves which can be expressed as either i vs E or log i vs E curves, and are based on classical electrochemical methods described in Section 2.2.1. Difficulty in identifying E_p from the break in i vs E curves, which according to Nisancioglu and Holtan [23] is due to the presence of an induction time, has led to the use of extrapolation methods that lead to slightly high values for E_p. Figure 2.10 shows a schematic representation of errors incurred by extrapolation using galvanokinetic and fast-scan potentiokinetic methods for obtaining E_p [23]. Log i vs E plots, should in terms of the Tafel equation, produce linear plots which can conveniently be extrapolated to give more reliable values of E_p.

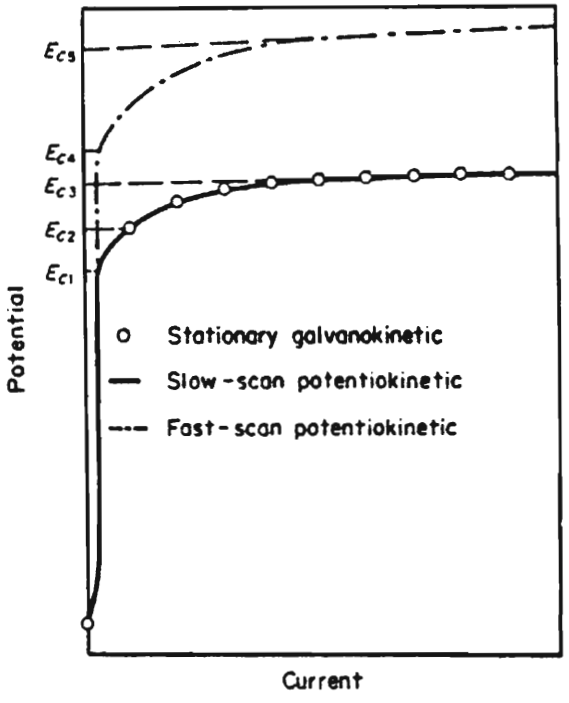

Figure 2.10 Schematic representation of errors incurred by extrapolation using i-E curves. E_{c1} is the true pitting potential. If applied current steps are too wide, the apparent pitting potential becomes E_{c2}. Extrapolation of high-current data shifts this further to E_{c3}. E_{c4} is due to fast potential scan and E_{c5} due to additional error resulting from extrapolation.

E_p can be increased or decreased by the presence of alloying elements in solid solution with aluminium, depending on whether these are more cathodic or anodic to aluminium, respectively [6, 13, 14, 16, 22-24, 37, 38, 44, 51, 65, 121]. The pitting potential of aluminium and its alloys is not affected by the presence of microstructural intermetallic phases [22, 23]. The composition of the electrolyte solution, and to a lesser extent the pH and temperature of the solution in which the aluminium samples are placed, greatly influences the value of E_p [1, 8, 10, 13, 14, 17, 18, 20, 23, 24, 35, 37, 38, 42, 46, 50, 53, 59-61, 63, 72-76, 79, 81, 82, 84, 85, 87, 117, 122-124]. Other factors that influence E_p are: the thickness and type of oxide film present at the surface, the surface treatment the sample has undergone prior to electrochemical testing, the presence of dissolved oxygen, convection, multiple polarisations, and the method as well as the equipment used for its determination [10, 13, 14, 16, 17, 19, 20, 22-24, 35, 37, 38, 41, 51, 65, 70, 73, 125].

3 EXPERIMENTAL PROCEDURE

3.1 ALUMINIUM ALLOYS

The chemical compositions of the aluminium alloy samples supplied by the manufacturer and used in this research project are listed in Table 3.1. Properties of the 'as-supplied' (AS) samples are given in Table 3.2. AS samples A, B and C represent the well-known aluminium alloy AA 3003, whilst AS samples D and E are supplier specific alloys. AS samples D and E are enriched in zinc and copper/magnesium respectively. AS samples B and C are identical in chemical composition and only differ in sample thickness by 100 μm.

Table 3.1 Chemical compositions of AS samples A, B, C, D and E (weight %).

Alloy	Si	Fe	Cu	Mn	Mg	Cr	Zn	Ti	Al
A	0.210	0.565	0.157	1.160	0.054	0.005	0.003	0.013	97.833
B,C	0.21	0.64	0.14	1.06	0.01	0.004	0.007	0.016	97.929
D	0.5-1.0	0.7	0.1	1.4 -1.8			1.2-1.8		96.1-94.6
E	0.40	0.50	0.50	0.80	0.20				97.60

Table 3.2 Properties of AS samples A, B, C, D and E.

Alloy	Supplied form	Thickness (μm)	Temper	Supplier
A	Finstock	100	H17	Hullets Aluminium
B	Tubestock	300	H18	Reynolds
C	Tubestock	400	H18	Reynolds
D	Finstock	100	H14	Finspong
E	Tubestock	320	F*	Hoogovens

* = As Fabricated

3.1.1 SAMPLE PREPARATION

3.1.1(a) Preparation of the 'as-supplied' (AS) samples

Aluminium finstock and tubestock material used for testing were cleaned employing a three-stage vapour degreasing system, with Methoklone (stabilised dichloromethane) as the degreasing substance. The three stages involved in the process were: exposure to hot vapour, ultrasonic degreaser emersion, and hot vapour drag out; after which the samples were allowed to dry in the open atmosphere.

3.1.1(b) Preparation of the 'heat-treated' (HT) samples

Aluminium finstock and tubestock material in the AS form were placed on and covered by aluminium foil trays (making sure the foil on top could not sag down and touch the samples) in order to prevent contamination by Composite Powder left behind on the fibreglass furnace curtains. These trays were then passed through the Composite Deposition (CD) brazing furnace (Section 3.1.1(d)) during a production run to ensure that the samples were treated in the same way as the actual radiators being manufactured. Once the production run was complete, the trays were removed from the production line and the samples were then examined and stored in a non-corrosive environment for future use.

3.1.1(c) Preparation of the 'Composite Powder coated' (CPC) samples

Aluminium finstock and tubestock material in the AS form were coated with an organic adhesive, namely polymethylmethacrylate (pmma), which thermally decomposes to pyrolysate during brazing. Thereafter Composite Powder was deposited onto the surface using standard production coating equipment. The coated samples were then placed on and covered by aluminium foil (as described in Section 3.1.1(b)) and passed through the CD brazing furnace during a production run to allow the Composite Powder to melt onto and partially diffuse into the finstock or tubestock material below. The important properties of the Composite Powder used for the coating of aluminium finstock and tubestock are listed in Table 3.3.

Table 3.3 Properties of Composite Powder.

Weight % Si	Weight % flux	Powder sieved to (μm)	Powder coating weight (g/m^2)	Supplier
10-11%, typically 11%	10-13%, typically 12%	10-100, median: 70	70	Osprey Metals Ltd.

The flux employed during the preparation of Composite Powder is Nocolok^{TM} flux [5], a mixture consisting of 40% to 50% KF and 50% to 60% AlF_3, which exists as $KAlF_4$ on the surface of the main constituent of Composite Powder, namely the Al-Si eutectic braze alloy.

3.1.1(d) CD Brazing Furnace

The FHE Automotive Technologies (PTY) Ltd Camlaw 4 Zone controlled atmosphere-brazing furnace, which operates under an atmosphere of dry nitrogen (dew point -40°C) and has an oxygen level less than 20 ppm (typically 5 ppm), was used for the preparation of the HT and CPC samples. The furnace was designed in such a way to ensure that the thermal decomposition products of the organic adhesive pmma were flushed away from the braze zone in a contra flow to the belt. This is to prevent poisoning of the finstock and tubestock material, as well as to prevent poisoning of the assembled radiators made for the automotive industry. The most important characteristics of the thermal profile used during the CD brazing production run are: the heating rate, the maximum temperature reached, the total time the sample or radiator spends in the furnace, and the maximum time spent above the eutectic temperature of the Al-Si filler alloy. These characteristics are recorded in Table 3.4.

Table 3.4 Essential characteristics of a typical heating profile.

Heating rate:	50°C/min to 80°C/min
Maximum temperature:	$T_{max} = 610°C$
Total time spend in furnace:	23 minutes
Time spend above eutectic temperature of Al-Si:	T_{max} (T > 577°C) = 3 minutes

Figure 3.1 shows a typical thermal profile obtained from one of the production runs.

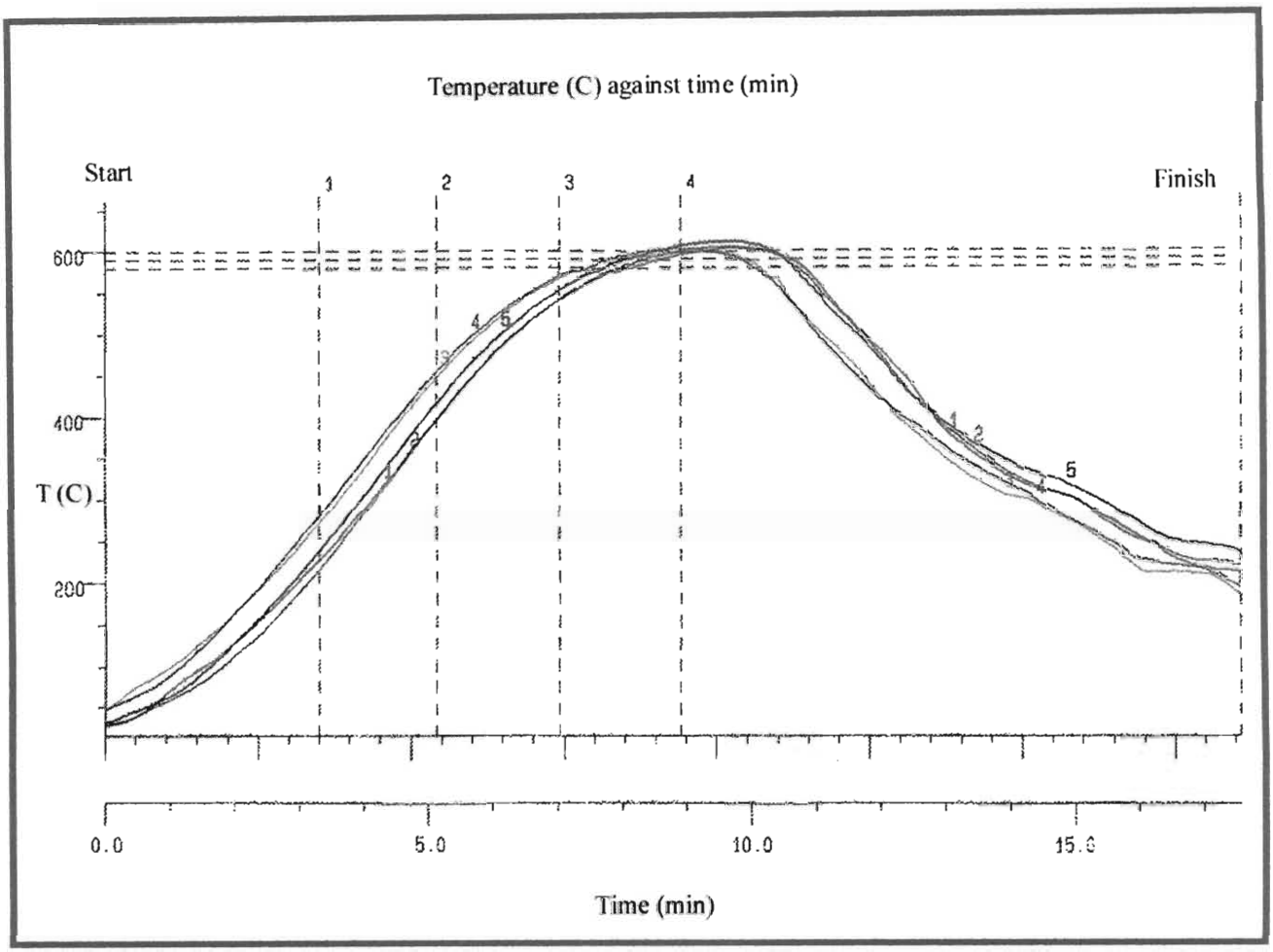

Probe position in furnace	Peak temperature (°C)		Threshold temperature: 580 °C	
	Reached	At time (min)	Time over	Time reached
1 Left Back	604	10:15	2:55	8:35
2 Right Back	605	10:05	2:55	8:30
3 Left Front	600	9:35	2:35	8:10
4 Right Front	604	9:25	2:45	7:55
5 Centre	612	10:10	3:05	8:15

Figure 3.1 Typical thermal profile for the CD brazing furnace.

3.2 ELECTROLYTES

The test solutions were made up using doubly distilled water and chemicals of analytical reagent (AR) quality. Table 3.5 lists the composition and pH (at 25°C) of each of the solutions used.

Table 3.5 Composition and pH of the test solutions used.

Electrolyte solution	Composition	pH at 25°C
1	1 M NaCl	4.06
2	0.5 M H_2SO_4 + 1 M NaCl	0.52
3	0.5 M H_2SO_4 + 1 M NaCl + 0.5 M $NaNO_3$	0.48
4	3% NaCl (0.512M)	6.49

3.3 ELECTROCHEMICAL APPARATUS

All electrochemical experiments were conducted in a conventional three electrode cell (at 25°C ± 1°C) consisting of a working electrode (the electrode under investigation), a 1 cm^2 platinum counter electrode, and a commercial saturated calomel reference electrode (SCE), as shown in Figure 3.2. The reference electrode (Schott Geräte B2910) was incorporated into a Luggin capillary that was positioned approximately 1 mm from the working electrode to minimise the contribution due to the ohmic potential or IR drop. These electrodes were all housed inside a 300 ml reaction vessel equipped with a magnetic stirrer bar. Unless otherwise indicated, all potential values quoted in this thesis were measured relative to the SCE.

Preparation of the working electrode involved cutting finstock and tubestock material into 1.4 cm by 1.4 cm token samples which were then placed in the nylon sample holder. The alloy sample was held in place, and kept in electrical contact with a copper contact positioned in the sample holder, by the nylon screw cap, which exposed a circular electrode surface area of exactly 1 cm^2 to the solution. The nylon sample holder is shown in Figure 3.3.

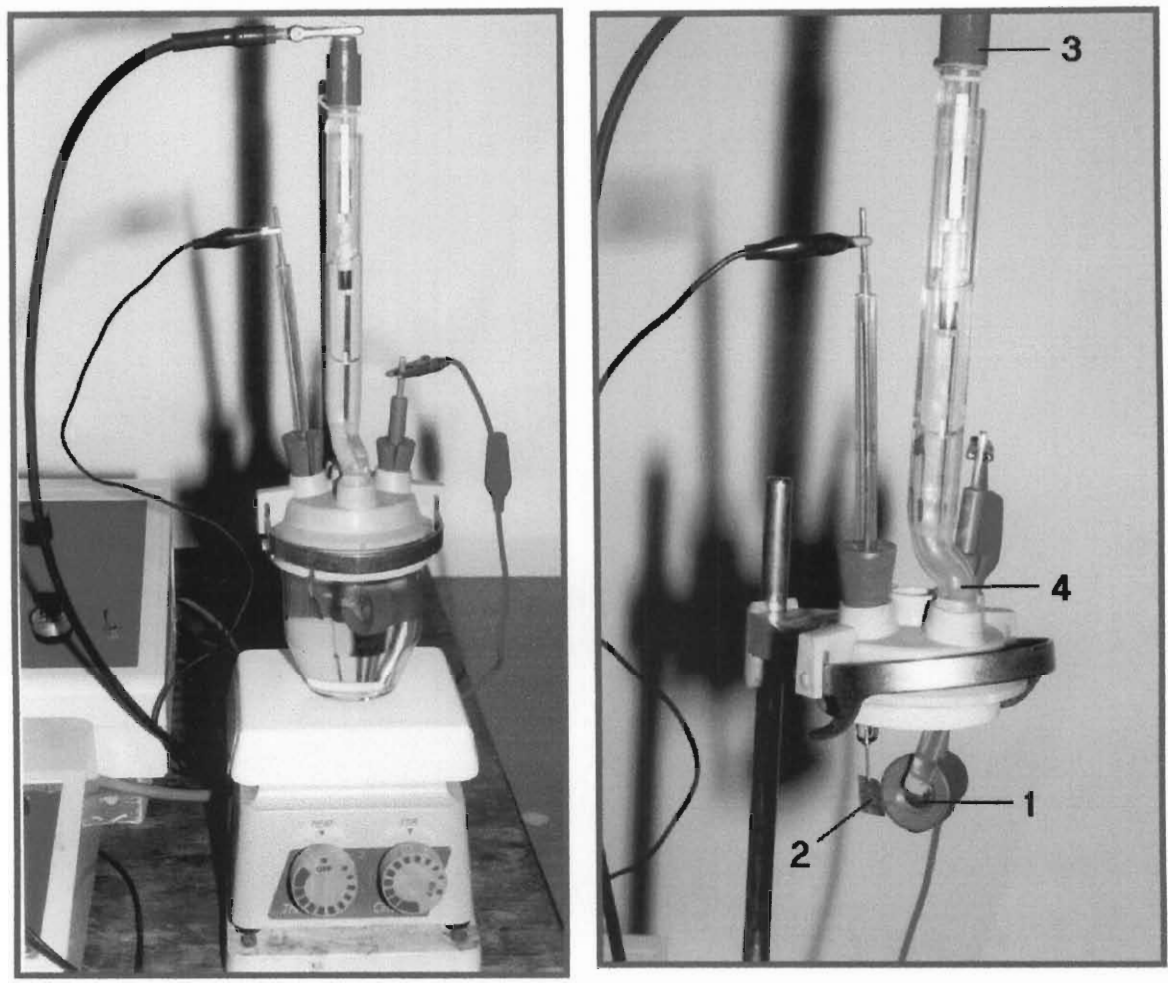

Figure 3.2 A conventional three electrode cell consisting of a working electrode marked '1', a 1 cm^2 platinum counter electrode marked '2', and a commercial saturated calomel reference electrode marked '3' housed in a Luggin capillary marked '4'.

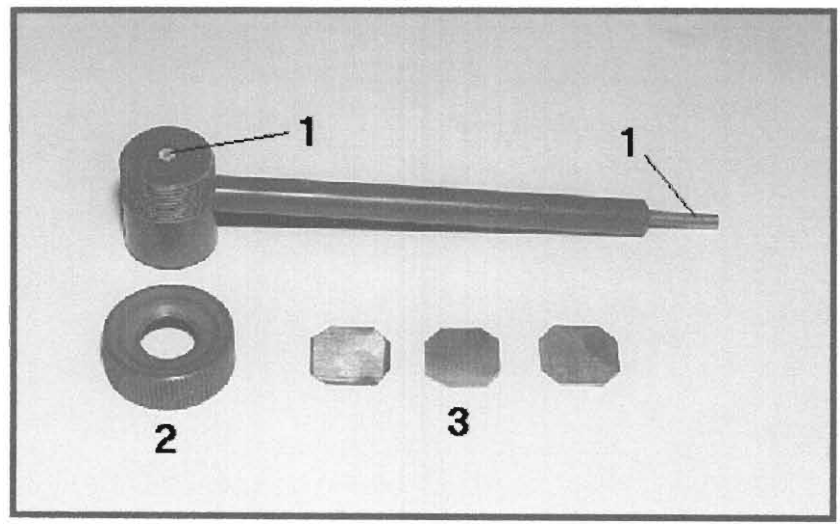

Figure 3.3 A typical nylon sample holder showing the exposed Cu contacts marked '1', the nylon screw cap marked '2', and three sample tokens marked '3'.

The electrochemical apparatus consisted of a potentiostat used in conjunction with a linear sweep generator and a logarithmic converter. A special electronic component was incorporated into the logarithmic current converter, which allowed the point at which the current equalled zero to be offset by a unit of one. All results were recorded on a Lloyd PL3 X-Y recorder. The electronic equipment used in the electrochemical experiments is shown in Figure 3.4, and was all specially designed and made by the Electronics Centre at the University of Natal, Pietermaritzburg (UNP). The nylon cell holders and the platinum counter electrodes were machined by the Mechanical Workshop at UNP, and all electrochemical glassware was made by the University Glass Blower.

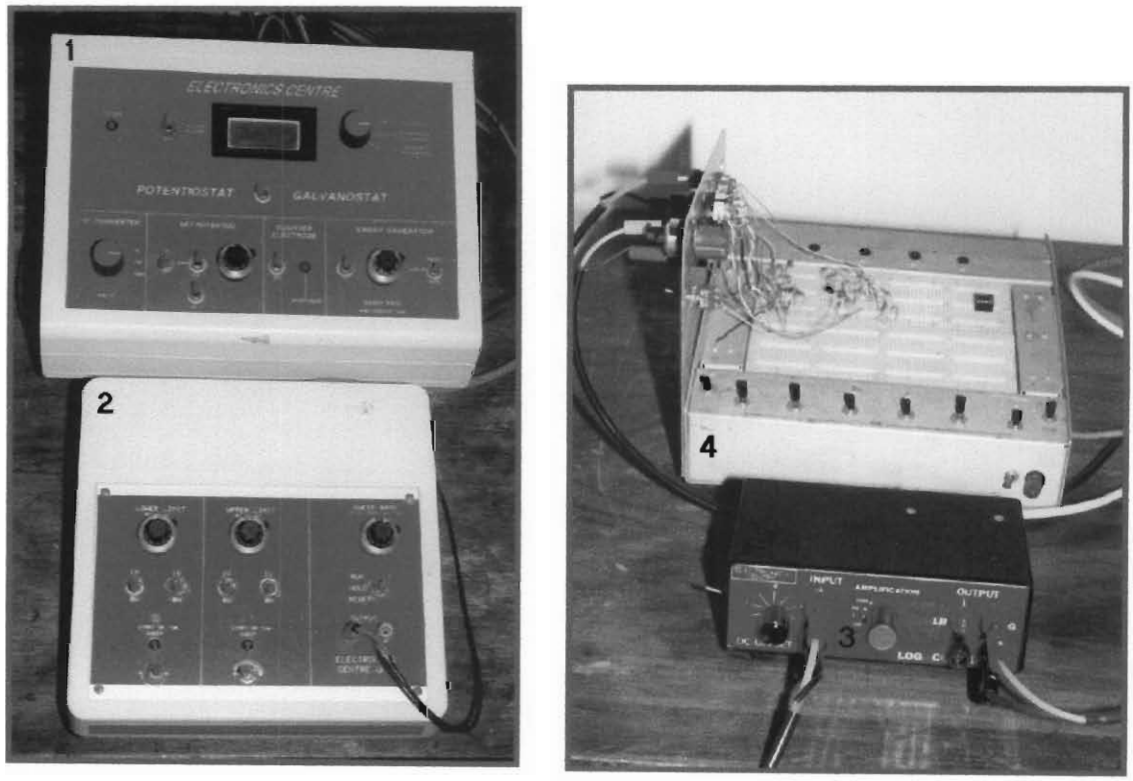

Figure 3.4 Electronic equipment used in the electrochemical experiments. The potentiostat is marked '1', the linear sweep generator is marked '2', the logarithmic converter is marked '3', and the logarithmic offset circuit board is marked '4'..

3.4 ELECTROCHEMICAL MEASUREMENTS

3.4.1 OPEN CIRCUIT POTENTIAL (OCP) MEASUREMENTS

The aluminium sample was placed in the nylon sample holder, and together with the counter electrode and reference electrode, was positioned in the cell top so that the Luggin capillary was about 1 mm from the aluminium sample. The electrodes were connected to the potentiostat with the counter electrode switched off. The assembly was then lowered into the stirred electrolyte solution and the OCP recorded immediately and for a further period of 75 minutes. After 75 minutes the sample was disconnected from the circuit, removed from the solution and sample holder, and the procedure was then repeated with a new sample.

All OCP measurements were performed in triplicate to ensure reproducibility and validity of the results obtained. The results that are quoted in this thesis are the averages of these triplicate runs. In order to avoid excessive solution contamination (which could adversely affect the results), the test solution was changed after each triplicate experiment was completed. It was established that if the solution was left unchanged for more than five runs, erratic results were obtained. In all cases, the test solution was stirred throughout the experiment to avoid the build-up of corrosion products at the aluminium electrode surface and to avoid diffusional problems. The test solutions were kept to within 1°C of 25°C in an air-conditioned thermostatted laboratory.

3.4.2 POTENTIODYNAMIC ANODIC POLARISATION

Potentiodynamic anodic polarisation curves were used to find the pitting potential, E_p, of the aluminium alloy samples in the various corrosive electrolyte solutions studied.

The aluminium sample was placed in the nylon sample holder, and positioned in the cell top together with the counter electrode and reference electrode, so that the Luggin capillary was about 1 mm from the aluminium sample. The electrodes were connected to the potentiostat with the counter electrode switched off. The assembly was then lowered into the stirred electrolyte solution and the counter electrode switched on. The initial applied

potential or 'switch-on' potential, i.e. the potential from which the anodic polarisation would begin, obviously needed to be lower than the pitting potential E_p. Experience showed that values between 20 mV to 200 mV more negative than the actual pitting potential were satisfactory. It was found that, by starting the anodic polarisations at these potentials and not at the OCP of the alloy, did not affect the final value of E_p obtained.

The sweep generator was then switched on and the applied potential was swept in the positive direction at a sweep rate of 1 mV/s. The log i vs E plot was recorded simultaneously. The initial applied 'switch on' potentials used for each of the alloy samples in the various corrosive electrolyte solutions are shown in Table 3.6.

The onset of pitting was accompanied by a large surge in current. Once a sufficiently large linear portion of the log i vs E plot had been obtained the experiment was switched off. The sweep generator was then reset to its original position and the counter electrode switched off. This procedure was repeated a further six times, until seven successive anodic polarisation curves were obtained per sample. The effect of multiple sweeps on the value of E_p could thus be determined. The sample was removed from the solution and sample holder, visually inspected and discarded. The procedure described above was further repeated at sweep rates of 2.5, 5, 10, 15, 20 and 25 mV/s.

Table 3.6 Initial or 'switch on' applied potentials used for alloys A, B, C, D and E in the AS, HT and CPC forms.

Alloy	Solution 1 (mV)	Solution 2 (mV)	Solution 3 (mV)	Solution 4 (mV)
A(AS)	-750	-900	-700	-850
A(HT)	-950	-950	-850	-900
A(CPC)	-1000	-900	-750	-1000
B(AS)	-800	-850	-750	-800
B(HT)	-950	-900	-850	-1000
B(CPC)	-1000	-850	-800	-1050
C(AS)	-800	-850	-700	-800
C(HT)	-950	-900	-850	-1000
C(CPC)	-1000	-850	-800	-1050
D(AS)	-950	-1000	-800	-1000
D(HT)	-900	-950	-850	-950
D(CPC)	-1100	-950	-900	-1100
E(AS)	-850	-800	-650	-800
E(HT)	-900	-900	-700	-850
E(CPC)	-1000	-900	-750	-1000

3.5 MICROGRAPHIC EXAMINATION

The corrosion occurring on an aluminium alloy sample can be studied by micrographic surface examination. Two techniques are available, namely optical microscopy and Scanning Electron Microscopy (SEM).

Both techniques use samples prepared in the same way. Samples were cut into 1.4 by 1.4 cm tokens, placed in the nylon sample holder exposing a surface area of exactly 1 cm^2, and immersed in the various corrosive electrolyte solutions and allowed to corrode for exactly one hour under open circuit conditions. The corroded sample was then removed from the

solution and sample holder, rinsed thoroughly with distilled water, dried and then stored in a desiccator.

3.5.1 OPTICAL MICROSCOPY

Samples of both the corroded aluminium alloy and the uncorroded parent metal were cross-sectioned and cold mounted in an acrylic non-conductive resin that was cured for 15 minutes under 3 atmosphere of pressure in a Kulzer Technomat pressuriser. The mounted samples were ground and polished on an Imptech 20DVT double wheel polisher down to 0.05 μm using the following procedure. Firstly, the samples were ground with 320 grit SiC paper, using water as a lubricant and coolant. This polishing procedure was repeated with 800 grit SiC and 1200 grit SiC. This was followed by polishing the samples with 1 μm and 0.05 μm diamond polish on a PSA backed velvet cloth using diamond extender as a lubricant. A final polish was done with 0.05 μm colloidal Silica suspension on a PSA backed velvet cloth using water as a lubricant. Rinsing with water and blow-drying the sample with warm air followed each consecutive grinding and polishing.

The grain structure could be revealed by etching the polished samples in an etch solution consisting of 50 ml of Poulton's reagent, 25 ml HNO_3 (conc.) and 40 ml of 3 g chrome oxide (green) in 10 ml of water. Poulton's reagent consists of 12 ml HCl (conc.), 15 ml HNO_3 (conc.), 1 ml HF (48%) and 1 ml H_2O. A one to two minute sample immersion in the etching solution was sufficient to reveal the grain size and shape.

Polished samples were examined and photographed before etching using Normanski techniques and after etching using polarised light on a Zeiss Axiotech 25HD optical microscope.

3.5.2 SCANNING ELECTRON MICROSCOPY

The corroded and uncorroded aluminium alloy samples were prepared for SEM analysis in the following way. A sample was held in position on a metal stub with carbon paste and was then carbon coated to prevent charging of the non-conducting Al_2O_3 film or flux layer. The surfaces were examined using a Hitachi S-520 SEM fitted with a LINK ISIS energy dispersive X-ray analyser, operated at 20 kV with a working distance of 15 mm.

4 RESULTS

The influence of heat treatment and Composite Powder coating on the microstructure and electrochemical behaviour of the aluminium alloys of interest can best be understood by comparing the microstructural and electrochemical characteristics of the 'as-supplied' (AS) samples with those of the 'heat-treated' (HT) samples and 'Composite Powder coated' (CPC) samples.

The results obtained in 1M NaCl and 3% NaCl (0.512M) solutions were virtually indistinguishable from one another, as were the results obtained for alloy samples B and C which have an identical chemical composition but differ in thickness by 100 μm. For this reason, all results for the 3% NaCl solution and for alloy sample C have not been reported on.

4.1 MICROGRAPHIC RESULTS

The AS, HT and CPC samples A, B, D and E, as prepared in Section 3.5, were placed in the nylon cell holder, immersed in the various corrosive electrolyte solutions and allowed to corrode for 60 minutes under open circuit conditions. The corroded samples, as well as the uncorroded parent metal samples of each of the alloys, were then examined using optical microscopy and Scanning Electron Microscopy (SEM).

4.1.1 MICROSTRUCTURE OF THE UNCORRODED PARENT METAL SAMPLES

4.1.1(a) 'As-supplied' and 'heat-treated' samples

Cross-sections of the initial AS and HT samples before being subjected to corrosion tests can only provide some information on the microstructural intermetallic phases or particles present as shown in Figure 4.1. The larger microstructural intermetallic phases represented by the particle group numbers 1 to 4 are primary microstructural intermetallic phases, while the particle groups 5 and 6 are most likely eutectic phases [54]. The AS and HT samples would not be expected to show any significant surface corrosion as shown in

Figure 4.2. Furthermore cross-section micrographs of the AS and HT samples were very similar and are typically represented in Figures 4.1 and 4.2.

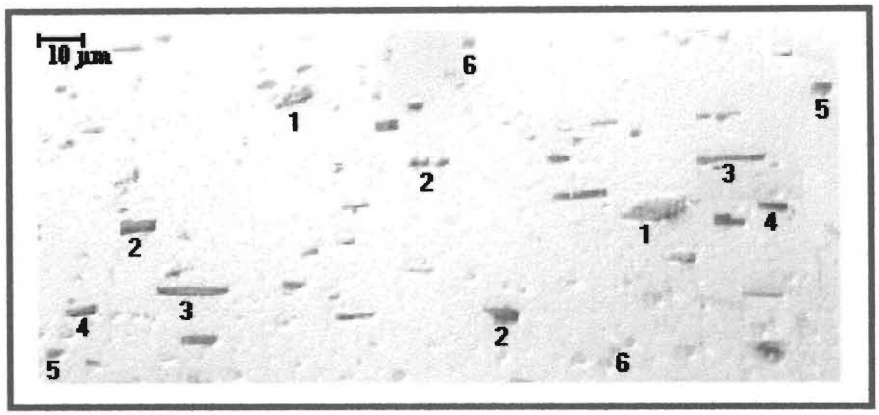

Particle group numbering	Description of 2-D shape and size	Surface area of particle (μm^2)
1	Large sized polygon	A > 35
2	Medium sized polygon	20 < A < 35
3	Long and thin	16 < A < 29
4	Medium length and thin	9 < A < 16
5	Very small polygon	3 < A < 9
6	Speck	A < 3

Figure 4.1 Cross-section of HT sample A showing different sized microstructural intermetallic phases present (500x).

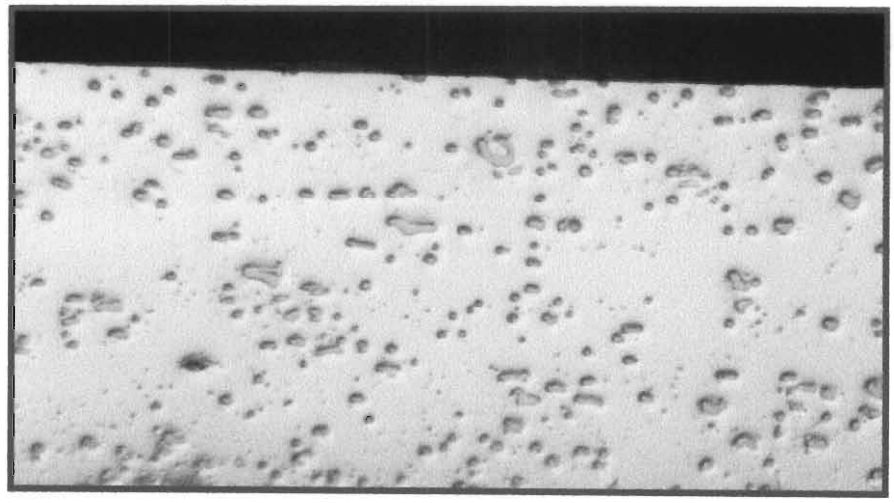

Figure 4.2 Typical cross-section of AS sample D showing minimal surface corrosion.

Energy Dispersive X-ray (EDX) spot analysis performed on the different microstructural intermetallic phases gave a rough indication of the alloying elements that were present. It is by no means an accurate method and cannot be used to determine the exact chemical composition of the microstructural phase or surface of interest. A lot of background composition that will significantly alter the results is picked up during the analysis, especially when analysing the smaller microstructural intermetallic phases.

The results obtained from EDX spot analysis taken of microstructural intermetallic phases on cross-sectioned surfaces of AS and HT samples A, D and E have been recorded in Table 4.1. It was observed that the chemical compositions of the six classes of microstructural intermetallic phases were different for each alloy sample, except alloy samples A and B, which were made of the same aluminium alloy but cold-rolled to a different thickness. The chemical compositions of the microstructural intermetallic phases before and after heat treatment were similar for alloy samples A and B. Some compositional differences were found before and after heat treatment for the microstructural intermetallic phases of alloy samples D and E.

Table 4.1 Chemical compositions of the microstructural intermetallic phases.

Particle group numbering	Alloy	Al	Si	Mn	Fe	Cu	Zn
Total Surface Area exposed	A(AS)	95.92	2.21	1.3	0.57		
	A(HT)	95.47	2.47	1.34	0.7		
	E(AS)	95.9	2.55	0.98	0.57		
	E(HT)	96.29	2.26	1.05	0.4		
	D(AS)	93.49	2.39	2.26	0.38		1.49
	D(HT)	93.43	2.43	1.81	0.38		1.95
1	A(AS)	70.57	2.98	12.03	14.43		
	A(HT)	71.58	1.33	12.37	14.71		
	E(AS)	—	—	—	—		
	E(HT)	71.72	4.93	6.47	16.88		
	D(AS)	*	*	*	*		*
	D(HT)	*	*	*	*		*
2	A(AS)	—	—	—	—		
	A(HT)	75.31	1.44	11.77	13.48		
	E(AS)	77.04	4.96	4.95	13.05		
	E(HT)	75.13	2.67	8.51	13.69		
	D(AS)	67.97	7.08	19.16	5.79		
	D(HT)	69.54	7.15	16.74	5.95		1.95
3	A(AS)	89.93	2.09	4.79	3.2		
	A(HT)	86.11	1.76	6.31	5.83		
	E(AS)	86.28	1.75	5.31	6.66		
	E(HT)	—	—	—	—		
	D(AS)	*	*	*	*		*
	D(HT)	*	*	*	*		*
4	A(AS)	—	—	—	—		
	A(HT)	92.78	1.99	3.25	1.97		
	E(AS)	85.14	1.99	5.53	7.34		
		84.81	2.79	6.22	6.18		
	E(HT)	83.11	2.61	7.05	6.74	0.49	
		79.34	4.12	3.69	12.31	0.55	
	D(AS)	*	*	*	*		*
	D(HT)	*	*	*	*		*
5	A(AS)	—	—	—	—		
	A(HT)	87.18	2.19	5.65	4.99		
	E(AS)	82.99	4.63	5.4	6.98		
	E(HT)	84.1	3.79	5.65	6.45		
	D(AS)	91.13	2.95	3.25	1.13		1.54
	D(HT)	85.63	4.6	6.41	2.19		1.16
		82.63	5.11	8.59	2.83		0.84
6	A(AS)	96.36	2.39	0.99	0.26		
	A(HT)	97.19	1.98	0.83	0.05		
	E(AS)	93.84	2.56	1.84	1.76		
		96.65	2.34	1.01			
	E(HT)	97.1	2.25	0.66			
	D(AS)	86.43	3.44	7.2	2.19		0.74
		76.71	5.9	12.07	4.32		1.00
	D(HT)	91.94	3.13	2.68	0.6		1.64

--- Particle group not analysed, * Particle group not present.

Electron micrographs of the initial surfaces of the AS and HT samples all show the surface ridges formed during the factory cold-rolling necessary to reduce the sheet to the required thickness. Surface corrosion would be expected to be minimal and the visual effect of heat treatment of the samples was merely to dull the appearance of the surface. Physical handling of the samples also revealed a softer metal that was easily malleable. A large number of surface electron micrographs were taken and they were, as expected, all very similar.

The surface of AS samples B and E and HT sample B all resembled the surface shown in Figure 4.3(a), which is that of AS sample B. Small initial pits were found around the peripheries of some of the microstructural intermetallic phases. These pits were formed because of localised galvanic cells that had been set up between the microstructural intermetallic phases and the aluminium matrix. The surface of AS and HT samples A and D were similar in appearance, and a typical example is shown for HT sample A in Figure 4.3(b). Small initial pits were common.

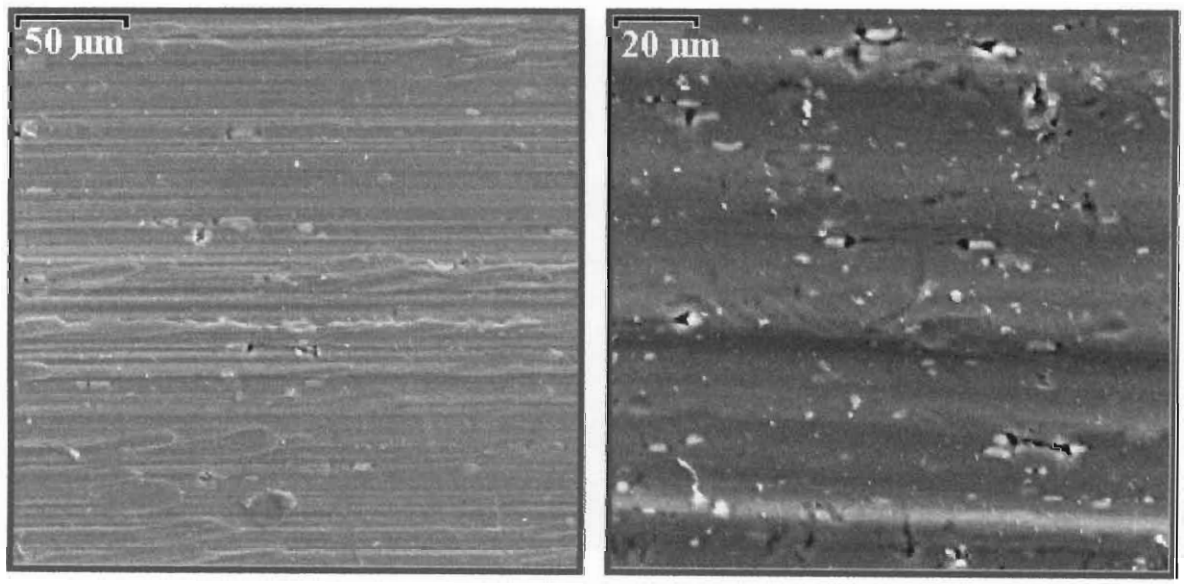

(a) **(b)**

Figure 4.3 Electron micrographs showing the unpolished surfaces of (a) AS sample B (1000x) and (b) HT sample A (500x).

Heat treatment of AS sample E revealed a different surface microstructure as shown in Figure 4.3(c). Large lightly coloured areas were found on the HT surface that on closer inspection appeared to be due to a localisation of one or more of the elements, probably

Cu/Mg, present in the aluminium solid solution. Around the periphery of one of these lighter areas initial pits had formed.

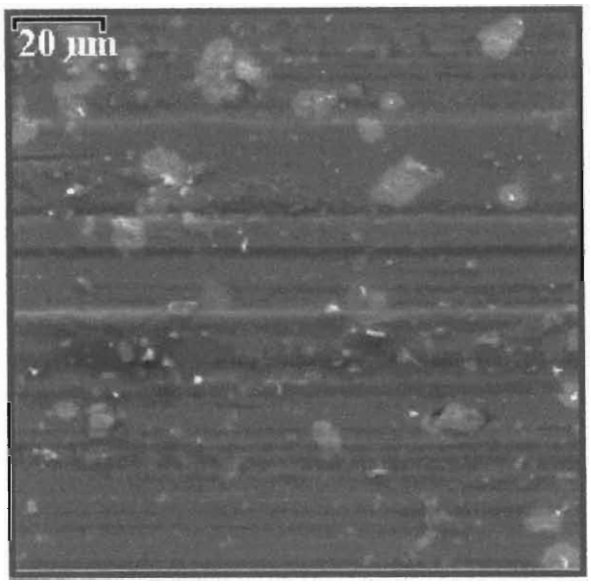

Figure 4.3(c) Uncorroded surface of HT sample E (1000x).

Heat treatment of the AS samples would be expected to increase the surface oxide layer. EDX analysis was used to confirm this. The effect of the thermal profile on the surface oxide content of the AS samples has been summarised in Table 4.2 below. All four AS samples showed an increase in surface oxide after heat treatment. AS samples A, B and D showed a small increase in surface oxide of 0.6% to 0.8% after heat treatment. Heat treatment of AS sample E resulted in a larger increase in surface oxide of 2.6%.

Table 4.2 Percentage surface oxide found on the uncorroded AS and HT samples of alloys A, B, D and E.

Alloy	A(AS)	A(HT)	B(AS)	B(HT)	D(AS)	D(HT)	E(AS)	E(HT)
Magn.*	500	500	500	500	500	500	200	200
% O	0.60	1.36	1.81	2.50	0.94	1.55	1.39	3.99

* Magn. = Magnification factor of micrograph.

4.1.1(b) 'Composite Powder coated' samples

Composite Powder coating results in a multi-layered structure consisting of four distinct layers [2]. These layers are listed below:

(a) A surface layer consisting of residual flux and partially reacted Composite Powder;

(b) A eutectic Al-Si melt layer including eutectic Al-Si diffusion zones containing $(Fe,Mn)Al_6$ microstructural intermetallic phases;

(c) A filler metal layer consisting mainly of α-Al (also referred to as the α-Al filler metal layer);

(d) The underlying base aluminium alloy.

When a cross-section of a CPC sample is analysed microscopically, the residual flux consisting of $KAlF_4$ crystals and the partially reacted Composite Powder cannot be clearly distinguished. A typical cross-sectioned view of a CPC sample showing all but the surface layer is shown in Figure 4.4. The eutectic Al-Si melt layer adjacent to the surface is marked 'b(i)', the eutectic Al-Si diffusion zones 'b(ii)', the α-Al filler metal layer 'c', and the base aluminium alloy 'd'.

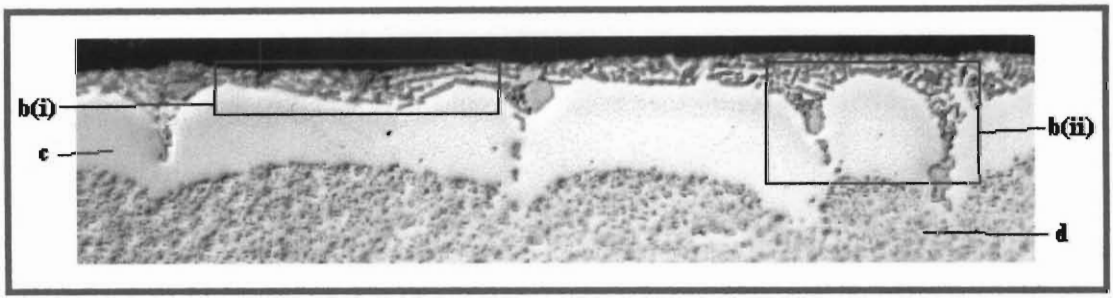

Figure 4.4 A typical cross-section of a CPC sample (500x).

The eutectic Al-Si melt layer is shown at a higher magnification in Figure 4.5. The eutectic Al-Si melt layer consists of an interconnected network [126] of eutectic β-Si particles rod-like in shape and up to 9 μm in length, and $(Fe,Mn)Al_6$ microstructural intermetallic phases [2] polygonal in shape and of varying sizes, suspended in a continuous matrix of α-Al. During heat treatment, diffusion of the eutectic Al-Si melt layer from the surface towards the base alloy below results in eutectic Al-Si diffusion zones that appear cone-like in shape. $(Fe,Mn)Al_6$ microstructural intermetallic phases precipitate out along

the eutectic Al-Si diffusion zones and at the filler metal/base alloy interface. The filler metal layer consists of a continuous matrix of α-Al containing a small percentage of silicon in solid solution. Except for the eutectic Al-Si diffusion zones, no β-Si or visible microstructural intermetallic phases were found in this layer. The depth of the entire Composite melt layer varied between 13 μm to 60 μm on the same sample, which was due to uneven spreading of the Composite Powder.

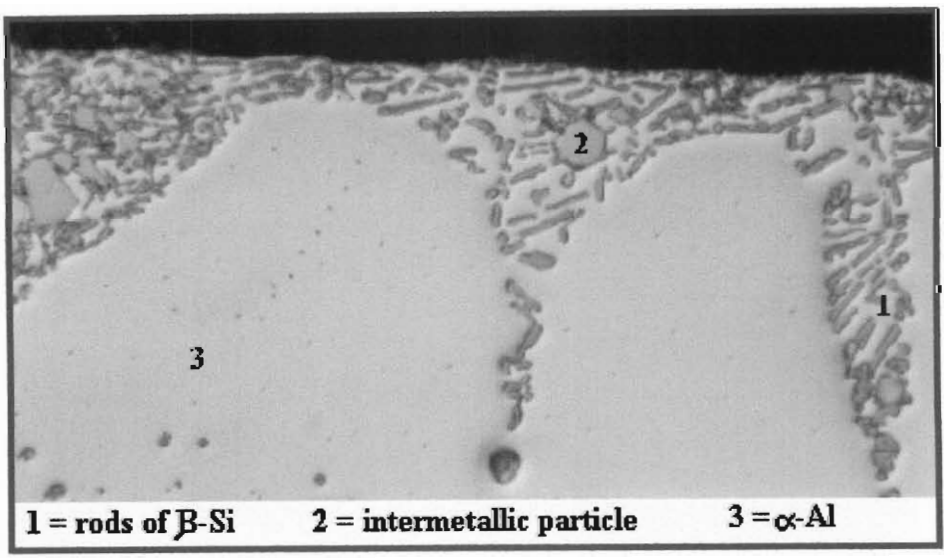

Figure 4.5 Eutectic Al-Si diffusion zones in a matrix of α-Al (1000x).

Further useful details on the CPC surface can be obtained from SEM analysis. A typical surface of an uncorroded CPC sample is shown in Figure 4.6. Identifiable details of the surface are marked. The area marked '1' represents partially reacted Composite Powder, which has been shown magnified at 1500x and 5000x in Figure 4.7(a) and 4.7(b) respectively. The partially reacted Composite Powder resembled globules that were 0.8 μm to 2.3 μm in diameter and consist of Si in solid solution with α-Al. The area marked '2' shows a conglomeration of $KAlF_4$ flux crystals that range in diameter from 10 μm to 500 μm. The area marked '3' shows a cell of α-Al surrounded by rods and needles of β-Si. This detail is shown again at a higher magnification in Figure 4.7(c). Needles of this type have also been found as an interconnected network partially covered by residual flux and partially reacted Composite Powder at the surface, as illustrated in Figure 4.7(d). The area marked '4' shows an unreacted particle of Composite Powder. A magnification of such a particle is shown in Figure 4.7(e). Crystals of flux are visible around the circumference of the unreacted Composite Powder particle in contact with the surface.

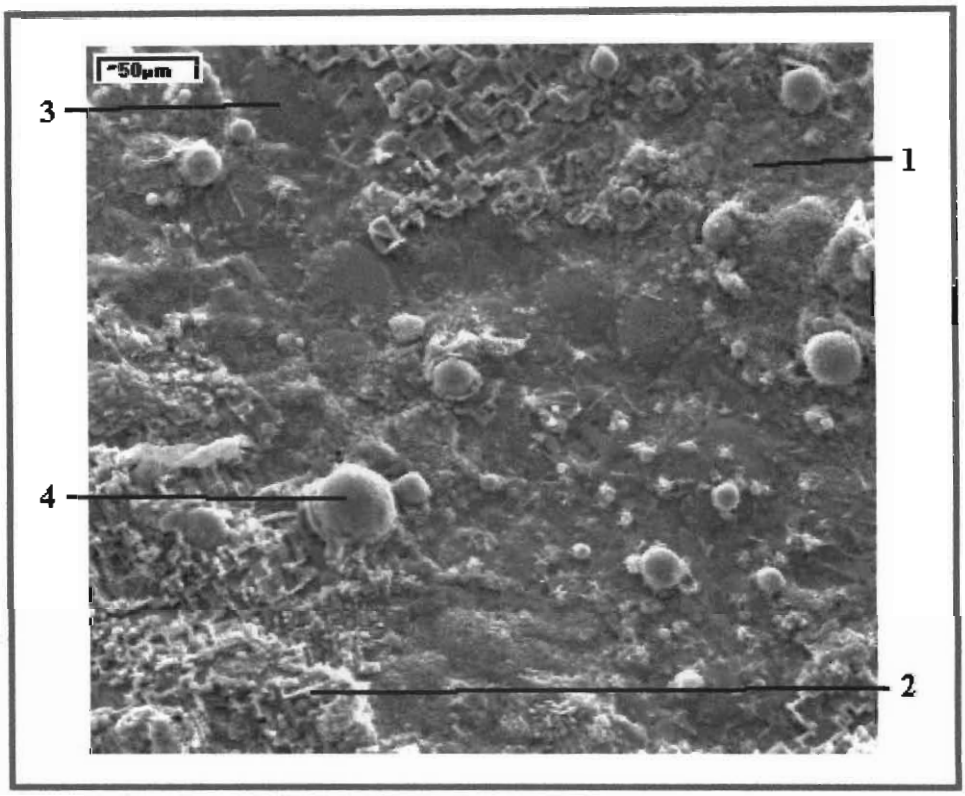

Figure 4.6 Surface details found on a typical CPC sample (300x).

The percentages of oxygen, silicon and flux present on the surfaces of all four CPC samples were measured using EDX analysis before exposure to a corrosive electrolyte solution. The results obtained are recorded in Table 4.3. The uncorroded CPC samples showed a surface oxide content of 3.7% to 6.8%, about 5.8% Si and a high percentage of flux.

Table 4.3 Percentage O, Si, K and F present on the uncorroded CPC samples A, B, D and E.

Alloy	A(CPC)	B(CPC)	D(CPC)	E(CPC)
Magn.*	200	100	100	100
% O	4.98	5.37	6.80	3.78
% Si	5.85	5.94	5.86	5.63
% K	20.61	12.28	15.03	18.93
% F	16.66	14.37	26.08	29.14

* Magn. = Magnification factor of micrograph.

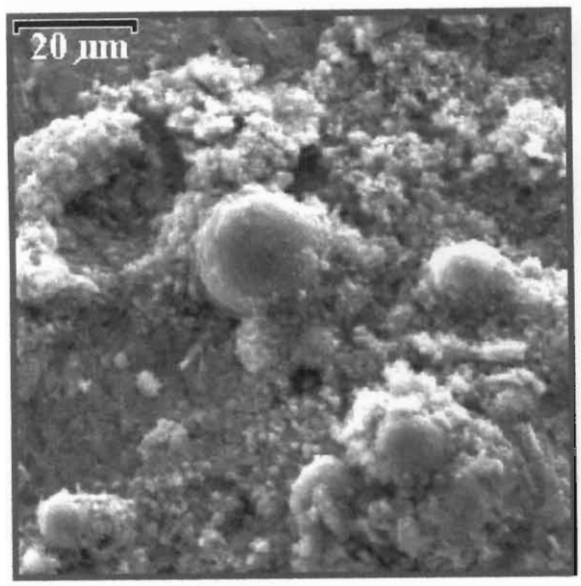

(a)

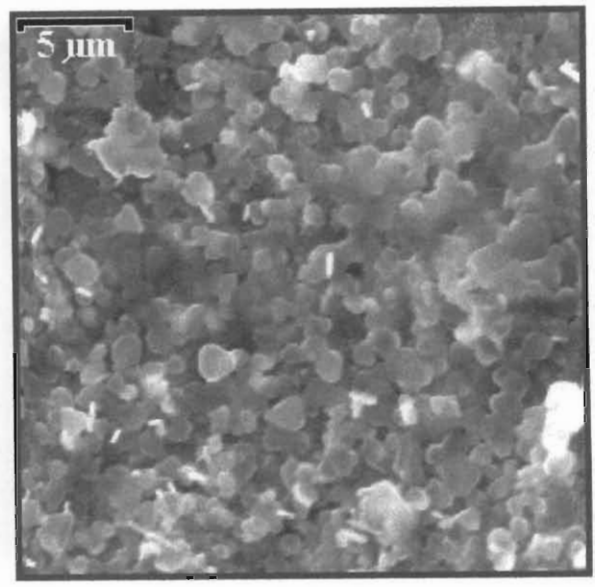

(b)

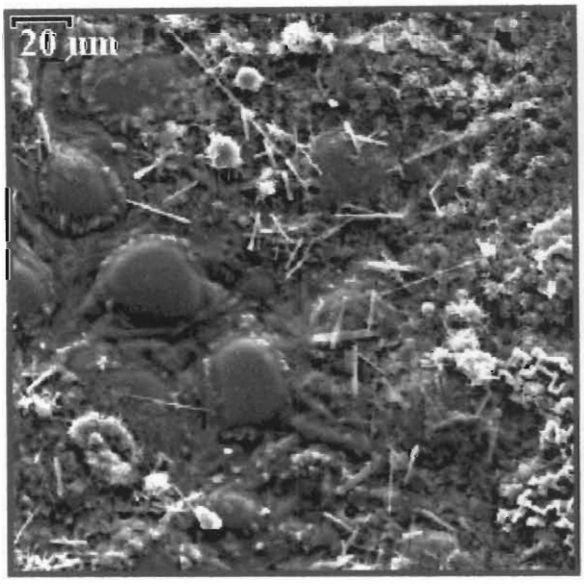

(c)

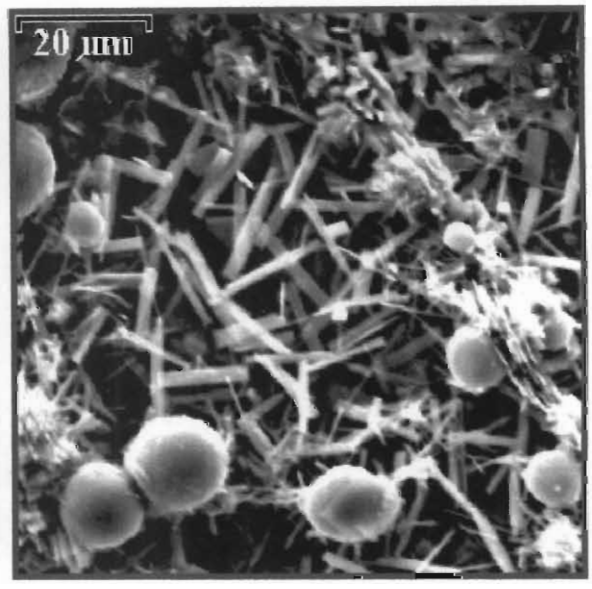

(d)

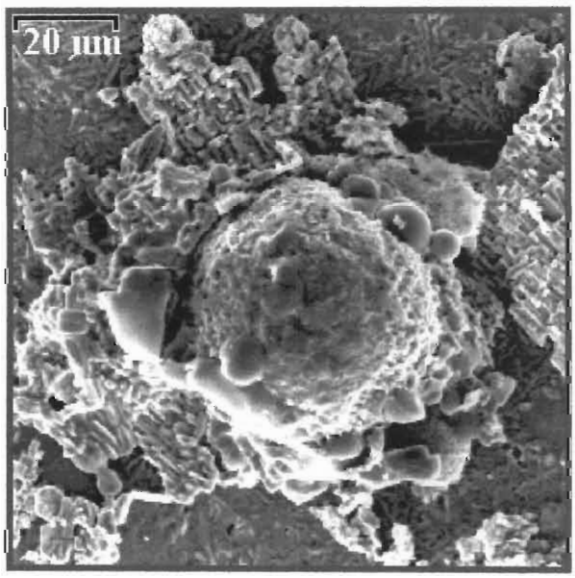

(e)

Figure 4.7 CPC surface details. (a), (b) Globules of partially reacted Composite Powder (1500x and 5000x), (c) Cells of α-Al and needles of β-Si (700x), (d) An interconnected network of β-Si needles (1500x) and (e) An unreacted particle of Composite Powder (1200x).

4.1.1(c) Grain size and shape of the 'as-supplied', 'heat-treated' and 'Composite Powder coated' samples

The grain size and shape of the AS, HT and CPC samples was revealed by etching polished cross-sections of the alloy samples for 30 to 60 seconds using the etch solution described in Section 3.5.1. Optical micrographs were taken of the etched sections using polarised light. Cross-sections cut along the direction of rolling showed the long-transverse (LT) face whilst those cut perpendicular to the rolling direction showed the short-transverse (ST) face.

AS samples A, B, D and E all revealed 'stringing' unrecrystallised grain as is typical of cold-rolled sheet products. This grain structure is shown for AS sample B in Figure 4.8.

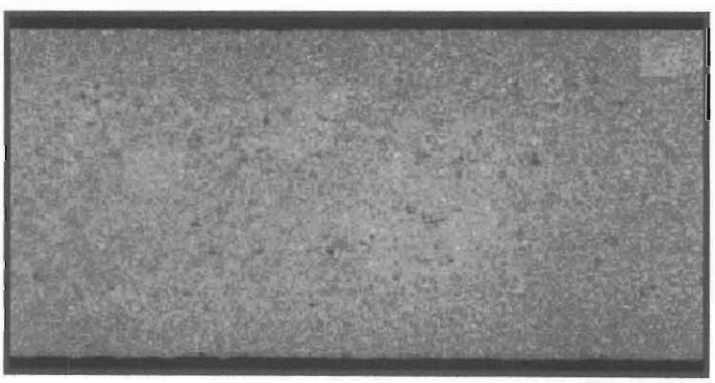

Figure 4.8 Unrecrystallised 'stringing' grain of AS sample B (200x).

Heat treatment of the AS samples resulted in recrystallisation of the grains to form a preferred, more thermally stable crystal lattice. This resulted in loss of rigidity and explained the softer metal structure that was observed. The HT samples B and E showed a similar grain structure to the base alloy of CPC samples B and E, and the same was found for the HT and CPC samples A and D. The only difference between the HT and CPC grain structures were cells of α-Al at the surface making up the α-Al filler metal layer. A cross-section of the ST face of HT sample B is shown in Figure 4.9. The grains show random reflection, indicating random crystallographic orientation. Black spots are etch pits.

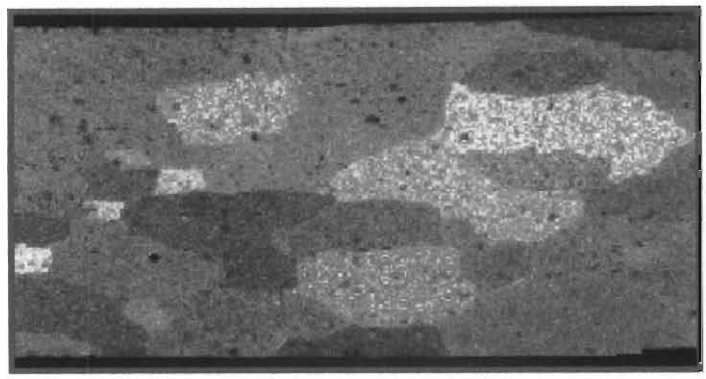

Figure 4.9 Recrystallised grain of a ST section of HT sample B (200x).

Depending on which face was being viewed, the HT and CPC samples B and E revealed a somewhat different grain size and shape. The ST face in general showed a larger grain than the LT face, but areas with smaller grains similar to those observed on the LT face were also found on the ST sections. This has been shown in Figure 4.10. Figure 4.10(a) shows a section of the ST face of CPC sample B, and Figure 4.10(b) shows the LT section of CPC sample E.

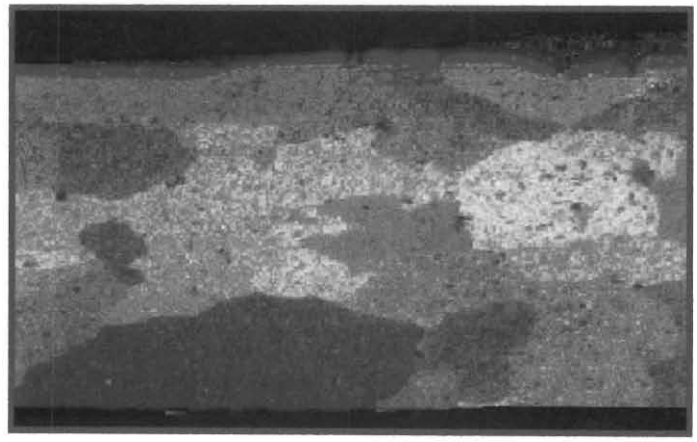

Figure 4.10(a) The grain size and shape of a ST section of CPC sample B (200x).

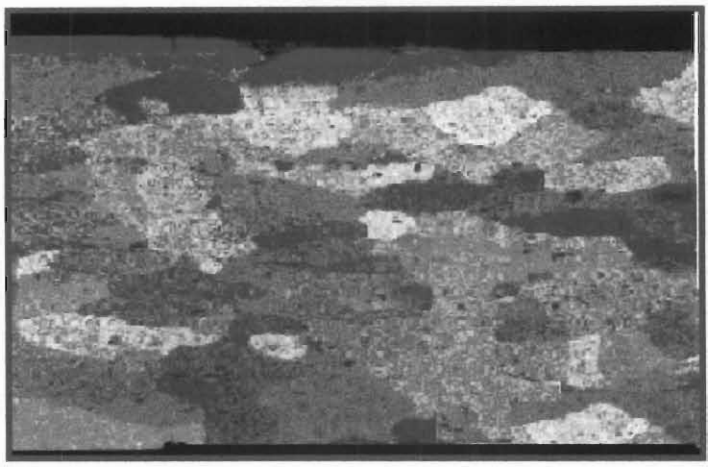

Figure 4.10(b) The grain size and shape of a LT section of CPC sample E (200x).

The HT and CPC samples A and D revealed an elongated grain structure that was similar for both ST and LT sections. In general the cross-sections showed only two layers of grain for the HT samples, whilst three layers were observed on the CPC samples, the top layer consisting of cells of α-Al in the α-Al filler metal layer. This is shown in Figure 4.11.

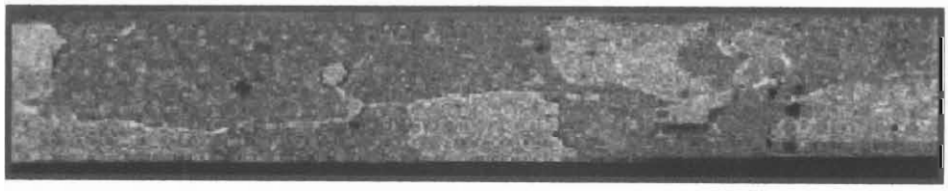

(a)

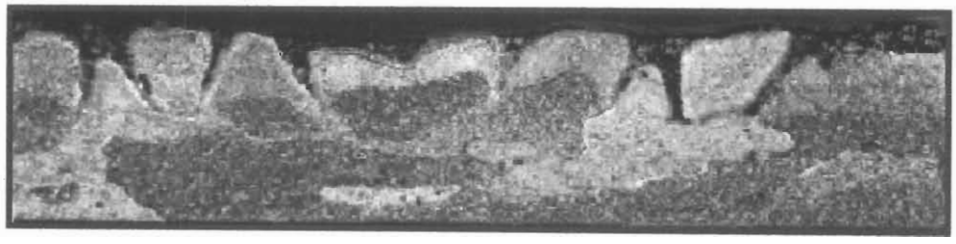

(b)

Figure 4.11 Elongated grain structure observed (a) the LT face of HT sample D (200x) and (b) the ST face of CPC sample A (200x).

4.1.2 MICROSTRUCTURE OF THE CORRODED SAMPLES IN 1M NaCl

4.1.2(a) 'As-supplied' and 'heat-treated' samples

Only minimal corrosion took place on the surface of AS samples A, B and E exposed to the solution containing chloride ions, and for this reason, micrographs are not reported on. AS sample D was the only sample that had corroded slightly in the presence of chloride ions. The nature of corrosion observed was preferential localised galvanic cell corrosion. The microstructural intermetallic phases closest to the surface were slightly corroded leaving small cavities behind. This is shown in Figure 4.12(a).

HT samples A, B, D and E all showed localised galvanic cell corrosion that increased along the series B≃E<A<D. HT sample D showed the same nature and extent of corrosion at its surface as AS sample D and hence the micrograph of its surface is not reported on. HT samples A, B and E were more susceptible to corrosion in the solution containing chloride ions than the AS samples. The type of corrosion observed for HT samples A, B and E when viewed at low magnification was preferential localised galvanic corrosion of a slightly different nature to the corrosion observed on the surface of HT sample D. The aluminium metal directly adjacent to the microstructural intermetallic phases was slightly corroded resulting in thin trenches (grooves) around their peripheries, or leaving behind cavities arising when the microstructural intermetallic phases had dislodged and fallen into solution. Figure 4.12(b) illustrates this corrosion.

When viewed at a higher magnification, it became evident that HT sample A corroded differently from HT samples B and E. Figure 4.13 illustrates this difference. Many pit cavities found on the surface of HT sample A were sharp and angular in shape, as shown in Figure 4.13(a), and not smooth and rounded as observed for HT samples B and E and displayed in Figure 4.13(b). Thinning of the aluminium surface of HT sample A adjacent to and near the microstructural intermetallic phases occurred in a layered fashion, giving the surface a slightly flaked appearance. HT samples B, D and E did not show any visible surface thinning. Figure 4.13(b) shows a magnification at 4000x of the corroded surface of HT sample B.

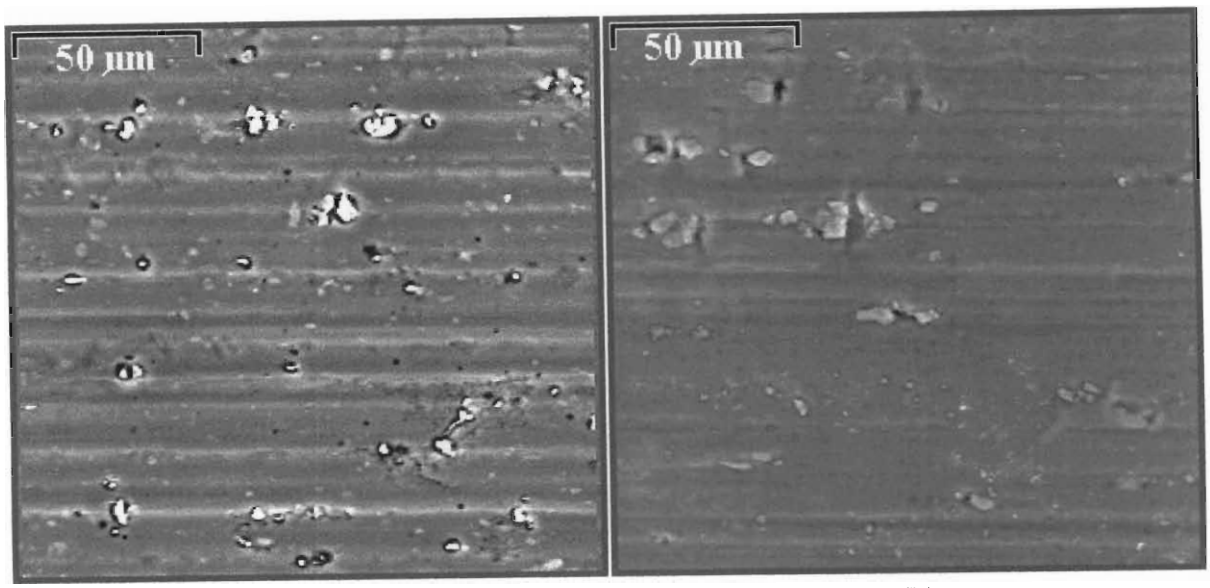

(a) **(b)**

Figure 4.12 Localised galvanic corrosion observed on (a) AS sample D (500x) and (b) HT sample E (500x).

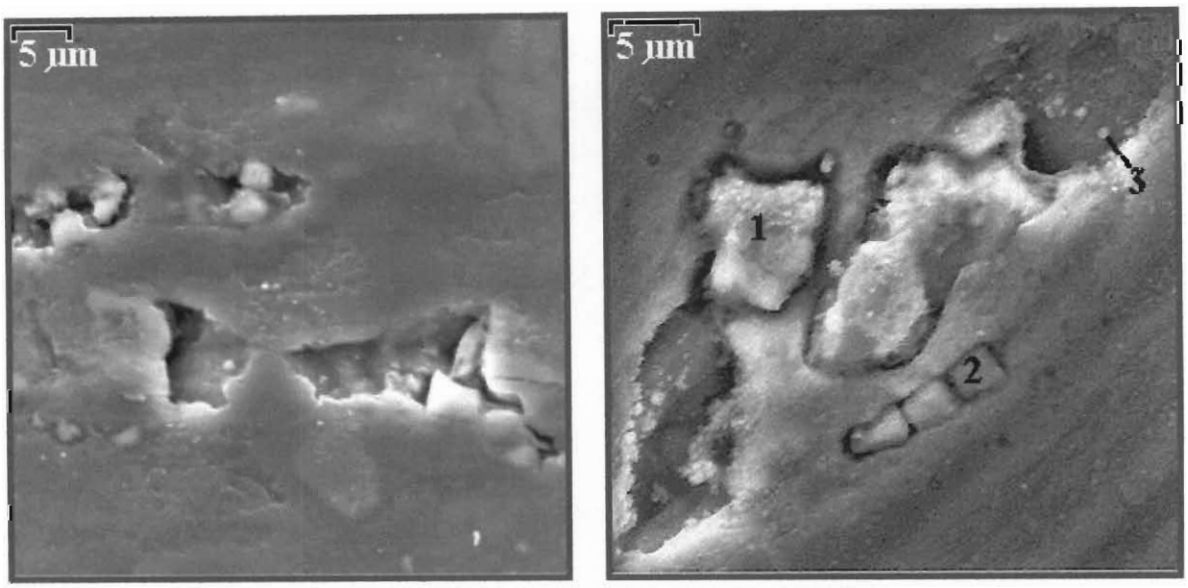

(a) **(b)**

Figure 4.13 The nature of the surface corrosion observed on (a) HT sample A (3000x) and (b) HT sample B (4000x).

Two microstructural intermetallic phases labelled '1' and '2' and a grain of oxide labelled '3' found on HT sample B are identified in Figure 4.13(b) and the results of their EDX analysis are reported in Table 4.4. Also listed in Table 4.4 are the EDX results of three microstructural intermetallic phases analysed on the corroded surface of HT sample D. Both sets of results show a high percentage of oxide covering the microstructural

intermetallic phases. A large amount of copper was found in the microstructural intermetallic phases of HT sample D.

Table 4.4 Chemical composition and surface oxide content of various microstructural intermetallic phases for HT samples B and D.

Alloy	Area	%O	%Al	%Si	%Mn	%Fe	%Zn	%Cu
B(HT)	1	7.14	56.76	4.43	15.99	15.69		
	2	9.02	66.59	1.45	10.64	11.68		
	3	23.08	72.95	1.37	0.98			
D(HT)	1	6.80	69.47	4.20	6.16	2.10	1.50	9.43
	2	8.86	79.00	2.94	2.85	0.81	1.34	3.89
	3	5.47	83.34	2.75	2.40	0.68	1.66	3.71

EDX analyses for oxide content on the surfaces of AS and HT samples A, B and D indicated the presence of a thicker oxide layer after corrosion. The AS and HT samples E on the other hand showed a loss of oxide at the surface due to corrosion. These EDX results have been compared in Table 4.5.

Table 4.5 Percentage surface oxide found on the AS and HT samples A, B, D and E before and after corrosion in 1M NaCl.

Alloy		A(AS)	A(HT)	B(AS)	B(HT)	D(AS)	D(HT)	E(AS)	E(HT)
Before corrosion	Magn.*	500	500	500	500	500	500	200	200
	% O	0.60	1.36	1.81	2.50	0.94	1.55	1.39	3.99
After corrosion	Magn.*	500	500	700	500	500	500	500	500
	% O	0.94	1.90	2.01	9.75	3.36	5.70	1.17	2.33

* Magn. = Magnification factor of micrograph.

4.1.2(b) 'Composite Powder coated' samples

Corrosion of CPC samples A, B and E during one hour of immersion in the solution containing chloride ions was minimal. CPC sample D had undergone a more severe type of corrosion, revealing the eutectic Al-Si melt layer.

The most noticeable effect of corrosion of CPC samples A, B and E was the presence of very large oxide deposits that were found on numerous parts of the surface. These oxide deposits showed a 'mud-crack' pattern and a typical example exhibited by CPC sample E is shown in Figure 4.14(a). At higher magnifications, much smaller oxide particles that were up to 8 μm in diameter and scattered over the entire surface became visible, and a typical example is shown for CPC sample E in Figure 4.14(b). Localised galvanic corrosion initiated adjacent to some of the microstructural intermetallic phases exposed at the surface was observed on CPC samples A, B and E, and a typical example is shown for CPC sample E in Figure 4.14(b).

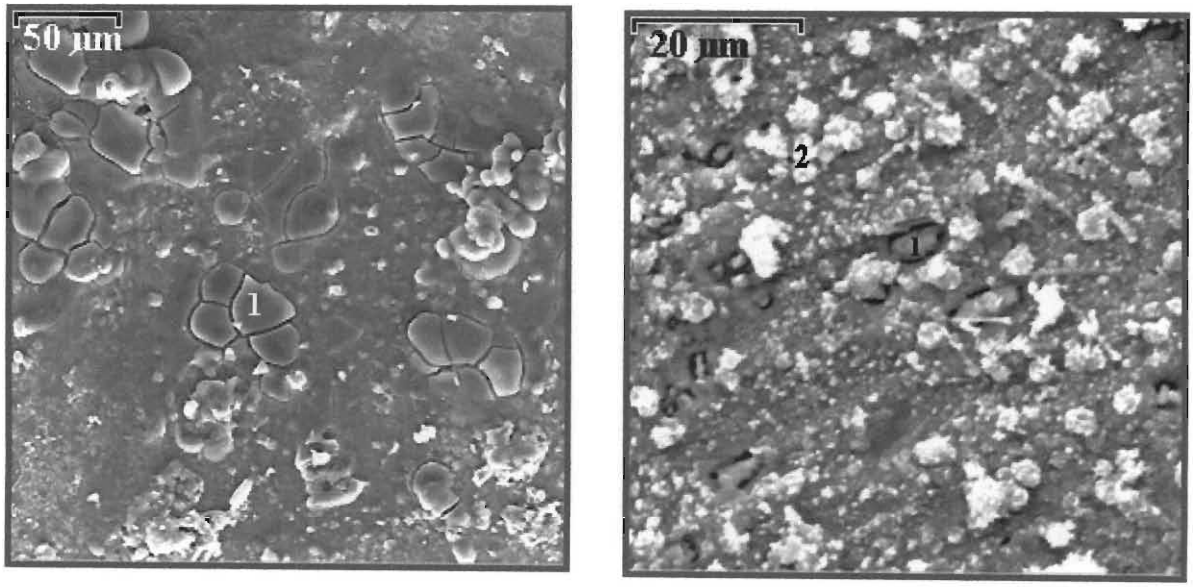

(a) **(b)**

Figure 4.14 Corroded surface of CPC sample E showing (a) 'Mud-crack' appearance of large oxide deposits marked '1' (500x), (b) Localised galvanic corrosion (2000x). A microstructural particle is marked '1'and small oxide particles are marked '2'.

To show the extent of corrosion of the eutectic Al-Si melt layer, optical micrographs were taken of cross-sections of CPC samples A, B and E. CPC samples B and E revealed a

small amount of corrosion that had penetrated into to the eutectic Al-Si diffusion zones as shown in Figure 4.15, whilst CPC sample A showed no corrosion of the eutectic Al-Si melt layer and has therefore not been reported on.

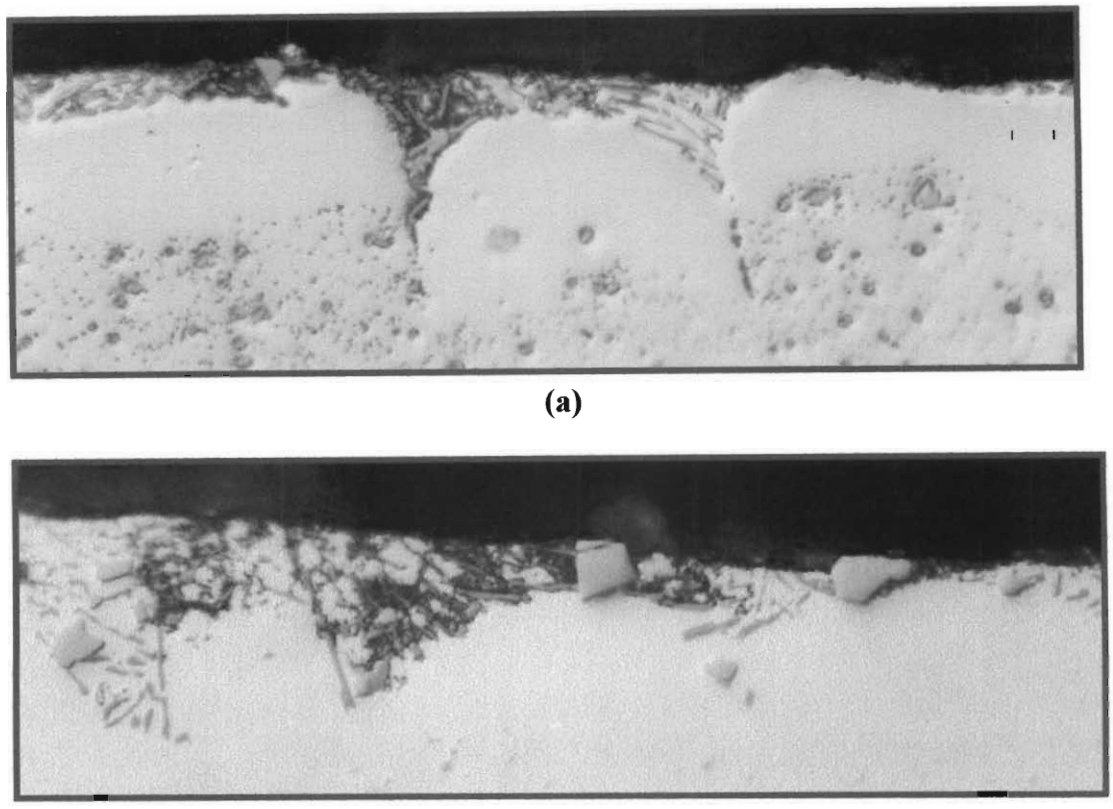

(a)

(b)

Figure 4.15 Degree of corrosion of the eutectic Al-Si melt layer of (a) CPC sample B (1000x) and (c) CPC sample E (1000x).

CPC sample D was the only sample that showed an appreciable amount of corrosion. Most of the residual flux had dissolved and most of the partially reacted Composite Powder had corroded. This exposed the eutectic Al-Si melt layer consisting of cells of α-Al surrounded by rods of β-Si. The eutectic Al-Si melt layer was corroded to different degrees, giving two distinctly different appearances, as illustrated in Figure 4.16.

Figure 4.16(a) represents the lesser degree of corrosion observed, and shows an uneven surface of spherical α-Al cells protruding outwards, surrounded by rods of β-Si at their bases. It appears as if only the partially reacted Composite Powder and flux had gone from these areas, thinning only the very top of the eutectic Al-Si melt layer, and most of the surface area showed this type of corrosion. Figure 4.16(b) shows an area of severely

corroded eutectic Al-Si melt layer that displayed a more even overall surface with an interconnected network of Si rods interspersed in a continuous matrix of α-Al. Only a very small amount of surface area revealed this type of corrosion. Small oxide particles were found on both types of corroded areas, but were less abundant than the number present on the surfaces of CPC samples A, B and E. Large oxide deposits were not observed on CPC sample D.

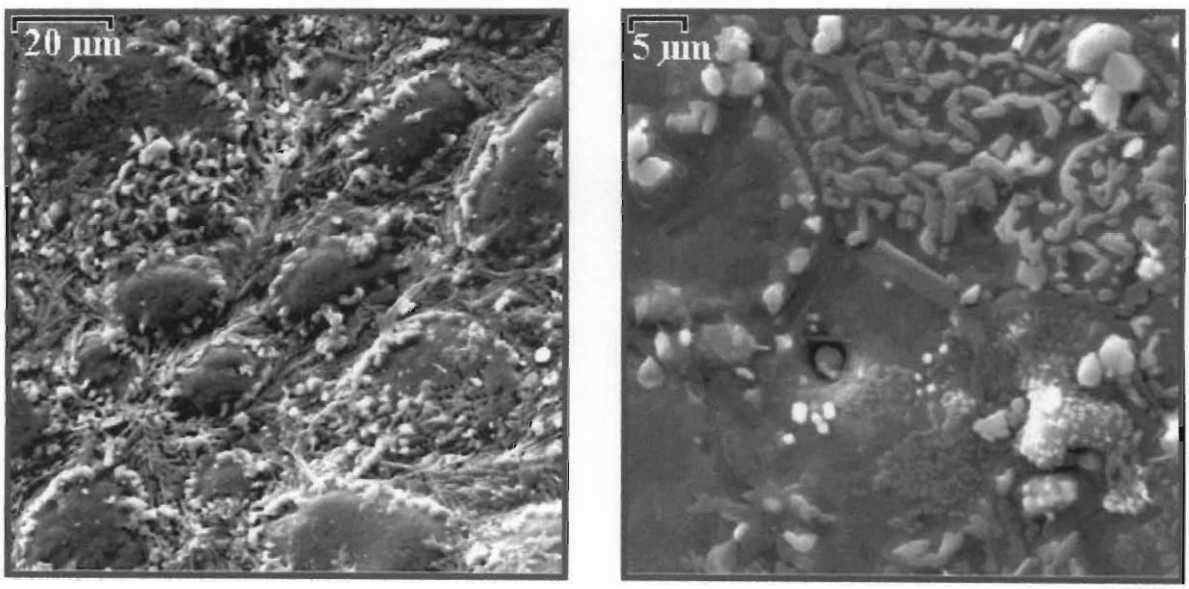

(a) **(b)**

Figure 4.16 Two different degrees of corrosion observed on CPC sample D, magnified (a) 1000x and (b) 3000x.

The extent of corrosion of CPC sample D is shown in Figure 4.17. The eutectic Al-Si melt layer and eutectic Al-Si diffusion zones of CPC sample D had been the most severely corroded of the four alloy samples. In many areas, the entire eutectic Al-Si melt layer had corroded leaving only the α-Al filler metal behind. Some intergranular corrosion of the base alloy directly adjacent to the α-Al filler metal layer was also observed.

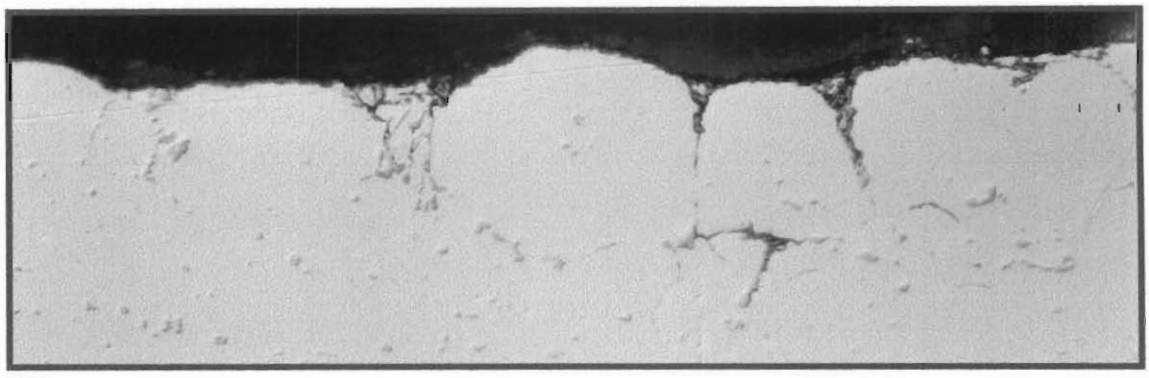

Figure 4.17 Degree of corrosion of the eutectic Al-Si melt layer of CPC sample D (500x).

The percentages of oxygen, silicon and flux present on the CPC samples were measured using EDX analysis before and after exposure to the solution containing chloride ions. The results obtained are recorded in Table 4.6 and the following observations were made from these. Corrosion of CPC sample D resulted in a very small increase in oxide. A much larger increase in oxide was observed on CPC samples A, B and E after corrosion. All four CPC samples showed an increase in the percentage of Si and a decrease in the percentage of potassium and fluoride on the surfaces after corrosion, the largest changes occurring for CPC sample D.

Table 4.6 Percentage O, Si, K and F present on the CPC samples A, B, D and E before and after corrosion in 1M NaCl.

Alloy	**A**		**B**		**D**		**E**	
Corrosion	**Before**	**After**	**Before**	**After**	**Before**	**After**	**Before**	**After**
Magn.*	200	200	100	300	100	200	100	500
% O	6.80	14.29	5.37	20.38	4.98	6.02	3.78	20.73
% Si	5.86	7.80	5.94	7.58	5.85	19.8	5.63	8.23
% K	15.03	8.85	12.28	6.57	20.61	1.79	18.93	4.99
% F	26.08	11.80	14.37	12.06	16.66		29.14	13.42

* Magn. = Magnification factor of micrograph.

4.1.3 MICROSTRUCTURE OF THE CORRODED SAMPLES IN 1M NaCl + 0.5M H_2SO_4

4.1.3(a) 'As-supplied' and 'heat-treated' samples

The addition of sulfuric acid to the solution containing chloride ions significantly altered the nature and extent of corrosion observed on the AS and HT samples of all four aluminium alloys studied.

The nature of corrosion of AS samples A, B and E was similar, namely localised pitting along the direction of rolling. The pitting took place in the form of many small pits that were between 5 μm and 16 μm deep. Growth of the pits had occurred through pit coalescence resulting in pits up to 130 μm long and 20 μm to 40 μm wide for AS sample E. Shorter and narrower pits were observed for AS samples A and B. This type of corrosion is shown for AS samples A, B and E in Figure 4.18. Shallow surface dissolution of the aluminium matrix directly adjacent to the pitted regions was also observed. The extent of corrosion observed differed for the different alloy samples. Both AS samples A and B showed corrosion of about 7% of the exposed surface area compared with about 45% for AS sample E.

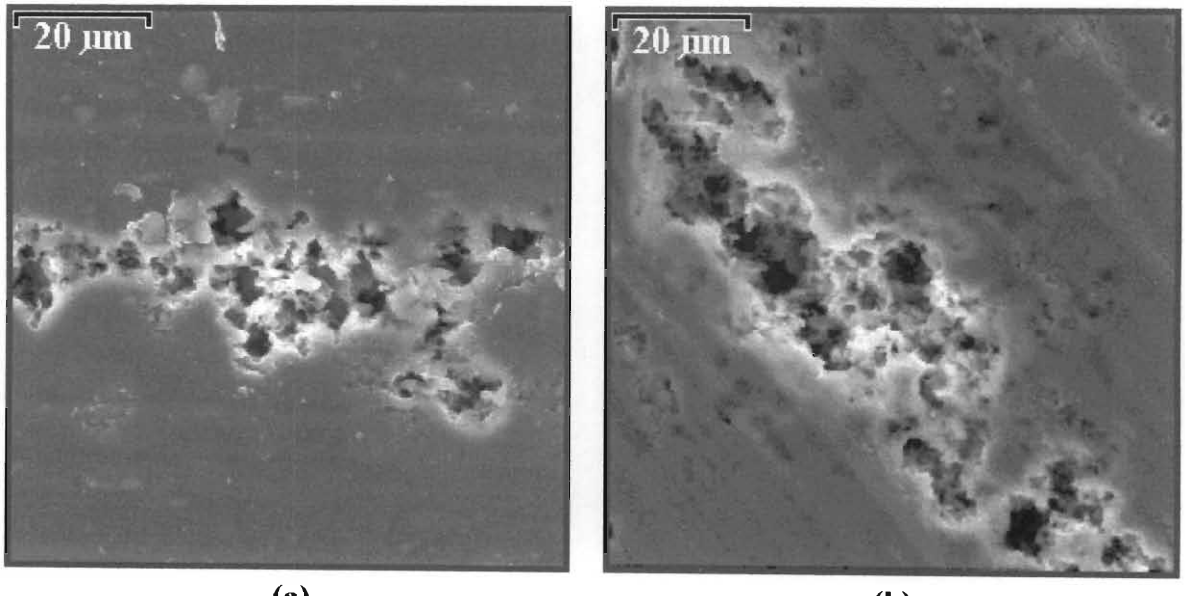

(a) **(b)**

Figure 4.18 Localised pitting on (a) AS sample A (1200x) and (b) AS sample B (1500x).

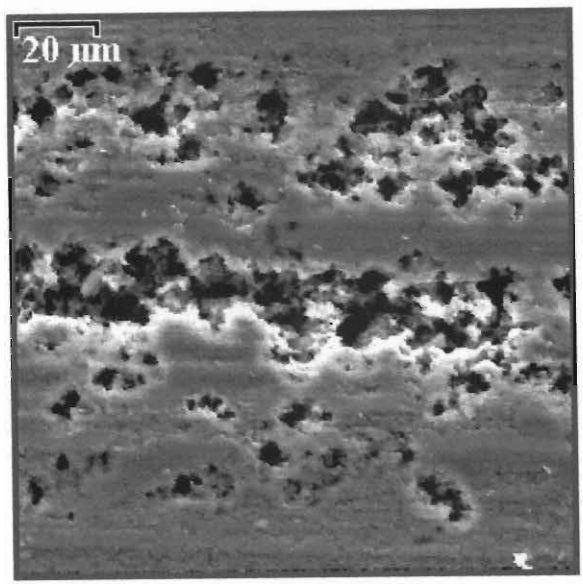

Figure 4.18(c) Localised pitting on AS sample E (1000x).

When viewing the samples at higher magnifications it was found that the pits consisted of small crystallographic facets and steps. A typical example of this is shown for AS sample A in Figure 4.19.

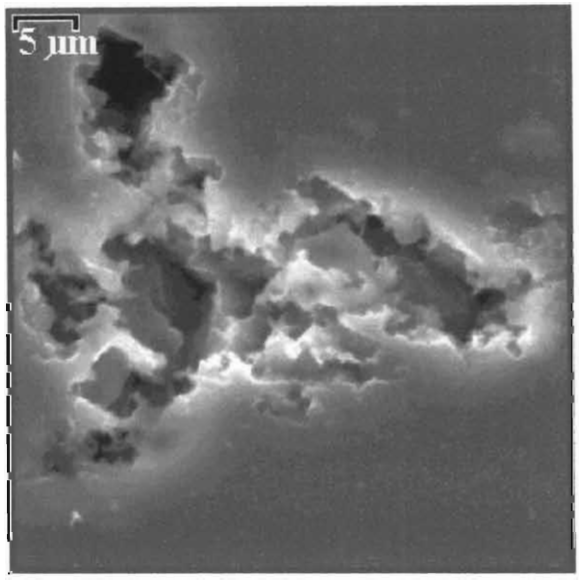

Figure 4.19 Crystallographic facets and steps of the pits on AS sample A (4000x).

Figure 4.20 and 4.21 show optical micrographs taken of cross-sections of AS samples A, B and E. Pits formed at the surface are shown in Figure 4.20, which revealed that the underlying pit cavities had been laterally undermined and shared numerous pit mouths. The pit mouths were generally narrower than the underlying pit cavities. The pit depths

were shallower for AS sample A (up to 13 μm) and slightly deeper for both AS samples B and E (up to 16 μm).

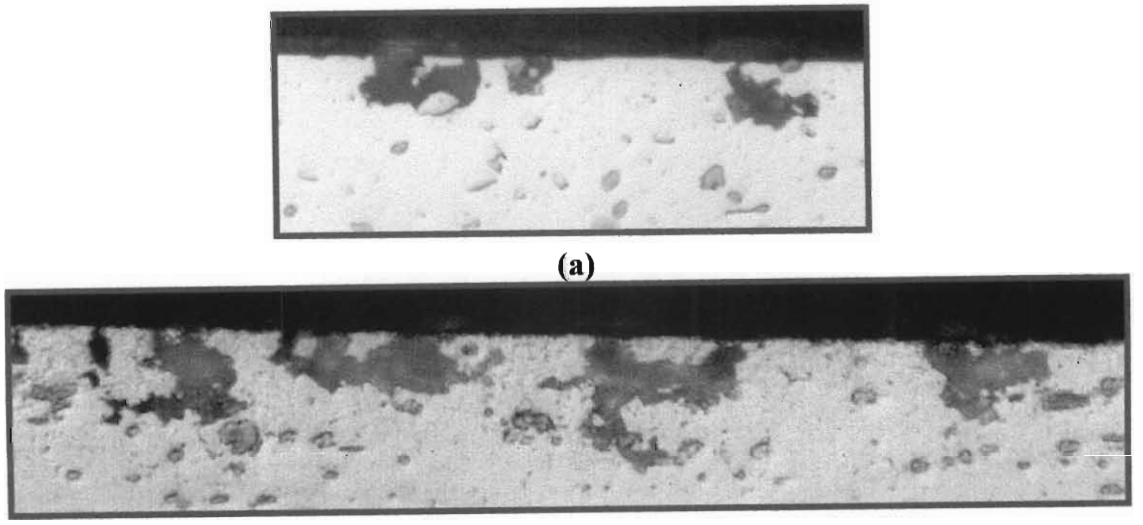

Figure 4.20 Cross-sectioned view of the nature and depth of pits on (a) AS sample A and (b) AS sample E (1000x).

Pits were also found below the surface for both AS samples B and E but not for AS sample A, and a typical example is shown for AS sample B in Figure 4.21.

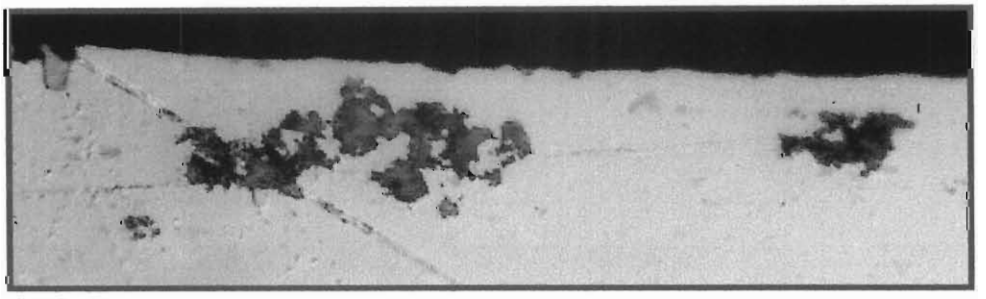

Figure 4.21 Cross-sectioned view of pits formed below the surface of AS sample B (1000x).

HT samples A, B and E also showed a similar type of corrosion that differed from that observed on the AS samples, as can be seen in Figure 4.22. These samples had undergone localised pitting corrosion that resulted in clearly defined individual pits that varied in depth and size. Intergranular corrosion was also found, and was least severe for HT sample A and most severe for HT sample E. Dissolution of the aluminium matrix in the

vicinity of the pitted regions was shallow and gave the appearance of grooved striations. A slight amount of pit coalescence was observed that resulted in longer and wider pits.

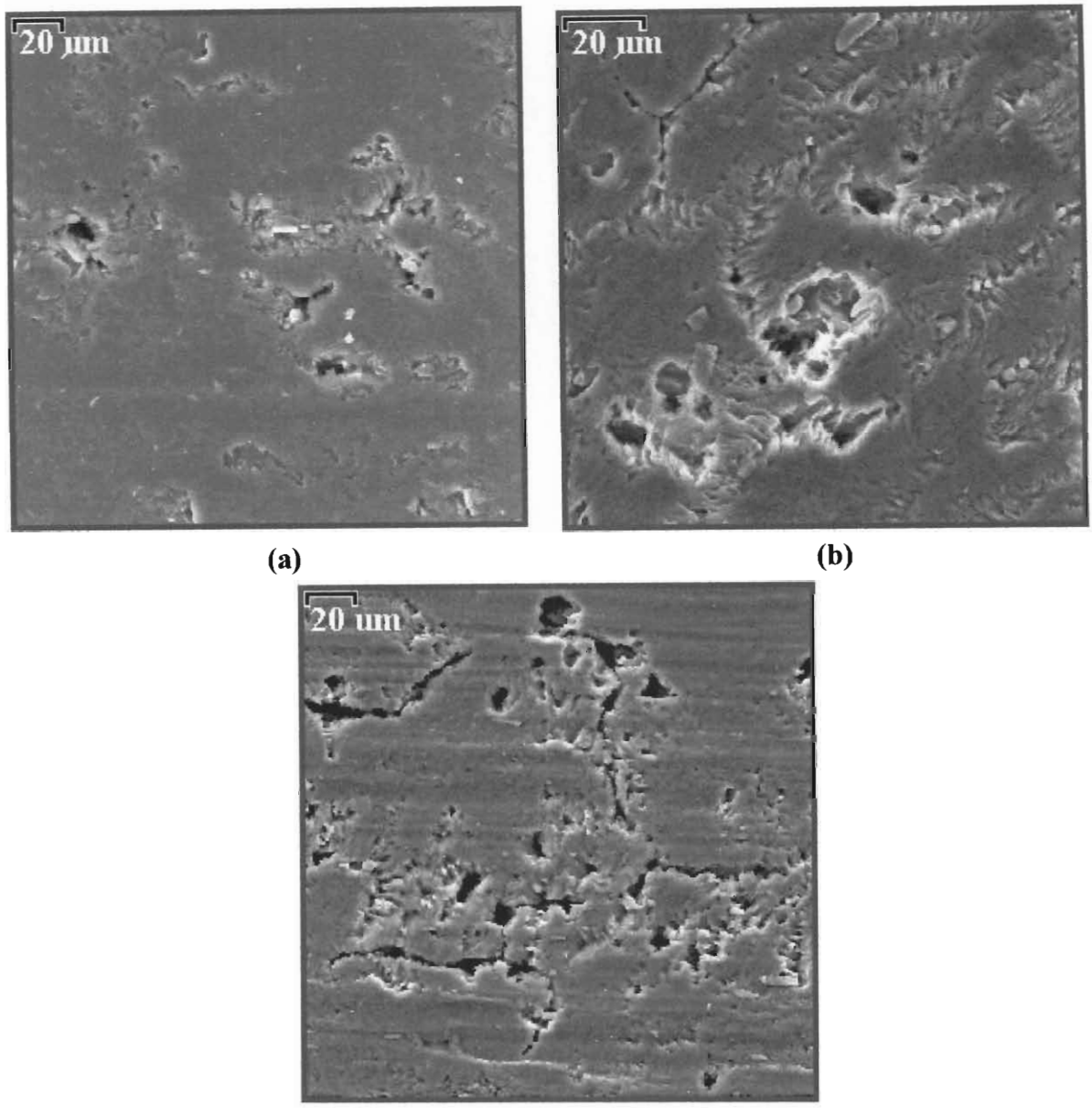

Figure 4.22 Localised crystallographic pitting and intergranular corrosion on (a) HT sample A (1000x), (b) HT sample B (1000x) and (c) HT sample E (700x).

The extent of corrosion observed differed for HT samples A, B and E and increased along the series A<B<E. HT sample A showed corrosion of about 15% of the exposed surface area, compared with about 35% for HT sample B and 45% for HT sample E. When viewed at higher magnifications the interior surface of the individual pits observed on HT

samples A, B and E showed well-defined crystallographic facets and steps, as can be seen in Figure 4.23.

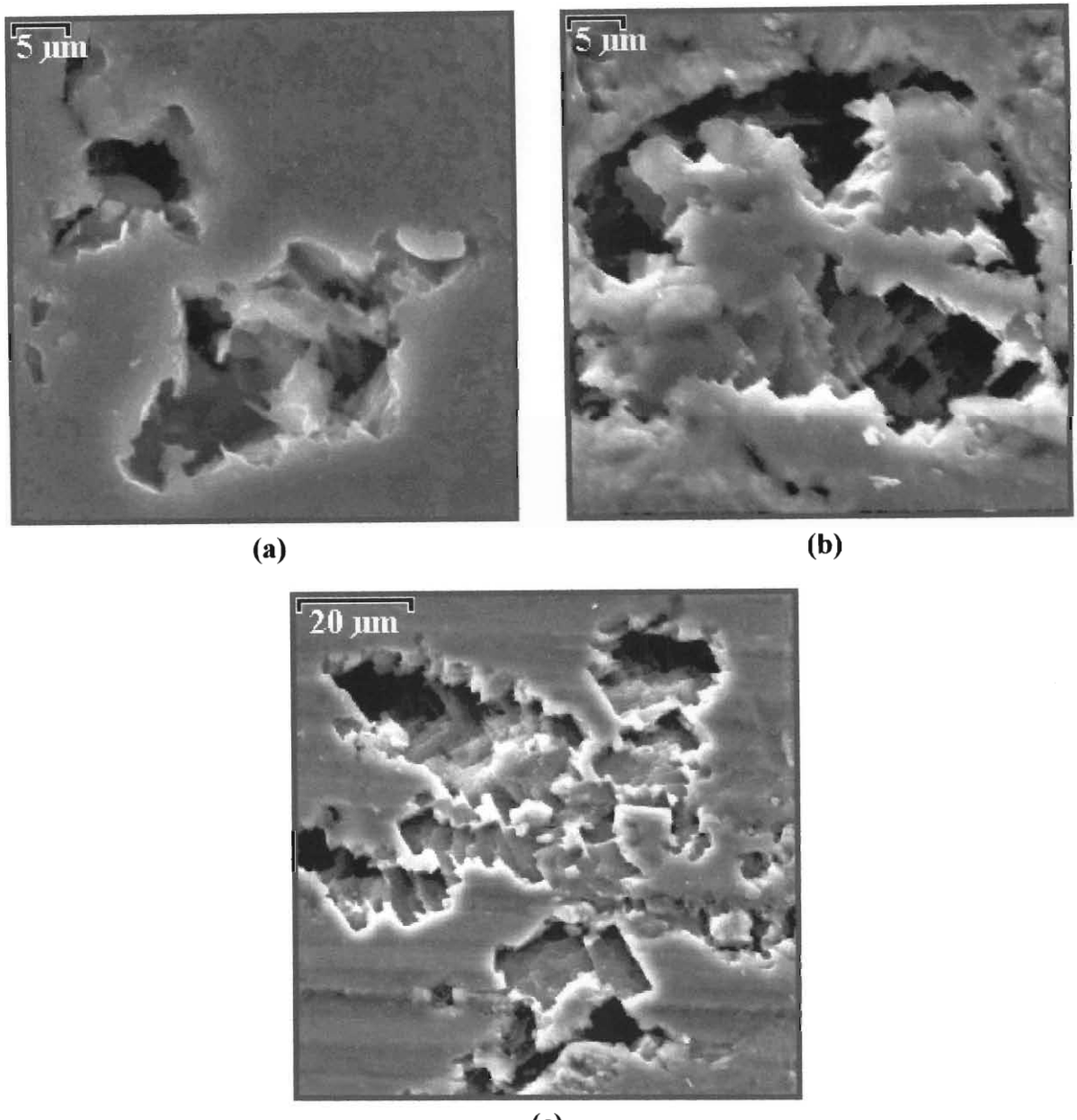

Figure 4.23 Crystallographic pits found on (a) HT sample A (4000x), (b) HT sample B (3000x) and (c) HT sample E (1500x).

Figure 4.24 shows cross-sectioned views of the corroded HT samples A and B revealing the nature and depth of pitting observed. HT sample E showed similar pits to those found on HT sample B, and has therefore not been reported on. The pit depths on HT sample A were shallower (up to 13 µm) than those found on HT samples B and E, where pit depths

of up to 20 μm were recorded. HT sample A did not reveal intergranular corrosion below the surface, whilst HT samples B and E showed intergranular corrosion that followed a path along microstructural intermetallic phases lying along the grain boundaries.

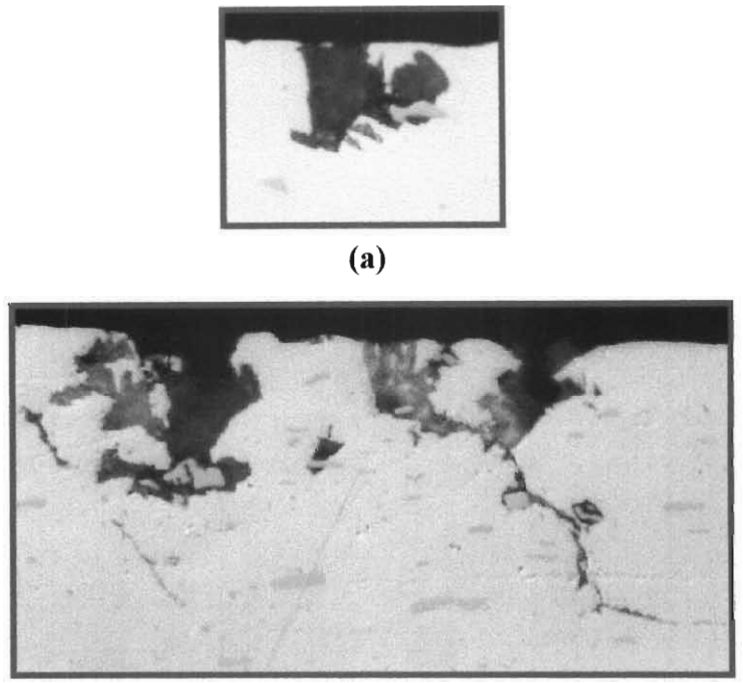

(a)

(b)

Figure 4.24 Cross-sectioned view of the pits found on (a) HT sample A (1000x) and (b) HT sample B, which also shows intergranular corrosion (1000x).

AS sample D was the only sample to experience delocalised corrosion of most of the exposed surface area, leaving very little uncorroded aluminium matrix. Individual pits could not be recognised and the corroded surface took on the appearance of 'crumbling concrete' that had penetrated the sample up to a depth of 20 μm. The nature of corrosion observed on the surface and cross-section of AS sample D is shown in Figure 4.25.

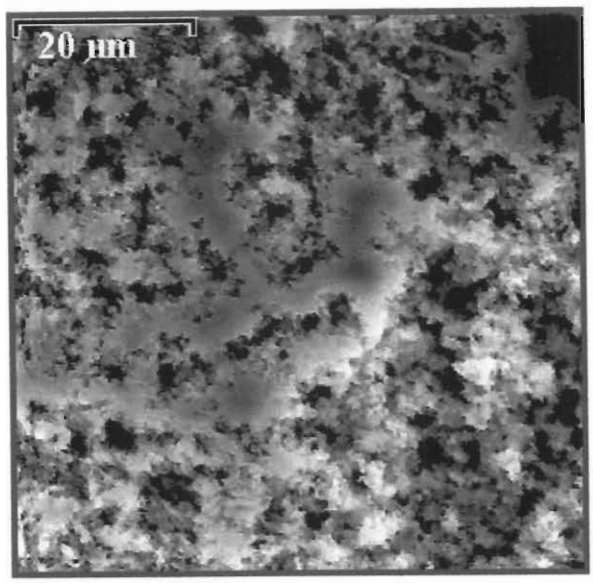

(a)

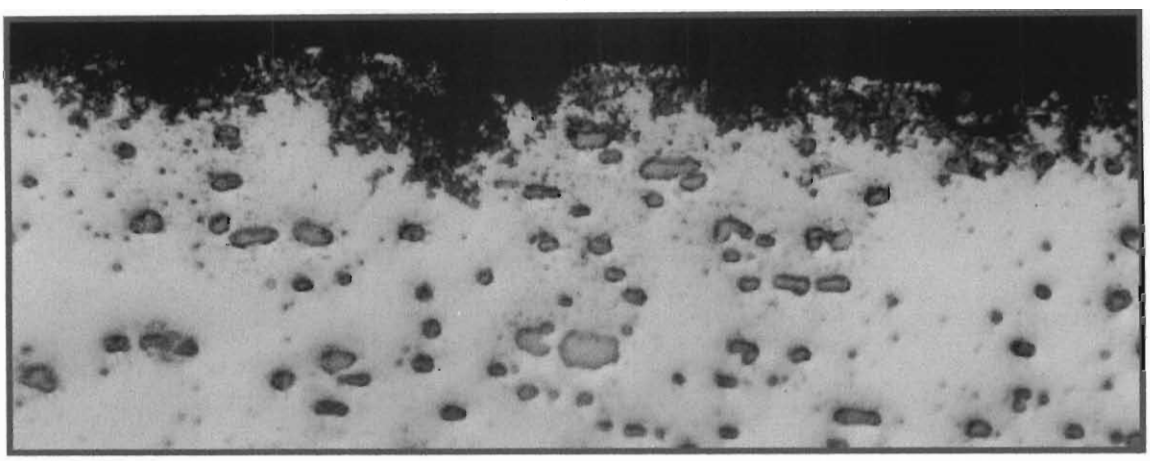

(b)

Figure 4.25 'Crumbling concrete' appearance of corrosion observed on AS sample D showing (a) a surface view (2000x) and (b) a cross-sectioned view (1000x).

HT sample D had also been severely corroded but the corrosion was of a different nature to that observed on AS sample D. Localised crystallographic corrosion of about 75% of the exposed surface area had resulted in an interconnected and extended network of many small pits, as is shown in Figure 4.26(a). The interior surface of the extended network of pits was composed of small but well-defined facets and steps, as is illustrated in Figure 4.26(b). Intergranular corrosion was again visible on the surface.

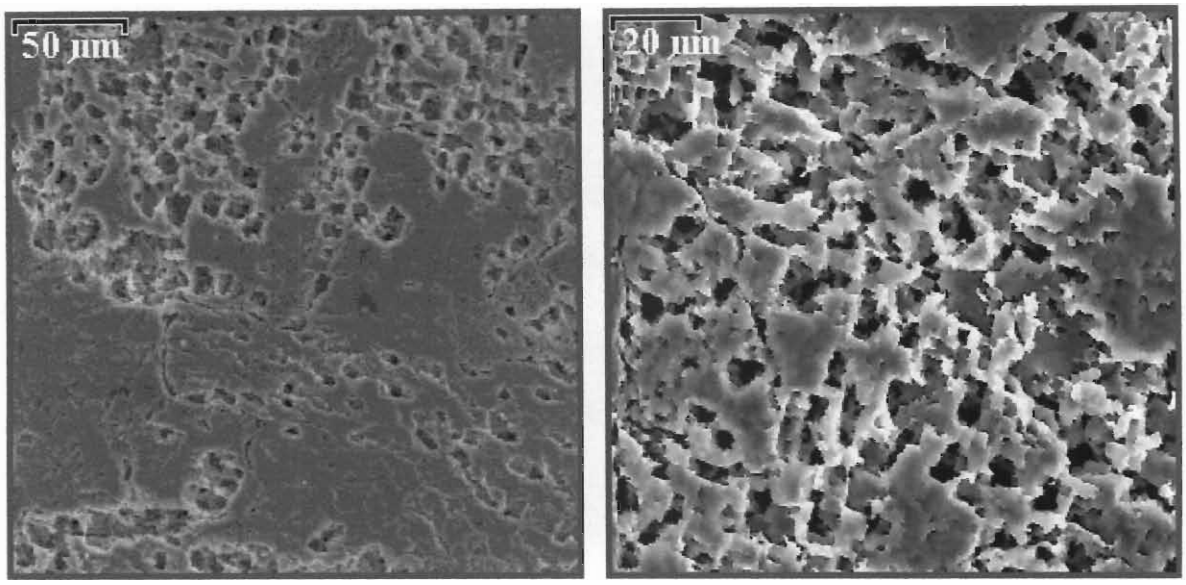

Figure 4.26 Crystallographic pitting found on HT sample D magnified (a) 200x and (b) 1000x.

Figure 4.27 shows a cross-sectioned view of the pits formed on HT sample D during corrosion. The depths of the pits ranged between 4 µm and 20 µm. Intergranular corrosion is visible and has outlined the periphery of the actual grains.

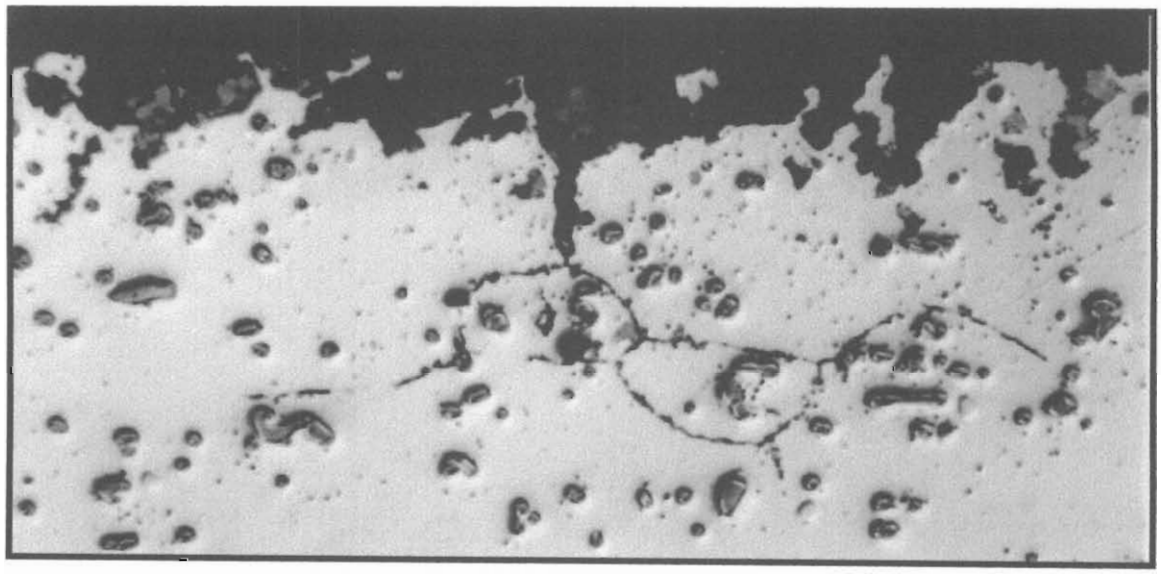

Figure 4.27 Cross-section of HT sample D showing crystallographic pits and intergranular corrosion (1000x).

EDX analyses for oxide content performed on both uncorroded and corroded surfaces of the AS and HT samples have been compared in Table 4.7. Again the AS and HT samples A, B and D showed the presence of a thicker oxide layer after corrosion, whilst the AS and HT sample E again showed a loss of oxide due to corrosion at its surface.

Table 4.7 Percentage oxide found on the surfaces of AS and HT samples A, B, D and E before and after corrosion in 1M NaCl + 0.5M H_2SO_4.

Alloy		A(AS)	A(HT)	B(AS)	B(HT)	D(AS)	D(HT)	E(AS)	E(HT)
Before corrosion	Magn.*	500	500	500	500	500	500	200	200
	% O	0.60	1.36	1.81	2.50	0.94	1.55	1.39	3.99
After corrosion	Magn.*	700	1200	200	200	2000	500	500	3000
	% O	1.35	1.90	2.63	2.74	3.50	2.31	0.91	1.21

*Magn. = Magnification factor of micrograph.

4.1.3(b) 'Composite Powder coated' samples

The presence of sulfuric acid in the solution containing chloride ions caused severe corrosion of the CPC samples. Of the four alloy samples, CPC sample A showed the least severe corrosion, whilst CPC sample D had endured the worst corrosion. Effervescence was observed on each of the surfaces when the samples were immersed into the electrolyte solution.

CPC sample A showed dissolution of all the residual flux and corrosion of the entire partially reacted Composite Powder. About 60% of the eutectic Al-Si melt layer had corroded, exposing the α-Al filler metal layer below. The exposed cells of α-Al had a 'flaked' appearance and were still surrounded around their peripheries by eutectic Al-Si melt. On some parts of the surface, large oxide deposits with a 'mud-crack' pattern were observed and this can be seen in Figure 4.28(a). The eutectic Al-Si diffusion zones were uncorroded in most places, but in the areas where more corrosion had taken place, deep grooves that separated the cells of α-Al, i.e. grain boundaries, became visible. This is shown in Figure 4.28(b).

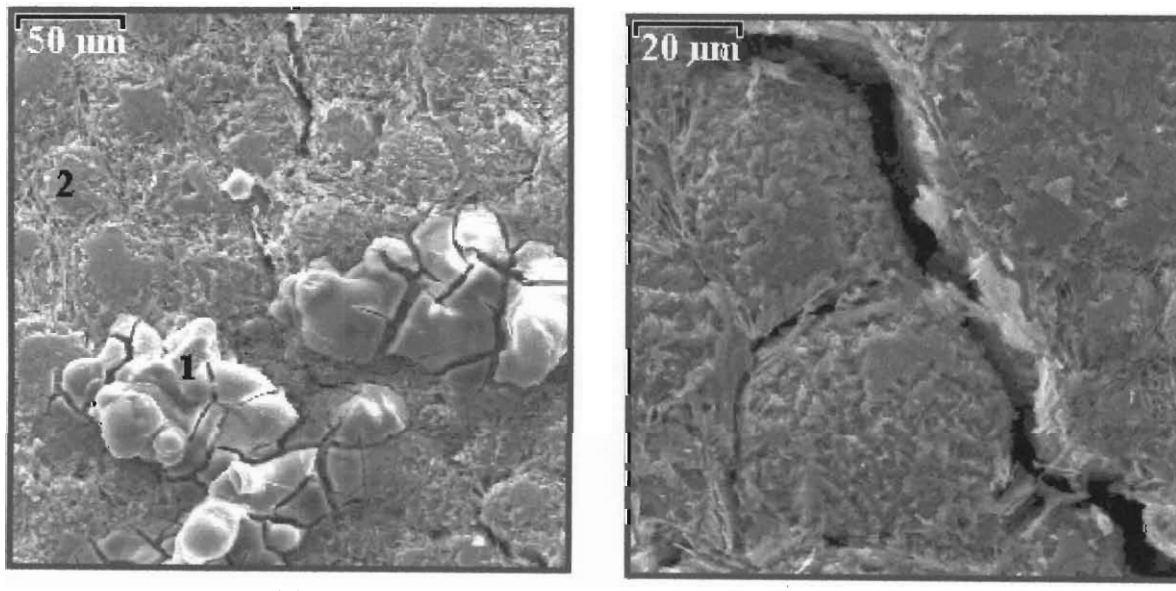

(a) **(b)**

Figure 4.28 Corrosion of CPC sample A showing (a) large oxide deposits marked '1' and a single cell of α-Al marked '2' on the exposed α-Al filler metal layer (500x) and (b) cells of α-Al separated by grain boundaries (1000x).

The extent of corrosion of the eutectic Al-Si melt layer of CPC sample A is shown in the cross-sectioned micrograph in Figure 4.29. A slight amount of intergranular corrosion is observed at the base of the eutectic Al-Si diffusion zones that extend into the base alloy below.

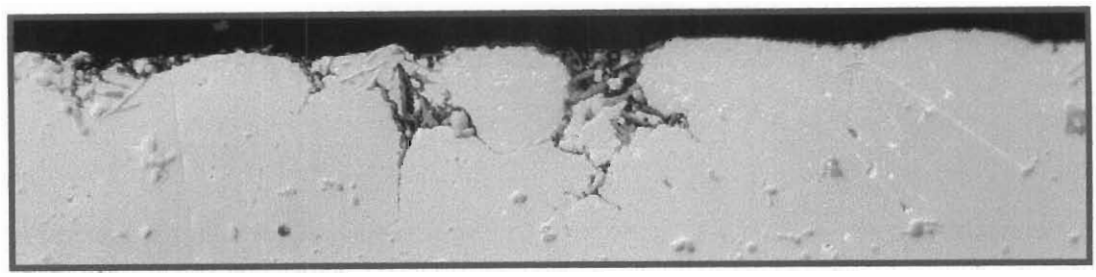

Figure 4.29 The extent of corrosion observed on the eutectic Al-Si melt layer of CPC sample A (500x).

The corroded CPC samples B, D and E experienced dissolution of all residual flux and corrosion of the entire partially reacted Composite Powder. The entire eutectic Al-Si melt layer including the eutectic Al-Si diffusion zones had also corroded, causing the individual cells of α-Al to become fully exposed, separated from one another by grooves marking the grain boundaries that were once filled by eutectic Al-Si melt making up the eutectic Al-Si diffusion zones. This allowed for corrosion of the underlying base alloy. At low magnification, the varying sizes of the α-Al cells could easily be identified under the electron microscope and Figure 4.30 illustrates this for CPC samples B and E. CPC sample D revealed a similar α-Al filler metal layer at low magnification and is therefore not reported on.

The cells of α-Al of CPC samples B, D and E had undergone crystallographic corrosion. Certain parts of the α-Al filler metal layer had corroded more than their surroundings, leaving various sized hollow areas that, if deep enough, exposed the base alloy below to further attack by the aggressive electrolyte solution. Figure 4.30(a) shows such hollow areas on the corroded α-Al filler metal layer of CPC sample B at the point where several cells of α-Al join each other, which is also representative of CPC sample D. Also visible are some small white deposits of oxide. The α-Al filler metal layer of CPC sample E on the other hand had been subjected to more severe corrosion, leaving large hollow areas in its structure that spread out over several cells of α-Al. This is shown in Figure 4.30(b).

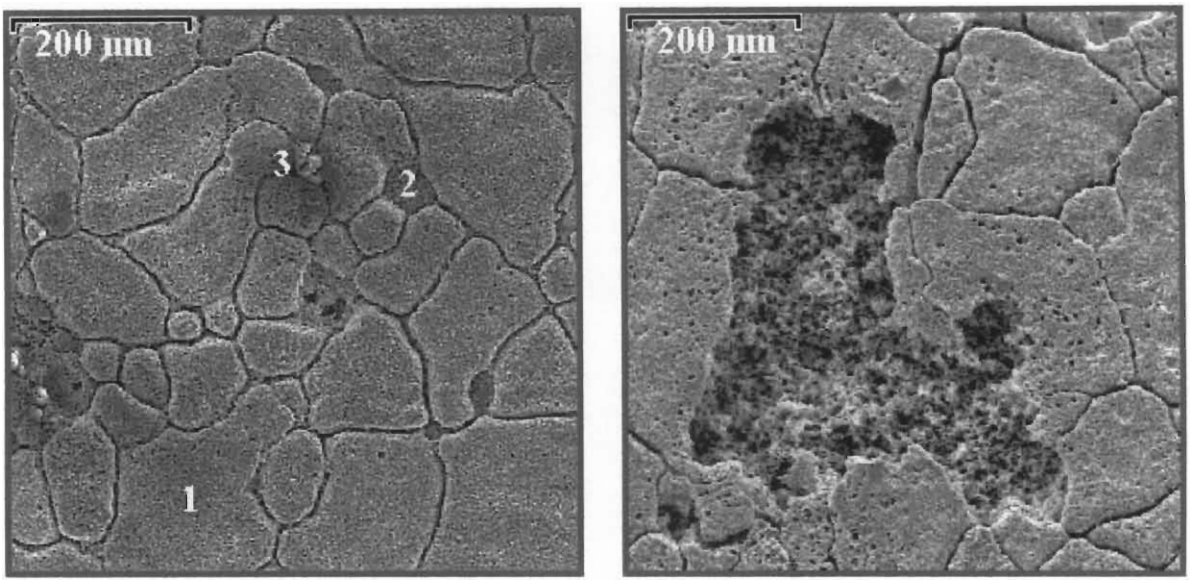

(a) **(b)**

Figure 4.30 Corroded α-Al filler metal layer of (a) CPC sample B showing a cell of α-Al marked '1', a hollow area marked '2' and an oxide deposit marked '3' (200x) and (b) CPC sample E (200x).

Small but deep localised individual pits had also formed in the individual α-Al cells of CPC samples B, D and E but were most abundant in CPC sample E. Magnifications of the cells of α-Al for CPC samples B, D and E are given in Figure 4.31, which clearly illustrate the crystallographic nature of corrosion.

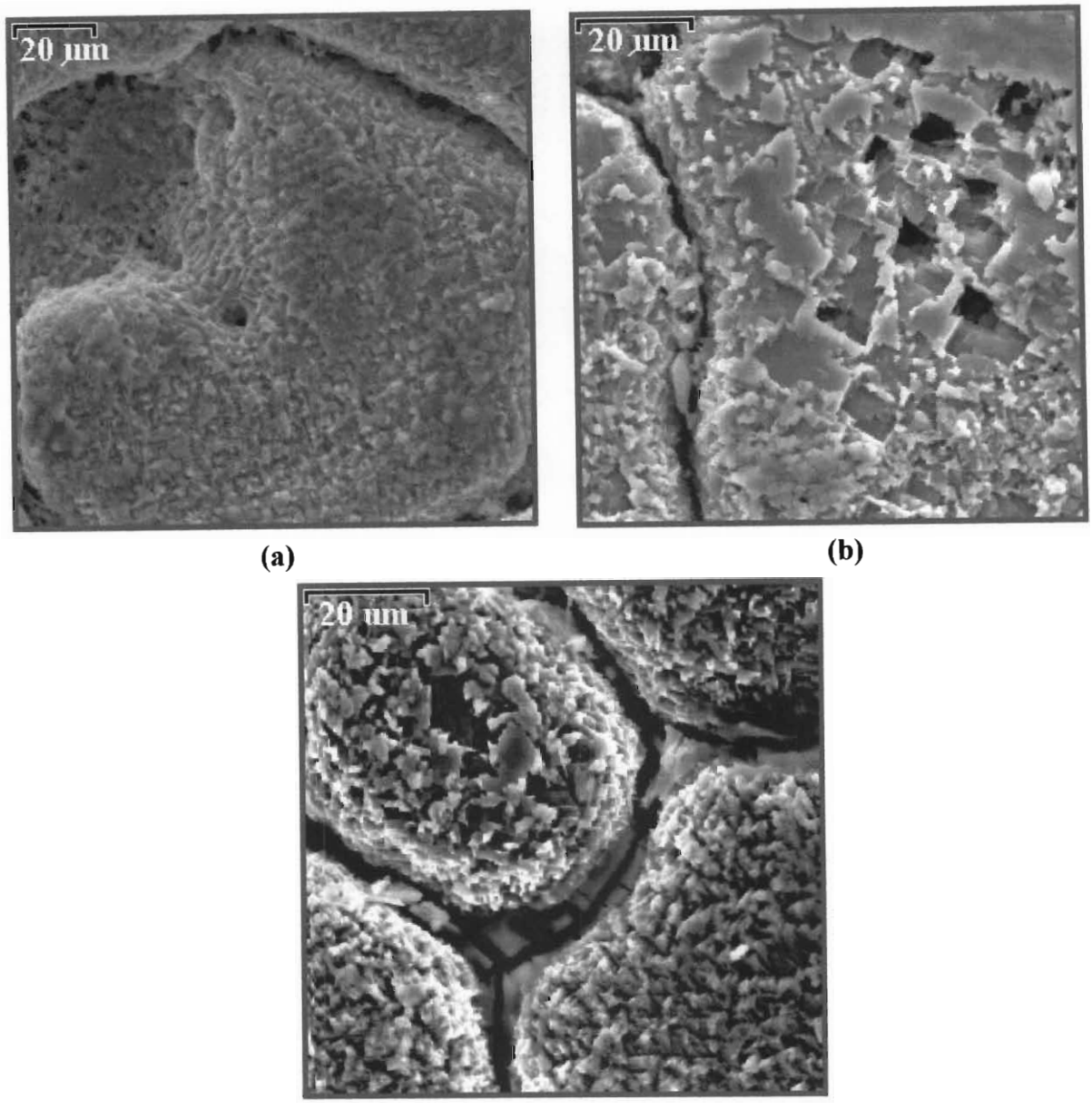

Figure 4.31 Exposed cells of α-Al of (a) CPC sample B (1000x), (b) CPC sample E (1500x) and (c) CPC sample D (1500x).

The CPC samples B, D and E all experienced crystallographic pitting of the base aluminium alloy as illustrated in the optical micrographs taken of cross-sections of the respective samples. The extent of corrosion of the base alloy was similar for CPC samples B and E and most severe for CPC sample D. Figure 4.32 shows the extent of corrosion observed on CPC samples E and B. Both surfaces show total corrosion of small sections of the α-Al cells. This in turn exposed fresh base alloy to the electrolyte solution. After initial penetration and corrosion of the base alloy for depths of up to 80 µm, further

corrosion spread laterally rather than vertically. The length of the pits varied, the longest pit found on CPC sample B was about 350 μm, whilst for CPC sample E the longest pit reached a length of about 290 μm. No perforation of the sample wall was observed on CPC samples B and E. Intergranular corrosion was again visible and appeared to aid the corrosion of the base alloy below the α-Al filler metal layer.

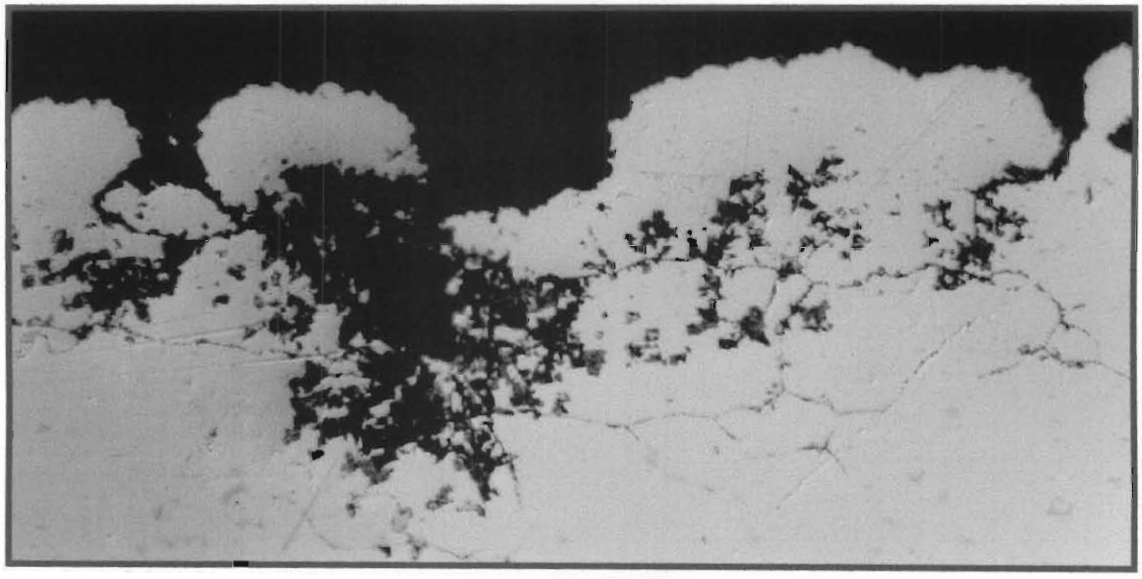

(a)

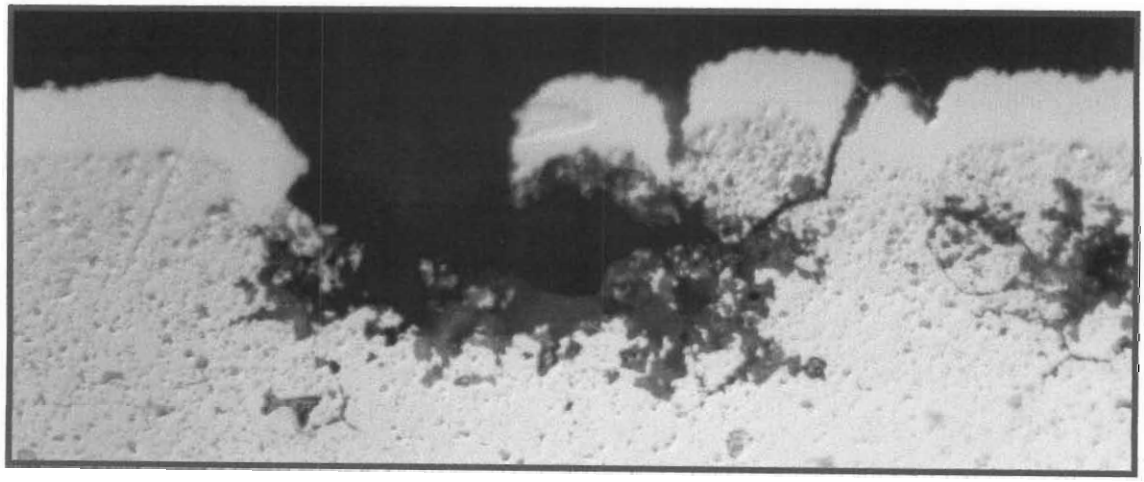

(b)

Figure 4.32 Extent of corrosion of the α-Al filler metal layer and underlying aluminium base alloy of (a) CPC sample B (500x) and (b) CPC sample E (500x).

CPC sample D had been corroded the most severely of the four alloy samples. Figure 4.33 shows the nature of attack CPC sample D had undergone. Corrosion of the base alloy was localised at the centre of the sample's thickness where it spread laterally rather than vertically. The pits reached lengths of up to 350 μm and depths of up to 50 μm. Intergranular corrosion was again visible and no perforation of the sample wall was observed for CPC sample D.

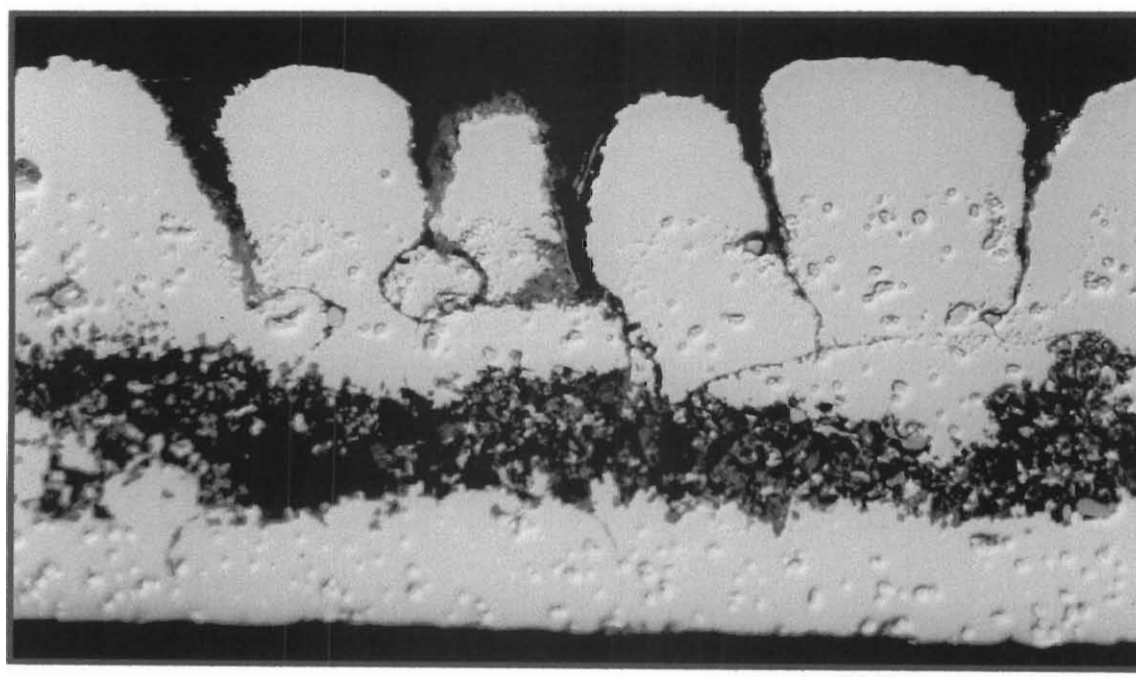

(a)

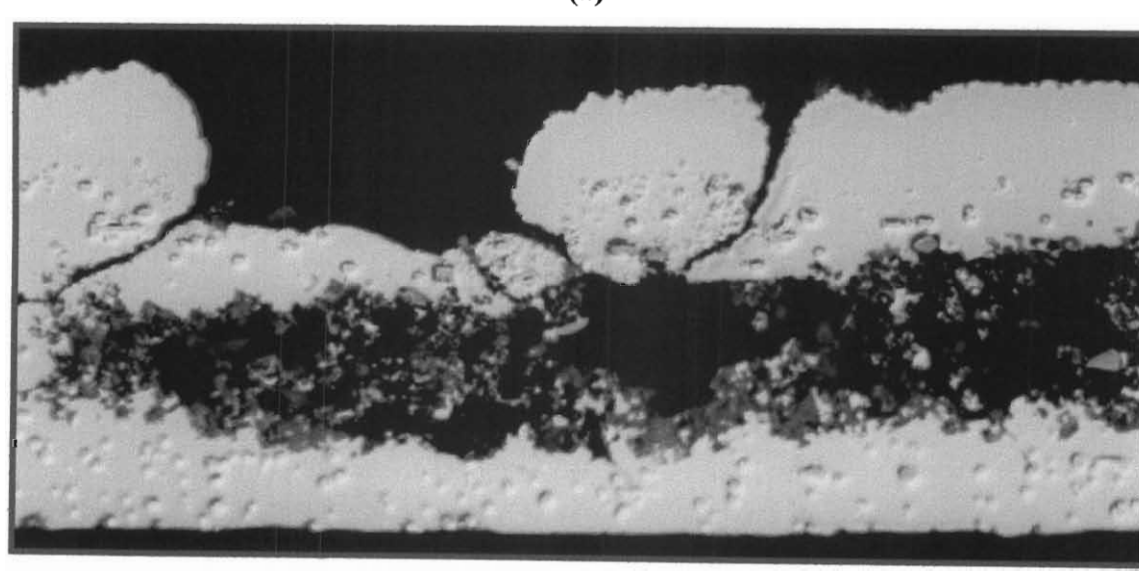

(b)

Figure 4.33 Cross-sections of CPC sample D showing the severity of corrosion of the eutectic Al-Si melt layer and underlying base alloy (500x).

Large corrosion deposits were found on the corroded α-Al filler metal layer of CPC sample D and are shown in Figure 4.34. These deposits, which contained a high percentage of both oxide and chloride as confirmed by EDX analysis, were not found on CPC samples A, B and E.

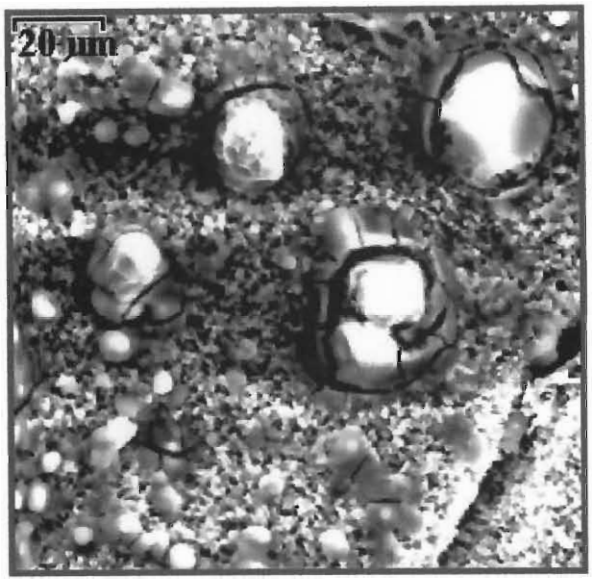

Figure 4.34 Oxide deposits on the corroded α-Al filler metal layer of CPC sample D (1000x).

The percentage oxygen, silicon and flux present on the surfaces of CPC samples A, B, D and E were measured before and after exposure to the solution containing chloride ions and sulfuric acid using EDX analysis. The results are recorded in Table 4.8 and indicate an increase in the percentage oxide found on the surfaces of CPC samples A, B and D. CPC sample E showed a decrease in its surface oxide content. The percentage Si exposed at the surface after corrosion had increased considerably for CPC sample A. The corroded surfaces of CPC samples B, D and E showed a small decrease in Si present. The absence of potassium and fluoride from the corroded CPC samples indicated that total dissolution of the flux had occurred.

Table 4.8 Percentage O, Si, K and F present on CPC samples A, B, D and E before and after corrosion in 1M NaCl + 0.5M H_2SO_4.

Alloy	A		B		D		E	
Corrosion	**Before**	**After**	**Before**	**After**	**Before**	**After**	**Before**	**After**
Magn.*	200	500	100	100	100	100	100	100
% O	4.98	9.05	5.37	7.05	6.80	10.53	3.78	0.98
% Si	5.85	17.53	5.94	3.59	5.86	3.66	5.63	4.93
% K	20.61		12.28		15.03		18.93	
% F	16.66		14.37		26.08		29.14	

*Magn. = Magnification factor of micrograph.

4.1.4 MICROSTRUCTURE OF THE CORRODED SAMPLES IN 1M NaCl + 0.5M H_2SO4 + 0.5M $NaNO_3$

4.1.4(a) 'As-supplied' and 'heat-treated' samples

The addition of nitrate ions to the solution containing chloride ions and sulfuric acid altered the nature and extent of corrosion observed on the AS and HT samples of the aluminium alloys studied.

AS sample A had corroded the least out of the four alloy samples. AS samples B, D and E all displayed localised crystallographic corrosion of the aluminium matrix. The nature and extent of crystallographic pitting observed on AS samples B, D and E all differed.

For AS sample A, localised galvanic corrosion of the aluminium matrix directly adjacent to microstructural intermetallic phases left wide trenches around their peripheries, or cavities if the microstructural intermetallic phases had become dislodged and fallen into solution. This resembled the nature of corrosion observed on HT sample A in the solution containing chloride ions only. For this reason, micrographs are not reported on.

About 9% of the exposed surface of AS sample B revealed shallow crystallographic pits that were localised and orientated in the direction of rolling. The pits showed well-defined facets and steps and reached depths of up to 7 μm. Further corrosion of the aluminium matrix between the pits was crystallographic in nature and spread in the lateral direction along the ridges that were formed by the rolling process. Figure 4.35 shows the corrosion observed on AS sample B at low and high magnifications.

AS sample E showed localised crystallographic pits orientated along the rolling direction on about 17% of the exposed surface. The pits were deeper and longer than those found on AS sample B, and did not contain well-defined facets or steps. Figure 4.36 shows this type of corrosion. Further corrosion of the aluminium matrix between and away from the pits was crystallographic in nature and spread along the ridges formed by the rolling process.

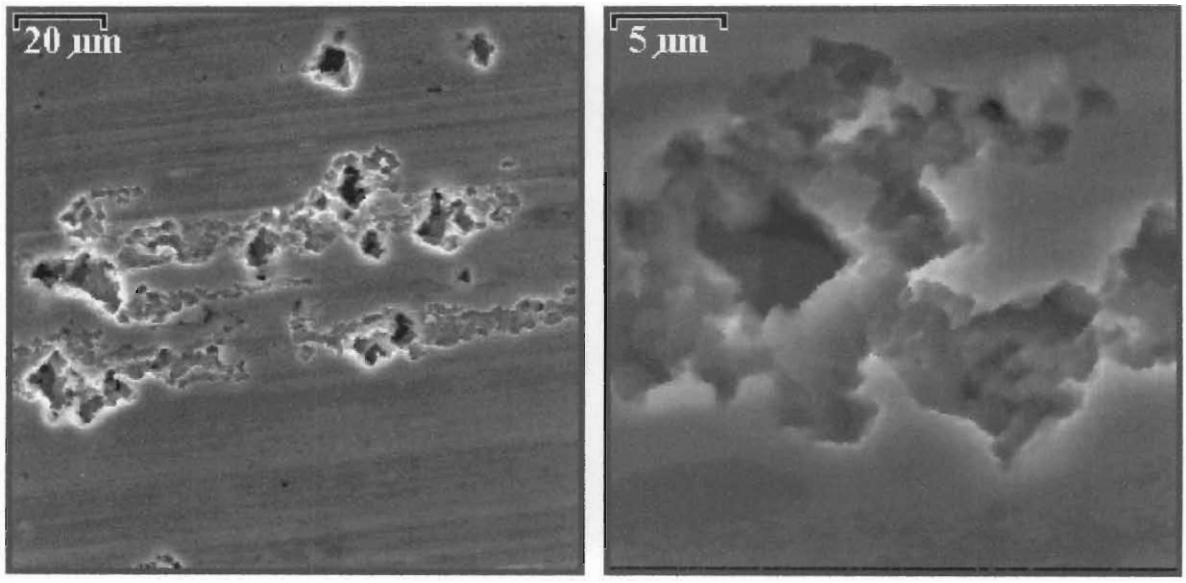

(a) **(b)**

Figure 4.35 Crystallographic pitting found on AS sample B magnified (a) 1000x and (b) 5000x.

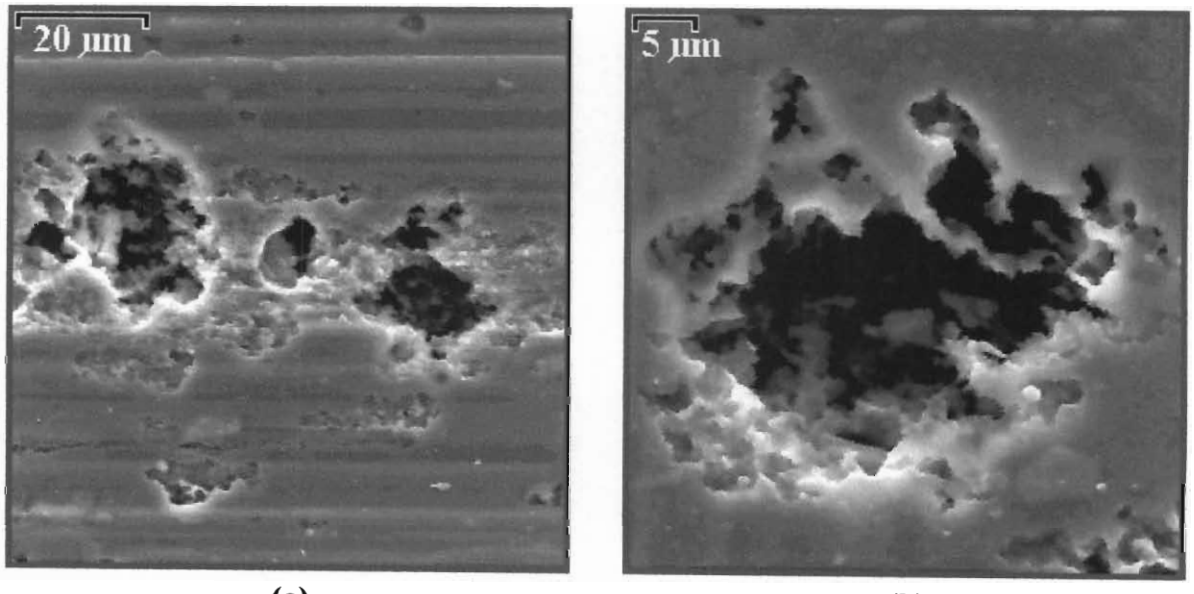

(a) **(b)**

Figure 4.36 Localised crystallographic pits and general surface corrosion observed on AS sample E, magnified (a) 1500x and (b) 3000x.

Approximately 40% of the surface of AS sample D had undergone shallow localised crystallographic pitting attack as shown in Figure 4.37(a). Individual pits were up to 30 μm long and showed interior surfaces composed of well-defined facets and steps as illustrated in Figure 4.37(b). Growth of some of the individual pits had occurred through pit coalescence resulting in pits up to 60 μm in length.

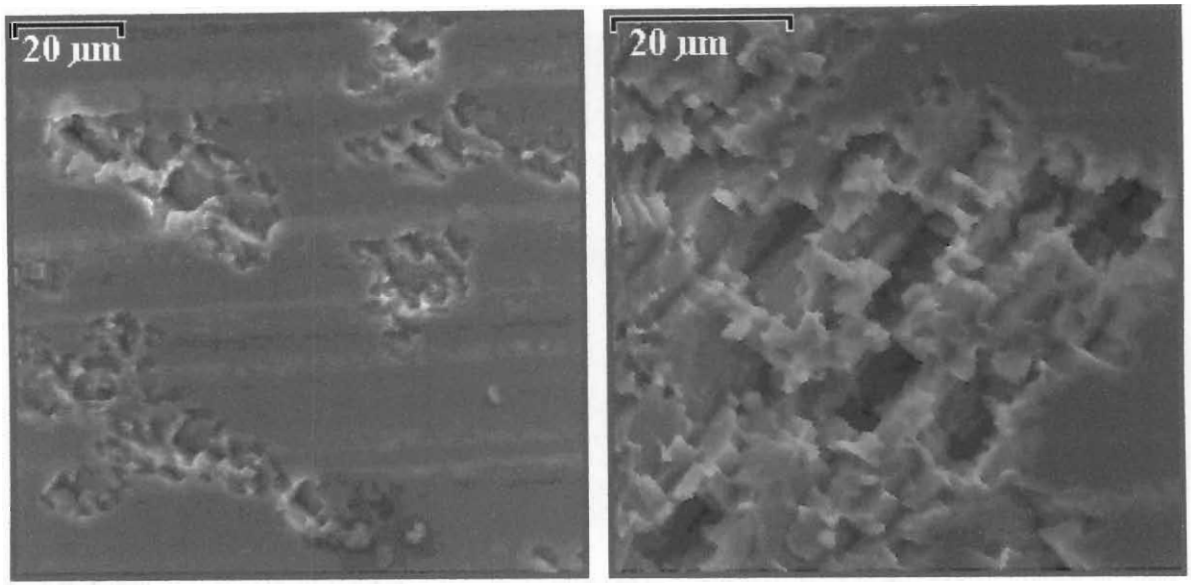

(a) **(b)**

Figure 4.37 Shallow crystallographic pits found on AS sample D, magnified (a) 1200x and (b) 2000x.

The HT samples showed a different type of corrosion to the AS samples. HT sample A had again corroded the least out of the four alloy samples, and showed shallow surface dissolution of a large amount of the exposed surface area leaving behind a rough surface.

HT sample B showed less damaging surface corrosion than AS sample B. No crystallographic pits were found, and the only corrosion observed was shallow surface dissolution that had occurred in a layered fashion on about 65% of the exposed aluminium matrix. This corrosion is shown in Figure 4.38. The aluminium matrix showed slightly more corrosion around the periphery of microstructural intermetallic phases, leaving wide but shallow trenches or cavities behind.

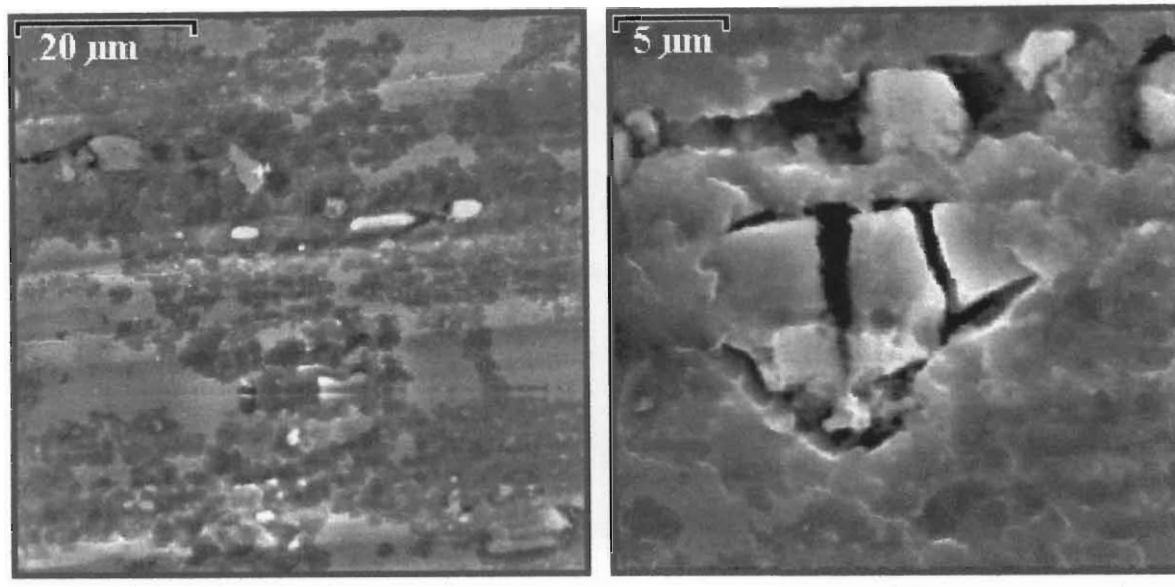

(a) **(b)**

Figure 4.38 Surface dissolution found on HT sample B, magnified (a) 2000x and (b) 5000x.

HT sample E revealed a different type of corrosion from AS sample E. Shallow surface corrosion on about 30% of the exposed area resulted in a rough appearance. Figure 4.39(a) illustrates this corrosion. A fair number of deep individual pits were found scattered over the sample surface, and were composed of sharply defined edges as can be seen in Figure 4.39(b).

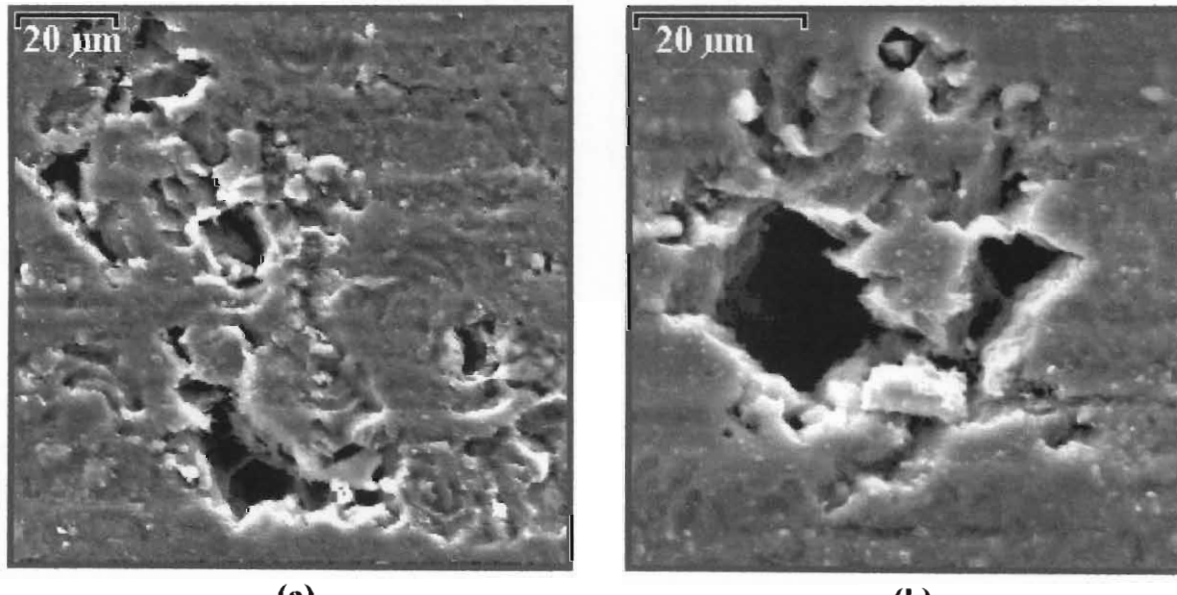

(a) **(b)**

Figure 4.39 Shallow surface corrosion and crystallographic pits found on HT sample E, enlarged (a) 1200x and (b) 2000x.

About 18% of the surface of HT sample D had experienced localised pitting corrosion resulting in large irregularly shaped pits that were shallow and up to 50 μm long. This type of corrosion is shown in Figure 4.40(a). The interior of the pits were composed of large steps with very smooth edges, giving the appearance of grooves. This is well illustrated in Figure 4.40(b). Thinning of the aluminium matrix had occurred on about 40% of the exposed area leaving a rough surface behind.

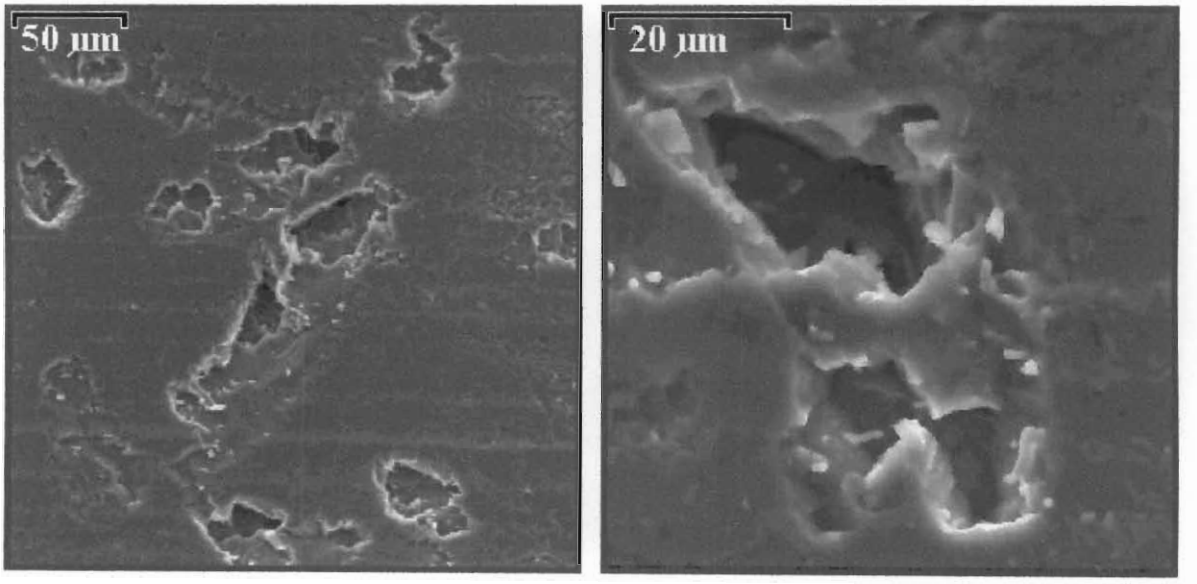

(a) **(b)**

Figure 4.40 Pitting corrosion of HT sample D, enlarged (a) 500x and (b) 2000x.

Cross-sectioned micrographs taken of the alloy samples revealed the nature and depth of pitting. A few small pits were found when a cross-section of HT sample B was viewed through the optical microscope, and these are shown in Figure 4.41. The nature and depth of pitting observed on AS and HT samples E is shown in Figure 4.42. Both the AS and HT samples E revealed pits ranging in depth between 14 μm and 40 μm. Figure 4.43 shows the 'groove-like' appearance of the pits found on cross-sections of AS and HT samples D.

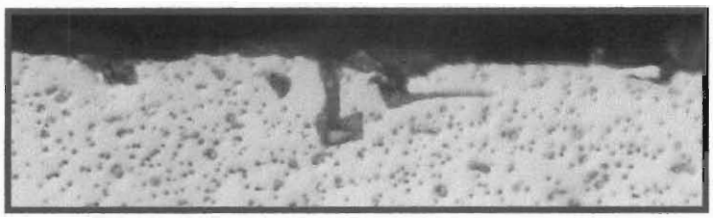

Figure 4.41 Small and narrow pits found on HT sample B (1000x).

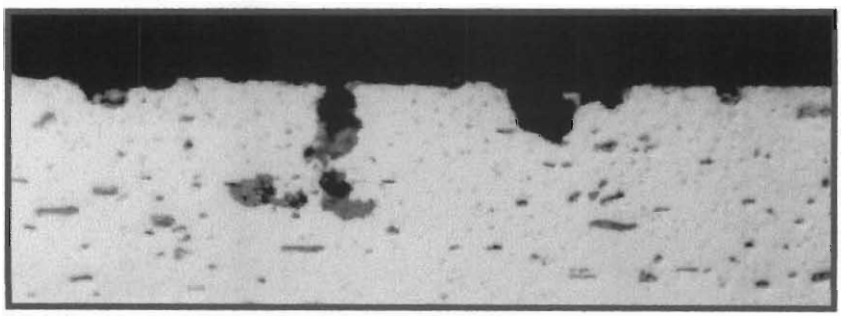

(a)

(b)

Figure 4.42 Nature and depth of pits found on (a) AS sample E (1000x) and (b) HT sample E (1000x).

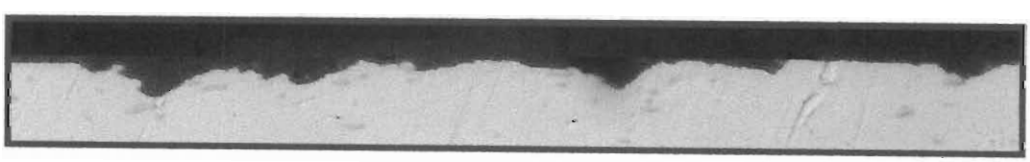

(a)

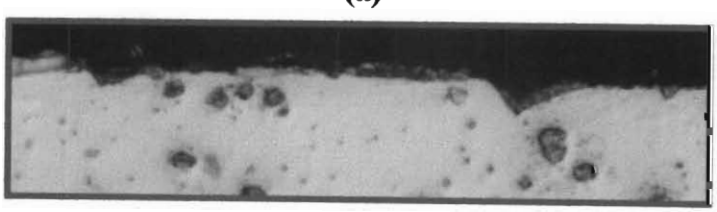

(b)

Figure 4.43 Nature of pits found on (a) AS sample D (1000x) and (b) HT sample D (1000x).

EDX analyses of the oxide content on the uncorroded and corroded surfaces of the AS and HT samples are compared in Table 4.9. After corrosion, AS and HT samples A, B and D once more showed an increase in their surface oxide layer, while AS and HT samples E again showed a loss of surface oxide after corrosion.

Table 4.9 Percentage oxide found on the surfaces of AS and HT samples A, B, D and E before and after corrosion in 1M NaCl + 0.5M H_2SO_4 + 0.5M $NaNO_3$.

Alloy		A(AS)	A(HT)	B(AS)	B(HT)	D(AS)	D(HT)	E(AS)	E(HT)
Before corrosion	Magn.*	500	500	500	500	500	500	200	200
	% O	0.60	1.36	1.81	2.50	0.94	1.55	1.39	3.99
After corrosion	Magn.*	700	700	1000	2000	200	500	200	200
	% O	3.05	1.62	2.20	3.26	1.45	2.45	0.35	0.64

* Magn. = Magnification factor of micrograph.

4.1.4(b) 'Composite Powder coated' samples

CPC samples A, B, D and E immersed for 60 minutes in a solution of chloride ions, sulfuric acid and nitrate ions exhibited a different type of corrosion, revealing the eutectic Al-Si melt layer. Effervescence was again observed on each of the surfaces once the samples were immersed into the solution.

Corrosion of CPC samples A and B was similar. Total dissolution of the residual flux and total corrosion of the partially reacted Composite Powder exposed a layer of eutectic β-Si dispersed in α-Al, and in some areas the α-Al filler alloy below. A typical example is shown for CPC sample B in Figure 4.44(a). Small, localised pits were found scattered over the entire eutectic Al-Si melt layer, and were more plentiful for CPC sample B, as shown in Figure 4.44(b). The pits had been initiated at microstructural intermetallic phases that were either exposed at, or just below, the surface. Where the microstructural intermetallic phases were exposed at the surface, wide grooves (trenches) were found around their peripheries, and an example of this is shown in Figure 4.44(c).

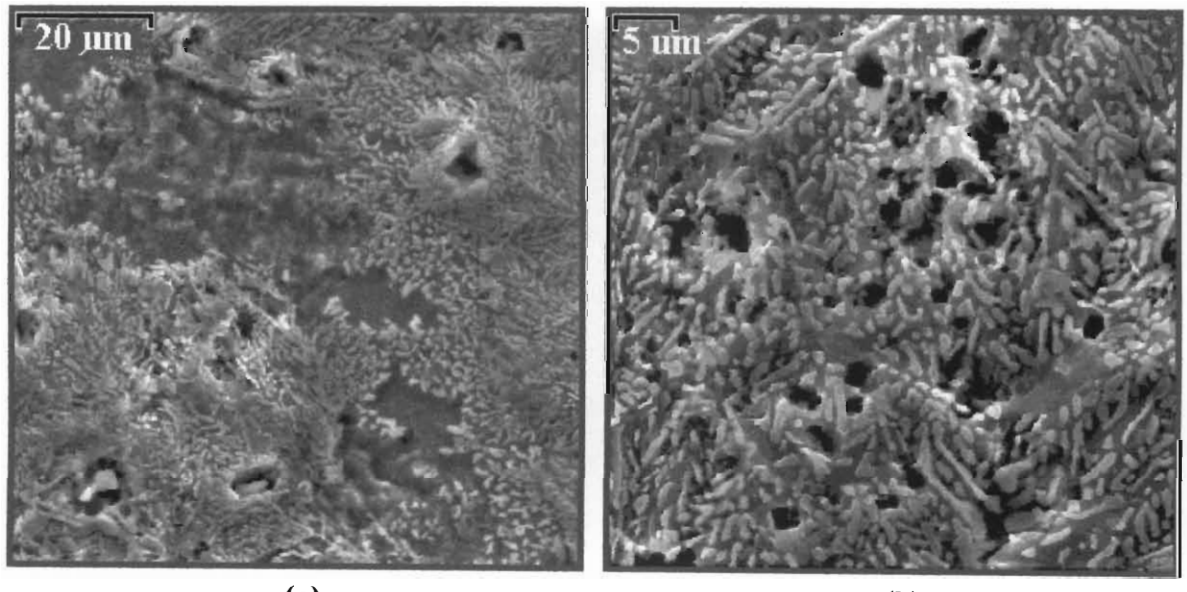

(a) **(b)**

Figure 4.44 Corrosion of the eutectic Al-Si melt layer of CPC sample B showing (a) the eutectic Al-Si melt and α-Al filler alloy (500x), (b) small localised pits (3000x).

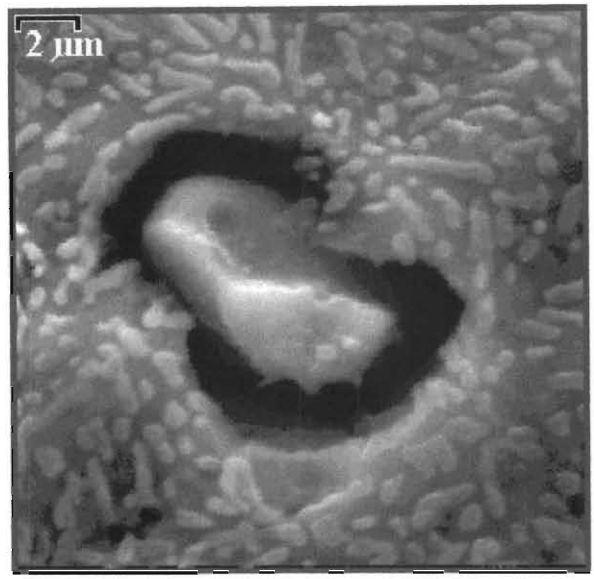

Figure 4.44(c) Localised galvanic corrosion of the α-Al adjacent to a microstructural phase on CPC sample B (7000x).

CPC sample E corroded in a similar way to CPC samples A and B, again exposing the eutectic Al-Si melt layer. Hardly any localised pits were found in the eutectic Al-Si melt, and localised galvanic corrosion of the α-Al adjacent to microstructural intermetallic phases left narrow trenches at their peripheries. This can be seen in Figure 4.45(a). Oxide deposits were scattered over most of the surface and can be seen in the top right hand corner of Figure 4.45(b). Certain parts of the eutectic Al-Si melt layer had suffered preferential corrosion of the α-Al, leaving an interconnected network of β-Si rods. This was not observed on CPC samples A and B.

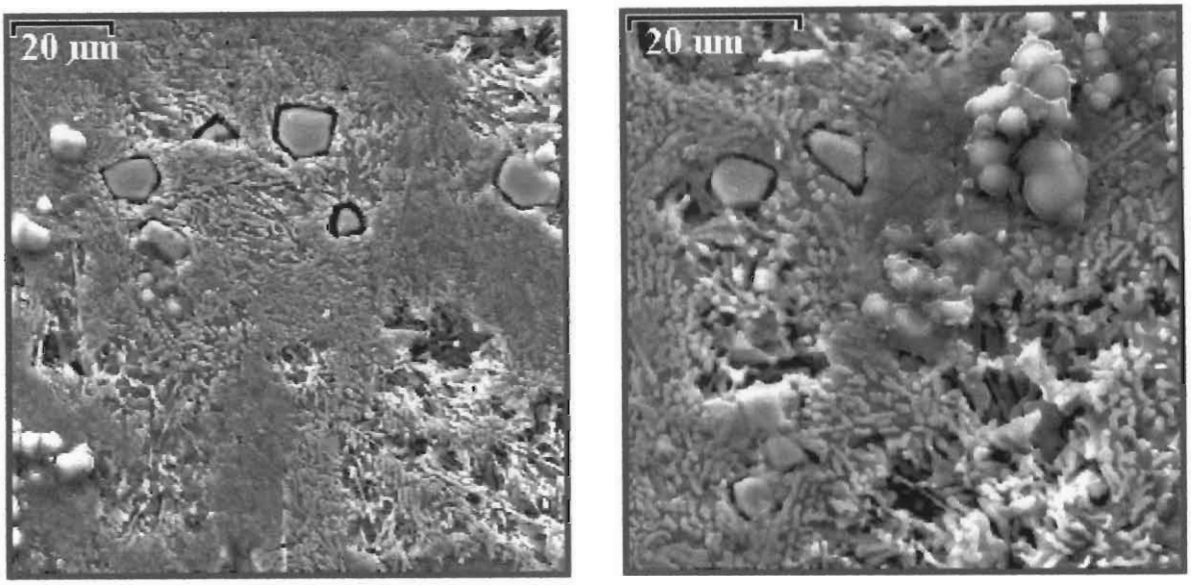

(a) **(b)**

Figure 4.45 Corrosion of the eutectic Al-Si melt layer of CPC sample E magnified (a) 1200x and (b) 2000x.

CPC sample D had suffered the most severe corrosion of the four CPC samples. On certain parts of the surface, the entire eutectic Al-Si melt layer had corroded away, exposing cells of α-Al below. This can be seen in Figure 4.46(a), which also shows a large number of white oxide deposits on the eutectic Al-Si melt layer but very little on the cells of α-Al. The largest part of the exposed surface area had suffered preferential corrosion of the α-Al in the eutectic Al-Si melt layer and eutectic Al-Si diffusion zones. This left the rods of eutectic β-Si and microstructural intermetallic phases suspended in their own interconnected network, as illustrated in Figure 4.46(b). Crystallographic pitting of the α-Al in the eutectic Al-Si melt layer was observed and is shown in Figure 4.46(c).

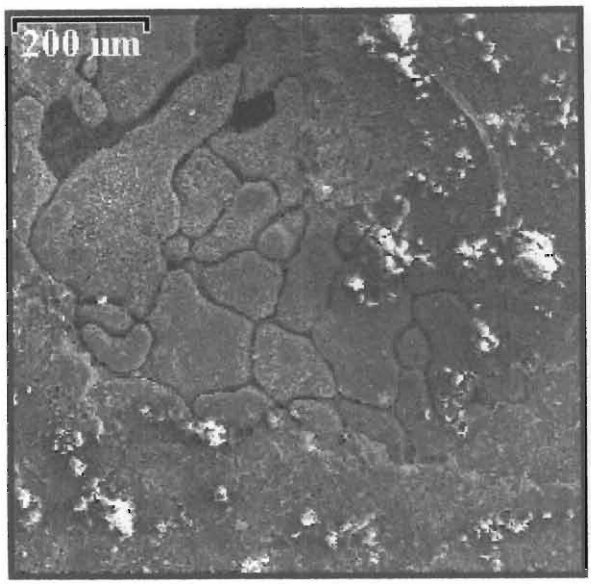

(a)

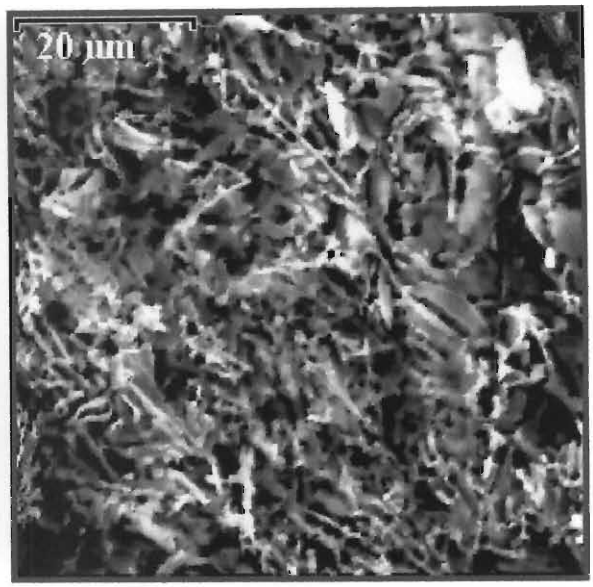

(b)

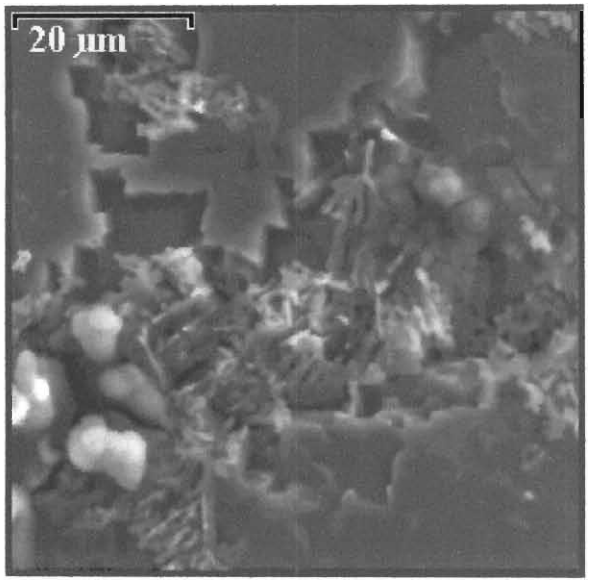

(c)

Figure 4.46 CPC sample D showing (a) Small area of exposed α-Al cells surrounded by corroded eutectic Al-Si melt layer (150x), (b) interconnected network of β-Si rods (2000x) and (c) crystallographic pitting of the α-Al (2000x).

The extent of corrosion of the eutectic Al-Si melt layer and eutectic Al-Si diffusion zones was very similar for CPC samples A and B, and a typical example is shown for CPC sample B in Figure 4.47(a). The eutectic Al-Si melt layer of CPC sample E had corroded more, as shown in Figure 4.47(b). No corrosion of the α-Al filler metal layer or base alloy was observed for CPC samples A, B and E.

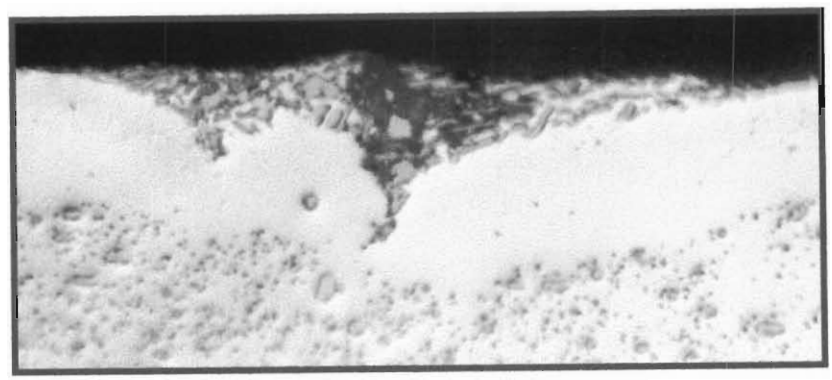

(a)

(b)

Figure 4.47 Cross-sectioned view of the extent of corrosion of the eutectic Al-Si melt layer of (a) CPC sample B (1000x) and (b) CPC sample E (500x).

The extent of corrosion of CPC sample D is shown in Figures 4.48, 4.49 and 4.50. Below the corroded eutectic Al-Si melt layer and α-Al filler metal layer, corrosion of CPC sample D had progressed along the eutectic Al-Si diffusion zones to the underlying base alloy. Corrosion of the base alloy was again localised at the centre of the samples' thickness. Here corrosion had spread laterally rather than vertically, resulting in pits that reached lengths of up to 800 μm. In some areas CPC sample D had undergone such severe corrosion that the entire base alloy had disappeared, leaving gaping holes that were up to 90 μm in depth. Only the cells of α-Al were left relatively uncorroded. Intergranular corrosion of the base alloy was again visible.

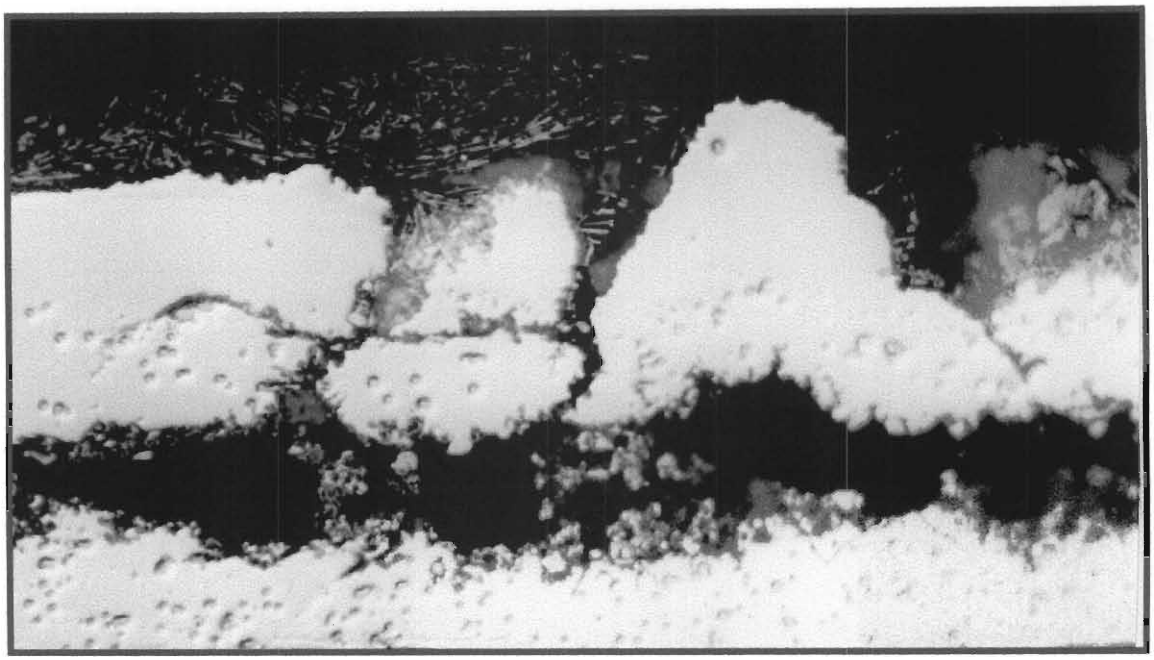

Figure 4.48 Cross-section of CPC sample D, showing localisation of corrosion at the centre of the sample's thickness (500x).

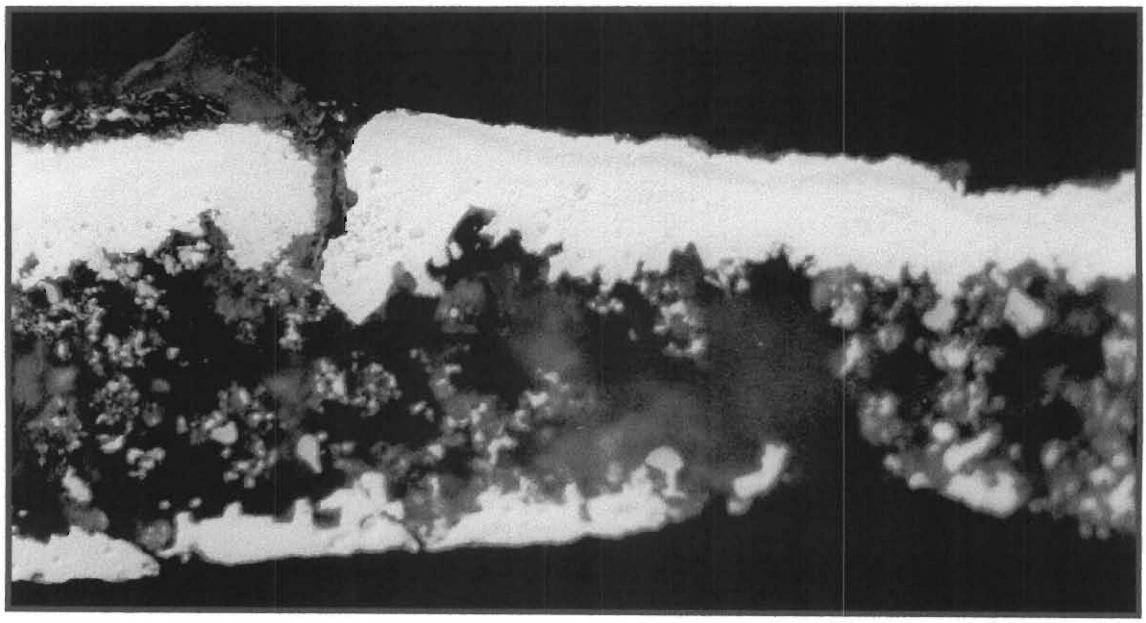

Figure 4.49 Extreme corrosion of CPC sample D showing perforation of the sample's thickness (500x).

(a)

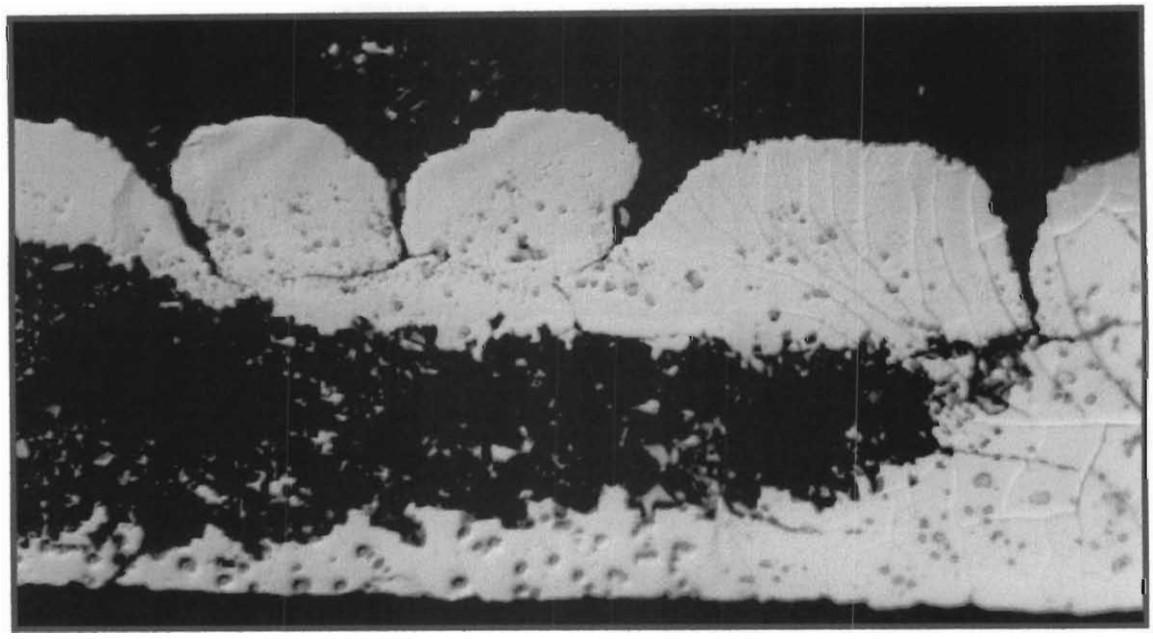

(b)

Figure 4.50 Extent of corrosion observed on CPC sample D (500x).

The percentage oxygen, silicon and flux present on the surfaces of the CPC samples were measured using EDX analysis before and after exposure to the solution containing chloride ions, sulfuric acid and nitrate ions. The results obtained are recorded in Table 4.10. All CPC samples showed an increase in surface oxide after corrosion. This increase was small for CPC samples A, B and E (< 2%) and much larger for CPC sample D (17%). The percentage of Si present on the corroded CPC surfaces was very high and ranged between 18% and 22%. The absence of potassium and fluoride from the corroded CPC surface indicated that the entire residual flux had dissolved.

Table 4.10 Percentage O, Si, K and F present on CPC samples A, B, D and E before and after corrosion in 1M NaCl + 0.5M H_2SO_4 + 0.5M $NaNO_3$.

Alloy	A		B		D		E	
Corrosion	**Before**	**After**	**Before**	**After**	**Before**	**After**	**Before**	**After**
Magn.*	200	500	100	500	100	150	100	500
% O	4.98	6.09	5.37	7.23	6.80	23.86	3.78	4.48
% Si	5.85	21.70	5.94	18.07	5.86	20.81	5.63	20.24
% K	20.61		12.28		15.03		18.93	
% F	16.66		14.37		26.08		29.14	

* Magn. = Magnification factor of micrograph.

4.2 ELECTROCHEMICAL RESULTS

4.2.1 OPEN CIRCUIT POTENTIALS

The open circuit potential (OCP) of the AS, HT and CPC samples in various corrosive electrolyte solutions was determined by mounting the sample in the electrode holder, immersing it in the solution of interest and recording its change in potential with time under open circuit conditions.

4.2.1.1 Open Circuit Potential measurements in 1M NaCl

4.2.1.1(a) 'As-supplied' samples

The variation of OCP with time for AS samples A, B, D and E immersed in the solution containing chloride ions is shown in Figure 4.51.

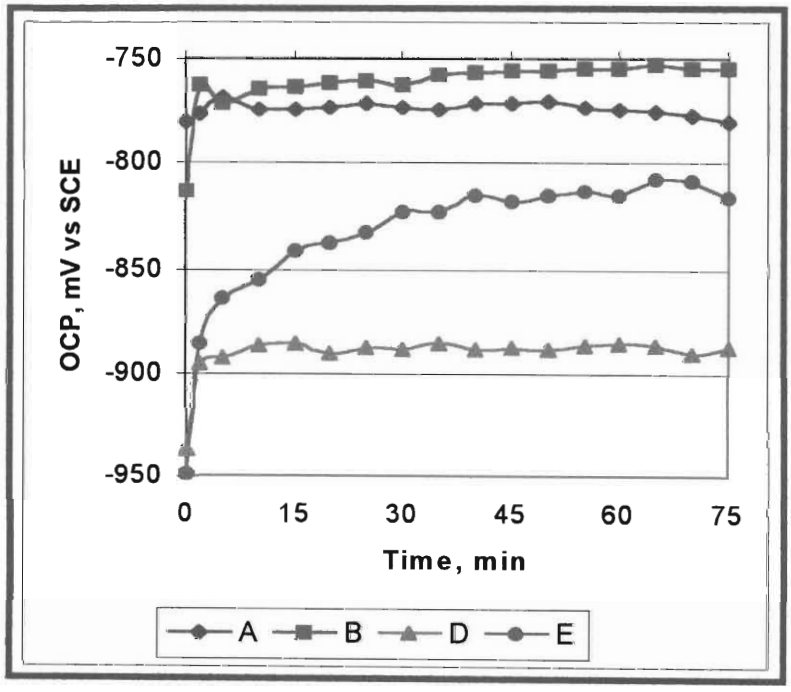

Figure 4.51 OCP behaviour of AS samples A, B, D and E in 1M NaCl.

The general trend for the OCP of the AS samples was to become more positive with time. For AS samples A, B and D, the rise in potential was largest during the first 2 minutes of immersion. After 5 minutes, the change in OCP with time became minimal for AS sample D, whose OCP varied around a fixed potential of –889 ± 3 mV (SCE). For AS sample B, the OCP increased slightly up to 35 minutes, then levelled out at –755 ± 2 mV (SCE). The OCP of AS sample A remained constant at –772 ± 2 mV up to 50 minutes, thereafter a slight decrease in potential was observed. AS sample E displayed a continuous and large increase in OCP during the first 40 minutes, which levelled out somewhat to a potential of –814 ± 7 mV (SCE).

4.2.1.1(b) 'Heat-treated' samples

The change in OCP with time of HT samples A, B, D and E immersed in the solution containing chloride ions is shown in Figure 4.52.

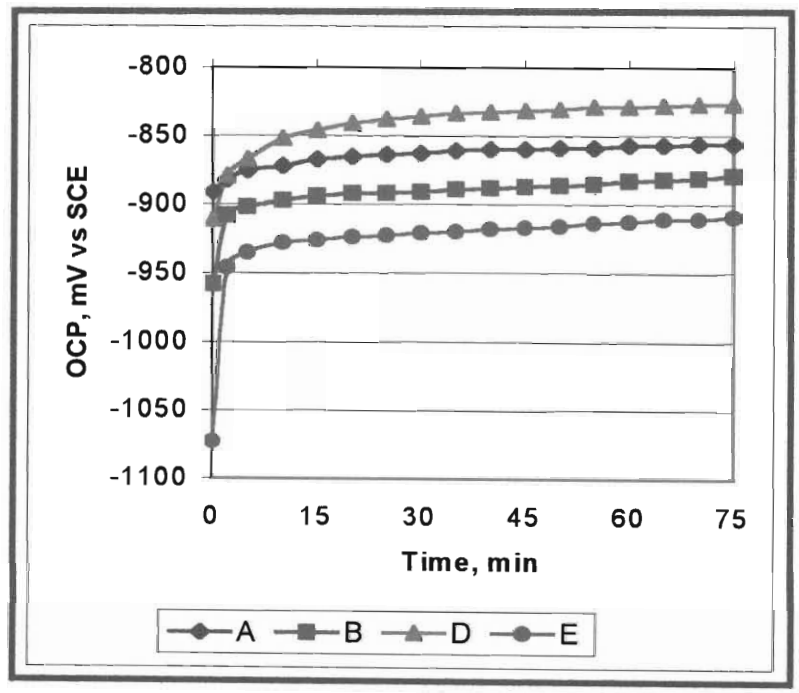

Figure 4.52 OCP behaviour of HT samples A, B, D and E in 1M NaCl.

The general trend for the OCP of the HT samples was to become more positive with time, the rise in potential being largest during the first 5 minutes. After 5 minutes, continuous

and very slow changes in OCP with time were observed. An increase in OCP of less than 30 mV was noted during the remaining 65 minutes of immersion.

4.2.1.1(c) 'Composite Powder coated' samples

The change in OCP with time for CPC samples A, B, D and E immersed in the solution containing chloride ions is shown in Figure 4.53.

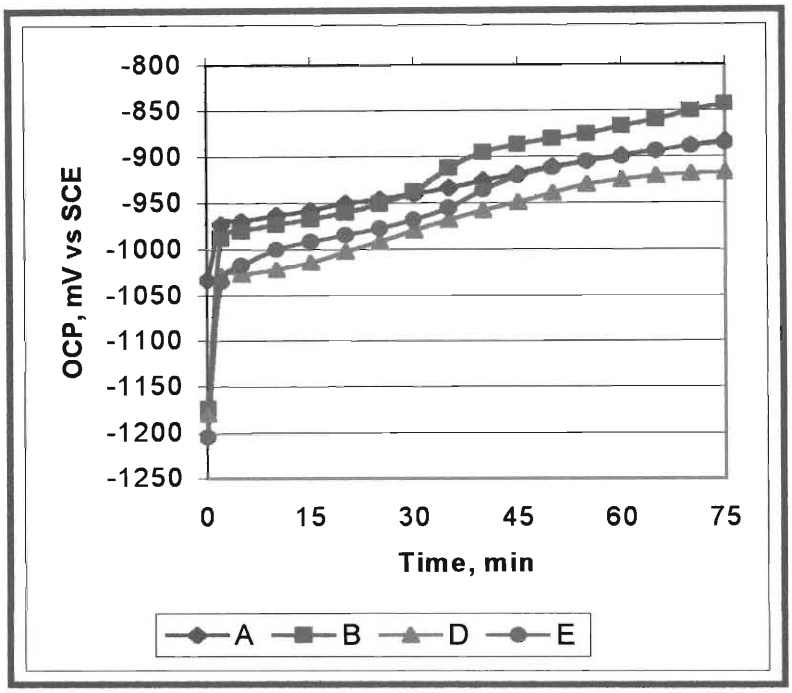

Figure 4.53 OCP behaviour of CPC samples A, B, D and E in 1M NaCl.

The general trend for the OCP of the CPC samples was to become more positive with time, the rise in potential being largest during the first 2 minutes of immersion. The OCP then changed continuously by 1 mV/min to 2 mV/min towards more positive potentials. The increase in OCP per minute of immersion for the CPC samples was 3 to 5 times larger than that noted for the HT samples.

4.2.1.1(d) Open circuit potential values in 1M NaCl

The OCPs of the AS, HT and CPC samples A, B, D and E obtained initially and after 60 minutes of immersion in the solution containing chloride ions are summarised in Table 4.11.

Table 4.11 OCPs obtained in 1M NaCl at initial time of immersion and at 60 minutes for the AS, HT and CPC samples A, B, D and E.

Form of sample preparation	OCP (mV) vs SCE at time t (min)							
	A		B		D		E	
	0	60	0	60	0	60	0	60
AS	-780	-774	-813	-755	-937	-886	-949	-815
HT	-891	-857	-958	-883	-911	-829	-1073	-913
CPC	-1033	-899	-1173	-867	-1179	-925	-1204	-900

4.2.1.2 Open circuit potential measurements in 1M NaCl + 0.5M H_2SO_4

4.2.1.2(a) 'As-supplied' samples

The change in OCP with time for AS samples A, B, D and E, immersed in the solution containing chloride ions and sulfuric acid, is shown in Figure 4.54.

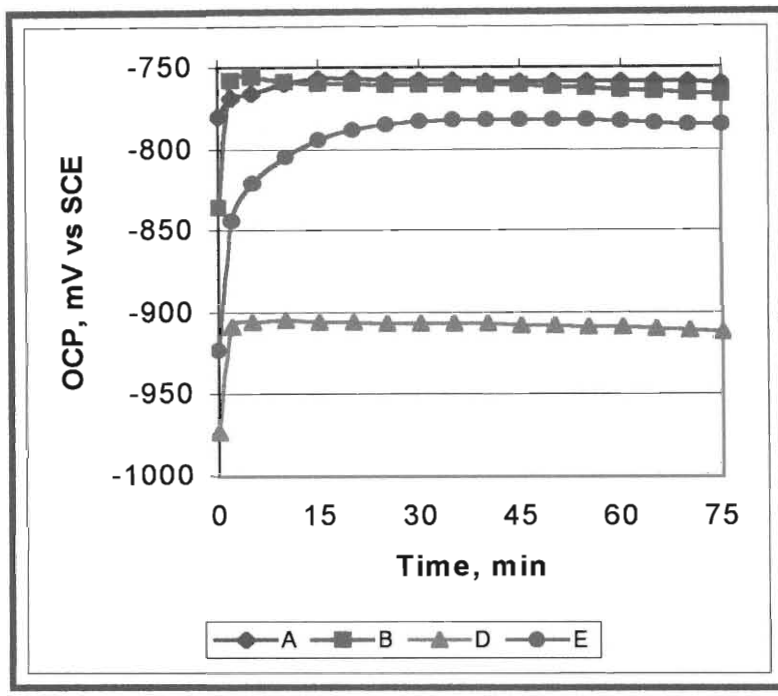

Figure 4.54 OCP behaviour of AS samples A, B, D and E in 1M NaCl + 0.5M H_2SO_4.

The general trend for the OCP of the AS samples was to become more positive for the first 45 minutes, the rise in potential being largest during the first 2 minutes. After 10 minutes, the change in OCP with time became minimal for AS sample A, whose OCP varied around a fixed potential of –759 ± 2 mV (SCE). For AS samples B and D the OCP stayed constant up to 45 minutes at –759 ± 2 mV and –906 ± 1 mV (SCE) respectively, thereafter a slight decrease in potential was observed. The change in OCP with time for AS sample E again differed, and increased dramatically for the first 30 minutes, then stabilised at a potential of –783 ± 2 mV (SCE).

The addition of sulfuric acid caused the OCP of AS samples A and E to become slightly more positive by 20 mV, whilst the OCP of AS samples B and D changed to more negative potentials by about 10 mV and 20 mV respectively.

4.2.1.2(b) 'Heat-treated' samples

The variation in OCP with time of HT samples A, B, D and E, immersed in the solution containing chloride ions and sulfuric acid, is shown in Figure 4.55.

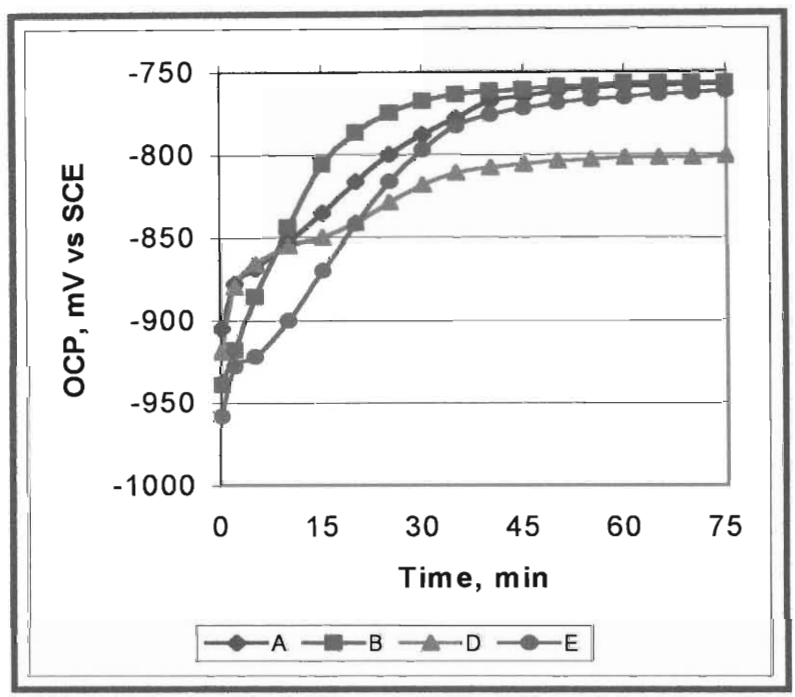

Figure 4.55 OCP behaviour of HT samples A, B, D and E in 1M NaCl + 0.5M H_2SO_4.

The general trend for the OCP of the HT samples was again to become more positive with time. A very large increase in potential was observed for the HT samples during the first 40 minutes of immersion. The magnitude of this increase depended on the chemical composition of the alloy sample. After 40 minutes, the OCP of the HT samples stabilised and changed only slightly to more positive potentials for the remainder of the experiment. For HT samples A, B and E the OCPs from this moment onwards were virtually the same, and varied between -768 mV and -757 mV (SCE). The OCP of HT sample D was the most negative at -804 ± 4 mV (SCE).

The addition of sulfuric acid caused the OCP of the HT samples to become more positive once the potential had stabilised after 40 minutes.

4.2.1.2(c) 'Composite Powder coated' samples

The variation of OCP with time for CPC samples A, B, D and E, immersed in the solution containing chloride ions and sulfuric acid, is displayed in Figure 4.56.

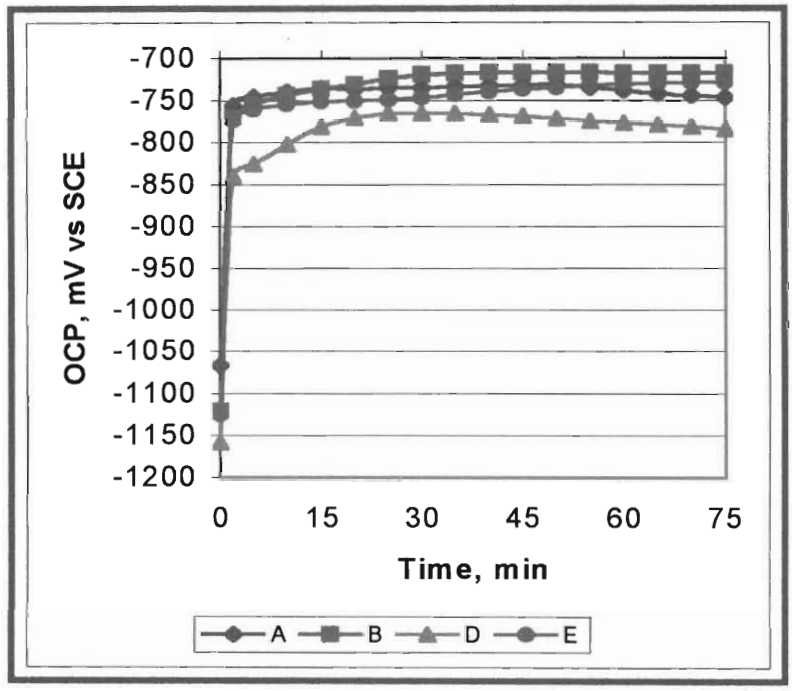

Figure 4.56 OCP behaviour of CPC samples A, B, D and E in 1M NaCl + 0.5M H_2SO_4.

The general trend observed for the OCP of the CPC samples was to become more positive with time for the first 45 minutes. Thereafter the OCP of CPC samples A, B and D decreased slightly whilst the OCP of CPC sample E continued to increase slightly. The initial OCPs were again highly negative and ranged between -1060 mV and -1160 mV (SCE). A very large increase in potential was again observed during the first 2 minutes of immersion.

The addition of sulfuric acid caused the OCP of the CPC samples to become considerably more positive and allowed for a relatively stable potential to be reached within 30 minutes.

4.2.1.2(d) Open circuit potential values in 1M NaCl + 0.5 M H_2SO_4

Addition of sulfuric acid to the solution containing chloride ions caused a change in the pH from near-neutral (pH 4.06) to acidic (pH 0.52). The OCPs of the AS, HT and CPC samples A, B, D and E obtained initially and after 60 minutes of immersion are summarised in Table 4.12.

Table 4.12 OCPs obtained initially and at sixty minutes in 1M NaCl + 0.5 M H_2SO_4 for the AS, HT and CPC samples A, B, D and E.

Form of sample preparation	OCP (mV) vs SCE at time t (min)							
	A		B		D		E	
	0	60	0	60	0	60	0	60
AS	-780	-759	-836	-764	-973	-909	-923	-783
HT	-905	-759	-939	-757	-919	-802	-958	-766
CPC	-1067	-737	-1121	-717	-1159	-776	-1125	-730

4.2.1.3 Open circuit potential measurements in 1M NaCl + 0.5M H_2SO_4 + 0.5M $NaNO_3$

4.2.1.3(a) 'As-supplied' samples

The change in OCP with time for AS samples A, B, D and E immersed in the solution containing chloride ions, sulfuric acid and nitrate ions is shown in Figure 4.57.

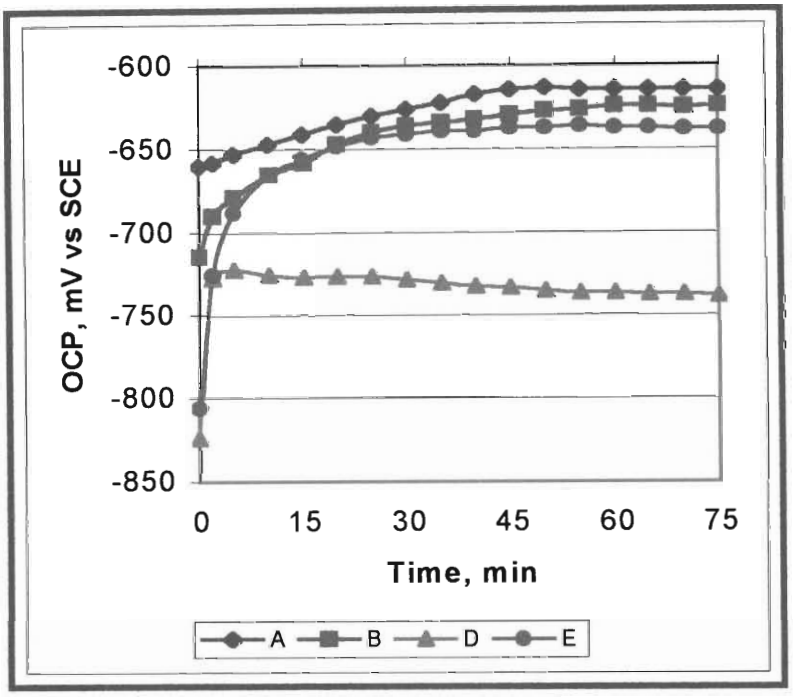

Figure 4.57 OCP behaviour of AS samples A, B, D and E in 1M NaCl + 0.5M H_2SO_4 + 0.5M $NaNO_3$.

The general trend for the OCP of AS samples A, B and E was again to become more positive with time. From 25 minutes onwards, AS samples A, B and E showed an almost identical rise in potential, and after 50 minutes, their OCPs remained constant at –614 mV, -626 mV and –638 mV respectively. For AS sample D, the OCP increased for the first 5 minutes, then became gradually more negative with time, and after 45 minutes had reached a constant value of –736 ± 2 mV (SCE).

The addition of nitrate ions to the solution containing chloride ions and sulfuric acid caused a large shift in the OCP of the AS samples to more positive potentials.

4.2.1.3(b) 'Heat-treated' samples

The variation in OCP with time for HT samples A, B, D and E immersed in the solution containing chloride ions, sulfuric acid and nitrate ions is shown in Figure 4.58.

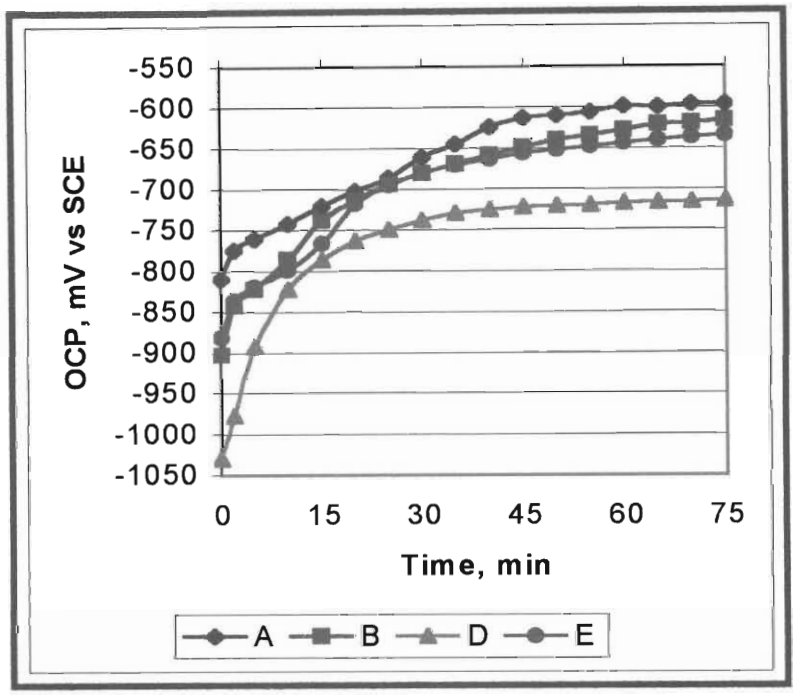

Figure 4.58 OCP behaviour of HT samples A, B, D and E in 1M NaCl + 0.5M H_2SO_4 + 0.5M $NaNO_3$.

The general trend observed for the OCP of the HT samples was again to become more positive with time. The increase in OCP was largest during the first 35 minutes. This was followed by a gradual change in OCP for HT sample D, and a moderate change in OCP for HT samples A, B and E towards more positive potentials.

The addition of nitrate ions caused a significant change in the OCP of the HT samples towards more positive potentials.

4.2.1.3(c) 'Composite Powder coated' samples

The OCP behaviour of CPC samples A, B, D and E immersed in the solution containing chloride ions, sulfuric acid and nitrate ions is shown in Figure 4.59.

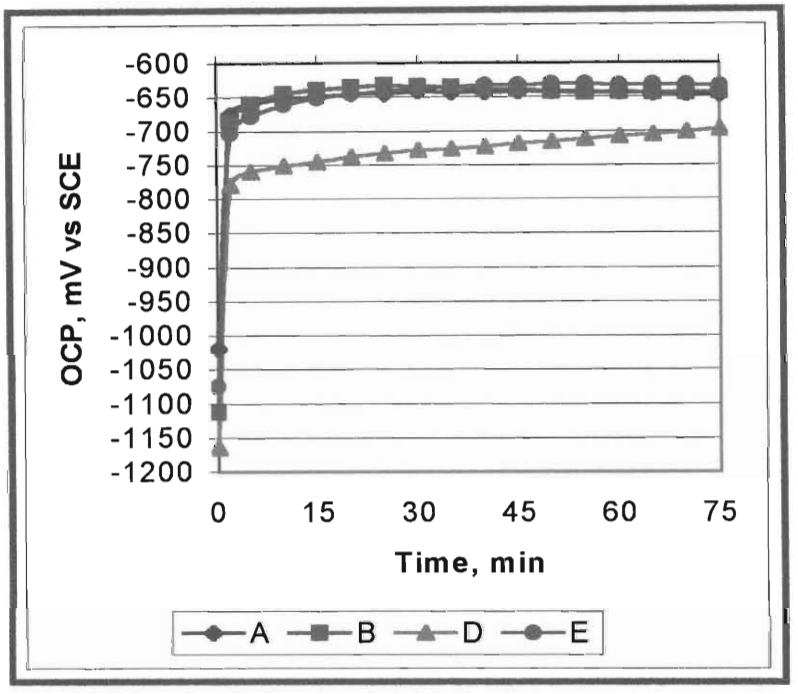

Figure 4.59 OCP behaviour of CPC samples A, B, D and E in 1M NaCl + 0.5M H_2SO_4 + 0.5M $NaNO_3$.

A very large increase in OCP was again observed for the CPC samples during the first 2 minutes of immersion. After 2 minutes, very similar changes in OCP were observed for CPC samples A, B and E. After 20 minutes of a gradual increase in potential, the OCPs of CPC samples A, B and E stabilised between –631 mV and –647 mV (SCE). CPC sample D showed a gradual increase in OCP of 62 mV from 5 minutes onwards, and had a more negative potential value than CPC samples A, B and E.

The addition of nitrate ions to the solution containing chloride ions and sulfuric acid resulted in more positive OCPs for the CPC samples.

4.2.1.3(d) Open circuit potential values in 1M NaCl + 0.5 M H_2SO_4 + 0.5M $NaNO_3$

Addition of nitrate ions to the solution containing chloride ions and sulfuric acid caused a very slight change in the pH from 0.52 to 0.48. The OCPs of the AS, HT and CPC samples A, B, D and E obtained initially and after 60 minutes of immersion are summarised in table 4.13.

Table 4.13 OCPs obtained initially and at 60 minutes in 1M NaCl + 0.5 M H_2SO_4 + 0.5M $NaNO_3$ for the AS, HT and CPC samples A, B, D and E.

Form of sample preparation	OCP (mV) vs SCE at time t (min)							
	A		B		D		E	
	0	60	0	60	0	60	0	60
AS	-660	-614	-714	-624	-824	-736	-806	-637
HT	-809	-598	-900	-628	-1030	-717	-881	-644
CPC	-1019	-643	-1113	-643	-1165	-708	-1075	-633

4.2.2 PITTING POTENTIALS

4.2.2.1 Pitting potential measurements in 1M NaCl

The values of the pitting potential, E_p, obtained in the solution containing chloride ions at sweep rates ranging from 1 mV/s to 25 mV/s for the AS, HT and CPC samples A, B, D and E are shown in Figure 4.60. Linear regressions were used to illustrate the observed trends more clearly. The detailed results of E_p values derived from the first sweep are reported in Appendix A, Table I.

The effect of sweep rate on E_p of the AS samples varied with the samples' chemical composition and is shown in Figure 4.60(a). The general trend was for E_p to become more positive as the sweep rate increased. For AS samples A and B the increase in E_p was very small, $\leq$ 15 mV. AS sample D showed a slight increase in E_p of 20 mV, and AS sample E showed the largest change in E_p of 60 mV to more positive potentials.

The effect of thermal treatment on E_p of the AS samples is shown in Figure 4.60(b). Both HT samples A and B displayed an increase in E_p with increasing sweep rate. HT sample D showed a slight decrease in E_p, whilst the value of E_p for HT sample E was not affected by the sweep rate at which the anodic polarisation curves were conducted.

The effect of Composite Powder coating on E_p is shown in Figure 4.60(c). E_p values of the CPC samples were least affected by accelerated sweep rates. For CPC samples A and B, increasing the sweep rate had no influence on the value of E_p. CPC sample D showed a slight change in E_p in the positive direction as faster sweep rates were used. The value of E_p obtained for CPC sample E at a sweep rate of 1 mV/s was considerably more positive by about 200 mV. At higher sweep rates, CPC sample E displayed a slight increase in E_p to more positive potentials with increasing sweep rate.

The multiple anodic polarisation curves for the AS, HT and CPC samples were typically very similar and some selected examples of these curves are given in Appendix B, Figure I.i. E_p values measured after each successive sweep for the AS, HT and CPC samples in the solution containing chloride ions are recorded in Appendix A, Table I. The general trend was for E_p to increase slightly after each successive sweep, this increase being largest

for the CPC samples. AS samples B, D and E showed a slight decrease in E_p with increasing number of sweeps.

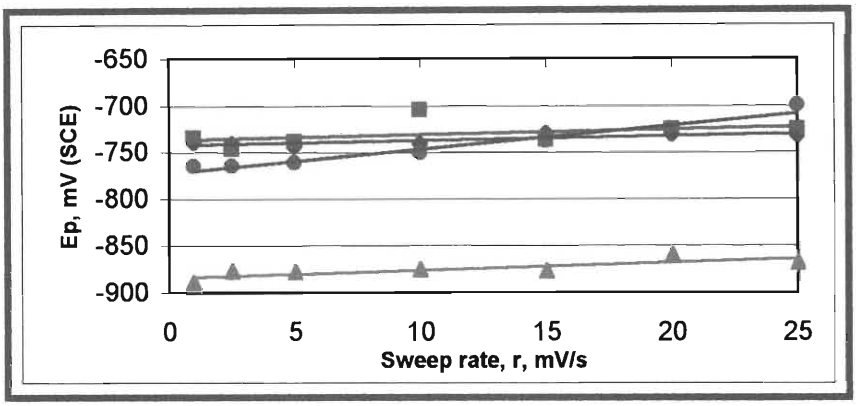

(a)

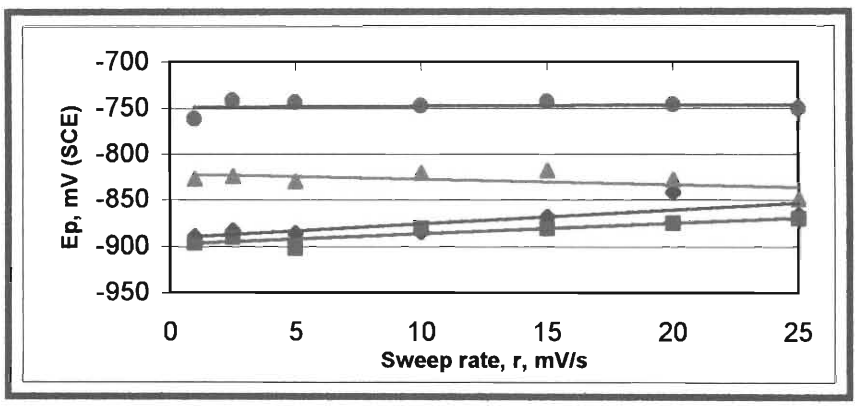

(b)

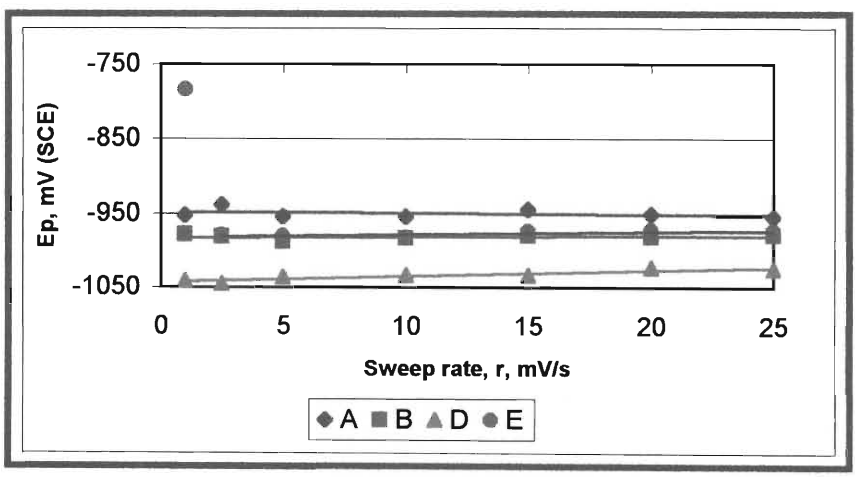

(c)

Figure 4.60 The effect of sweep rate on E_p of alloy samples A, B, D and E in the (a) AS, (b) HT and (c) CPC forms, exposed to 1M NaCl.

E_p values obtained for the AS, HT and CPC samples A, B, D and E in the solution containing chloride ions at sweep rates of 1mV/s and 5 mV/s are summarised in the bar graphs shown in Figure 4.61.

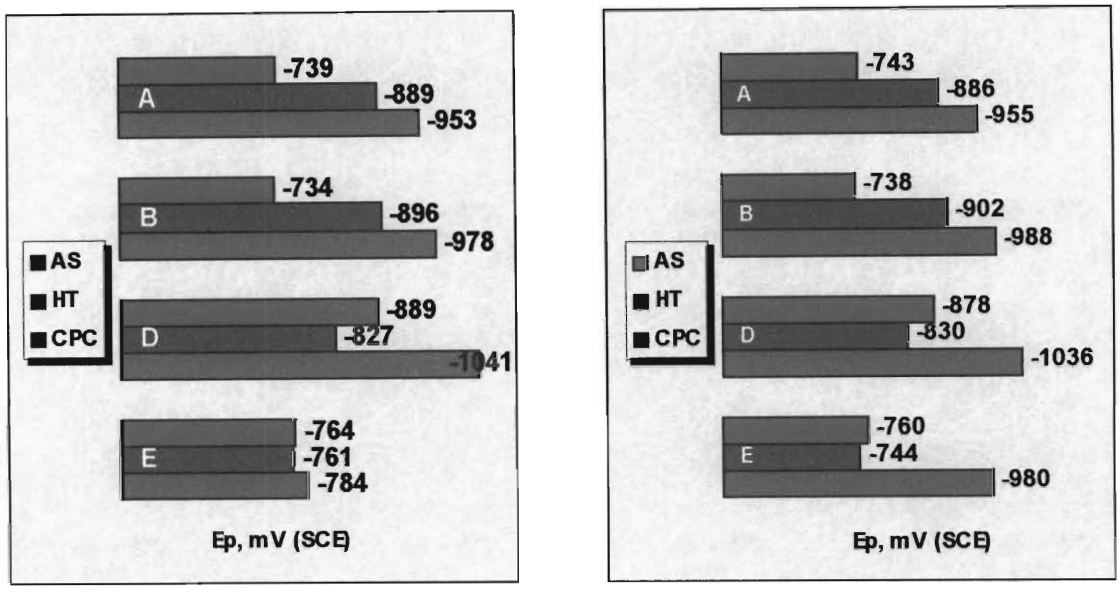

(a) **(b)**

Figure 4.61 E_p values in 1M NaCl for the AS, HT and CPC samples A, B, D and E at sweep rates of (a) 1 mV/s and (b) 5 mV/s.

The above results show the influence of heat treatment and Composite Powder coating on E_p. With heat treatment, E_p became significantly more negative for both HT samples A and B, whilst for HT sample D a change to more positive potentials was found. Heat treatment of AS sample E seemed to have little effect on E_p, and alloy sample E displayed virtually identical values of E_p for both AS and HT samples. Composite Powder coating resulted in the most negative E_p values to be realised.

4.2.2.2 Pitting potential measurements in 1M NaCl + 0.5M H_2SO_4

The values of E_p obtained in the solution containing chloride ions and sulfuric acid at sweep rates ranging from 1 mV/s to 25 mV/s for the AS, HT and CPC samples A, B, D and E are shown in Figure 4.62. The detailed results are reported in Appendix A, Table II.

The effect of sweep rate on E_p of the AS samples is shown in Figure 4.62(a). The AS samples all showed an increase in E_p to more positive potentials with increasing sweep rate. The observed increase in E_p was small for AS samples A, D and E, whilst AS sample B showed a larger increase of 42 mV to more positive potentials.

The effect of thermal treatment on E_p of the AS samples is shown in Figure 4.62(b). HT samples A and B showed a small increase in E_p with increasing sweep rate. The increase in sweep rate did not affect the value of E_p for HT samples D and E.

The effect of Composite Powder coating on E_p is shown in Figure 4.62(c). CPC samples A, B, D and E displayed the most positive E_p values at a sweep rate of 1 mV/s. At higher sweep rates, E_p values of CPC samples A and B were not affected by the increase in sweep rate. CPC samples D and E showed a slight decrease in E_p with increasing sweep rates.

The multiple anodic polarisation curves for the AS, HT and CPC samples obtained in the solution containing chloride ions and sulfuric acid were very similar to those obtained in the solution containing chloride ions and some selected examples of these curves are given in Appendix B, Figure I.ii. The values of E_p obtained after each successive sweep are recorded in Appendix A, Table II. The general trend was again for E_p to increase slightly after each successive sweep, the increase being larger for the CPC samples.

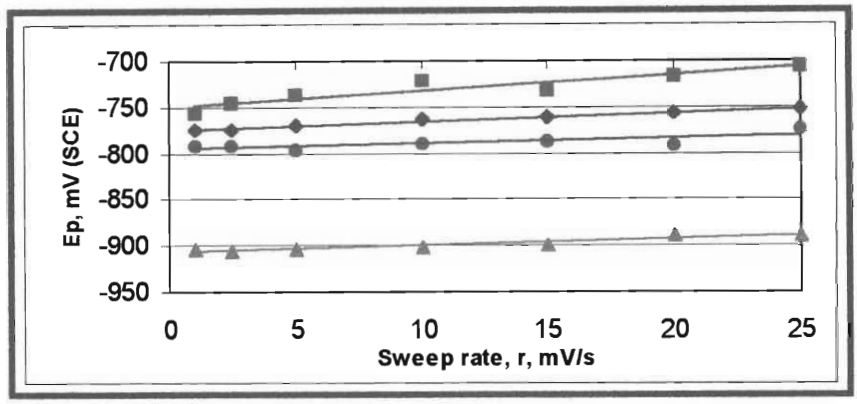

(a)

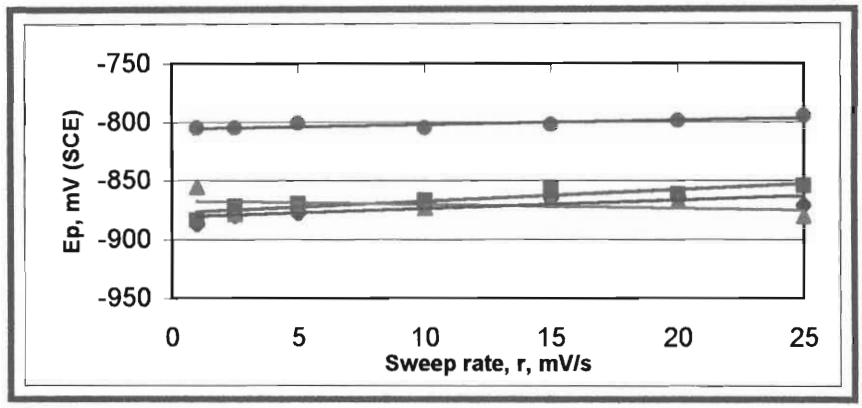

(b)

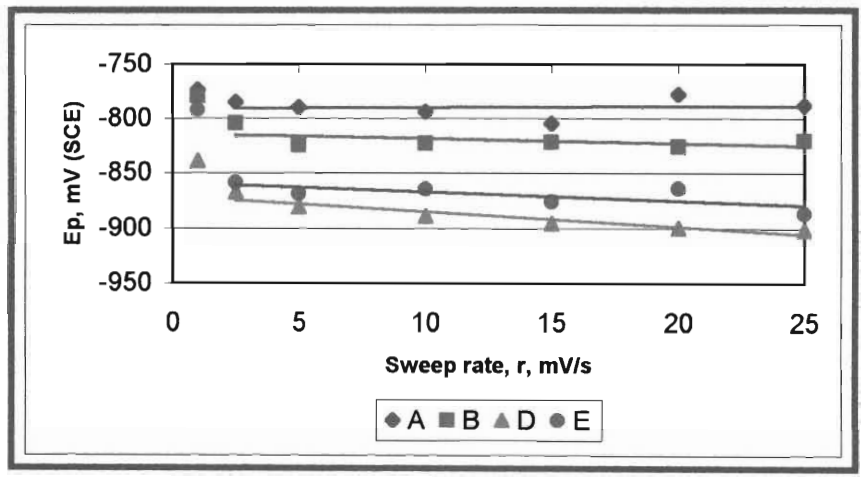

(c)

Figure 4.62 The effect of sweep rate on E_p of alloy samples A, B, D and E in the (a) AS, (b) HT and (c) CPC forms, exposed to 1M NaCl + 0.5M H_2SO_4.

E_p values of the AS, HT and CPC samples A, B, D and E in the solution containing chloride ions and sulfuric acid were obtained at sweep rates of 1mV/s and 5 mV/s and are summarised in the bar graphs in Figure 4.63.

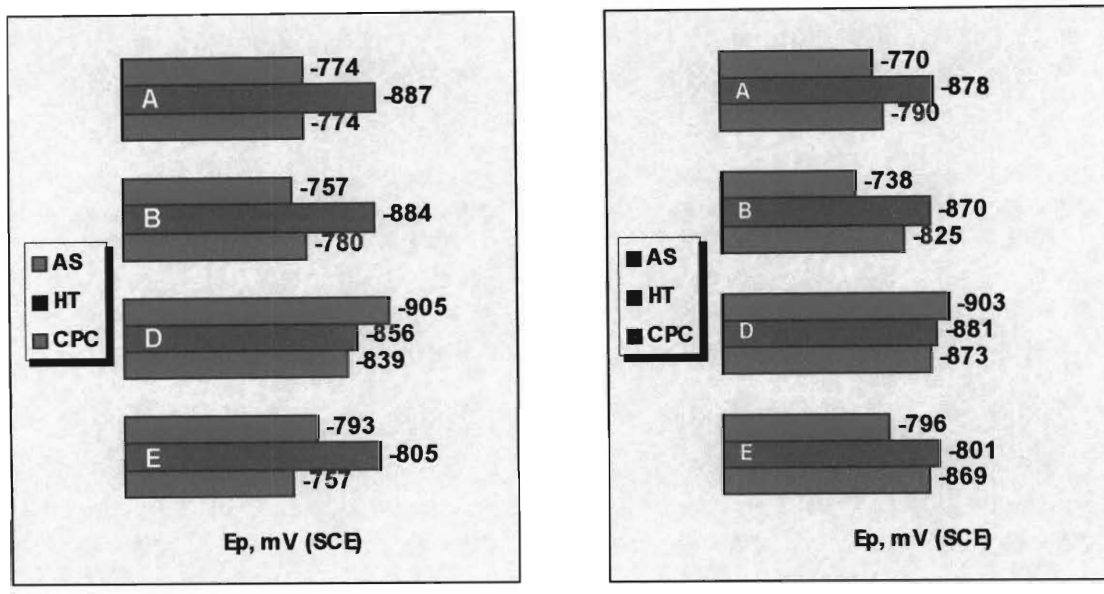

(a) **(b)**

Figure 4.63 E_p values in 1M NaCl + 0.5M H_2SO_4 for the AS, HT and CPC samples A, B, D and E at sweep rates of (a) 1 mV/s and (b) 5 mV/s.

Thermal treatment of AS samples A and B caused the E_p values to become substantially more negative. Heat treatment of AS sample D on the other hand caused a slight increase in E_p to more positive potentials. The effect of heat treatment on the value of E_p for AS sample E was again negligible.

Composite Powder coating resulted in more positive E_p values compared with the HT samples. This difference in E_p observed between the HT and CPC samples A, B and E was larger than that observed between the HT and CPC sample D.

The addition of sulfuric acid to the solution containing chloride ions caused for various changes in E_p of the alloy samples and depended on the type of treatment the alloy sample had been exposed to. The AS samples all showed a slight decrease in the value of E_p. The effect of sulfuric acid on E_p of the HT samples depended on the alloy composition. The E_p values of AS samples A and B were not effected by heat treatment, whilst HT samples D

and E showed more negative values of E_p. E_p values of the CPC samples had changed to considerably more positive potentials in the presence of sulfuric acid.

4.2.2.3 Pitting potential measurements in 1M NaCl + 0.5M H_2SO_4 + 0.5M $NaNO_3$

The values of E_p of the AS, HT and CPC samples A, B, D and E obtained in the solution containing chloride ions, sulfuric acid and nitrate ions at sweep rates ranging from 1 mV/s to 25 mV/s are shown in Figure 4.64. The detailed results are reported in Appendix A, Table III.

The effect of sweep rate on E_p of the AS samples is shown in Figure 4.64(a). For AS samples A, B and E, E_p became more positive as the sweep rate increased. AS samples A and E displayed a slight increase in E_p of about 20 mV, the increase in E_p being even less for AS sample B. E_p of AS sample D was not affected by sweep rate.

The effect of thermal treatment on E_p of the AS samples is shown in Figure 4.64(b). HT sample A showed a very small increase in E_p with increasing sweep rate, whilst HT sample B showed a slight decrease in E_p. For HT samples D and E, the value of E_p was not influenced by increasing sweep rates.

The effect of Composite Powder coating on E_p is shown in Figure 4.64(c). The CPC samples again showed more positive E_p values at a sweep rate of 1 mV/s. At higher sweep rates, E_p for the CPC samples again became more negative with increasing sweep rate. CPC samples A and D showed a consistent decrease in E_p, while the decrease in E_p for CPC samples B and E was smaller.

The multiple anodic polarisation curves obtained for the AS, HT and CPC samples in the solution containing chloride ions, sulfuric acid and nitrate ions were very similar to those obtained in the other electrolyte solutions, and some selected examples of these curves are given in Appendix B, Figure I.iii. The values of E_p obtained after each successive sweep are recorded in Appendix A, Table III. The general trend was again for E_p to increase somewhat after each successive sweep, the increase being larger for the CPC samples.

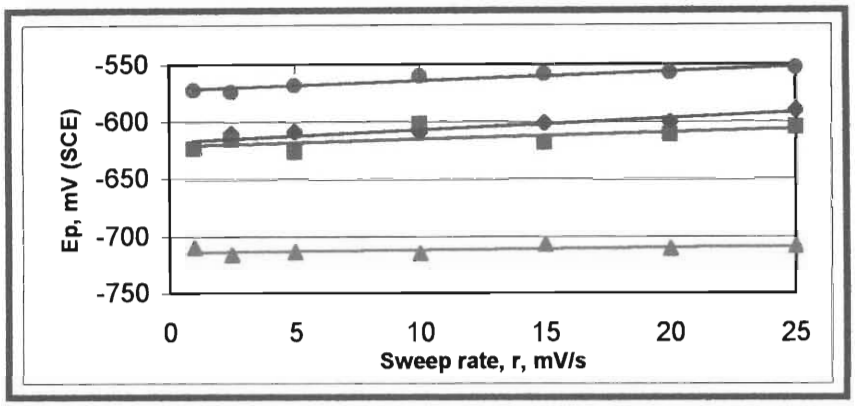

(a)

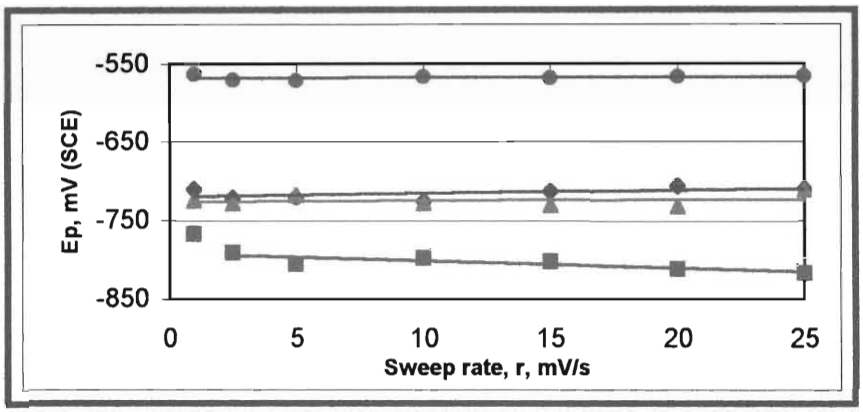

(b)

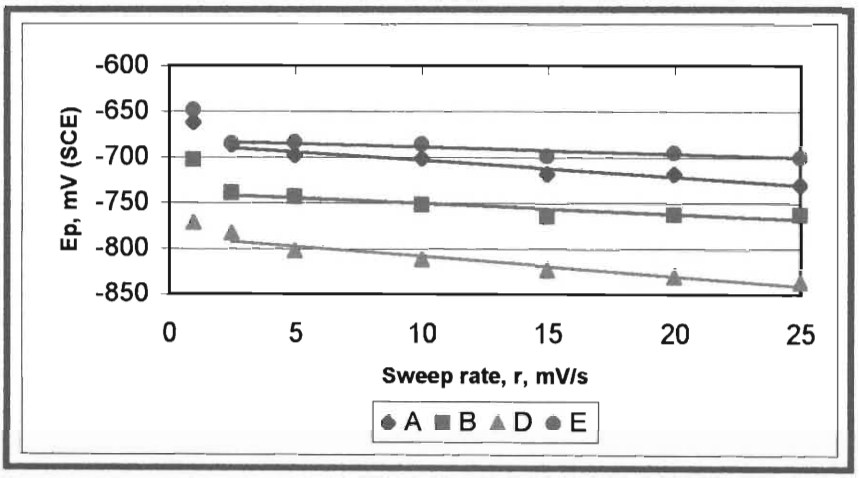

(c)

Figure 4.64 The effect of sweep rate on E_p of alloy samples A, B, D and E in the (a) AS, (b) HT and (c) CPC forms, exposed to 1M NaCl + 0.5M H_2SO_4 + 0.5M $NaNO_3$.

E_p values for the AS, HT and CPC samples A, B, D and E when exposed to a solution containing chloride ions, sulfuric acid and nitrate ions at sweep rates of 1mV/s and 5 mV/s are summarised in the bar graphs in Figure 4.65.

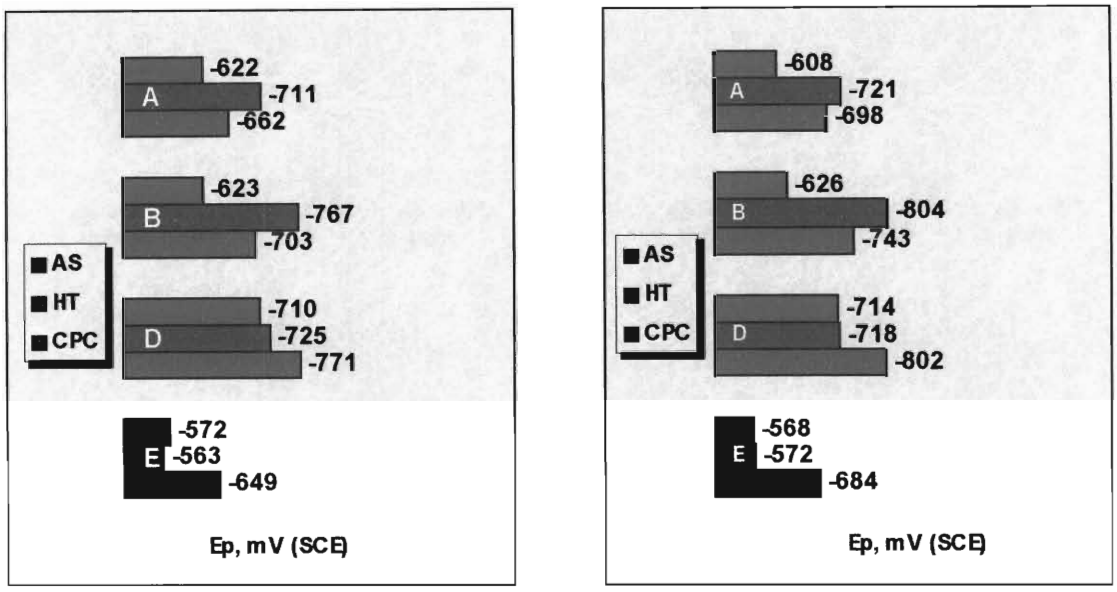

(a) **(b)**

Figure 4.65 E_p values in 1M NaCl + 0.5M H_2SO_4 + 0.5M $NaNO_3$ for the AS, HT and CPC samples A, B, D and E at sweep rates of (a) 1 mV/s and (b) 5 mV/s.

The effect of thermal treatment on E_p of the AS samples varied with the chemical composition of the AS samples. Heat treatment of AS samples A and B resulted in E_p values that were again significantly more negative. For AS samples D and E, heat treatment had little effect on the value of E_p.

Composite Powder coating resulted in more positive E_p values for CPC samples A and B, whilst more negative E_p values were obtained for CPC samples D and E.

The addition of nitrate ions to the solution containing chloride ions and sulfuric acid resulted in a large increase to more positive pitting potentials for the AS, HT and CPC samples.

5 DISCUSSION

5.1 MICROGRAPHIC DISCUSSION

5.1.1 MICROSTRUCTURE OF THE 'AS-SUPPLIED' SAMPLES

5.1.1(a) Solid solution composition and microstructural intermetallic phases

The microstructure of an aluminium alloy is determined by its chemical composition, its thermal history and fabrication procedures. In aluminium alloys, alloying elements may be present as solid solutions with aluminium, or as microstructural intermetallic phases such as: micro-constituents comprising the element itself, e.g. Si; microstructural intermetallic phases between one or more elements and aluminium, e.g. Al_2CuMg; or as microstructural intermetallic phases between one or more elements, e.g. Mg_2Si. Any or all of the above conditions may exist in the aluminium alloy.

AS samples A and B are the well-known aluminium alloy AA 3003 and information on their microstructure is available. Since AS samples D and E are supplier specific aluminium alloys and only their chemical compositions have been supplied, plausible assumptions have to be made as to the possible composition of the solid solution and microstructural intermetallic phases that may exist. These assumptions are based on previous work for aluminium alloys containing the same alloying elements present in different proportions. The elemental percentages obtained from EDX surface analysis could not be used to help establish the solid solution composition since EDX analysis is taken of the entire surface area and therefore includes both the solid solution and microstructural phase compositions. EDX results taken of microstructural intermetallic phases in the alloys could not be used to determine the exact nature of these phases, as explained in Section 4.1.1(a).

The chemical composition of AS samples A, B, D and E as supplied by the manufacturer are given in Table 3.1 in Section 3.1. The manufacturing process of the AS samples was aimed to achieve uniformity of the sizes of possible microstructural intermetallic phases as well as their distribution, and to achieve uniformity of the grain size. Cross-sectioned micrographs of the uncorroded AS samples were very similar, as shown in Figures 4.1 and

4.2 in Section 4.1.1(a). The uncorroded surfaces of AS samples A and D differed somewhat from the uncorroded surfaces of AS samples B and E, and these differences arise because of the different thickness' these alloy samples have been cold-rolled to.

AS samples A and B contain, in decreasing order of weight percentage, the alloying elements Mn>>Fe>Si>>Cu>>Mg. The dominant microstructural intermetallic phases present in alloy AA 3003 were reported as $(Mn,Fe)Al_6$ and $(Fe,Mn)_3SiAl_{12}$ [12, 54, 55]. Some of the Mn present remains in solid solution and could also be found as submicroscopic particles of precipitate [12, 54, 55]. It is probable that the very small amounts of Cu and Mg present exist as part of the solid solution or as submicroscopic particles of precipitate dispersed uniformly throughout the matrix [12, 54, 55]. The tempers of AS samples A and B differ only slightly. The designated temper of AS sample A is H17 while the designated temper of AS sample B is H18. Both AS samples have been strain hardened, which increases the strengthening arising from solid solution and dispersion hardening, and is a natural consequence of most working and forming operations on aluminium alloys [54]. The difference in tempers of AS samples A and B lies in the amount of cold working the alloy sample has been subjected to. AS sample B has been severely cold-worked and is in a fully hard condition that is equal to a 75% reduction in original cross-sectional area. AS sample A is about 87% hard conditioned. The strain hardened H tempers have not been subjected to annealing or ageing practices after cold rolling.

AS sample E contains, in decreasing order of weight percentage, the alloying additions Mn>Cu≈Fe>Si>Mg, and has a designated temper H14. Likely microstructural intermetallic phases present in AS sample E are $(Mn,Fe)Al_6$, $(Fe,Mn)_3SiAl_{12}$, Mg_2Si, $CuAl_2$, Al_2CuMg and Al-Cu-Fe compounds [54, 55]. It is likely that some of the Mn, Cu, Mg and the Mg_2Si phase will be present in the solid solution because of their relative solubility in aluminium, or as submicroscopic particles of precipitate dispersed uniformly throughout the matrix [12, 55]. The H14 temper indicates that AS sample E has been cold worked to the 50% hard condition.

AS sample D contains, in decreasing order of percentage, the alloying elements Mn≈Zn>>Si>Fe>>Cu. Likely microstructural intermetallic phases present in AS sample D are $(Mn,Fe)Al_6$ and $(Fe,Mn)_3SiAl_{12}$. Most of the Zn and some of the Mn and Cu will be

present in the solid solution because of their relative solubility in aluminium [12, 55]. It is likely that some of the Zn, Mn and Cu will also be present as submicroscopic particles of precipitate dispersed uniformly throughout the matrix. During fabrication, AS sample D has been cold-rolled to get to its required thickness of 100 μm. The reduction in original cross-sectional area was not reported on, hence the designated as fabricated or F temper.

Additional information on the microstructure of the AS samples is provided by looking at the nature and extent of corrosion of the AS samples exposed to the acidified chloride solution. This is because these solutions are best suited to reveal the susceptibility of an aluminium alloy to localised corrosion [123] and will be discussed in Section 5.1.4.2(a). Open circuit potential (OCP) measurements will provide more information about the solid solution composition of the AS samples, and will be discussed in Section 5.2.1.1(a).

5.1.1(b) Grain size and shape

A typical grain structure of the AS samples is shown in Figure 4.8 in Section 4.1.1(c). All AS samples show an elongated deformed stringing grain that has the appearance of long flat platelets. The grains are forced in this position by the cold-rolling working process the samples have been exposed to during manufacturing, and the direction of the grains corresponds to the direction of applied effort. The microstructural intermetallic phases present are aligned as stringers along the direction of working.

5.1.2 THE EFFECT OF HEAT TREATMENT ON THE ALLOY MICROSTRUCTURE

Heat treatment affects the microstructure of the aluminium alloy and the most noticeable changes observed are:

(i) A change in solid solution composition and microstructural intermetallic phases.
(ii) Recrystallisation of the grains resulting in an increase in grain size and shape.
(iii) Clearly defined grain boundaries.
(iv) A softer more malleable metal structure.
(v) A thicker oxide layer.
(vi) A dull non-metallic shine of the surface.
(vii) A general increase in susceptibility to corrosion.

5.1.2(a) The effect of heat treatment on the solid solution composition and microstructural intermetallic phases

It is well documented that heat treatment and subsequent ageing of aluminium alloys leads to decomposition of the solid solution and increased precipitation of microstructural intermetallic phases. The various changes in solid solution composition and microstructural intermetallic phases are a function of the alloying additions present, the thermal history and fabrication procedures, and the exact thermal profile that the aluminium alloy has been subjected to during brazing. Alloying elements with low diffusion rates and a low solubility in aluminium, such as Fe, Mn and Si, generally precipitate out of solid solution during heat treatment to form microstructural intermetallic phases [12, 43, 46, 55]. Alloying elements with high diffusion rates and a high solubility in aluminium, such as Zn and Mg and to a lesser extent Cu, are also depleted from the solid solution during heat treatment. These alloying elements can precipitate from the solid solution to form microstructural intermetallic phases or form localised concentrated areas or clusters of these elements by 'uphill diffusion' in the solid solution [8, 9, 12-15, 22, 30, 31, 54, 55]. Diffusion of the alloying elements in the solid solution also results in enrichment of these elements in grain boundary regions during heat treatment [15, 30, 49].

Cross-sectioned micrographs and surface micrographs of the uncorroded HT samples A, B, D and E are shown in Section 4.1.1(a), and were very similar in appearance to those of the AS samples. It was impossible to tell from these micrographs whether the number and size of microstructural intermetallic phases had increased or not during heat treatment. Only the uncorroded HT sample E revealed a surface microstructure different to that of AS sample E, as shown in Figure 4.3(c) in Section 4.1.1(a).

Likely microstructural phase changes and solid solution compositional changes that occur during heat treatment are now discussed for HT samples A, B, D and E. These changes are discussed in terms of the probable solid solution composition and microstructural intermetallic phases present in the AS samples, as discussed in Section 5.1.1. Heat treatment of the AS samples to some extent destroys the uniformity of the microstructural phase size and distribution as well as the uniformity of the grain size.

Heat treatment of AS samples A and B causes a transformation from the $(Mn,Fe)Al_6$ phase to the $(Fe,Mn)_3SiAl_{12}$ phase by a delayed peritectic reaction [54]. It is likely that some Mn, Cu and Mg diffuse through the solid solution and localise as clusters in the solid solution and grain boundary regions, possibly precipitating out of solid solution on cooling forming the possible microstructural intermetallic phases $CuAl_2$ and $Cu_2Mn_3Al_{20}$. Mg-containing microstructural intermetallic phases are less likely to form because of the extremely small percentage of Mg present in AS samples A and B.

Heat treatment of AS sample E dissolves much of the Cu and Mg but leaves some of the Al_2CuMg and $CuAl_2$ that is present out of solid solution. It is likely that Cu, Mg and Mn diffuse through the solid solution matrix, localising as concentrated clusters in the matrix and grain boundary regions, where they may or may not precipitate on cooling as the possible microstructural intermetallic phases Al_2CuMg, $CuAl_2$ and $Cu_2Mn_3Al_{20}$ dispersoids. Figure 4.3(c) shows large lightly coloured localised areas or clusters on the surface of HT sample E. It is highly probable that the difference in colour between the clusters and aluminium matrix is due to the oxides CuO and MgO. The $(Mn,Fe)Al_6$ phase may undergo a transformation to the $(Fe,Mn)_3SiAl_{12}$ phase, and both these phases, which are virtually insoluble, may undergo a further transformation to Al_7Cu_2Fe, possibly accompanied by other minor phases.

Heat treatment of AS sample D causes a transformation from the $(Mn,Fe)Al_6$ phase to the $(Fe,Mn)_3SiAl_{12}$ phase. It is likely that the Zn, Cu and Mn diffuse through the solid solution matrix and localise as concentrated clusters in the matrix and grain boundary regions. Cooling results in the precipitation of the possible microstructural intermetallic phases $CuAl_2$ and $Cu_2Mn_3Al_{20}$. The Zn is likely to stay in solid solution, probably as localised clusters, thereby depleting the solid solution to a certain extent.

Additional information on the microstructure of the HT samples is provided by looking at the nature and extent of corrosion of the HT samples exposed to the acidified chloride solution. The pattern of diffusion of alloying elements through the matrix by localising as concentrated clusters in the matrix and grain boundary regions should be revealed and will be discussed further in Section 5.1.4.2(a). Open circuit potential (OCP) measurements will provide more information about the solid solution composition of the HT samples, and will be discussed further in Section 5.2.1.1(b).

5.1.2(b) The effect of heat treatment on the grain size and shape

The most noticeable effect of heat treatment was the change in grain size as shown in the optical micrographs of etched cross sections of the HT samples in Section 4.1.1(c). The HT samples showed large, spherical grains with clearly defined grain boundaries. The increase in grain size causes a corresponding decrease in the total surface area of the alloy sample, which is due to recrystallisation of the grains and can be explained as follows. The grains expand and spheridise to release built up energy due to mechanical strain forced on the grain structure of the AS samples. The thermodynamically most stable grain and crystal lattice structure is reached within the restrictions that are imposed by the heating profile.

Recrystallisation of the grains results in more space between the individual grains thereby weakening the crystal lattice structure and revealing clearly defined grain boundaries. This accounts for a certain loss in rigidity of the metal, which was observed when physically handling the samples, revealing a softer and more malleable metal. In other words the hardness and strength of the metal is partly lost due to heat treatment. After heat treatment, HT sample E showed a slightly harder and less malleable metal structure than HT samples A, B and D. A possible explanation is that some of the Mg and Si present as alloying

elements in HT sample E exists as particles of $MgSi_2$, which are known to strengthen aluminium alloys [47, 55].

5.1.2(c) The effect of heat treatment on the surface oxide

Heat treatment of the AS samples results in an increase in oxide content which was confirmed by EDX analysis [Section 4.1.1(a), Table 4.2]. A rapid increase in aluminium oxide with the application of heat has previously been reported [2, 74, 99], and at temperatures greater than 500°C, the oxide film can reach a thickness of about 200 Å. The oxide that is formed under these conditions is the amorphous aluminium hydroxide, $Al(OH)_3$. The thicker oxide layer results in a dull non-metallic appearance of the surface of the HT samples. HT sample E showed the highest increase in oxide that is most likely due to the increase in Cu at its surface, which is reported to enhance formation and growth of the aluminium oxide [33].

5.1.3 THE EFFECT OF COMPOSITE POWDER COATING ON THE ALLOY MICROSTRUCTURE

Composite Powder is a unique powdered filler material used for brazing aluminium alloys and consists of an atomised Al-Si alloy cosprayed with a potassium alumino fluoride flux, $KAlF_4$. Deposition and adhesion of the Composite Powder on the base alloy substrate is achieved using an acrylic resin (pmma). The presence of fluoride ions in the flux inhibits the formation of a stable oxide on the surface of Composite Powder particles, thereby making them more reactive under the brazing conditions. Composite Powder containing 12% flux and 11% Si in the Al-Si filler alloy results in optimum surface wettability and spreading of the molten filler material on the base alloy substrate during heat treatment, as reported by Hawksworth [2]. A Composite Powder coating of 70 g/m^2 was found to be sufficient for brazing of aluminium radiators.

During heat treatment the acrylic pmma resin used as an adhesive decomposes and is completely removed from the component surface at a temperature considerably lower than that at which the brazing process occurs. The reactivity of the Composite Powder with the base alloy substrate depends on the effective dissolution of the surface oxide by the flux. The mechanism by which the flux reacts with the surface oxide covering the base alloy during brazing is not well documented and is assumed to be one of dissolution in which a series of ionic species are produced in the molten flux [2]. Once the surface oxide is removed, the molten Al-Si filler alloy wets the base alloy surface and allows for spreading or flowing of the molten Al-Si filler alloy on the base alloy substrate by capillary action. The wetting and flowing actions are strongly influenced by interfacial reactions between the different phases involved [2].

Heat treatment of the CPC samples results in a multi-layered structure consisting of four distinct layers, as described in detail in Section 4.1.1(b). These layers are listed below:

(a) A surface layer consisting of residual flux and partially reacted Composite Powder;
(b) An eutectic Al-Si melt layer including eutectic Al-Si diffusion zones containing $(Fe,Mn)Al_6$ microstructural intermetallic phases;
(c) An α-Al filler metal layer;
(d) The underlying base aluminium alloy.

The structure of the Al-Si melt layer that forms depends on the cooling rate. The relatively slow cooling rates employed result in a eutectic microstructure that consists of cells of α-Al surrounded by rods of eutectic β-Si. The whole array of seemingly separate rods are actually interconnected and together constitute a grain of Si phase [126].

Some alloying between the Composite melt layer and base alloy occurs during heat treatment by molten Al-Si filler metal diffusion into the base alloy and/or dissolution of the base alloy into the molten Al-Si filler metal [2]. This results in dilution of the base alloy and a slight loss of its thickness, and alloying element enrichment of the Composite melt layer. The rest of the base alloy is similar in composition and microstructure (i.e. grain size and shape [Section 4.1.1(c)], solid solution composition, microstructural intermetallic phases) to that of the HT samples.

5.1.4 THE NATURE AND EXTENT OF CORROSION OF ALUMINIUM ALLOYS IN VARIOUS CORROSIVE ELECTROLYTE SOLUTIONS

5.1.4.1 1M NaCl

5.1.4.1(a) 'As-supplied' and 'heat-treated' samples

AS samples A, B and E immersed for 60 minutes in a 1M NaCl solution of pH 4.06 showed minimal visible surface corrosion [Section 4.1.2(a)]. AS sample D and the HT samples showed some surface corrosion in the form of localised galvanic cell corrosion and general shallow surface dissolution. AS and HT samples A, B and D all showed an increase in percentage oxide on the surface after corrosion, whereas AS and HT samples E showed a decrease in oxide present [Section 4.1.2(a), Table 4.5].

The minimal corrosion observed in 1M NaCl could be explained by the lack of hydrogen ions present at a pH of 4.06. According to Pourbaix diagrams of the Al-H_2O system, a pH of 4.06 lies just inside the passivity range of aluminium [80, 104, 107]. A high concentration of hydrogen ions is necessary if oxide dissolution is to be observed. Thinning of the oxide is further aided by adsorption of chloride ions through the formation of chloride containing complexes [40, 42, 61, 66, 69-71, 113], although this is also retarded under near neutral conditions. At near neutral pH values, oxide formation is dominant and results from adsorption of hydroxide ions and dissolved oxygen on the exposed alloy surface, resulting in a thicker oxide layer.

Corrosion by chloride ions is primarily initiated in places where a potential difference is established between the aluminium solid solution and microstructural intermetallic phases dispersed within the solid solution matrix, resulting in galvanic cell corrosion. Chloride ions are adsorbed at the active sites and aid dissolution of the oxide and corrosion of the bare aluminium surface. The more reactive metal or microstructural phase (the most active or anodic on the galvanic corrosion scale) corrodes preferentially, and hydrogen evolution occurs on the most cathodic species. The visible effects of this corrosion are trenches and cavities that have formed around the periphery of the microstructural intermetallic phases in the aluminium alloy matrix. Flaws in the oxide layer such as scratches and ridges

formed by the cold rolling process are also preferential sites for corrosion initiation [7, 13, 40, 61, 83, 85, 110, 127].

The thicker oxide layer present initially on the HT samples did not provide better corrosion protection of the HT samples. This is because the amorphous aluminium oxide layer formed during heat treatment is more porous compared with the oxide layer originally present on the AS samples, which has aged and crystallised with time to form a tightly bound oxide film.

HT samples A, B and E are more susceptible to corrosion than AS samples A, B and E. The formation of clusters of alloying elements in the solid solution and increased precipitation of microstructural intermetallic phases during heat treatment results in stronger and a larger number of galvanic corrosion cells at the surface of the HT samples, and is thus responsible for the increase in corrosion observed. The AS and HT samples D showed a similar extent of corrosion, which is possibly due to the sacrificial nature of the Zn present.

The percentage oxide present after corrosion appears to be influenced by the composition of the alloy sample rather than the composition of the NaCl solution. Cu present in AS and HT samples E provides sites for the cathodic reduction of water, oxygen and hydrogen ions, thereby accelerating dissolution of the aluminium oxide.

5.1.4.1(b) 'Composite Powder coated' samples

The formation of various sized oxide deposits on the residual flux and partially reacted Composite Powder was the most noticeable form of corrosion observed on CPC samples A, B and E after 60 minutes of immersion in a 1M NaCl solution [Section 4.1.2(b)]. The CPC samples showed a decrease in potassium and fluoride content, an increase in Si and a very large increase in oxide [Section 4.1.2(b), Table 4.6]. CPC sample D had been the most severely corroded of the four CPC samples, exposing the eutectic Al-Si melt layer. CPC sample D showed a very large decrease in potassium and fluoride content, a small increase in oxide and a very large increase in Si, when compared with CPC samples A, B and E. The extent of corrosion increased along the series A<B<E<D.

The decrease in potassium and fluoride content indicates dissolution of the flux layer. It has been reported that when the potassium alumino fluoride flux is exposed to water and mechanical work, either in solution or at a high humidity, the following reaction occurs [128]:

$$2KAlF_4 + 3H_2O = 2KF + Al_2O_3 + 6HF$$

The solubility of Nocolok^{TM} flux in water is 0.5g/100ml [2]. It is therefore plausible to assume that the flux dissolves in a similar way when exposed to the 1M NaCl solution. Dissolution of the residual flux therefore reveals more partially reacted Composite Powder.

For CPC samples A, B and E, exposure of more partially reacted Composite Powder explains the slight increase in Si observed, since partially reacted Composite Powder consists of Si in solid solution with α-Al. For CPC sample D, almost all of the residual flux had dissolved and most of the partially reacted Composite Powder had corroded, exposing the eutectic Al-Si melt layer thus explaining the much larger increase in Si content.

Corrosion of the partially reacted Composite Powder on CPC samples A, B and E results in formation of surface oxide deposits that account for the very large increase in oxide content of these alloy samples. In the regions where a considerable amount of partially reacted Composite Powder had corroded, microstructural intermetallic phases of $(Fe,Mn)Al_6$ were exposed, creating initiation sites for preferential galvanic corrosion of the α-Al by chloride ions. Once pitting of the partially reacted Composite Powder is initiated, pit propagation allows chloride ions to penetrate deeper, and into the underlying eutectic Al-Si melt layer below. Corrosion of the eutectic Al-Si melt layer can be explained as follows. After pit initiation, pit propagation is rapid because of the large difference in potential between the anodic α-Al and significantly more cathodic rods of β-Si, resulting in preferential corrosion of the α-Al.

The anodic character and potential of the base alloy in a CPC sample is mainly determined by the chemical composition of the respective HT sample. The α-Al in the eutectic Al-Si melt layer and the α-Al filler metal layer, which is in electronic contact with the base alloy, will be strongly influenced by the potential of the base alloy. Consequently, the anodic

base alloy accelerates pit propagation and galvanic corrosion of the eutectic Al-Si melt layer by chloride ions. The extent of corrosion of the eutectic Al-Si melt layer of CPC samples A, B and E is limited because of the mildly aggressive electrolyte conditions and can be explained by the lower concentration of hydrogen ions present at a pH of 4.06. CPC sample D showed more severe corrosion of the eutectic Al-Si melt layer. This can be explained by the presence of anodic Zn in the base alloy, which strongly influences the potential of the α-Al in the eutectic Al-Si melt layer, thereby accelerating the overall corrosion process.

5.1.4.2 1M NaCl + 0.5M H_2SO_4

5.1.4.2(a) 'As-supplied' and 'heat-treated' samples

AS samples A, B, D and E immersed for 60 minutes in a 1M NaCl + 0.5M H_2SO_4 solution of pH 0.52 showed 'delocalised' crystallographic pitting on localised regions of the exposed surface area, consisting of coalesced pits rather than individual pits [Section 4.1.3(a)]. HT samples A, B, D and E showed localised crystallographic pitting corrosion consisting of many clearly defined individual pits [Section 4.1.3(a)]. Intergranular corrosion was observed on all HT samples and was most severe for HT sample E. The extent of corrosion on both the AS and HT samples increased along the series A<B<E<D. AS and HT samples A, B and D all showed an increase in percentage surface oxide after corrosion, whilst AS and HT samples E again showed a decrease in surface oxide present after corrosion [Section 4.1.3(a), Table 4.7].

The addition of sulfuric acid to the solution containing chloride ions results in a higher concentration of hydrogen ions (pH = 0.52) that form a synergistic relationship with the chloride ions. The hydrogen ions aid the pitting process of chloride ions by accelerating dissolution of the aluminium oxide layer, thereby exposing bare aluminium alloy surface. The exposed aluminium alloy then attracts chloride ions towards its surface and initiates the chloride ion pitting process. Pitting propagates rapidly due to the continuous removal of oxide and results in the formation of crystallographic pits, as observed on the micrographs of the corroded AS and HT samples. The sulfate and bisulfate ions present in solution act mainly as spectator ions and participate very little in the corrosion process of

AS and HT samples A, B and D. Some of the sulfate ions do however complex with the aluminium oxide layer, forming complexes such as $AlSO_4^+$, $Al(OH)SO_4$ and $[Al(OH)_2]_2SO_4$ [71, 101, 114]. In the presence of a fair amount of Cu, sulfate ions are reported to become aggressive and aid the corrosion process of Cu containing aluminium alloys [48].

Crystallographic pits arise from chloride ions pitting the aluminium alloy surface along a preferred crystallographic direction in the lattice. Inside the pits, the base and sides were composed of facets and steps which are usually reported to be characterised by {100} planes and <100> directions [17, 25, 34, 59, 112], although other directions such as <011>, <001> and <111> have also been reported for aluminium alloys [51]. The nature of the crystallographic pits formed, as well as the direction in the crystal lattice along which the pits are formed, depends on the thermal history and composition of each alloy sample. Heat treatment of the AS samples changes their grain and crystal lattice structure and thus allows for more directional crystallographic pitting of the HT samples.

AS samples A, B, D and E showed 'delocalised' crystallographic pitting on localised regions of the exposed surface area, resulting in a 'crumbling concrete' appearance of the corroded areas on AS samples D and E. Strictly speaking, this pitting is localised but since it is difficult to recognise individual pits in the corroded areas, the corrosion is referred to as delocalised. This nature of corrosion is observed because the alloying elements, present either in solid solution or as microstructural intermetallic phases, are spread out more uniformly, i.e. delocalised, in the solid solution matrix of the AS samples. HT samples A, B, D and E all showed localised crystallographic pitting consisting of clearly defined individual pits. This nature of corrosion is observed because of uphill diffusion and increased precipitation of the alloying elements resulting in highly concentrated and localised areas or clusters of these elements in the solid solution matrix of the HT samples.

The increase in grain size and presence of grain boundaries in the HT samples makes it easier for chloride ions to penetrate the aluminium matrix. This in turn increases the susceptibility of the HT samples to intergranular corrosion since intergranular corrosion results from selective corrosion at grain boundaries or any precipitate free zones that may have formed adjacent to them [49, 55]. The extent of intergranular corrosion observed depends on the amount and type of alloying element enrichment at the grain boundaries,

the dispersion of these alloying element particles, as well as the interparticle spacing (a minimum connectivity between particles being favourable) [9, 30, 55].

Intergranular corrosion of the HT samples increased along the series A<B<D<E, and was considerably less for HT samples A and B. This is related to the amount and type of alloying element enrichment at the grain boundaries. Enrichment of Fe, Mn and Si at the grain boundaries occurs on a much smaller scale than grain boundary enrichment of Zn, Cu and Mg. This is determined by the solubility and diffusion rates of the alloying elements in the aluminium solid solution. Fe, Mn and Si have a low solubility and low diffusion rates in aluminium and therefore slightly enrich grain boundaries. Grain boundary enrichment of Cu, Mg or Zn will be much higher because of the high diffusion rates and a higher solubility of these elements in aluminium. Grain boundaries enriched in Fe, Mn and Si will have potentials similar to that of the aluminium matrix and will therefore not induce strong galvanic corrosion cells at which intergranular corrosion can be initiated [8, 12, 29, 55]. Grain boundary enrichment of Zn, Cu and Mg will set up stronger galvanic corrosion cells because of the larger potential difference between these microstructural intermetallic phases and the aluminium solid solution [8, 9, 12-14, 29, 30, 55]. Aluminium alloys containing a higher percentage of Zn, Cu and Mg will therefore show a greater amount of intergranular corrosion, as was observed.

Intergranular corrosion was more severe for HT sample E than HT sample D, and resulted in deeper grooves at the surface of HT sample E. This can be explained in terms of the potential difference between the grain boundaries and grain interiors. Since Zn is more soluble in the aluminium matrix than either Cu or Mg, a smaller potential difference will exist between the grain boundary regions and the grain interior of HT sample D. HT sample E on the other hand will contain less Cu and Mg in the aluminium solid solution and a larger potential difference will exist between the grain boundaries and grain interior. Corrosion of Cu rich grain boundaries by sulfate ions will be restricted because of the large size of the sulfate ions, which explains the larger amount of intergranular corrosion observed at the surface of HT sample E compared with that found below the surface.

The overall extent of corrosion of the AS and HT samples exposed to the solution containing sulfuric acid and chloride ions increased along the series A<B<E<D. This increase in extent of corrosion is a result of the difference in potential between the

microstructural intermetallic phases and/or localised concentrated clusters of the alloying elements and the aluminium matrix. The greater the difference in potential between these phases and the aluminium matrix, the greater the extent of corrosion of the most anodic species. The percentage of each alloying addition present further influences the extent of corrosion observed.

Alloy samples A and B have an almost identical chemical composition and differ only in thickness. The dominant microstructural intermetallic phases of alloy samples A and B are $(Mn,Fe)Al_6$ and $(Fe,Mn)_3SiAl_{12}$, which are similar in potential to the aluminium matrix [8, 12, 29, 55]. These microstructural intermetallic phases are also found in alloy samples D and E. Alloy sample E contains a much higher percentage of Cu and Mg than alloy samples A, B and D. The phases containing Cu but no Mg are more cathodic to the aluminium matrix [8, 14, 29, 40, 42, 47, 51, 55], thereby promoting corrosion of the aluminium matrix. The phases containing Mg are always more anodic than the aluminium matrix and are therefore corroded preferentially to the aluminium matrix [8, 29, 55]. Alloy sample E therefore shows a greater amount of corrosion than alloy samples A and B. Alloy sample D contained the highest percentage of Si, Fe and Mn, in addition to a relatively high percentage of Zn. The Zn containing phases present in alloy sample D are considerably more anodic to aluminium [8, 13, 22, 29, 55] and corrode preferentially. Alloy sample D therefore shows the most severe corrosion of all the alloy samples.

The percentage oxide present after corrosion appears to be influenced by the composition of the alloy sample rather than the addition of sulfuric acid to the solution containing chloride ions. Cu present in alloy sample E again accelerated aluminium oxide dissolution by providing sites for the cathodic reduction reactions.

5.1.4.2(b) 'Composite Powder coated' samples

CPC samples A, B, D and E immersed for 60 minutes in a 1M NaCl + 0.5M H_2SO_4 solution showed dissolution of all the residual flux and entire corrosion of the partially reacted Composite Powder [Section 4.1.3(b)]. About 60% of the eutectic Al-Si melt layer of CPC sample A had corroded, compared with the entire eutectic Al-Si melt layer on CPC samples B, D and E. Total corrosion of the eutectic Al-Si melt layer exposes cells of α-Al in the α-Al filler metal layer that are separated by grain boundaries where corrosion of the

eutectic Al-Si diffusion zones had taken place. For CPC samples B, D and E, the entire α-Al filler metal layer was exposed, and corrosion of the base alloy below resulted. The extent of corrosion increased along the series A<B<E<D. Oxide deposits were found on CPC samples A, B and D but not on CPC sample E, and this is reflected in the EDX results [Section 4.1.3(b), Table 4.8]. The Si content on CPC sample A was very high, whilst the Si content of CPC samples B, D and E had decreased. The amount of eutectic Al-Si melt layer that corrodes appears to be inversely proportional to the Si content of the CPC samples.

The hydrogen ions present at a pH of 0.52 greatly accelerate dissolution of the residual flux and corrosion by chloride ions of the partially reacted Composite Powder. Within a very short period, bare eutectic Al-Si melt layer is exposed. Rapid corrosion of the eutectic Al-Si melt layer by chloride ions is accompanied by hydrogen evolution on the cathodic β-Si particles. The rate at which the eutectic Al-Si melt layer of the CPC samples corrodes is influenced by the composition of the base alloy. Complete corrosion of the eutectic Al-Si melt layer exposes the underlying α-Al filler metal layer. Further corrosion of the α-Al filler metal layer and base alloy is influenced by the composition of the base alloy, base alloy dissolution and molten filler metal diffusion, as well as the thickness of the base alloy.

CPC sample A showed the least amount of corrosion of the CPC samples, which was considerably less than that observed on CPC sample B having the same alloy composition. It is likely that the ultimate thickness of the base alloy influences the extent of corrosion observed. The thickness before Composite Powder treatment was 100 μm for CPC sample A and 300 μm for CPC sample B. Since both CPC samples A and B were coated with 70 g/m^2 of Composite Powder prior to brazing, it is not unreasonable to assume that base alloy dissolution and molten filler metal diffusion occurs in similar proportions during heat treatment. This results in a similar loss in base alloy thickness and alloying enrichment of the α-Al filler metal. The resulting base alloy of CPC sample B will therefore be 3 to 4 times thicker than the base alloy of CPC sample A. The anodic character of the base alloy in the thinner CPC sample A will thus be influenced more by diffusion and dissolution, resulting in a reduction in anodic character and hence less severe corrosion.

The nature of crystallographic corrosion of the α-Al filler metal layer differed for CPC samples B, D and E, and this can be attributed to increased dissolution of alloying elements from the base alloy into the molten filler metal during heat treatment. Localised enrichment of Fe, Mn and Si in the α-Al layer of CPC sample B was small and had very little influence on the nature of corrosion observed due to the similarity in potential between these phases and the α-Al solid solution. This explains why crystallographic corrosion of the α-Al filler metal layer of CPC sample B is limited to the regions that are in direct contact with the eutectic Al-Si melt layer. A higher enrichment of Cu and Mg as localised clusters in the α-Al filler metal layer of CPC sample E results in a larger potential difference between the more anodic microstructural clusters and the α-Al solid solution. Corrosion of the α-Al filler metal results in hollow areas spread out over several cells of the α-Al filler metal, exposing the base alloy. A high enrichment of Zn localised in the α-Al filler metal layer of CPC sample D results in a large potential difference between the Zn and α-Al solid solution, and accounts for the porous appearance of the α-Al cells that results from preferential corrosion of Zn particles.

The extent and nature of corrosion of the base alloys of CPC samples B, D and E is composition dependent, and follows the same explanation used to describe corrosion of the HT samples exposed to the same solution [Section 5.1.2.2(a)]. Since the more cathodic α-Al filler metal layer is in electronic contact with the more anodic base alloy, a galvanic corrosion cell will exist between them, resulting in accelerated corrosion of the base alloy.

The overall extent of corrosion of the alloys depends on the composition of the base alloy and dissolution of the alloying elements from the base alloy into the Composite melt during heat treatment. The greater the number of highly anodic or highly cathodic alloying elements in the base alloy and Composite melt, the greater the extent of corrosion observed.

5.1.4.3 1M NaCl + 0.5M H_2SO_4 + 0.5M $NaNO_3$

5.1.4.3(a) 'As-supplied' and 'heat-treated' samples

AS samples B, D and E immersed for 60 minutes in a 1M NaCl + 0.5M H_2SO_4 + 0.5M $NaNO_3$ solution of pH 0.48 all showed localised crystallographic pitting corrosion. AS sample A on the other hand had undergone only a small amount of galvanic cell corrosion [Section 4.1.4(a)]. HT samples A and B had experienced shallow surface thinning of most of the exposed sample surface. HT samples D and E had corroded more severely and showed localised pitting in addition to shallow surface thinning [Section 4.1.4(a)]. The extent of corrosion of both the AS and HT samples again increased along the series A<B<E<D. AS and HT samples A, B and D all showed an increase in the percentage of surface oxide after corrosion, whilst AS and HT samples E showed a decrease in oxide present after corrosion [Section 4.1.4, Table 4.9].

The addition of nitrate ions to the solution containing chloride ions and sulfuric acid results in a significant decrease in the severity of corrosion observed on the AS and HT samples. The inhibiting nature of nitrate ions that compete with chloride ions for adsorption sites on the aluminium alloy surface cause a reduction of the active centres on which chloride ions may initiate pitting while hydrogen ions are discharged [87].

The presence of nitrate ions is insufficient to completely inhibit corrosion of the AS and HT samples A and B. This is mainly because of a higher concentrationof hydrogen ions present in the solution at a pH of 0.48. The hydrogen ions still cause enough surface oxide dissolution to allow for some corrosion of AS and HT samples A and B by the chloride ions [50]. Another reason is that at low pH values, nitrate ions can act as cathodic depolarisers because of their kinetically facile reduction. The possible cathodic reactions that can occur under these conditions are [50, 87]:

$$O_2 + 2H_2O + 4e^- = 4OH^- \quad (5.2)$$

$$NO_3^- + H_2O + 2e^- = NO_2^- + 2OH^- \quad (5.3)$$

$$NO_2^- + 7H^+ + 6e^- = NH_3 + 2H_2O \quad (5.4)$$

The cathodic reactions of nitrate ions and nitrite ions will therefore serve to sustain the corrosion process in the absence of a continuous supply of oxygen.

Pitting of AS and HT samples D and E occurs because of the alloying element Zn in alloy sample D and Cu and Mg in alloy sample E. Preferential dissolution of these alloy samples may be attributed to the formation of $M(NH_3)_4^{2+}$ complexes, where M = Zn, Mg or Cu [87, 98]. The ammonia is formed by electrochemical reduction of nitrate ions according to reactions (5.2), (5.3) and (5.4).

The nitrate ions are therefore found to have two opposing effects on the corrosion of the AS and HT samples. The presence of alloying additions for which nitrate ions have a great affinity, such as Zn and Mg, and to a lesser extent Cu, thus determine the extent of corrosion of the alloy samples. The nitrate ions become aggressive instead of inhibiting in nature and aid the corrosion process in the vicinity of the microstructural intermetallic phases containing these alloying elements. Pitting by nitrate ions is more severe for alloy sample D because of a higher dissolution of the Zn containing ammonia complex compared with the Mg or Cu containing ammonia complexes [87].

The nature of pitting corrosion on AS and HT samples D and E in the presence and absence of nitrate ions in a solution of chloride ions and hydrogen ions differed. The size, shape and depth of the individual pits were larger, wider and shallower in the presence of nitrate ions. This is reported to be due to the large size of the nitrate ions [1, 83].

The overall extent of corrosion of the AS and HT samples exposed to the solution containing nitrate ions, sulfuric acid and chloride ions again increased along the series A<B<E<D. This occurs for the same reasons as described in Section 5.1.2.2(a) for the solution containing sulfuric acid and chloride ions.

The composition of the alloy samples appears to influence the percentage of surface oxide during corrosion rather than the presence of nitrate ions in a solution containing chloride ions and sulfuric acid. Cu present in alloy sample E is again responsible for accelerated aluminium oxide dissolution.

5.1.4.3(b) 'Composite Powder coated' samples

CPC samples A, B, D and E immersed for 60 minutes in a 1M NaCl + 0.5M H_2SO_4 + 0.5M $NaNO_3$ solution all showed complete dissolution of the residual flux and corrosion of the entire partially reacted Composite Powder [Section 4.1.4(b)]. This exposes the eutectic Al-Si melt layer on all four CPC samples and explains the large increase in Si from EDX analysis [Section 4.1.4(b), Table 4.10]. CPC samples A, B and E showed partial corrosion of the eutectic Al-Si melt layer, in some places exposing the α-Al filler metal. No corrosion of their base alloys was observed. Corrosion of the eutectic Al-Si melt layer of CPC sample D was much more severe. CPC sample D was the only alloy sample to show corrosion of the base alloy which in many places had perforated the full thickness of the sample. The extent of corrosion again increased along the series A<B<E<D.

The addition of nitrate ions to the solution containing chloride ions and sulfuric acid results in a significant decrease in the severity of corrosion of CPC samples A, B and E. Hydrogen ions still allow for complete dissolution of the residual flux and accelerated corrosion by chloride ions of the partially reacted Composite Powder. Corrosion of the eutectic Al-Si melt layer is inhibited to a large degree by the adsorption of nitrate ions to the surface. Pits are initiated by chloride ions in the α-Al adjacent to rods of β-Si and at microstructural intermetallic phases of $(Fe,Mn)Al_6$ exposed at the surface. Pit propagation results in the formation of small but deep pits in the eutectic Al-Si melt layer, leaving behind an interconnected network of β-Si particles suspended above the α-Al layer, forming oxide corrosion products with the aluminium ions that are then deposited on the surface. The interconnected network of β-Si becomes more noticeable as the extent of corrosion increases along the series A<B<E<D, which was not observed in the other electrolyte solutions. This suggests that nitrate ions adsorbed on the eutectic Al-Si melt layer prevent the interconnected network of β-Si rods from entering the solution. The eutectic Al-Si melt layer of CPC sample E had corroded slightly more than the eutectic Al-Si melt layer of CPC samples A and B. This is because of the influence of anodic Mg-Cu containing microstructural intermetallic phases in the base alloy of CPC sample E resulting in accelerated corrosion of the eutectic Al-Si melt layer.

The severity of corrosion of CPC sample D can be explained as follows. The presence of anodic Zn in the base alloy strongly influences the potential of the eutectic Al-Si melt

layer, and causes for rapid corrosion by chloride ions of the α-Al in the eutectic Al-Si melt layer. The presence of nitrate ions results in an interconnected network of β-Si particles suspended above the α-Al filler metal layer, covered with many large oxide corrosion products. Only on certain regions of the surface, cells of α-Al separated by grain boundaries are exposed in the α-Al filler metal layer. The electrolyte solution is then able to follow a path between the interconnected network of β-Si particles along the eutectic Al-Si diffusion zones to the base alloy below. Corrosion of the base alloy thus results. Chloride ions corrode the aluminium matrix while nitrate ions corrode localised areas containing Zn and Cu, which has been explained in Section 5.1.2.2(a). The presence of the interconnected network of β-Si rods results in a very strong galvanic corrosion cell with the base alloy, accelerating the corrosion process of the base alloy significantly. Perforation of the sample thickness results.

5.2 ELECTROCHEMICAL DISCUSSION

5.2.1 OPEN CIRCUIT POTENTIALS

OCP values are influenced by both chemical and electrochemical reactions that occur at the aluminium alloy surface/electrolyte solution interface due to corrosion of the alloy sample. The chemical composition and microstructure of the aluminium alloy determine its susceptibility to corrosion in a particular environment and the OCP measured at any time while immersed in this environment. The most important of these properties is the aluminium solid solution, which has a major influence on the OCP, while microstructural intermetallic phases present in the aluminium solid solution affect the OCP very little [8, 9, 22-24, 29]. The relative ranking of the OCPs of aluminium alloys having different chemical compositions in a galvanic series is dependent on the electrolyte solution in which the alloy is immersed. The relative rates of the anodic and cathodic reactions at the surface oxide film/electrolyte solution interface as well as the type, structure, thickness and conductivity of the surface oxide film, and the time of immersion, all effect the change in OCP with time [6, 7, 10, 13, 40, 42, 46, 60, 64, 82, 83, 100, 117].

5.2.1.1 Open circuit potential measurements in 1M NaCl

The 1M NaCl solution, with a pH of 4.06, was chosen as a reference solution to establish the effects of heat treatment and Composite Powder coating on the OCP, as this solution is only mildly aggressive and causes for a minimal amount of corrosion of the samples [Sections 4.1.2 and 5.4.1.1]. The OCP values obtained under these conditions will therefore be best suited to reveal the true character of the exposed aluminium alloy surface.

The affect of principal alloying elements present in the solid solution of high purity binary aluminium alloys on the OCP measured in 53 g/l NaCl plus 3 g/l H_2O_2 (aerated chloride solution) at 25°C are shown in Figure 2.9(a) in Section 2.2.2. The authors [8] observed that an increase in Mn and Cu resulted in considerably more positive OCPs while the addition of Si caused only a slight increase in OCP. The addition of Mg made the OCP slightly negative, while the addition of Zn caused a much larger decrease in OCP. Most aluminium alloys contain additions of one or more of these elements, and the effects of multiple elements in solid solution are approximately additive. The solubility of Fe in

aluminium is very small and Fe exists as microstructural intermetallic phases in aluminium [46, 55]. Fe-Al and Fe-Si-Al containing phases are more cathodic to the aluminium matrix, while the inclusion of Mn to these phases results in an OCP similar to that of the aluminium matrix [8, 9, 29, 55]. Similar results for the effect of principal alloying elements on the OCP have been reported elsewhere [8, 9, 13, 14, 22, 27, 29, 31, 40, 42, 43, 47, 51, 55, 85, 129].

5.2.1.1(a) 'As-supplied' samples

The OCP values of AS samples A, B, D and E obtained initially and after 60 minutes of immersion in the solution containing chloride ions at 25°C are given in Table 5.1.

Table 5.1 Initial OCPs and OCP after 60 minutes immersion in 1M NaCl for AS samples A, B, D and E.

OCP at time t (min)	OCP (mV) vs SCE			
	A	B	D	E
0	-780	-813	-937	-949
2	-776	-763	-895	-886
60	-774	-755	-886	-815

When an aluminium alloy is immersed in an electrolyte solution, a certain amount of time is necessary to establish the necessary double layer and other equilibria. This accounts for the large change in OCP during the first 2 minutes of immersion, $\Delta OCP_{(0\text{-}2)}$, for AS samples B, D and E. AS sample A shows a smaller change in $\Delta OCP_{(0\text{-}2)}$ indicating that less time is necessary for the quasi-equilibria to be established. This suggests that AS sample A has a more uniform surface with less surface defects than AS samples B, D and E. The OCP at the initial time of immersion is unlikely to give a true reflection of the initial exposed surface. For this reason, the OCP after 2 minutes of immersion, OCP_2, is preferred.

AS samples A and B are the known alloy AA 3003, rolled to a different thickness, and have essentially the same chemical composition. Very small differences in chemical

composition are found, and these explain the slight difference in OCP_2 values of the AS samples A and B. The slightly more negative values for OCP_2 of AS sample A can be explained in terms of a slightly higher percentage of anodic Mg in the aluminium solid solution. AS sample A contains 0.054% Mg whereas AS sample B contains only 0.01% Mg.

AS sample E shows a more negative OCP_2 than AS samples A and B, and this difference can be attributed to the difference between their chemical composition and microstructure. The most influential difference in the chemical composition is that AS sample E contains an additional 0.34% Cu and 0.15% Mg. Since a much larger percentage of cathodic Cu than anodic Mg is present, one would expect a more positive OCP_2. The significantly more negative OCP_2 therefore suggest that Cu is present mostly as microstructural intermetallic phases containing little Mg, and that Mg is present mostly as part of the aluminium solid solution. These are reasonable assumptions since microstructural intermetallic phases have very little influence on the OCP, and Mg has a significantly higher solubility than Cu in aluminium [8, 12, 32, 55, 87].

Of the four AS samples, AS sample D shows the most negative OCP_2. This is because Zn is anodic to aluminium and is present mostly in the solid solution matrix due to its very high solubility in aluminium [8, 12, 13, 22, 32, 43, 54, 55].

AS samples A, B, D and E exposed for 60 minutes to the solution containing chloride ions all showed an increase in OCP with time [Section 4.2.1.1(a), Figure 4.51] and minimal surface corrosion [Sections 4.1.2(a) and 5.4.1.1(a)]. Under these conditions it is reasonable to assume that the solid solution composition is virtually unaffected and the observed change in OCP from 2 minutes to 60 minutes, $\Delta OCP_{(2\text{-}60)}$, can therefore be explained in terms of surface oxide corrosion [10, 53, 60]. $\Delta OCP_{(2\text{-}60)}$ was very small for AS samples A, B and D, and a lot larger for AS sample E. This is because a small amount of oxide formation had taken place on AS samples A, B and D, while oxide dissolution was observed on AS sample E [Section 4.1.2(a), Table 4.5]. The oxide film present on the AS samples is tightly bound and oxide dissolution required breaking the bonds. A much larger driving force is therefore needed for oxide dissolution, resulting in a larger $\Delta OCP_{(2\text{-}60)}$ for AS sample E. Cu, which is present mainly as microstructural intermetallic phases in AS

sample E, aids the dissolution of aluminium oxide by providing sites for the cathodic reduction of water, oxygen and hydrogen ions needed to sustain the corrosion process.

5.2.1.1(b) 'Heat-treated' samples

OCP measurements are useful for investigating the effects of heat-treating, quenching and ageing practices, and have been used to verify the temper of aluminium alloys [8, 9, 12-16]. The alloying elements Cu, Mg, or Zn have especially large effects on the OCP, depending on whether they are present in solid solution or as microstructural intermetallic phases. It is reported that the OCP of Zn-containing alloys increases as Zn precipitates from solid solution during heat treatment, while the OCP of Cu-containing alloys decreases as Cu precipitates from solid solution [9].

The change in solid solution composition, caused by diffusion of the more soluble alloying elements during heat treatment, resulting in localised concentrated clusters in the matrix and increased precipitation of microstructural intermetallic phases [Section 5.1.2(a)], is expected to change the OCP values. The thicker and more porous oxide layer present on the HT samples is also expected to influence $\Delta OCP_{(2\text{-}60)}$ in the mildly aggressive electrolyte conditions encountered.

The OCP values of HT samples A, B, D and E obtained initially and after 60 minutes of immersion in the solution containing chloride ions are given in Table 5.2.

Table 5.2 Initial OCPs and OCP after 60 minutes immersion in 1M NaCl for HT samples A, B, D and E.

OCP at time t (min)	**OCP (mV) vs SCE**			
	A	**B**	**D**	**E**
0	-891	-958	-911	-1073
2	-882	-908	-879	-946
60	-857	-883	-829	-913

A large increase in $\Delta OCP_{(0\text{-}2)}$ is observed for the HT samples while the corrosive electrolyte solution and the exposed surface reach quasi-equilibria with one another. HT sample A shows the smallest increase in $\Delta OCP_{(0\text{-}2)}$.

Heat treatment of AS samples A and B resulted in a considerably more negative OCP_2. This is mainly due to transformation of the $(Mn,Fe)Al_6$ phase to the $(Fe,Mn)_3SiAl_{12}$ phase, depleting the solid solution of Mn, Fe and Si, all of which are cathodic to aluminium. Precipitation of $CuAl_2$ and $Cu_2Mn_3Al_{20}$ dispersoids depletes the solid solution of Mn and Cu, which are both cathodic to aluminium. The overall effect is a significant decrease of cathodic alloying elements originally present in the solid solution, resulting in a more anodic solid solution and hence a more negative OCP_2 for HT samples A and B.

Heat treatment of AS sample E resulted in a more negative OCP_2. This is the result of an increase in precipitation of the microstructural intermetallic phases $CuAl_2$, $Cu_2Mn_3Al_{20}$, $(Fe,Mn)_3SiAl_{12}$ and Al_7Cu_2Fe, which deplete the solid solution of the cathodic alloying elements Cu, Fe, Mn and Si, leaving a more anodic solid solution behind. Precipitation of Al_2CuMg accounts for some loss of anodic Mg, and diffusion of Cu, Mn and Mg through the solid solution matrix forming localised clusters in the matrix and grain boundary regions also depletes the solid solution from these alloying elements. The loss of anodic Mg from the solid solution of HT sample E during heat treatment explains the smaller decrease in OCP_2 compared with the decrease in OCP_2 of AS samples A and B.

Heat treatment of AS sample D resulted in a slightly more positive OCP_2. This can be explained by diffusion of anodic Zn through the solid solution matrix forming localised concentrated clusters of Zn in the matrix and grain boundary regions, depleting the solid solution to a certain extent and resulting in a more cathodic solid solution. The observed increase in OCP_2 is small and suggests that only a small amount of Zn precipitates from solid solution, which is plausible because of the very high solubility of Zn in aluminium. Transformation from the $(Mn,Fe)Al_6$ phase to the $(Fe,Mn)_3SiAl_{12}$ phase, and precipitation of $CuAl_2$ and $Cu_2Mn_3Al_{20}$ deplete the solid solution of cathodic elements and shifts the OCP_2 in the negative direction.

The HT samples exposed for 60 minutes to a solution containing chloride ions all showed an increase in OCP with time [Section 4.2.1.1(b), Figure 4.52] and minimal surface

corrosion [Section 4.1.2(a) and 5.4.1.1(a)]. The solid solution composition is virtually unchanged and $\Delta OCP_{(2\text{-}60)}$ can again be explained in terms of surface oxide corrosion. After heat treatment, $\Delta OCP_{(2\text{-}60)}$ increased for HT samples A, B and D due to an increase in oxide formation [Section 4.1.2(a), Table 4.5]. The increase in $\Delta OCP_{(2\text{-}60)}$ observed for HT sample E was smaller after heat treatment. Cu present as microstructural intermetallic phases in HT sample E aid dissolution of the surface oxide. Because the oxide film formed on HT sample E is more porous compared with the more compact and tightly bound oxide film formed on AS sample E [60], dissolution is easier and a smaller driving force is required, resulting in a smaller $\Delta OCP_{(2\text{-}60)}$.

5.2.1.1(c) 'Composite Powder coated' samples

Composite Powder has been studied by D.K. Hawksworth [2] with reference to microstructural and surface characteristics of the particles, brazing substrate interaction and joint formation. Measurement of the change in potential with time under open circuit conditions has not been carried out on CPC samples previously. The presence of fluoride ions in the residual $KAlF_4$ flux, and the different layers of the Composite melt are expected to influence the OCP measurements.

The OCP values of CPC samples A, B, D and E obtained initially and after 60 minutes of immersion in the solution containing chloride ions are given in Table 5.3.

Table 5.3 Initial OCPs and OCP after 60 minutes immersion in 1M NaCl for CPC samples A, B, D and E.

OCP at time t (min)	OCP (mV) vs SCE			
	A	B	D	E
0	-1033	-1173	-1179	-1204
2	-973	-988	-1029	-1035
60	-899	-867	-925	-900

The initial OCPs of the CPC samples indicate a very anodic surface which is characteristic of the fluoride present in the residual flux partially covering the surface [2]. Quasi-

equilibration of the CPC sample surface with the corrosive electrolyte resulted in a very large increase in $\Delta OCP_{(0-2)}$ caused by the presence of crystals of $KAlF_4$ at the surface.

Composite Powder coating results in highly negative OCP_2 and OCP_{60} values for all CPC samples. At pH > 3.17, fluoride ions are the predominant species in solution, while at pH < 3.17, hydrofluoric acid is the main species in solution [119]. Since the solution containing chloride ions has a pH of 4.06, the dissolved flux exists as fluoride ions in solution, which results in highly negative OCPs for aluminium alloys [119]. The OCP_{60} values decreased along the series D<E<A<B, which indicates diffusion of alloying elements from the base alloy into the molten Al-Si filler metal during heat treatment.

A gradual but large increase in $\Delta OCP_{(2-60)}$ was observed for all CPC samples immersed in the solution containing chloride ions [Section 4.2.1.1(c), Figure 4.53], which can be explained by the continuous but slow dissolution of the residual flux and the increased exposure of eutectic Al-Si melt layer, which is highly cathodic in nature.

5.2.1.2 Open circuit potential measurements in 1M NaCl + 0.5M H_2SO_4

The addition of sulfuric acid to the solution containing chloride ions resulted in a decrease in pH from 4.06 to 0.52. The OCP of aluminium alloys is reported to increase with decreasing pH [42, 50, 53, 59, 81, 124]. Other research shows that the OCP increases as the pH decreases from 14 to 8 and 4 to 0, but decreases as the pH decreases from 8 to 4 [57]. Generally, sulfate ions and bisulfate ions are weak inhibitors of corrosion [24, 72, 88] and as such are expected to have little influence on the OCP.

The effect of sulfuric acid on the OCP measurements of the AS, HT and CPC samples A, B, D and E will now be discussed.

5.2.1.2(a) 'As-supplied' samples

The OCP values of AS samples A, B, D and E obtained initially and after 60 minutes of immersion in the solution containing chloride ions and sulfuric acid are given in Table 5.4.

Table 5.4 Initial OCPs and OCP after 60 minutes immersion in 1M NaCl + 0.5M H_2SO_4 for AS samples A, B, D and E.

OCP at time t (min)	OCP (mV) vs SCE			
	A	B	D	E
0	-780	-836	-973	-923
2	-769	-758	-909	-844
60	-759	-764	-909	-783

A large increase in $\Delta OCP_{(0\text{-}2)}$ is again observed for the AS samples while the necessary quasi-equilibria are established between the sample surface and the corrosive electrolyte solution. AS sample A again shows the smallest increase in $\Delta OCP_{(0\text{-}2)}$.

The effect of sulfuric acid on the $\Delta OCP_{(2\text{-}60)}$ of AS samples A, B and D is minimal and within 10 mV, AS sample E again showing the largest increase in $\Delta OCP_{(2\text{-}60)}$ [Section 4.2.1.2(a), Figure 4.54]. The small change in $\Delta OCP_{(2\text{-}60)}$ for AS samples A, B and D

indicates that even though a significant amount of corrosion has taken place, the newly exposed surface has a solid solution composition similar to the initial uncorroded surface. This shows that uniformity of the solid solution composition, microstructural phase size and distribution, and grain size throughout the AS samples was indeed achieved by the manufacturing process. The larger initial increase in $\Delta OCP_{(2\text{-}60)}$ of AS sample E is again due to oxide dissolution aided by the increase in cathodic reduction reactions occurring on the Cu-containing phases.

5.2.1.2(b) 'Heat-treated' samples

The OCP values of HT samples A, B, D and E obtained initially and after 60 minutes of immersion in the solution containing chloride ions and sulfuric acid are given in Table 5.5.

Table 5.5 Initial OCPs and OCP after 60 minutes immersion in 1M NaCl + 0.5M H_2SO_4 for HT samples A, B, D and E.

OCP at time t (min)	OCP (mV) vs SCE			
	A	B	D	E
0	-905	-939	-919	-958
2	-878	-918	-880	-928
60	-759	-757	-802	-766

Quasi-equilibria established between the HT sample surface and the corrosive electrolyte solution again results in a large increase in $\Delta OCP_{(0\text{-}2)}$ for the HT samples.

After heat treatment, the presence of sulfuric acid caused for a much larger change in OCP with time, being largest for HT samples A, B and E, and smallest for HT sample D [Section 4.2.1.2(b), Figure 4.55]. The increase in OCP with time for the HT samples was largest during the first 40 minutes of immersion. This can be explained by localised corrosion of the more anodic phases in the solid solution, causing a change in the ratio of anodic/cathodic phases exposed to the corrosive electrolyte solution until a more uniform solid solution composition is reached, at which time the OCP levels off. The change is largest initially because of rapid dissolution of the porous surface oxide by hydrogen ions,

resulting in an increase in adsorption of both hydrogen ions and chloride ions and hence corrosion of the exposed sample surface. AS sample D experiences the smallest change in solid solution composition during heat treatment, and hence a smaller increase in $\Delta OCP_{(2-60)}$ is observed for HT sample D.

5.2.1.2(c) 'Composite Powder coated' samples

The OCP values of CPC samples A, B, D and E obtained initially and after 60 minutes of immersion in the solution containing chloride ions and sulfuric acid are given in Table 5.6.

Table 5.6 Initial OCPs and OCP after 60 minutes immersion in 1M NaCl + 0.5M H_2SO_4 for CPC samples A, B, D and E.

OCP at time t (min)	**OCP (mV) vs SCE**			
	A	**B**	**D**	**E**
0	-1067	-1121	-1159	-1125
2	-755	-769	-840	-773
60	-737	-717	-776	-730

The increase in $\Delta OCP_{(0-2)}$ observed is extremely large for the CPC samples. This is mainly due to rapid dissolution of the residual flux present on the sample surface, exposing the more cathodic eutectic Al-Si melt layer.

The effect of sulfuric acid on $\Delta OCP_{(2-60)}$ of the CPC samples is minimal [Section 4.2.1.2(c), Figure 4.56]. Corrosion of the partially reacted Composite Powder and eutectic Al-Si melt layer is rapid and uniform and explains the gradual but small increase in $\Delta OCP_{(2-60)}$. The OCP levels off once the α-Al filler metal is exposed, and starts to decrease once sufficient corrosion of the more anodic base alloy has been initiated. CPC sample D shows a larger initial increase in OCP that levels of in a shorter time because corrosion of the eutectic Al-Si melt layer is more rapid and the α-Al filler metal is exposed earlier.

5.2.1.3 Open circuit potential measurements in 1M NaCl + 0.5M H_2SO_4 + 0.5M $NaNO_3$

The addition of nitrate ions to the solution containing sulfuric acid and chloride ions made very little change to the pH. The OCP of aluminium alloys is reported to increase upon the addition of nitrate ions to an electrolyte solution [50, 82-84, 87]. This increase is believed to be due to the strong and rapid adsorption of nitrate ions and nitrite ions on active sites on the alloy surface [83], and to the reduction of nitrate ions to nitrite ions [82]. In acidic solutions, the nitrite ions are reduced further to ammonia [50, 87]. Competitive adsorption between chloride ions and nitrate ions results in less active sites available for the adsorption and hence corrosion of the exposed surface by chloride ions. The chemical composition and microstructure of the alloy further influence the extent of nitrate ion adsorption, as does the pH of the solution [50, 86, 87].

The effect of nitrate ions on the OCP measurements of AS, HT and CPC samples A, B, D and E will now be discussed.

5.2.1.3(a) 'As-supplied' samples

The OCP values of AS samples A, B, D and E obtained initially and after 60 minutes of immersion in the solution containing chloride ions, sulfuric acid and nitrate ions are given in Table 5.7.

Table 5.7 Initial OCPs and OCP after 60 minutes immersion in 1M NaCl + 0.5M H_2SO_4 + 0.5M $NaNO_3$ for AS samples A, B, D and E.

OCP at time t (min)	OCP (mV) vs SCE			
	A	B	D	E
0	-660	-714	-824	-806
2	-658	-690	-727	-725
60	-614	-624	-736	-637

The increase in $\Delta OCP_{(0-2)}$ observed is small for AS samples A and B, and larger for AS samples D and E. This indicates that a longer time is necessary for AS samples D and E to establish the necessary quasi-equilibria with the corrosive electrolyte solution, which is probably due to the affinity of nitrate ions for Cu, Zn, and Mg.

The presence of nitrate ions in the solution containing chloride ions and sulfuric acid results in an increase in $\Delta OCP_{(2-60)}$ for AS samples A, B and E, while $\Delta OCP_{(2-60)}$ for AS sample D was virtually unaffected by nitrate ions [Section 4.2.1.3(a), Figure 4.57]. Since the rate of oxide film growth or dissolution is not higher in relationship to solutions containing chloride ions and sulfuric acid [Section 4.1.4(a), Table 4.9], the increase in $\Delta OCP_{(2-60)}$ is likely to be caused by adsorption of nitrate ions on the sample surface necessary for the cathodic reduction of nitrate ions to nitrite ions and ammonia, and depends on the number of cathodic microstructural intermetallic phases present in the matrix of these alloys. A higher number of cathodic microstructural intermetallic phases will therefore result in an increase in cathodic reduction reactions and hence an increase in $\Delta OCP_{(2-60)}$. This was indeed observed. For AS sample D, anodic Zn is present mainly in the solid solution matrix. Less sites will therefore be available for the cathodic reduction of nitrate ions, which explains the small magnitude of $\Delta OCP_{(2-60)}$.

5.2.1.3(b) 'Heat-treated' samples

The OCP values of HT samples A, B, D and E obtained initially and after 60 minutes of immersion in the solution containing chloride ions, sulfuric acid and nitrate ions are given in Table 5.8.

Table 5.8 Initial OCPs and OCP after 60 minutes immersion in 1M NaCl + 0.5M H_2SO_4 + 0.5M $NaNO_3$ for HT samples A, B, D and E.

OCP at time t (min)	OCP (mV) vs SCE			
	A	B	D	E
0	-809	-902	-1030	-881
2	-774	-842	-977	-836
60	-598	-628	-717	-644

A considerable increase in $\Delta OCP_{(0-2)}$ is again found while the HT sample surface reaches equilibrium with the corrosive electrolyte solution. HT sample A again shows the smallest increase in $\Delta OCP_{(0-2)}$.

A very large increase in $\Delta OCP_{(2-60)}$ was observed for the HT samples when immersed in the solution containing chloride ions, sulfuric acid and nitrate ions [Section 4.2.1.3(b), Figure 4.58]. The increase is largest during the first 45 minutes of immersion and can be explained by the combined effect of hydrogen ions and nitrate ions, causing rapid dissolution of the porous oxide layer and an increase in adsorption of ions. Competitive adsorption of nitrate ions results in less active sites available for the adsorption of chloride ions, and hence reduces corrosion of the samples. Increased precipitation of cathodic microstructural intermetallic phases during heat treatment results in an increase in the number of cathodic reduction reactions involving nitrate ions and again explains the large value of $\Delta OCP_{(2-60)}$ for the HT samples.

5.2.1.3(c) 'Composite Powder coated' samples

The OCP values of CPC samples A, B, D and E obtained initially and after 60 minutes of immersion in the solution containing chloride ions, sulfuric acid and nitrate ions are given in Table 5.9.

Table 5.9 Initial OCPs and OCP after 60 minutes immersion in 1M NaCl + 0.5M H_2SO_4 + 0.5M $NaNO_3$ for CPC samples A, B, D and E.

OCP at time t (min)	OCP (mV) vs SCE			
	A	B	D	E
0	-1019	-1113	-1165	-1075
2	-676	-686	-780	-703
60	-643	-643	-708	-633

The increase in $\Delta OCP_{(0-2)}$ observed is extremely large for the CPC samples. This is again mainly due to rapid dissolution of the residual flux present at the surface.

The increase in $\Delta OCP_{(2\text{-}60)}$ observed is very small and the OCP levels out after 15 minutes for CPC samples A, B and E, while the OCP of CPC sample D continues to increase slowly [Section 4.2.1.3(c), Figure 4.59]. Competitive adsorption of nitrate ions and chloride ions on the exposed eutectic Al-Si melt layer reduces the number of active sites available for corrosion by chloride ions, and results in uniform delocalised corrosion of the eutectic Al-Si melt layer. Because the corrosion is delocalised over the entire surface, the chemical composition of the surface remains constant, which explains the stable OCP value for CPC samples A, B and E after 15 minutes of corrosion. Corrosion of the eutectic Al-Si melt layer of CPC sample D was accelerated by the presence of Zn in the Composite melt layer and base metal, resulting in rods of cathodic β-Si suspended in an interconnected network above the α-Al layer, followed by severe corrosion of the anodic base metal. The anodic character of the exposed surface is continuously reduced and results in a gradual increase in $\Delta OCP_{(2\text{-}60)}$ of CPC sample D.

5.2.1.4 A summary of the effect of ionic media on the value of OCP_2

To discuss the effect of ionic media on the OCP most representative of the uncorroded aluminium alloy, OCP_2 values are used to allow for the aluminium alloy surface and ionic media to establish the necessary double layer and other equilibria. The pH and presence of sulfate ions, bisulfate ions and nitrate ions will influence the OCP as mentioned in Sections 5.2.1.2 and 5.2.1.3. A summary of the OCP_2 values of AS, HT and CPC samples A, B, D and E immersed in three different electrolyte solutions are given in Table 5.10.

Table 5.10 OCP_2 values of the AS, HT and CPC samples A, B, D and E in three different electrolyte solutions.

Alloy sample		Electrolyte solution		
		1M NaCl	1M NaCl + 0.5M H_2SO_4	1M NaCl + 0.5M H_2SO_4 + 0.5M $NaNO_3$
'As-supplied' samples	A	-776	-769	-658
	B	-763	-758	-690
	D	-895	-909	-727
	E	-886	-844	-725
'Heat-treated' samples	A	-882	-878	-774
	B	-908	-918	-842
	D	-879	-880	-977
	E	-946	-928	-836
'Composite Powder coated' samples	A	-973	-755	-676
	B	-988	-769	-686
	D	-1029	-840	-780
	E	-1035	-773	-703

AS samples A, B and D are hardly affected by pH and the presence of sulfate ions and bisulfate ions, as is reflected by the minimal change in OCP_2. This can be explained by the compact and tightly bound oxide film on the AS samples making oxide dissolution by hydrogen ions and adsorption of chloride ions, sulfate ions and bisulfate ions on the

surface more difficult. AS sample E shows the largest increase in OCP_2, which is due to the affinity of sulfate ions for Cu [48], resulting in an increase in the number of ions adsorbed onto the alloy surface.

The effect of sulfuric acid on the OCP_2 values of the HT samples is minimal. HT sample E shows the largest increase in OCP_2, which is due to the affinity of sulfate ions for Cu. The increase in OCP_2 for HT sample E is considerably smaller than that observed on AS sample E, and can be explained by the thicker oxide layer present initially on HT sample E, making adsorption of sulfate ions onto the bare metal surface more difficult.

The decrease in pH causes a very large increase in OCP_2 values of all CPC samples. This results because of rapid dissolution of the residual flux and rapid corrosion of the partially reacted Composite Powder, exposing the more cathodic eutectic Al-Si melt layer, accompanied by a large amount of hydrogen evolution on the β-Si rods. The magnitude of the OCP_2 values is not as positive as would be expected for eutectic Al-Si. This is probably due to hydrogen evolution on the β-Si rods, causing convection and agitation at the surface, which is reported to shift the OCP in the negative direction [7, 13].

The effect of nitrate ions on the OCP_2 of the AS samples is, as expected, an increase in magnitude due to adsorption of nitrate ions and nitrite ions on the alloy surface, and is largest for alloy D, probably because of the stronger affinity of N-containing species for Zn.

Strong adsorption of nitrate ions causes a large increase in OCP_2 of HT samples A, B and E. The large decrease in OCP_2 for HT sample D is probably due to heat treatment causing clusters of concentrated Zn to localise in the aluminium matrix.

The effect of nitrate ions on the OCP_2 of the CPC samples is an increase in magnitude, due to an increase in the number of adsorbed ions at the surface. The eutectic Al-Si melt layer is exposed and reduction of hydrogen ions on the β-Si rods is inhibited considerably because of the strong adsorption of nitrate ions on the active sites for cathodic reduction. A reduction in hydrogen evolution results in less convection and agitation at the surface and hence a more positive OCP_2 of the exposed eutectic Al-Si melt layer.

5.2.2 PITTING POTENTIALS

Localised corrosion of aluminium alloys by aggressive ions, which usually appears as pitting, is a multi-step process involving adsorption of ions on the oxide surface, chemical reaction of the adsorbed ion with the metal ions in the surface oxide layer, thinning of the oxide by dissolution, and direct attack of the exposed metal by the ion. This has been described in greater detail in Section 2.1.5. Two characteristic potentials of localised pitting are reported to exist, namely (1) the pitting potential E_p, and (2) the protection potential against pitting, E_{pp}, where $E_{pp} < E_p$ [8, 17-21]. Both these potentials can be obtained from cyclic polarisation curves. The pitting potential is also referred to as the pit formation potential, the potential of pit nucleation (E_{np}), or the oxide breakdown potential (E_{br}). The protection potential is also called the critical pitting potential (E_{cp}) or the repassivation potential (E_{rp}). E_{pp} separates passivity from pitting and is that potential below which no pits nucleate or propagate. In the potential range between E_{pp} and E_p no new pits nucleate but already existing pits may propagate, while at potentials greater than E_p pits both nucleate and propagate.

E_p is measured by anodically polarising the sample surface and driving the corrosion process of the aluminium alloy in the electrochemically positive direction. E_p is therefore a measurement of the electron transfer reactions involving oxidation of the ultimately exposed aluminium alloy surface. With regards to localised corrosion of aluminium alloys, the potential enters the mechanism in two ways: firstly concerning pit initiation; and secondly concerning pit propagation. The pitting potential, E_p, thus reflects the ease by which aggressive ions, such as chloride ions, can penetrate the exposed surface (forming soluble compounds or transitory species at critical sites) and cause a sufficient amount of pit initiation to trigger a sudden large increase in current [61]. It is postulated that the potential enters the pit initiation step by providing the potential for anion adsorption on the surface. The ease of pit initiation, and hence the value of E_p in a particular electrolyte solution, is influenced greatly by the chemical composition of the aluminium solid solution and to a lesser extent its microstructure, the thickness and type of film present at the surface, and the ions present in the electrolyte solution.

5.2.2.1 The effect of sweep rate on the pitting potential

A major factor in potential controlled methods is the induction time or incubation period that is necessary for pit initiation and pit growth (i.e. pit propagation) to cause an appreciable anodic current to flow at a given anodic potential. At high sweep rates, less time is available for the initiation of pitting, leading to an overshoot of the steady state value and hence too noble a value of E_p [10, 20, 23, 35, 61, 125]. Recent work indicates that optimum sweep rates for aluminium alloys should be in the range 0.1 mV/s and 10 mV/s [20, 23, 37, 51]. The induction time for pit initiation is influenced by the electrolyte solution, the structure and composition of the surface oxide film, and the applied potential. The induction time decreases with increasing chloride concentration, decreases with increasing applied potential and increases with increasing oxide film thickness [10, 23, 53, 125].

The effect of sweep rate on E_p of the AS samples exposed to the corrosive electrolyte solutions was to change E_p to slightly more positive potentials as the sweep rate increased from 1 mV/s to 25 mV/s [Section 4.2.2, Figures 4.60(a), 4.62(a) and 4.64(a)]. This is due to less time available at high sweep rates for the adsorption of chloride ions on the surface oxide layer, a necessary part of localised pitting, resulting in a slower pit initiation as the sweep rate increases.

In the absence of nitrate ions, the effect of increasing sweep rate on E_p of HT samples A, B and E was a slight increase to more positive potentials [Section 4.2.2, Figures 4.60(b) and 4.62(b) respectively]. In the presence of nitrate ions, the value of E_p for HT samples A, B and E was not affected by increasing sweep rate [Section 4.2.2, Figure 4.64(a)]. This is probably due to adsorption of nitrate ions on the exposed surface oxide layer, thereby occupying critical adsorption sites that are necessary for chloride ions to initiate pitting of the bare HT surface. HT sample D showed a slight decrease in E_p with increasing sweep rate in all three electrolyte solutions, which is probably due to localised concentrated clusters of highly anodic Zn that are present in the solid solution matrix [Section 4.2.2, Figures 4.60(b), 4.62(b) and 4.64(b)]. The addition of Zn to an aluminium alloy is reported to result in highly negative E_p values [6, 13, 16, 17, 22, 38, 45].

Increasing the sweep rate affects E_p of the CPC samples differently, depending on the electrolyte solution and which of the multiple anodic polarisation sweeps is chosen. From the second anodic polarisation sweep onwards, the CPC samples showed a decrease in E_p with increasing sweep rate in all three electrolyte solutions [Section 4.2.2, Figures 4.60(c), 4.62(c) and 4.64(c)]. When considering the first anodic sweep, only CPC samples A, B and D exposed to the solution containing chloride ions showed a slight increase in E_p with increasing sweep rate. The general decrease in E_p with increasing sweep rate is probably due to dissolution of the highly anodic flux present on the surface. The large difference in E_p between sweep rates of 1 mV/s and 5 mV/s for CPC sample E is most likely due to the presence of Cu in the base alloy and Composite melt layer.

5.2.2.2 The effect of multiple anodic polarisation on the pitting potential

Little information is available in the literature on the effect of multiple anodic polarisation sweeps on E_p. Øvari, Tomcsányi and Turmezey [37] found that E_p increased with multiple sweeps. The values of E_p obtained for the seven successive anodic polarisation sweeps for each of the alloy samples in the three different electrolyte solutions are summarised in Appendix A.

The general trend observed was a slight increase in E_p for the AS and HT samples and a larger increase in E_p for the CPC samples with multiple anodic polarisation sweeps. This results because of corrosion of the sample surface that accompanies each anodic sweep, thereby changing the surface chemistry. Each time a new anodic polarisation sweep is started, a different surface is exposed which will effect E_p accordingly. AS samples B, D and E showed a slight decrease in E_p with increasing number of sweeps in the solution containing chloride ions. This is most likely because of the presence of a compact and tightly bound surface oxide layer, which is highly insoluble at a pH of 4.06. The values of E_p for the AS and HT samples derived from the first anodic sweep are likely to be the most representative of the initial surface and are accordingly reported in Section 4.2.2, Figures 4.61, 4.63 and 4.65.

The CPC samples showed a larger change in E_p as the number of sweeps increased because of the much larger change in surface chemistry. After each anodic sweep, less flux is

present, and more partially reacted Composite Powder, Al-Si eutectic melt and α-Al are exposed. It is therefore likely that E_p values for the CPC samples derived from the first anodic polarisation sweep do not represent the sample surface on which pitting is being investigated. The value of E_p obtained from the fourth or fifth anodic polarisation sweep is therefore likely to be more representative of the sample surface, and for this reason the average value of E_p for the fourth and fifth anodic polarisation sweeps has been quoted for the CPC samples in the following discussion.

5.2.2.3 The effect of solution composition on the pitting potential

5.2.2.3(a) 1M NaCl

The 1M NaCl solution was chosen as a reference solution to establish the effects of alloy composition, heat treatment and Composite Powder coating on E_p. Because this solution is only mildly aggressive at a pH of 4.06, and very little corrosion of the samples has occurred [Section 4.1.2 and 5.4.1.1], the values of E_p will be best suited to reveal the true character of the exposed sample surface.

E_p is not affected by the presence of alloying elements in the precipitated form [22, 23], but can be increased or decreased by the presence of alloying elements in solid solution with aluminium depending on whether the alloying element is more noble or active than aluminium. The presence of Cu or Zn in an aluminium alloy is reported to result in highly positive or negative values of E_p respectively [6, 13, 16, 17, 22, 38, 40, 41, 44, 45, 51]. The presence of Mg is said to change E_p to more negative potentials, although the observed shift is very small [6, 13, 14, 16, 17, 24, 44]. E_p increases as the solubility of the alloying element oxide decreases, the increase being highest for alloys containing alloying elements whose oxides exhibit the lowest solubilities [65, 121]. Zn oxides and Mg oxides are highly soluble while Fe oxides and Cu oxides are less soluble than aluminium oxides [65].

E_p also depends on the surface concentration of chloride ions and therefore time dependent sorption processes can influence it. The number of chloride ions occupying critical sites for pit initiation at the oxide/solution interface increases as E_p is approached. Once sufficient pit initiation has occurred and the E_p has been reached, the concentration of

adsorbed chloride ions decreases as soluble aluminium-chloride containing complexes are formed [18, 61].

The values of E_p obtained in the 1M NaCl solution for the AS, HT and CPC samples A, B, D and E have been summarised in Table 5.11.

Table 5.11 E_p values obtained at a sweep rate 1 mV/s for the AS, HT and CPC samples A, B, D and E in 1M NaCl.

Sample	A	B	D	E
AS	-739	-734	-889	-764
HT	-889	-896	-827	-761
CPC	-852	-887	-936	-731

The E_p results obtained for the AS samples in the solution containing chloride ions are greatly influenced by the solid solution composition of the samples. This also influences the OCP results obtained after 2 minutes of immersion, as discussed in Section 5.2.1.1(a). AS sample A shows a slightly more negative E_p than AS sample B due to a slightly higher percentage of anodic Mg. AS sample E shows a more negative E_p than AS samples A and B because of more anodic Mg present in the solid solution matrix. AS sample D shows the most negative E_p due to a fair amount of highly anodic Zn present in the solid solution matrix.

The effect of heat treatment on E_p of the AS samples A, B and D in the solution containing chloride ions can be explained by the change in solid solution composition and microstructural intermetallic phases. These factors also influence the OCP results obtained after 2 minutes of immersion, as discussed in Section 5.2.1.1(b). HT samples A and B showed a considerably more negative E_p, which can be explained by the increased precipitation of cathodic microstructural intermetallic phases resulting in a more anodic solid solution and a more soluble surface oxide. Heat treatment of AS sample D resulted in a more positive E_p which can be explained by diffusion of Zn into localised concentrated clusters in the solid solution matrix and grain boundary regions, resulting in a more cathodic solid solution and a less soluble surface oxide.

Heat treatment of AS sample E had little effect on E_p, which is not expected since the overall solid solution composition has become more anodic due to increased precipitation of cathodic microstructural intermetallic phases. The observed change is most likely caused by the increased presence of microstructural intermetallic phases containing cathodic Cu, which provide sites for the cathodic reduction of water, dissolved oxygen and hydrogen ions, thereby increasing the polarisation time for the aluminium alloy to reach the potential at which sufficient pit initiation takes place.

The E_p values for the CPC samples appear to be influenced by diffusion of the main alloying elements from the base alloy into the Composite melt layer during heat treatment, affecting the polarisation time needed for a sufficient amount of pit initiation to be realised. CPC sample D showed a highly negative E_p because of the presence of anodic Zn in the Composite melt layer decreasing the polarisation time for pit initiation, while CPC sample E shows a more positive E_p due to cathodic Cu in the Composite melt layer increasing the polarisation time needed for pit initiation.

5.2.2.3(b) 1M NaCl + 0.5M H_2SO_4

The addition of sulfuric acid to the solution containing chloride ions results in a decrease in pH from 4.06 to 0.52. The effect of pH on E_p has been studied extensively and conflicting results have been reported. Several researchers have reported that E_p is independent of the pH of the solution, but is a function of the chloride concentration [18, 24, 38, 42, 75]. Other researchers disagree and claim that the influence of pH prevails over the concentration of chloride ions in determining E_p, which was found to decrease with decreasing pH [81, 117, 121]. An increase in E_p with decreasing pH has also been reported for hydrochloric acid solutions [37, 38, 59]. Sulfate ions and bisulfate ions are weak inhibitors of corrosion and as such are expected to have little influence on E_p [24, 72, 88].

The values of E_p obtained in the 1M NaCl + 0.5M H_2SO_4 solution for the AS, HT and CPC samples A, B, D and E have been summarised in Table 5.12.

Table 5.12 E_p values obtained at a sweep rate 1 mV/s for the AS, HT and CPC samples A, B, D and E in 1M NaCl + 0.5M H_2SO_4.

Sample	A	B	D	E
AS	-774	-757	-905	-793
HT	-887	-884	-856	-805
CPC	-747	-758	-774	-745

All four AS samples show a decrease in E_p with decreasing pH. This can be explained by the more rapid dissolution of the thin and compact surface oxide covering the aluminium alloy, allowing the rate of pit initiation of the AS samples to be increased, and resulting in a more negative E_p as polarisation of the AS sample surface has become easier. This can be explained by specific adsorption of hydrogen ions on the oxide covered surface in acid media, which enhance electron passage through the oxide lattice [88]. The chemical composition of the AS samples is again found to influence E_p.

E_p of HT samples A and B is virtually unaffected by pH, while both HT samples D and E show a decrease in E_p with decreasing pH. It is reported that E_p decreases as the solubility

of the alloying element oxide increases and the increase in E_p is highest for alloys containing alloying elements whose oxides exhibit lowest solubilities [65, 121]. This explains the decrease in E_p with decreasing pH for HT samples D and E, since ZnO and MgO are highly soluble in acidic media. The solid solution composition is again found to influence the E_p results of the HT samples.

CPC samples A, B and D show an increase in E_p with decreasing pH, which can be explained by the rapid dissolution of residual flux in the presence of hydrogen ions. A more cathodic surface will be left behind and this is reflected in the E_p results. CPC sample E shows a slight decrease in E_p with decreasing pH. The E_p values are again influenced by diffusion of the main alloying elements from the base alloy into the Composite melt layer during heat treatment, affecting the polarisation time needed for a sufficient amount of pit initiation to be realised.

The results satisfactorily explain why, in certain circumstances, E_p decreases with decreasing pH and in other circumstances E_p increases with decreasing pH. The effect of pH on E_p is primarily dependent on the microstructure of the aluminium alloy as determined by its chemical composition, fabrication process and thermal history.

5.2.2.3(c) 1M NaCl + 0.5M H_2SO_4 + 0.5M $NaNO_3$

The addition of nitrate ions to the solution containing chloride ions and sulfuric acid is reported to increase E_p of aluminium alloys, which is believed to be due to the strong and rapid adsorption of nitrate ions on active sites on the alloy surface [24, 50, 72, 82, 84, 85, 87]. The chemical composition and microstructure of the aluminium alloy further influence the extent of nitrate ion adsorption, as does the pH of the solution [50, 86, 87].

The values of E_p obtained in the 1M NaCl + 0.5M H_2SO_4 + 0.5M $NaNO_3$ solution for the AS, HT and CPC samples A, B, D and E have been summarised in Table 5.13.

Table 5.13 E_p values obtained at a sweep rate 1 mV/s for the AS, HT and CPC samples A, B, D and E in 1M NaCl + 0.5M H_2SO_4 + 0.5M $NaNO_3$.

Sample	A	B	D	E
AS	-622	-623	-710	-572
HT	-711	-767	-725	-563
CPC	-610	-654	-728	-596

The effect of nitrate ions on E_p of the AS, HT and CPC samples A, B, D and E was a large increase towards more positive potentials. This can be explained by competitive adsorption of nitrate ions and chloride ions onto active sites on the sample surface. The presence of adsorbed nitrate ions makes polarisation of the sample surface more difficult, and as a result pit initiation is delayed resulting in a more positive E_p. These factors also influence the OCP results obtained after 2 minutes of immersion, as discussed in Section 5.2.1.1(c).

6 CONCLUSION

The object of this investigation has been the study of corrosion in four aluminium alloy samples used in the automotive industry for the construction of aluminium radiators. The logical conclusion of the investigation would be the examination of the results to see whether they can be satisfactorily used to select a combination of alloys that will produce an aluminium radiator that is less susceptible to general corrosion and hence will have a longer life expectancy.

6.1 NATURE OF CORROSION

The nature and extent of corrosion in the four aluminium alloy samples of interest to the automotive industry have been described and discussed in detail. From a manufacturer's point of view, two situations are of importance and interest. Aluminium radiators can either be produced by mechanical assembly of the components or by using brazing techniques. The observations and results of the AS samples are therefore important to the understanding of corrosion in Mechanically Assembled aluminium radiators. On the other hand, the observations and results of the HT and CPC samples are important to the understanding of corrosion in Composite Powder Brazed aluminium radiators.

The micrographic results of the AS, HT and CPC samples obtained after one hour of immersion in the various corrosive electrolyte solutions must be used with caution, as they will only illustrate the likely nature of corrosion of an aluminium alloy in a radiator, and cannot be used to predict the extent of corrosion and life expectancy of an aluminium radiator.

The chemical composition of an aluminium alloy influences the nature and extent of corrosion, and the general trend for corrosion damage of the AS, HT and CPC samples increased along the series A<B<E<D. The presence of Zn, Cu and Mg makes the alloy sample more susceptible to corrosion, the effect of Zn being strongest. The chemical composition also affects surface oxide corrosion during one hour of immersion in the various corrosive electrolyte solutions. The presence of Cu results in dissolution of the surface oxide whilst the absence of Cu results in increased oxide formation.

The nature of corrosion of the AS, HT and CPC samples, is also dependent on the ions present in the corrosive electrolyte solution. The pH of the electrolyte solution greatly influences the extent of corrosion, acidified chloride solutions are the most corrosive and near neutral solutions of chloride are the least corrosive.

Heat treatment during the CD brazing profile results in a general increase in the corrosion susceptibility for non Zn containing alloy samples. The most noticeable difference in the nature of corrosion between the AS and HT samples becomes evident in the acidified chloride solution. The AS samples show delocalised crystallographic pitting at localised regions of the exposed surface area revealing coalesced pits rather than clearly defined individual pits.

Heat treatment of the AS samples causes a change in solid solution composition and microstructural intermetallic phases, recrystallisation of the grains resulting in clearly defined grain boundaries and an increase in grain size and shape. The resulting softer, more malleable metal structure containing a thicker surface oxide layer gives rise to a general increase in susceptibility to corrosion. When exposed to the acidified chloride solution, the HT samples show localised crystallographic pitting consisting of many clearly defined individual pits, as well as intergranular corrosion at and below the sample surface. Intergranular corrosion on the HT samples was most severe for HT sample E containing Cu.

Composite Powder coating results in a very different surface microstructure. The base alloy is essentially the same as the HT sample of the same alloy, and is covered by a Composite melt layer consisting of residual flux, partially reacted Composite Powder, a eutectic Al-Si melt layer and an α-Al layer. Dissolution of the residual flux and corrosion of the partially reacted Composite Powder covering the CPC samples is greatly accelerated in acidified environments. The chemical composition of the base alloy and dissolution of alloying elements into the Composite melt during heat treatment influences both the extent and nature of corrosion of the eutectic Al-Si melt layer, the α-Al filler alloy and the base alloy. The presence of Zn, Mg and Cu makes the CPC samples more susceptible to corrosion, the effect of Zn again being strongest. In the acidified chloride solution, the entire eutectic Al-Si melt layer corroded, leaving the α-Al filler alloy and base alloy exposed, which both corroded to different degrees for the various aluminium alloys.

The addition of nitrate ions greatly reduces the extent of corrosion in acidified chloride solutions. Nitrate ions have two opposing effects on the corrosion of the aluminium alloys of interest, depending on the affinity of nitrate ions for the alloying elements present in the alloy sample, and on the solubility of the possible metal-ammonia complexes formed. The presence of Zn, Mg and Cu again makes the alloy more susceptible to corrosion, the effect of Zn again being strongest.

Strong adsorption of nitrate ions onto the eutectic Al-Si melt layer inhibits corrosion of non Zn containing CPC samples to a certain degree, by preventing the interconnected network of β-Si rods from entering the solution. Nitrate ions in the presence of Zn however, cause for the most severe case of corrosion of the CPC samples, resulting in perforation of the base alloy of CPC sample D.

6.2 A COMPARISON OF EXPERIMENTAL PREDICTIONS AND SWAAT EXPOSURE TEST RESULTS

The diagnostic use of OCP and E_p data for the selection of suitable aluminium alloys for the manufacture of automotive radiators should be of interest to the manufacturer. The electrochemical properties of the four aluminium alloy samples of special interest to industry have been described and discussed in detail. In industry, AS samples A and D are supplied as finstock material, while AS samples B and E are supplied as tubestock material.

The durability of an aluminium radiator can be enhanced by selecting finstock material used for the cooling airways that is slightly anodic in potential, i.e. sacrificial, to the tubestock, which carries the coolant liquid under pressure. It is obviously desirable to have non-perforating tubestock because any failure in the tubestock would result in considerable engine damage due to loss of coolant liquid and consequent overheating. Corrosion of the finstock would result in the loss of thermal cooling efficiency of the aluminium radiator. Loss of cooling efficiency would then be an inexpensive early warning that the aluminium radiator may require replacing.

In a radiator, the finstock has a much larger total surface area when compared with the tubestock. Since the rate of corrosion is directly proportional to the corrosion current density, the larger surface area of the finstock will reduce the observed corrosion and thus increase the overall life expectancy of the aluminium radiator provided it is sacrificial to the tubestock.

The electrochemical and micrographic results provide information on which part of the radiator is likely to corrode first, and the nature of corrosion that will take place respectively, but cannot be used to indicate the life expectancy of an aluminium radiator. SWAAT exposure test results give a better indication of the life expectancy of an aluminium radiator. The SWAAT exposure test is a cyclic salt spray test that involves spraying the aluminium radiator for 30 minutes at 50°C with an acetic acid acidified chloride solution, followed by a 90 minute dewing period. To test for failure of the aluminium radiator, the radiator is submerged in a water tank and water is run through the

radiator under 150 kPa of pressure to test for water leaks. Leak tests are carried out after 10 days exposure and every 5 days thereafter.

The effect of electrolyte composition on the OCP and E_p is primarily dependent on the microstructure of the aluminium alloy, which is determined by its chemical composition, fabrication process and thermal history. The near neutral chloride solution is best suited to firstly reveal the effect of chemical composition on the electrochemical properties of the AS samples, and secondly to reveal the effect of solid solution compositional changes on the electrochemical properties of the HT samples. Predictions based on the electrochemical results obtained in acidified chloride solutions should correlate with the reported findings of SWAAT exposure test results.

OCP data can be used with caution as the first diagnostic tool for choosing the appropriate aluminium alloys for finstock and tubestock respectively. Judicious use of E_p data can, in certain instances, be used to further validate the choice of aluminium alloys for the use as finstock and tubestock.

OCP data will indicate which aluminium alloy is the most anodic in a galvanic series. The more anodic aluminium alloy in a couple should corrode preferentially when in contact with a corrosive environment, and hence provide sacrificial protection. In a galvanic couple, the aluminium alloy with the more negative E_p will generally pit first. It is in this context, that the observations and results of the AS samples can be used to choose combinations of finstock and tubestock for use in Mechanically Assembled radiators. Recommended combinations and the corrosion likely to occur are given in Table 6.1.

On the basis of the results quoted in Table 6.1, possible finstock and tubestock combinations for use in Mechanically Assembled radiators would be A and B, D and B, and D and E. The use of AS sample D as finstock, in combination with either AS samples B or E as tubestock, should give rise to aluminium radiators that will be least susceptible to perforation of the tubestock, although these combinations will result in a significant loss of heat transfer efficiency with time.

Table 6.1 Recommended aluminium alloy combinations of finstock and tubestock for Mechanically Assembled radiators.

Finstock			Tubestock			Comments on likely corrosion
Alloy sample	OCP_2	E_p	Alloy sample	OCP_2	E_p	
A	-769	-774	B	-758	-757	Very slight pitting of finstock, possible pitting of tubestock.
D	-909	-905	B	-758	-757	Pitting of finstock, no pitting of tubestock.
D	-909	-905	E	-844	-793	Pitting of finstock, no pitting of tubestock.

The results of a SWAAT exposure test performed on a Mechanically Assembled aluminium radiator are reported on in Table 6.2. The only Mechanically Assembled aluminium radiator that has been tested uses aluminium alloy AA 1145 as finstock with AS sample B as tubestock. AA 1145 has similar microstructural and electrochemical properties as AS sample A, and as such gives a good reflection of using AS samples A and B together in a Mechanically Assembled aluminium radiator. The SWAAT exposure test confirms the predictions based on the electrochemical and micrographic results.

Table 6.2 SWAAT exposure test results for aluminium alloy combinations of finstock and tubestock for Mechanically Assembled radiators.

Car Model	Finstock	Tubestock	SWAAT exposure test results	Corrosion observed
BMW	1145	B	Pass > 20 days	Virtually no pitting of both the finstock and tubestock.

Table 6.3 shows the combination of finstock and tubestock that is not recommended for use in a Mechanically Assembled aluminium radiator, based on the electrochemical and

micrographic results obtained. Using AS sample A as finstock and AS sample E as tubestock may result in pitting of the tubestock leading to premature failure of the aluminium radiator.

Table 6.3 Non-recommended aluminium alloy combinations of finstock and tubestock for Mechanically Assembled radiators.

Finstock			Tubestock			Comments on likely corrosion
Alloy sample	OCP_2	E_p	Alloy sample	OCP_2	E_p	
A	-769	-774	E	-844	-793	Very slight pitting of tubestock, possible pitting of finstock.

In order to predict the nature of corrosion of Brazed aluminium radiators, the electrochemical and micrographic results of the HT samples should provide information on the susceptibility to corrosion of both the finstock and tubestock material, while the results of the CPC samples should help to indicate the stability of the brazed filler joint. Choosing finstock material with an OCP and E_p that are both more negative than the OCP and E_p of the tubestock material for Mechanically Assembled aluminium radiators was a fairly straight forward exercise. The production of aluminium radiators using brazing technology introduces new and complex circumstances. Heat treatment introduces changes in solid solution composition and microstructure of the AS samples, and a brazed filler joint further complicates the corrosion process. These changes affect both the OCP and E_p, and an intuitive decision has to be made on which of these two parameters is going to be the most important in determining the sacrificial nature of the aluminium alloy. E_p has been chosen as the better diagnostic tool. It is on this basis that the recommended combinations of finstock and tubestock to use in Brazed aluminium radiators are given in Table 6.4. Comments on the corrosion likely to occur are included.

On the basis of the results quoted in Table 6.4, the best possible aluminium alloy combinations for use in Brazed radiators would be alloy samples A and D for use as finstock and alloy sample E for use as tubestock. Finstock samples A and D will

sacrificially protect tubestock sample E, at the cost of loss in thermal efficiency due to corrosion of the finstock.

Table 6.4 Recommended aluminium alloy combinations of finstock and tubestock for Brazed radiators exposed to the acidified chloride solution.

Finstock			Tubestock			Comments on likely Corrosion
Alloy sample	OCP_2	E_p	Alloy sample	OCP_2	E_p	
A(HT)	-878	-887	E(HT)	-928	-805	Pitting of finstock, slight pitting of fillet joint.
A(CPC)	-755	-747	E(CPC)	-773	-745	
D(HT)	-880	-856	E(HT)	-928	-805	Pitting of finstock, pitting of fillet joint closest to fin.
D(CPC)	-840	-774	E(CPC)	-773	-745	

Table 6.5 shows the combinations of finstock and tubestock not recommended for use in a Brazed aluminium radiator based on the electrochemical and micrographic results obtained. Using finstock samples A and D and tubestock sample B may result in pitting of the tubestock leading to premature failure of the Brazed aluminium radiator.

Table 6.5 Non-recommended aluminium alloy combinations of finstock and tubestock for Brazed radiators exposed to the acidified chloride solution.

Finstock			Tubestock			Comments on likely Corrosion
Alloy sample	OCP_2	E_p	Alloy sample	OCP_2	E_p	
A(HT)	-878	-887	B(HT)	-918	-884	Slight pitting of both finstock and tubestock, slight pitting of fillet joint closest to tube.
A(CPC)	-755	-747	B(CPC)	-769	-758	
D(HT)	-880	-856	B(HT)	-918	-884	Pitting of tubestock, pitting of fillet joint closest to fin.
D(CPC)	-840	-774	B(CPC)	-769	-758	

SWAAT exposure tests have been performed on Brazed aluminium radiators containing a combination of either alloy sample A or D as finstock, or either alloy sample B or E as tubestock. These results are reported on in Table 6.6. Optical micrographs [130, 131] of the observed corrosion during SWAAT exposure tests are given in Figures 6.1, 6.2 and 6.3 for the four possible alloy combinations. Most alloy combinations passed the SWAAT exposure test at 20 days, which is sufficiently satisfactory for the manufacturer to offer a 5 year warranty. Using alloy sample B as tubestock in combination with either alloy sample A or D as finstock resulted in its pitting, and was worst if alloy sample A was used, resulting in failure of the SWAAT exposure test between 10 and 15 days. The theoretical predictions made support the SWAAT exposure test results.

Table 6.6 Aluminium alloy combinations of finstock and tubestock for Brazed radiators exposed to the SWAAT exposure test.

Car Model	**Finstock**	**Tubestock**	**SWAAT exposure test results**	**Corrosion observed**
Experimental	A	B	Pass > 10 days	Severe pitting of finstock, pitting of tubestock, pitting of fillet joint.
Mercedes Benz	A	E	Pass > 20 days	Lots of pitting of finstock, no pitting of tubestock.
Mercedes Benz	A	E	Pass > 20 days	Pitting of finstock, pitting of fillet joint.
BMW	D	B (320 μm)	Pass > 20 days	Lots of pitting of finstock, no pitting of tubestock.
BMW	D	B (220 μm)	Pass > 20 days	Lots of pitting of finstock, very little pitting of tubestock.
BMW	D	B	Pass > 20 days	Slight pitting of finstock, no pitting of tubestock.
Mercedes Benz	D	E	Pass > 20 days	Some pitting of finstock, no pitting of tubestock.
Mercedes Benz	D	E	Pass > 20 days	Lots of pitting of finstock, no pitting of tubestock.

The theoretical predictions based on the electrochemical and micrographic results obtained in laboratory experiments correlate well with the SWAAT exposure test results for the alloy combinations studied. From both these results it follows that using alloy sample D as finstock and alloy sample E as tubestock results in the best possible alloy combination for use in Brazed aluminium radiators.

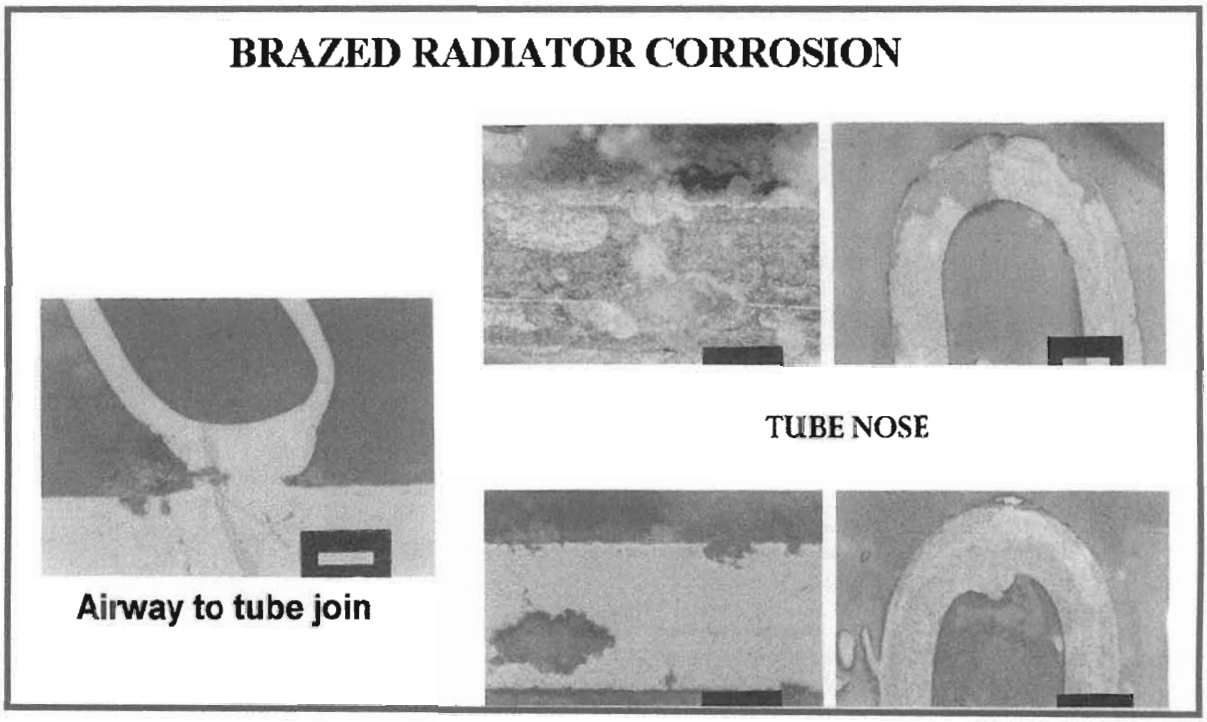

Figure 6.1 Corrosion of Brazed radiator core made of finstock alloy A and tubestock alloy C after exposure to the SWAAT test.

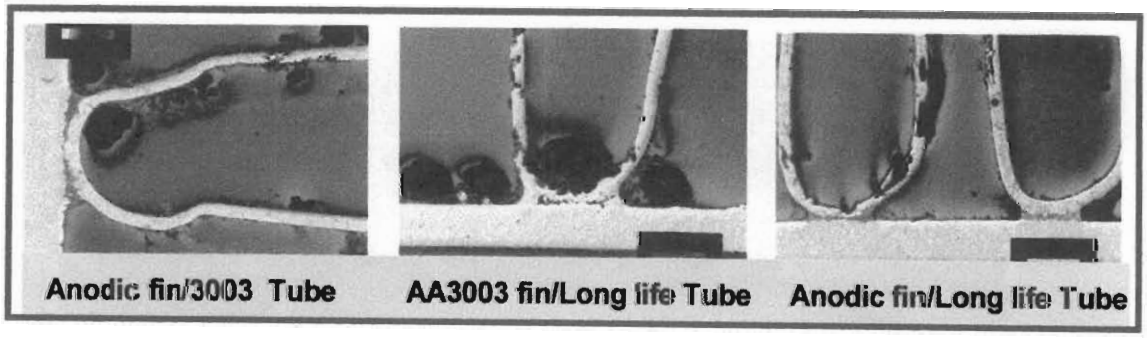

Figure 6.2 Corrosion of Brazed radiator cores after exposure to the SWAAT test. Combinations of finstock and tubestock respectively (from left to right): D and B, A and E, D and E.

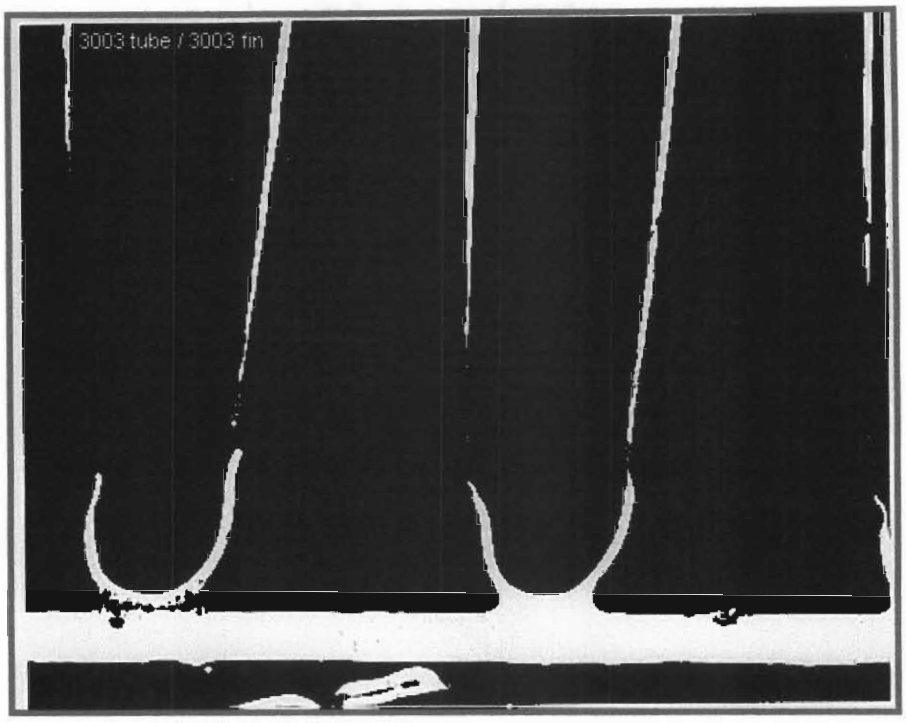

(a)

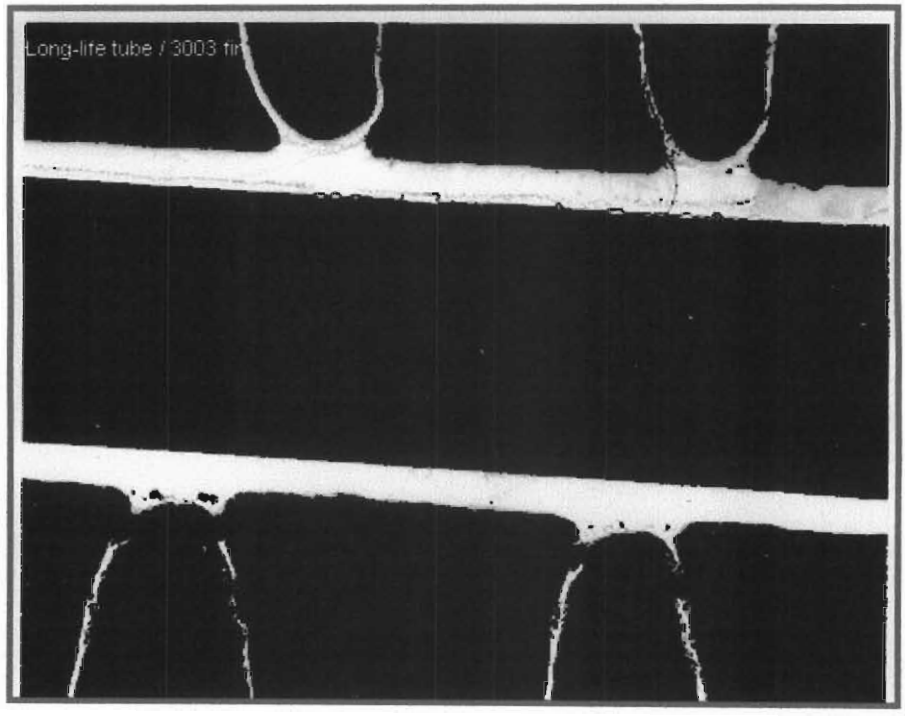

(b)

Figure 6.3 Corrosion of Brazed radiator cores after exposure to the SWAAT test. Combinations of finstock and tubestock respectively: (a) A and B (b) A and E.

6.3 FURTHER WORK

The needs and demands of the automotive industry could be eminently satisfied if suitable laboratory experiments could be designed to predict the life expectancy of an aluminium radiator. The rate of corrosion of an aluminium radiator will give a better indication of the life expectancy and can in principle be determined by measuring the corrosion current and surface area of the components. Further work involving measurement of the actual anodic currents flowing during the corrosion process can easily be designed and the relative surface areas of the various components should not present insurmountable difficulties.

The terrestrial environment to which the aluminium radiator is subjected is imponderable. M. Ainali, R. Sundberg and D.K. Miner [132] have suggested a Road Environment Pollutant (REP) solution which is meant to represent 'an average and representative environment' which the radiator is likely to encounter. The REP solution consists of chloride ions, nitrate ions, nitrite ions, sulfate ions and sulfite ions at a pH of 3.5. Electrochemical and micrographic measurements taken of the alloy samples exposed to the REP solution revealed results that were similar to those obtained in the solution containing chloride ions only. Nevertheless, an automobile driven along an inland country road will encounter an atmospheric environment which is very different to that encountered by an automobile driven in an urban industrial environment. An automobile driven in a humid coastal industrial environment will encounter the most severe corrosive atmosphere. Tests concluded in the latter environment should be of greatest interest to the automotive industry.

The automotive industry has successfully produced aluminium radiators with a life expectancy of about 10 years and they therefore confidently offer a 5-year warranty on their products to the motor assembly plants. A sobering observation is that 80% of all automotive radiator replacements in the first five years are caused by 'front-end' collisions and not by failure due to corrosion.

7 REFERENCES

[1] D.E. Davies and R.M. Prigmore, *British Corrosion Journal*, 21, No. 3, 191 (1986).

[2] Douglas Kenneth Hawksworth, *A Study of Aluminium Brazing Technology using Cosprayed Al-Si Alloy/$KAlF_4$ Flux Powders*, PhD Thesis (1998).

[3] Patent by T&N Technologies.

[4] Patent by R.M. Prigmore : WO 94/29072.

[5] Developed by Alcan International.

[6] M.C. Reboul, *Corrosion*, 35, No. 9, 423 (1979).

[7] K.P. Sherif; R. Narayan, *British Corrosion Journal*, 24, No. 3, 199 (1989).

[8] *ASM Handbook: Properties of Aluminium and Aluminium Alloys; Corrosion Behaviour*, 579 (1994).

[9] T.D. Burleigh, R.C. Rennick and F.S. Bovard, *Corrosion*, 49, No. 8, 683 (1993).

[10] R.A. Bonewitz, *Corrosion*, 30, No. 2, 53 (1974).

[11] R.A. Bonewitz, *Corrosion*, 29, No. 6, 215 (1973).

[12] E. Mattsson, L.-O. Gullman, L. Knutsson, R. Sundberg and B. Thundal, *British Corrosion Journal*, 6, 73 (1971) March.

[13] P.L. Cabot, F. Centellas, J.A. Garrido, R.M. Rogríguez, E. Brittas, E. Pérez; A.V. Benedetti; P.T.A. Sumodjo, *Journal of Applied Electrochemistry*, 22, 541 (1992).

[14] H.J. Raetzer-Scheibe and C.D.S. Tuck, *Corrosion Science*, 36, No. 6, 941 (1994).

[15] K. Kowal, J. DeLuccia, J.Y. Josefowicz, C. Laird and G.C. Farrington, *Journal of Electrochemical Society*, 143, No. 8, 2471 (1996).

[16] J.A. Garrido, P.L. Cabot, A.H. Moreira, R.M. Rodríguez, P.T.A. Sumodjo and E. Pérez, *Electrochimica Acta*, 41, No. 13, 1933 (1996).

[17] M. Baumgärtner and H. Kaesche, *Corrosion Science*, 29, No. 2/3, 363 (1989).

[18] E. McCafferty, *Corrosion Science*, 37, No. 3, 481 (1995).

[19] Z. Szklarska-Smialowska and M. Janik-Czacho, *Corrosion Science*, 11, 901 (1971).

[20] Aasmund Broli and Hans Holtan, *Corrosion Science*, 13, 237 (1973).

[21] Norvald Nilsen and Einar Bardal, *Corrosion Science*, 17, 635 (1977).

[22] E. Lunarska, E. Trela, and Z. Szklarska-Smialowska, *Corrosion*, 43, No. 4, 219 (1987).

[23] K. Nisancioglu and H. Holtan, *Corrosion Science*, 18, 835 (1978).

[24] H. Böhni and H.H. Uhlig, *Journal of Electrochemical Society*, 116, No. 7, 906 (1969).

[25] P.P. Trzaskoma, *Corrosion*, 46, No. 5, 402 (1990).

[26] R.G. Buchheit Jr., J.P. Moran and G.E Stoner, *Corrosion*, 46, No. 8, 610 (1990).

[27] G.S. Chen, M. Gao and R.P. Wei, *Corrosion*, 52, No. 1, 8 (1996).

[28] Kemal Nişancioğlu, *Journal of Electrochemical Society*, 137, No. 1, 69 (1990).

[29] R.G. Buchheit, *Journal of Electrochemical Society*, 142, No. 11, 3994 (1995).

[30] T.D. Burleigh, *Corrosion*, 47, No. 2, 89 (1991).

[31] T.J. Langan, L. Christodoulou, D. Venables, J.A.S. Green, and J.R. Pickens, *Corrosion*, 44, No. 3, 165 (1988).

[32] E. Lunarska and Z. Szklarska-Smialowska, *Corrosion*, 43, No. 6, 353 (1987).

[33] A.C. Fraker and A.W. Ruff, Jr., *Corrosion*, 27, No. 4, 151 (1971).

[34] A.H. Roebuck and J.V. Luhan, *Corrosion*, 47, 268 (1967).

[35] M. Elboujdaina and E. Ghali; R.G. Barradas and M. Girgis, *Corrosion Science*, 30, No. 8/9, 855 (1990).

[36] A.A. Aksűt and G. Bayramoğlu, *Corrosion Science*, 36, No. 3, 415 (1994).

[37] F. Øvari, L. Tomcsanyi and T. Tumezey, *Electrochimica Acta*, 33, No. 3, 323 (1988).

[38] P.L. Bonora, G.P. Ponzano and V. Lorenzelli, *British Corrosion Journal*, Quarterly, No. 2, 108 (1974).

[39] R. Babić, M. Metikoš- Huković, S. Omanović, Z. Grubač and S. Brinić, *British Corrosion Journal*, 30, No. 4, 288 (1995).

[40] Rajan Ambak and E.S. Dwarakadasa, *British Corrosion Journal*, 28, No. 2, 142 (1993).

[41] S. Spathis, J. Poulios and E. Papastergiadis, *British Corrosion Journal*, 30, No. 3, 233 (1995).

[42] R. Ambat and E.S. Dwarakadasa, *Journal of Applied Electrochemistry*, 24, 911 (1994).

[43] T. Xwe, W.C. Cooper, R. Pascual and S. Saimoto, *Journal of Applied Electrochemistry*, 21, 238 (1991).

[44] Dr. Zaki Ahmad, *Anti-Corrosion*, 4 (1986).

[45] R.R. Wiggle and V. Hospadaruk, *SAE Technical Paper Series*, No. 800800, 1 (1980).

[46] O. Seri, *Corrosion Science*, 36, No. 10, 1789 (1994).

[47] W.A. Badawy and F.M. Al-Kharafi, *Corrosion Science*, 39, No. 4, 681 (1997).

[48] C. Blanc and G. Mankowski, *Corrosion Science*, 39, No. 5, 949 (1997).

[49] D.W. Berkeley, H.E.M. Sallam and H. Nayeb-Hashemi, *Corrosion Science*, 40, No.

2/3, 141 (1998).

[50] J.F. McIntyre and T.S. Dow, *Corrosion*, 48, No. 4, 308 (1992).

[51] M. Yasuda, F. Weinberg and D. Tromans, *Journal of Electrochemical Society*, 137, No. 12, 3708 (1990).

[52] Faiza M. Al-Kharafi and Waheed A. Badawy, *Electrochimica Acta*, 40, No. 12, 1811 (1995).

[53] Joong-Do Kim and Su-il Pyun, *Electrochimica Acta*, 40, No. 12, 1863 (1995).

[54] *ASM Handbook: Aluminium and Aluminium Alloys; Metallographic Practices*, 485 (1994).

[55] I.J. Polmear, *Light Alloys: Metallurgy of the Light Alloys*, Second Edition, Edward Arnold (1989).

[56] Alcibiades Becerra and Ron Darby, *Corrosion*, 30, No. 5, 153 (1974).

[57] G.A. DiBari and H.J. Read, *Corrosion*, 27, No. 11, 483 (1971).

[58] A.M. Beccaria and G. Poggi, *Corrosion*, 42, No. 8, 470 (1986).

[59] Ph. Gimenez, J.J. Rameau and M.C. Reboul, *Corrosion*, 37, No. 12, 673 (1981).

[60] R.T. Foley and P.P. Trzaskoma, *Corrosion*, 33, No. 12, 435 (1977).

[61] R.T. Foley, *Corrosion*, 42, No. 5, 277 (1986).

[62] M. Baumgärtner and H. Kaesche, *Corrosion Science*, 31, No. , 231 (1990).

[63] Stella M. de De Micheli, *Corrosion Science*, 18, 605 (1978).

[64] Christopher M.A. Brett, *Corrosion Science*, 33, No. 2, 203 (1992).

[65] Z. Szklarska-Smialowska, *Corrosion Science*, 33, No. 8, 1193 (1992).

[66] J.W. Diggle, T.C. Downie and C.W. Goulding, *Electrochimica Acta*, 15, 1079 (1970).

[67] P.L. Cabot, F.A. Centellas, J.A. Garrido, E. Pérez and H. Vidal, *Electrochimica Acta*, 36, No. 1, 179 (1991).

[68] L. Tomcsányi, K. Varga, I. Bartik, G. Horányi and E. Maleczki, *Electrochimica Acta*, 34, No. 6, 855 (1989).

[69] Kai P. Wong and Richard C. Alkire, *Journal of Electrochemical Society*, 137, No. 10, 3010 (1990).

[70] Z.A. Foroulis and M.J. Thibrikar, *Journal of Electrochemical Society*, 122, No. 10, 1296 (1975).

[71] R.T. Foley and T.H. Nguyen, *Journal of Electrochemical Society*, 129, No. 3, 464 (1982).

[72] B.N. Stirrup, N.A. Hampson and I.S. Midgley, *Journal of Applied Electrochemistry*,

5, 229 (1975).

[73] S. Paul, P.K. Mitra and S.C. Sirkar, *Trans. Indian Inst. Met.*, 45, No. 4, 219 (1992).

[74] Nikolaos Lampeas and Petros G. Koutsoukos, *Corrosion Science*, 36, No. 6, 1011 (1994).

[75] W.M. Carroll, C.B. Breslin, *British Corrosion Journal*, 26, No. 4, 255 (1991).

[76] Stephen C. Dexter, *Corrosion*, 36, No. 8, 423 (1980).

[77] E. Deltombe and M. Pourbaix, *Corrosion*, 14, 496t (1958).

[78] W.C. Moshier, G.D. Davis and J.S. Ahearn, *Corrosion Science*, 27, No. 8, 785 (1987).

[79] T.C. Tan and D-T. Chin, *Journal of Electrochemical Society*, 132, No. 4, 766 (1985).

[80] E. Deltombe, C. Vanleugenhaghe and M. Pourbaix, *Atlas of Electrochemical Equilibrium in Aqueous Solutions*, Pergamon Press, Section 5.2, Aluminium, 168 (1966).

[81] Rajan Ambat and E.S. Dwarakadasa, *Corrosion Science*, 33, No. 5, 681 (1992).

[82] A.A. Adams and R.T. Foley, *Corrosion*, 31, No. 3, 84 (1975).

[83] Christopher M.A. Brett, Isabel A.R. Gomes and Jenny P.S. Martins, *Corrosion Science*, 36, No. 6, 915 (1994).

[84] T.M. Salem, J. Horvath and P.S. Sidky, *Corrosion Science*, 18, 363 (1978).

[85] W.K. Johnson, *British Corrosion Journal*, 6, 200 (1971).

[86] Rolf Sundberg, Rolf Holm and Lars Hassel, *SAE Technical Paper Series*, No. 870181, 1.621 (1988).

[87] G. Lyberatos and L. Kobatiatis, *Corrosion*, 47, No. 11, 820 (1991).

[88] M.G.A. Khedr and A.M.S. Lashien, *Corrosion Science*, 33, No. 1, 137 (1992).

[89] Ulick R. Evans, *An Introducion to Metallic Corrosion*, Second Edition, Edward Arnold, London (1963).

[90] J.M. West, *Electrodeposition and Corrosion Processes*, Van Nostrand, London (1965).

[91] John M. West, *Basic Corrosion and Oxidation*, Ellis Horwood (1980).

[92] (a) J.O.M. Bockris and A.K.N. Reddy, *Modern Electrochemistry*, Vol. 2, Macdonald & Co., London (1970).

(b) K.J. Vetter, *Electrochemical Kinetics*, New York: Academic Press, 737 (1967).

[93] School of Pure and Applied Electrochemistry, *Lecture Notes*, National Institute for Metallurgy, Randburg, South Africa (1979).

[94] F. Albert Cotton and Geoffrey Wilkinson, F.R.S., *Advanced Inorganic Chemistry*,

Second Edition, Interscience Publishers (1966).

[95] J.D. Lee, *Concise Inorganic Chemistry*, Fourth Edition, Chapman and Hall (1991).

[96] K.M. Mackay and R.A. Mackay, *Intoduction to Modern Inorganic Chemistry*, Second Edition, Intertext Books, London (1972).

[97] Arthur I. Vogel, *A Textbook of Macro and Semi-micro Qualitative Inorganic Analysis*, Fourth Edition, Longmans, Green and Co. Ltd. (1954).

[98] Cotton and Wilkinson, *Advanced Inorganic Chemistry – A Comprehensive Text*, Fourth Edition, Interscience Publishers (1980).

[99] P.E. Blackburn and E.A. Gulbransen, *Journal of Electrochemical Society*, 107, No. 12, 944 (1960).

[100] W. Vedder and D.A. Vermilyea, *Trans. Faraday Society*, 65, 561 (1969).

[101] D.G. Altenpohl, *Corrosion*, 18, 143t (1962).

[102] R.K. Hart, *Trans. Faraday Society*, 53, 1020 (1957).

[103] M.S. Hunter and P. Fowle, *Journal of Electrochemical Society*, 103, 342 (1956).

[104] Digby D. MacDonald and P. Butler, *Corrosion Science*, 13, 259 (1973).

[105] Paul A. Malachesky, *Encyclopedia of Electrochemistry of the Elements*, Vol. VI, Chpt. VI-3, 63 (1970).

[106] J.W. Diggle, *Oxide and Oxide Films*, Volume 14, Marcel Dekker Inc., New York, Chpt. 3, (1972).

[107] M. Pourbaix, *Atlas of Electrochemical Equilibrium in Aqueous Solutions*, Pergamon Press, Section 4, Corrosion, 70 (1966).

[108] M.A. Poole, *Effect of Activator Elements on the Anodic Behaviour of Aluminium*, Thesis submitted to the University of Manchester, September (1994).

[109] Charles F. Baes, Jr. and Robert E. Mesmer, *The Hydrolysis of Cations*, John Wiley & Sons (1976).

[110] J.A. Richardson and G.C. Wood, *Corrosion Science*, 10, 313 (1970).

[111] J. Augustynski, *Passivity of Metals*, R.P. Frankenthal, J. Kruger Eds., Electrochemical Society, Pennington, New Jersey, 989 (1978).

[112] R.C. Newman, *Corrosion Science*, 37, No. 3, 527 (1995).

[113] T.H. Nguyen and R.T. Foley, *Journal of Electrochemical Society*, 129, No. 1, 27 (1982).

[114] A.M. Beccaria and G. Poggi, *Corrosion*, 34, No. 3, 153 (1987).

[115] K. Sotoudeh, T.H. Nguyen, R.T. Foley and B.F. Brown, *Corrosion*, 37, No. 6, 350 (1981).

[116] C. Edeleanu and U.R. Evans, *Trans. Faraday Society*, 47, 1121 (1951).

[117] J.W. Diggle, T.C. Downie and C.W. Goulding, *Corrosion Science*, 8, 907 (1968).

[118] T. Hagyard and J.R. Williams, *Trans. Faraday Society*, 56, 2288 (1960).

[119] J. Radošević, Z. Mentus, A. Djordjević and A.R. Despić, *Journal of Electroanalytical Chemistry*, 193, 241 (1985).

[120] Aasmund Broli, Hans Holtan and Kristofer L. Prestud, *Corrosion*, 30, No. 12, 427 (1974)

[121] Rama B. Inturi and Z. Szklarska-Smialowska, *Corrosion Science*, 34, No. 4, 705 (1993).

[122] D.M. Dražić, S.K. Zečević, R.T. Atanasoski and A.R. Despić, *Electrochimica Acta*, 28, No. 5, 751 (1983).

[123] P.L. Bonora, G. P. Ponzano and V. Lorenzelli, *British Corrosion Journal*, Quarterly, No. 2, 112 (1974).

[124] G.D. Davis, W.C. Moshier, J.S. Ahearn, H.F. Hough and G.O. Cote, *Journal Vac. Sci. Technol. A 5*, 4, 1152 (1987) July/August.

[125] Denise M. Aylor and Patrick J. Moran, *Journal of Electrochemical Society*, 133, No. 5, 868 (1986).

[126] A.G. Guy and J.J. Hren, *Elements of Physical Metallurgy*, Third Edition, Addison-Wesley (1974).

[127] J.-F. Equey, S. Müller, J. Desilvestro and O. Haas, *Journal of Electrochemical Society*, 139, No. 6, 1499 (1992).

[128] H. Flor, *High purity potassium tetrafluoro-aluminate and method of making some*, United States Patent No. 5,242,669, September 7 (1993).

[129] D. Wong, L. Swette and F.H. Cocks, *Journal of Electrochemical Society*, 126, No. 1, 11 (1979).

[130] D.K. Hawksworth, Seminar on: *The Electrochemical and Metallurgical Properties of Materials Used for the Manufacture of Brazed Aluminium Heat Exchangers* (1996).

[131] Dr. D.K. Hawksworth, *A Review of the Corrosion Durability of Composite Deposition Technology Brazed Aluminium Heat Exchangers, Corrosion 5-99*, 19 may (1999).

[132] Markku Ainali and Rolf Sundberg; Donald K. Miner, *SAE Technical Paper Series*, No. 931108, 311 (1993).

APPENDIX A

Table I.i E_p values for multiple anodic polarisation of the AS, HT and CPC samples A exposed to 1M NaCl at various sweep rates.

Alloy sample	Sweep rate (mV/s)	E_p (mV) vs SCE at multiple sweeps						
		1	2	3	4	5	6	7
AS sample A	1	-739	-738	-739	-738	-736	-735	-737
	2.5	-740	-739	-741	-739	-737	-739	-738
	5	-743	-741	-741	-740	-739	-739	-737
	10	-740	-738	-739	-735	-735	-735	-735
	15	-729	-732	-735	-734	-737	-737	-735
	20	-730	-731	-734	-734	-735	-736	-735
	25	-732	-728	-730	-730	-731	-731	-732
HT sample A	1	-889	-883	-879	-878	-875	-870	-863
	2.5	-883	-877	-872	-869	-867	-858	-856
	5	-886	-873	-869	-868	-868	-870	-866
	10	-884	-879	-878	-879	-880	-882	-882
	15	-868	-876	-869	-872	-875	-875	-879
	20	-841	-834	-836	-834	-832	-824	-818
	25	-866	-861	-869	-840	-838	-847	-832
CPC sample A	1	-953	-882	-863	-855	-848	-837	-814
	2.5	-939	-906	-896	-885	-878	-861	-856
	5	-955	-936	-917	-906	-894	-887	-879
	10	-955	-935	-926	-911	-907	-900	-894
	15	-945	-928	-926	-921	-909	-904	-893
	20	-951	-938	-931	-926	-916	-918	-914
	25	-955	-943	-938	-937	-936	-935	-933

Table I.ii E_p values for multiple anodic polarisation of the AS, HT and CPC samples B exposed to 1M NaCl at various sweep rates.

Alloy sample	Sweep rate (mV/s)	E_p (mV) vs SCE at multiple sweeps						
		1	2	3	4	5	6	7
AS sample B	1	-734	-743	-744	-747	-746	-748	-748
	2.5	-746	-746	-749	-750	-753	-751	-751
	5	-738	-744	-740	-742	-744	-744	-745
	10	-704	-715	-730	-733	-736	-736	-738
	15	-736	-724	-724	-740	-742	-744	-745
	20	-725	-740	-740	-740	-739	-742	-745
	25	-725	-719	-728	-737	-737	-732	-733
HT sample B	1	-896	-891	-889	-888	-882	-879	-874
	2.5	-890	-884	-882	-879	-879	-880	-875
	5	-902	-893	-897	-897	-896	-897	-899
	10	-881	-877	-878	-877	-883	-887	-887
	15	-881	-876	-882	-875	-877	-875	-875
	20	-875	-865	-869	-877	-870	-873	-877
	25	-870	-873	-870	-872	-877	-887	-888
CPC sample B	1	-978	-953	-907	-894	-880	-861	-843
	2.5	-981	-972	-966	-960	-957	-954	-951
	5	-988	-979	-971	-965	-964	-961	-956
	10	-983	-977	-974	-972	-969	-967	-968
	15	-979	-973	-971	-966	-963	-963	-961
	20	-981	-976	-972	-968	-966	-961	-961
	25	-978	-971	-969	-963	-963	-962	-961

Table I.iii E_p values for multiple anodic polarisation of the AS, HT and CPC samples D exposed to 1M NaCl at various sweep rates.

Alloy sample	Sweep rate (mV/s)	E_p (mV) vs SCE at multiple sweeps						
		1	2	3	4	5	6	7
AS sample D	1	-889	-884	-884	-885	-883	-884	-883
	2.5	-877	-877	-875	-876	-881	-880	-882
	5	-878	-882	-884	-881	-878	-880	-883
	10	-875	-888	-888	-887	-886	-883	-884
	15	-876	-878	-873	-882	-880	-880	-883
	20	-860	-872	-878	-883	-882	-883	-882
	25	-868	-875	-871	-878	-873	-879	-879
HT sample D	1	-827	-821	-815	-815	-810	-810	-807
	2.5	-824	-821	-818	-814	-814	-812	-810
	5	-830	-832	-829	-826	-828	-824	-824
	10	-821	-833	-827	-824	-820	-820	-821
	15	-818	-822	-822	-822	-817	-818	-817
	20	-828	-842	-834	-830	-829	-830	-830
	25	-849	-858	-853	-848	-847	-840	-838
CPC sample D	1	-1041	-1027	-1000	-948	-925	-909	-895
	2.5	-1045	-1043	-1038	-1031	-1024	-1018	-1012
	5	-1036	-1031	-1033	-1032	-1026	-1017	-1015
	10	-1033	-1037	-1035	-1034	-1031	-1028	-1027
	15	-1033	-1034	-1036	-1036	-1038	-1038	-1036
	20	-1023	-1027	-1026	-1026	-1024	-1025	-1022
	25	-1025	-1027	-1029	-1032	-1028	-1025	-1026

Table I.iv E_p values for multiple anodic polarisation of the AS, HT and CPC samples E exposed to 1M NaCl at various sweep rates.

Alloy sample	Sweep rate (mV/s)	E_p (mV) vs SCE at multiple sweeps						
		1	2	3	4	5	6	7
AS sample E	1	-764	-767	-768	-764	-767	-763	-762
	2.5	-764	-762	-772	-767	-761	-767	-761
	5	-760	-759	-765	-763	-757	-759	-765
	10	-750	-769	-764	-770	-771	-764	-762
	15	-737	-769	-772	-766	-765	-763	-764
	20	-727	-780	-764	-761	-761	-766	-762
	25	-699	-758	-754	-765	-763	-760	-761
HT sample E	1	-761	-729	-719	-703	-688	-686	-680
	2.5	-742	-732	-723	-720	-714	-710	-706
	5	-744	-737	-735	-731	-727	-724	-720
	10	-747	-731	-726	-719	-715	-712	-710
	15	-743	-732	-724	-719	-714	-712	-709
	20	-746	-737	-725	-721	-719	-714	-715
	25	-750	-736	-730	-728	-722	-718	-713
CPC sample E	1	-784	-745	-736	-732	-730	-726	-723
	2.5	-979	-954	-938	-886	-865	-850	-834
	5	-980	-971	-961	-955	-941	-929	-911
	10	-982	-972	-965	-960	-957	-951	-946
	15	-974	-968	-966	-958	-956	-947	-945
	20	-972	-965	-962	-955	-950	-945	-941
	25	-973	-967	-963	-957	-956	-951	-944

Table II.i E_p values for multiple anodic polarisation of the AS, HT and CPC samples E exposed to 1M NaCl + 0.5M H_2SO_4 at various sweep rates.

Alloy sample	Sweep rate (mV/s)	E_p (mV) vs SCE at multiple sweeps						
		1	2	3	4	5	6	7
AS sample A	1	-774	-772	-769	-764	-760	-759	-757
	2.5	-774	-773	-775	-771	-768	-766	-763
	5	-770	-769	-768	-767	-768	-767	-766
	10	-763	-769	-769	-769	-770	-770	-769
	15	-762	-765	-761	-762	-760	-759	-760
	20	-758	-763	-764	-764	-765	-766	-765
	25	-752	-744	-748	-752	-750	-754	-753
HT sample A	1	-887	-878	-865	-851	-838	-829	-822
	2.5	-880	-875	-866	-865	-862	-856	-851
	5	-878	-875	-872	-868	-867	-862	-858
	10	-868	-865	-862	-864	-863	-859	-863
	15	-865	-863	-862	-862	-859	-857	-856
	20	-864	-858	-856	-855	-859	-853	-849
	25	-871	-866	-865	-865	-864	-861	-858
CPC sample A	1	-774	-762	-755	-749	-745	-743	-740
	2.5	-785	-770	-765	-761	-756	-754	-748
	5	-790	-777	-768	-764	-761	-757	-754
	10	-794	-785	-771	-766	-762	-760	-754
	15	-805	-781	-771	-766	-762	-763	-756
	20	-778	-768	-765	-762	-759	-755	-754
	25	-788	-777	-773	-769	-766	-762	-761

Table II.ii E_p values for multiple anodic polarisation of the AS, HT and CPC samples B exposed to 1M NaCl + 0.5M H_2SO_4 at various sweep rates.

Alloy sample	Sweep rate (mV/s)	E_p (mV) vs SCE at multiple sweeps						
		1	2	3	4	5	6	7
AS sample B	1	-757	-757	-758	-763	-762	-763	-761
	2.5	-745	-747	-743	-744	-747	-749	-752
	5	-738	-731	-728	-730	-735	-736	-733
	10	-721	-733	-722	-715	-727	-737	-729
	15	-733	-725	-723	-726	-729	-731	-732
	20	-718	-727	-739	-731	-728	-731	-727
	25	-706	-727	-716	-717	-713	-721	-727
HT sample B	1	-884	-882	-880	-874	-872	-869	-865
	2.5	-872	-874	-871	-869	-864	-864	-863
	5	-870	-872	-869	-868	-871	-865	-861
	10	-867	-864	-861	-862	-859	-862	-859
	15	-857	-853	-857	-854	-848	-848	-849
	20	-862	-860	-860	-862	-859	-855	-853
	25	-855	-859	-861	-864	-858	-853	-859
CPC sample B	1	-780	-773	-768	-760	-757	-756	-755
	2.5	-805	-785	-776	-770	-769	-766	-766
	5	-825	-799	-788	-780	-774	-771	-767
	10	-823	-802	-794	-787	-786	-781	-779
	15	-822	-803	-793	-789	-784	-781	-777
	20	-826	-801	-789	-783	-782	-778	-774
	25	-821	-804	-789	-788	-783	-780	-777

Table II.iii E_p values for multiple anodic polarisation of the AS, HT and CPC samples D exposed to 1M NaCl + 0.5M H_2SO_4 at various sweep rates.

Alloy sample	Sweep rate (mV/s)	E_p (mV) vs SCE at multiple sweeps						
		1	2	3	4	5	6	7
AS sample D	1	-905	-904	-903	-901	-901	-902	-901
	2.5	-907	-904	-901	-901	-898	-896	-896
	5	-903	-891	-895	-891	-890	-886	-884
	10	-901	-890	-884	-881	-881	-880	-880
	15	-899	-889	-886	-888	-884	-881	-878
	20	-889	-880	-878	-875	-874	-871	-869
	25	-888	-877	-869	-868	-866	-863	-860
HT sample D	1	-856	-848	-843	-837	-831	-823	-814
	2.5	-879	-865	-859	-856	-854	-850	-850
	5	-873	-855	-855	-849	-846	-845	-846
	10	-874	-866	-863	-858	-857	-852	-851
	15	-867	-851	-840	-839	-837	-836	-834
	20	-868	-852	-848	-851	-846	-844	-845
	25	-881	-867	-854	-846	-847	-850	-842
CPC sample D	1	-839	-816	-793	-778	-769	-763	-761
	2.5	-868	-847	-839	-832	-819	-810	-797
	5	-881	-865	-859	-850	-847	-842	-839
	10	-889	-875	-867	-860	-856	-851	-847
	15	-896	-881	-872	-865	-858	-851	-845
	20	-900	-880	-871	-865	-859	-850	-850
	25	-902	-886	-880	-873	-864	-860	-856

Table II.iv E_p values for multiple anodic polarisation of the AS, HT and CPC samples E exposed to 1M NaCl + 0.5M H_2SO_4 at various sweep rates.

Alloy sample	Sweep rate (mV/s)	E_p (mV) vs SCE at multiple sweeps						
		1	2	3	4	5	6	7
AS sample E	1	-793	-787	-782	-777	-776	-773	-774
	2.5	-792	-789	-787	-784	-786	-781	-778
	5	-796	-792	-789	-789	-788	-785	-781
	10	-789	-789	-791	-790	-789	-788	-786
	15	-788	-790	-791	-789	-786	-785	-785
	20	-793	-791	-792	-788	-786	-787	-784
	25	-775	-781	-784	-778	-775	-773	-774
HT sample E	1	-805	-798	-794	-790	-788	-774	-764
	2.5	-805	-797	-792	-790	-788	-784	-782
	5	-801	-798	-794	-788	-785	-784	-780
	10	-805	-798	-791	-790	-787	-777	-776
	15	-803	-795	-795	-789	-784	-787	-787
	20	-795	-799	-793	-796	-788	-785	-778
	25	-796	-795	-785	-778	-783	-779	-774
CPC sample E	1	-792	-767	-757	-747	-743	-735	-728
	2.5	-859	-830	-813	-802	-794	-790	-784
	5	-869	-843	-819	-806	-799	-794	-788
	10	-865	-846	-829	-816	-803	-799	-794
	15	-876	-847	-830	-819	-809	-801	-795
	20	-864	-840	-827	-818	-810	-803	-800
	25	-887	-865	-845	-831	-821	-812	-806

Table III.i E_p values for multiple anodic polarisation of the AS, HT and CPC samples A exposed to 1M NaCl + 0.5M H_2SO_4 + 0.5M $NaNO_3$ at various sweep rates.

Alloy sample	Sweep rate (mV/s)	E_p (mV) vs SCE at multiple sweeps						
		1	2	3	4	5	6	7
AS sample A	1	-622	-618	-616	-608	-605	-604	-602
	2.5	-610	-614	-612	-612	-612	-612	-612
	5	-608	-608	-611	-609	-609	-610	-609
	10	-609	-608	-608	-610	-607	-610	-608
	15	-601	-606	-609	-610	-609	-612	-610
	20	-600	-600	-602	-604	-605	-606	-604
	25	-590	-596	-598	-600	-602	-604	-605
HT sample A	1	-711	-684	-672	-667	-662	-656	-650
	2.5	-722	-701	-692	-685	-681	-673	-669
	5	-721	-710	-703	-699	-696	-692	-688
	10	-726	-716	-712	-710	-707	-706	-701
	15	-713	-699	-696	-693	-694	-693	-700
	20	-706	-717	-705	-701	-699	-696	-692
	25	-709	-703	-695	-695	-690	-691	-698
CPC sample A	1	-662	-626	-616	-611	-609	-607	-608
	2.5	-687	-666	-652	-638	-626	-619	-612
	5	-698	-686	-673	-666	-660	-653	-649
	10	-702	-686	-677	-673	-663	-657	-657
	15	-718	-699	-689	-686	-684	-680	-679
	20	-718	-700	-695	-691	-689	-685	-682
	25	-730	-714	-702	-698	-695	-693	-689

Table III.ii E_p values for multiple anodic polarisation of the AS, HT and CPC samples B exposed to 1M NaCl + 0.5M H_2SO_4 + 0.5M $NaNO_3$ at various sweep rates.

Alloy sample	Sweep rate (mV/s)	E_p (mV) vs SCE at multiple sweeps						
		1	2	3	4	5	6	7
AS sample B	1	-623	-619	-621	-621	-619	-617	-617
	2.5	-615	-605	-606	-611	-614	-610	-617
	5	-626	-614	-611	-604	-601	-603	-606
	10	-602	-620	-612	-614	-607	-611	-611
	15	-618	-608	-618	-609	-610	-610	-603
	20	-611	-593	-602	-600	-603	-603	-602
	25	-605	-598	-580	-600	-601	-602	-592
HT sample B	1	-767	-763	-760	-758	-754	-748	-741
	2.5	-790	-778	-775	-771	-771	-767	-763
	5	-804	-797	-791	-788	-784	-778	-776
	10	-797	-791	-788	-783	-779	-777	-775
	15	-801	-791	-781	-784	-776	-768	-765
	20	-810	-807	-804	-807	-808	-806	-808
	25	-815	-805	-800	-796	-788	-785	-778
CPC sample B	1	-703	-682	-671	-661	-647	-643	-640
	2.5	-739	-712	-699	-689	-678	-671	-658
	5	-743	-721	-706	-690	-687	-676	-667
	10	-752	-724	-703	-690	-682	-670	-667
	15	-764	-737	-719	-707	-699	-690	-685
	20	-762	-739	-728	-714	-707	-701	-689
	25	-762	-737	-727	-717	-710	-703	-696

Table III.iii E_p values for multiple anodic polarisation of the AS, HT and CPC samples D exposed to 1M NaCl + 0.5M H_2SO_4 + 0.5M $NaNO_3$ at various sweep rates.

Alloy sample	Sweep rate (mV/s)	E_p (mV) vs SCE at multiple sweeps						
		1	2	3	4	5	6	7
AS sample D	1	-710	-712	-710	-708	-710	-709	-709
	2.5	-716	-717	-717	-717	-720	-717	-718
	5	-714	-714	-716	-716	-719	-716	-717
	10	-715	-707	-706	-707	-705	-706	-706
	15	-707	-704	-704	-705	-702	-701	-702
	20	-711	-707	-707	-703	-705	-703	-704
	25	-709	-707	-706	-704	-704	-706	-705
HT sample D	1	-725	-721	-720	-719	-722	-711	-706
	2.5	-728	-722	-727	-722	-722	-721	-724
	5	-718	-708	-708	-712	-705	-707	-710
	10	-728	-719	-717	-714	-722	-724	-718
	15	-731	-722	-718	-728	-724	-719	-718
	20	-732	-720	-727	-723	-725	-729	-720
	25	-711	-700	-700	-710	-694	-690	-697
CPC sample D	1	-771	-746	-738	-731	-726	-717	-717
	2.5	-783	-758	-749	-738	-737	-725	-725
	5	-802	-773	-763	-755	-750	-740	-740
	10	-811	-789	-776	-773	-758	-745	-745
	15	-822	-798	-787	-772	-760	-756	-756
	20	-829	-794	-782	-772	-764	-747	-747
	25	-835	-807	-794	-779	-773	-773	-773

Table III.iv E_p values for multiple anodic polarisation of the AS, HT and CPC samples E exposed to 1M NaCl + 0.5M H_2SO_4 + 0.5M $NaNO_3$ at various sweep rates.

Alloy sample	Sweep rate (mV/s)	E_p (mV) vs SCE at multiple sweeps						
		1	2	3	4	5	6	7
AS sample E	1	-572	-571	-567	-567	-564	-567	-568
	2.5	-574	-568	-564	-565	-565	-572	-569
	5	-568	-567	-564	-565	-567	-570	-569
	10	-560	-553	-550	-542	-546	-551	-556
	15	-558	-551	-550	-541	-542	-541	-544
	20	-557	-551	-550	-543	-557	-551	-554
	25	-553	-542	-538	-535	-542	-543	-539
HT sample E	1	-563	-553	-550	-548	-546	-544	-547
	2.5	-571	-562	-561	-557	-556	-553	-553
	5	-572	-559	-557	-553	-551	-551	-550
	10	-567	-558	-556	-554	-553	-553	-550
	15	-568	-561	-562	-552	-556	-549	-548
	20	-567	-566	-563	-556	-553	-552	-552
	25	-566	-558	-557	-555	-551	-547	-546
CPC sample E	1	-649	-612	-600	-597	-595	-589	-584
	2.5	-685	-641	-623	-613	-602	-598	-594
	5	-684	-643	-620	-607	-596	-592	-589
	10	-686	-665	-641	-627	-615	-610	-604
	15	-699	-682	-660	-639	-633	-622	-616
	20	-695	-680	-661	-642	-628	-618	-613
	25	-700	-685	-675	-655	-647	-629	-626

APPENDIX B

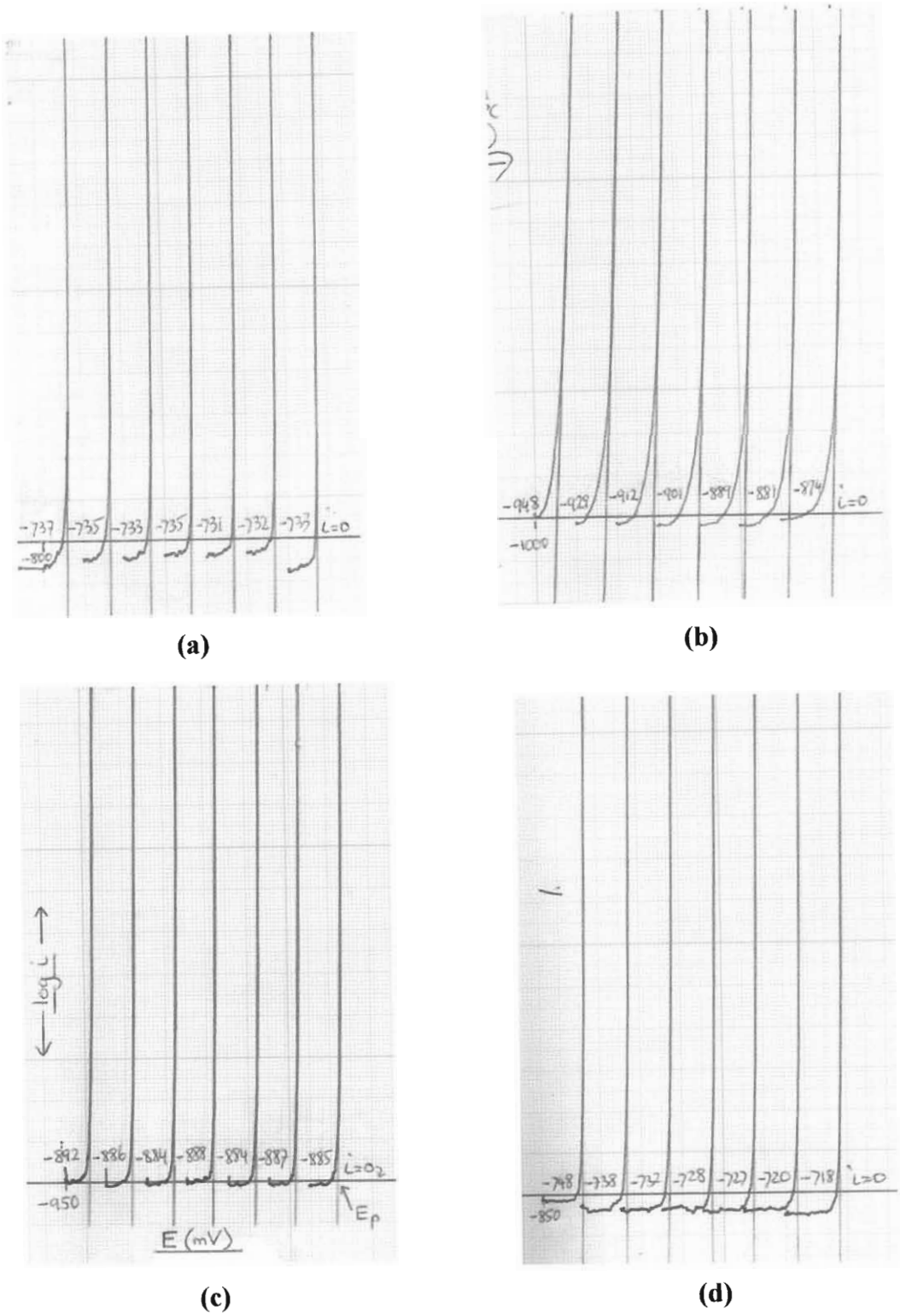

(a) **(b)**

(c) **(d)**

Figure I.i Multiple anodic polarisation curves obtained in the 1M NaCl solution for (a) AS sample A, (b) CPC sample A, (c) AS sample D and (d) HT sample E.

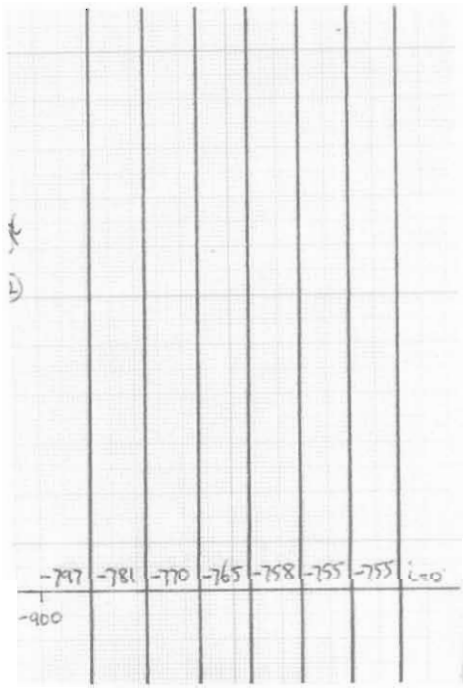

(a)

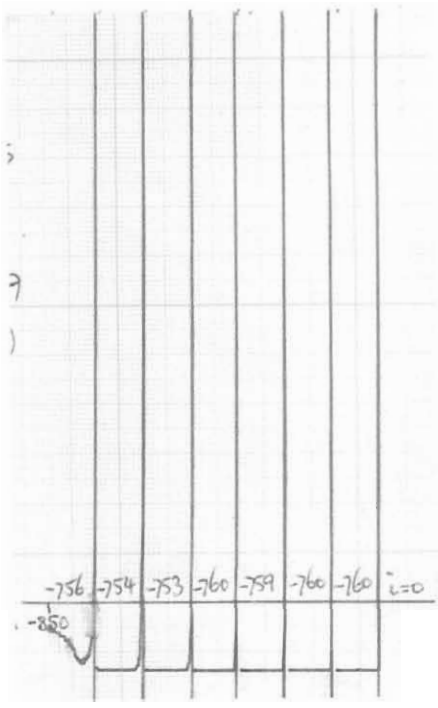

(b)

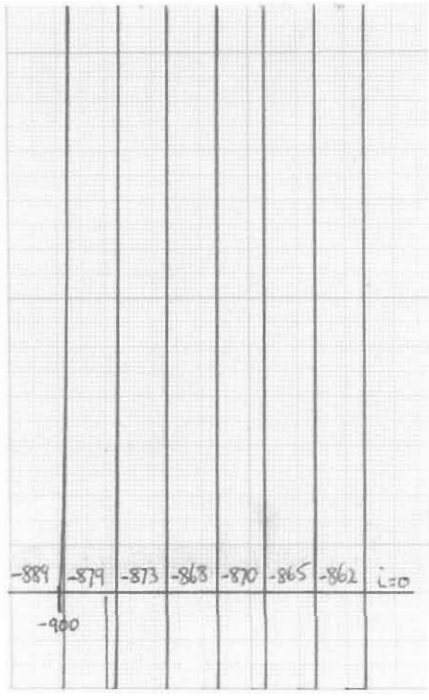

(c)

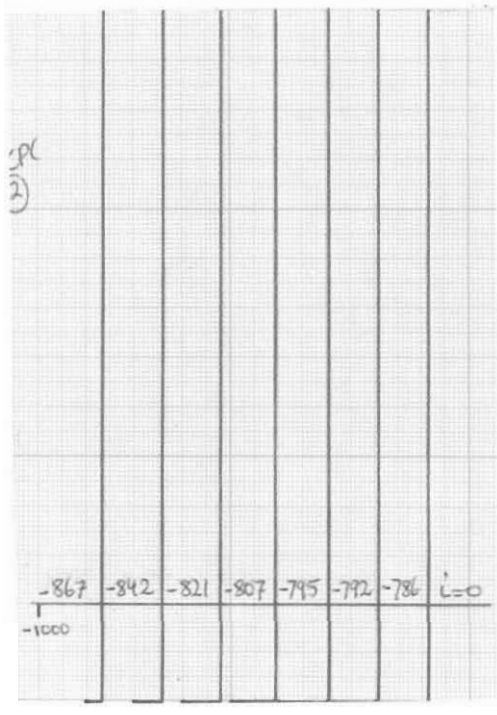

(d)

Figure I.ii Multiple anodic polarisation curves obtained in the 1M NaCl + 0.5M H_2SO_4 solution for (a) CPC sample A, (b) AS sample B, (c) HT sample E and (d) CPC sample E.

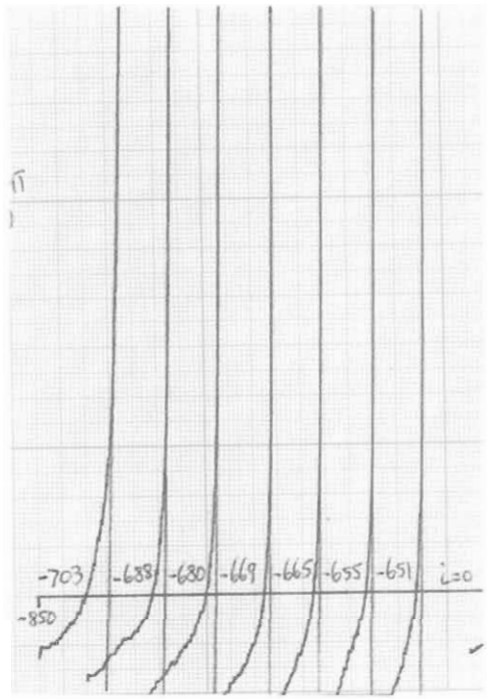

(a)

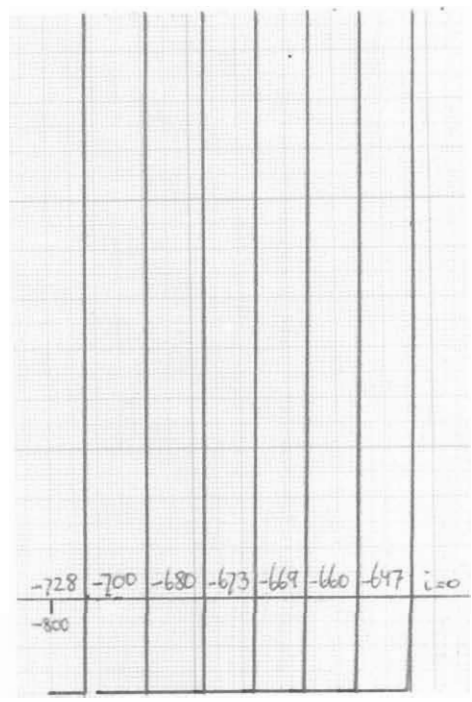

(b)

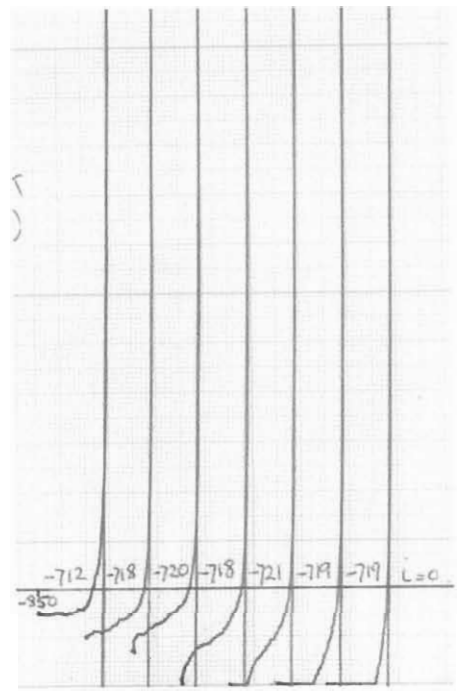

(c)

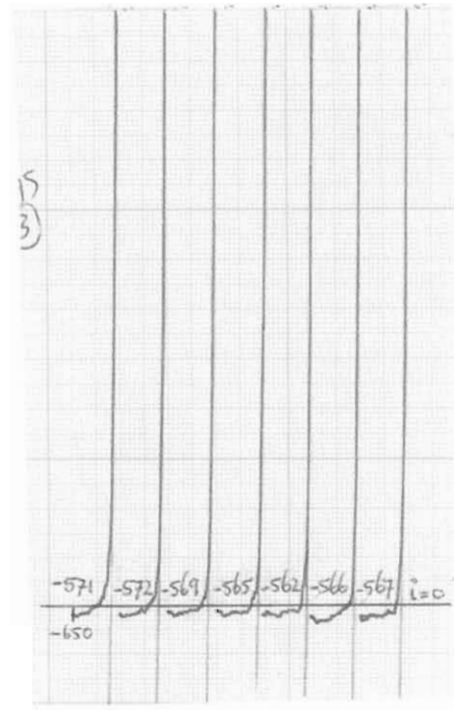

(d)

Figure I.iii Multiple anodic polarisation curves obtained in the 1M NaCl + 0.5M H_2SO_4 + 0.5M $NaNO_3$ solution for (a) HT sample A, (b) CPC sample B, (c) HT sample D and (d) AS sample E.